

Parametric instabilities in variable angle tow composite panels

Surya Samukham

A Thesis Submitted to
Indian Institute of Technology Hyderabad
in Partial Fulfillment of the Requirements for
the Degree of Doctor of Philosophy



भारतीय प्रौद्योगिकी संस्थान हैदराबाद
Indian Institute of Technology Hyderabad

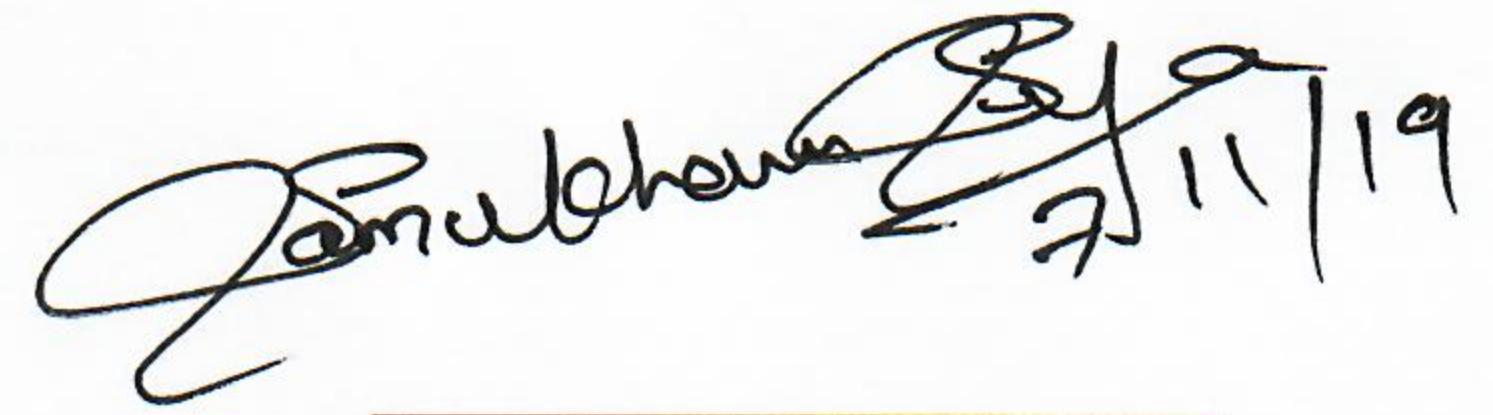
DEPARTMENT OF MECHANICAL AND AEROSPACE ENGINEERING

AUGUST 2019

© Copyright by Surya Samukham, 2019.
All Rights Reserved

Declaration

I declare that this written submission represents my ideas in my own words, and where ideas or words of others have been included, I have adequately cited and referenced the original sources. I also declare that I have adhered to all principles of academic honesty and integrity and have not misrepresented or fabricated or falsified any idea/data/fact/source in my submission. I understand that any violation of the above will be a cause for disciplinary action by the Institute and can also evoke penal action from the sources that have thus not been properly cited, or from whom proper permission has not been taken when needed.



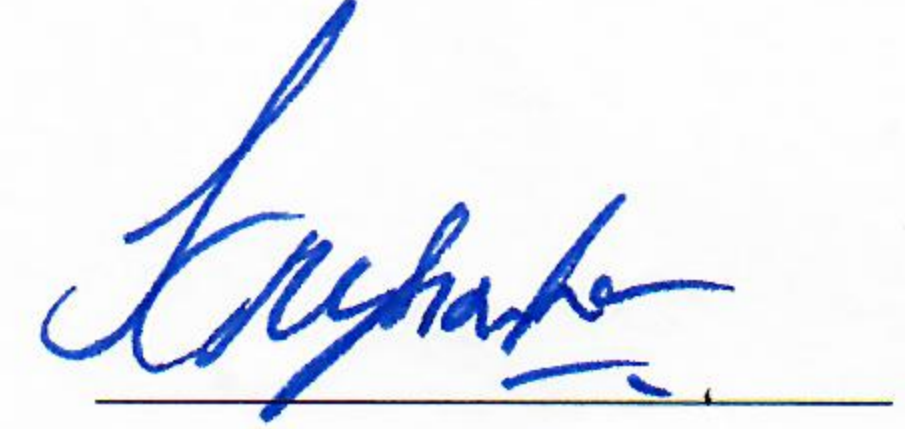
(Signature)

Surya Samukham

Roll No.: ME13M15P000008

Approval Sheet

This Thesis entitled "Parametric instabilities in variable angle tow composite panels" by Surya Samukham is approved for the degree of Doctor of Philosophy from Indian Institute of Technology Hyderabad



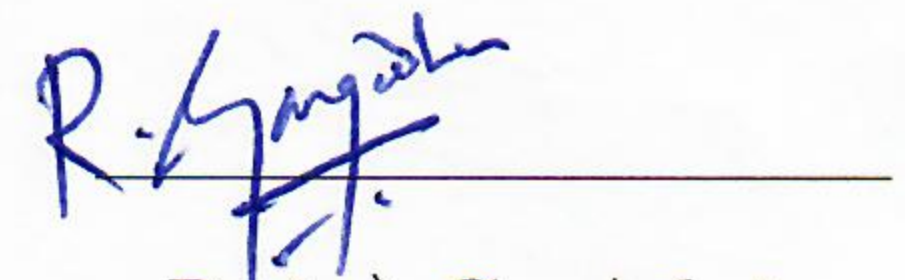
(Prof. K. R. Yogendra Simha) Examiner
Department of Mechanical Engineering
Indian Institute of Science, Bangalore



(Dr. Viswanath Chinthapenta) Examiner
Dept. of Mech. and Aerospace Eng.
Indian Institute of Technology Hyderabad



(Dr. C. P. Vyasarayani) Adviser
Dept. of Mech. and Aerospace Eng.
Indian Institute of Technology Hyderabad



(Dr. Gangadharan Raju) Co-Adviser
Dept. of Mech. and Aerospace Eng.
Indian Institute of Technology Hyderabad



(Dr. S. Suriya Prakash) Chairman
Dept. of Civil Eng.
Indian Institute of Technology Hyderabad

Acknowledgements

First, I would like to offer my sincerest gratitude to my advisers Dr. Chandrika Prakash Vyasarayani and Dr. Gangadharan Raju for their continuous support during my Ph.D. study and research. Their patience, motivation, enthusiasm, and immense knowledge was much appreciated. Their guidance was helpful both, during the time of my research and in the writing of this thesis. I was always welcome to discuss both professional and personal matters at any time without any hesitation. It was a fantastic experience to work with them. I feel blessed to have them as my advisers and mentors for my Ph.D. study.

I would like to extend my gratitude to the doctoral committee: Prof. Ramji M., Dr. Viswanath Chinthapenta, and Dr. Balaji Iyer, for their insightful comments, encouragement, and also for the challenging questions that encouraged me to widen the scope of my research and have a multi-perspective approach to it.

I am particularly grateful to the Ministry of Human Resource Development, Government of India, for their financial assistance during my Ph.D., and the Department of Mechanical and Aerospace Engineering for providing all the resources that were required to carry out hassle-free research.

I would also like to thank Prof. R. Prasanth Kumar, Dr. Ashok Kumar Pandey, Dr. Harish Nagaraj Dixit, Dr. Venkatesham, and Dr. Syed Nizamuddin Khaderi for teaching me various interesting courses that broadened my knowledge.

I thank my fellow labmates Ajinkya, Ashwanth, Damodar, Junaidvali, Lala Bahadur, Naresh, Nitish, Sayan, Shanti, Sumit and Varun, for the stimulating discussions and friendly diversions over the last four years. These are the people who made our research lab a fantastic place to work. Also, I thank my friend and roommate, Suman for his companionship that brought levity to my academic life during my stay here.

I would like to offer my special thanks to Roshni, who offered me immense moral and emotional assistance with her own brand of humor over the last several years. I am also indebted to all my family members who have supported me along the way.

Most importantly, I must express my very profound gratitude to my parents for providing me with all forms of support and continuous encouragement throughout my life. This dissertation stands as a testament to their unconditional love. Thank you.

Abstract

Advancement in the automation of composite manufacturing techniques like automated fiber placement, embroidery fiber placement, and continuous tow shearing enables the three-dimensional elastic tailoring and the concept of tow placement. This technology allows the tows to be steered in principal load direction paths in composite structures. These composites with curvilinear fibers exhibit spatially varying stiffness, and are termed as variable angle tow (VAT) composite laminates. Elastic tailoring has been successfully performed to improve the modal, buckling, and post-buckling performance of the VAT structures.

Aircraft structures like fuselage and wings are often subjected to dynamic loads in addition to the static loads. These structures, under periodic in-plane loads, exhibit parametric resonance for certain combinations of the excitation frequencies and loads. Therefore, the present thesis work focuses on investigating the dynamic stability behavior of VAT composite panels under in-plane periodic compression load. Since the fiber orientation in the VAT panel changes with the position, the stiffness properties vary continuously across the lamina. As a result, unlike straight-fiber composites, in VAT panels, the in-plane stress distributions over the laminate are non-uniform even under uniform compression load. Therefore, pre-buckling analysis has to be carried out first to determine the non-uniform in-plane stress distributions due to the applied load along the edges. Then the evaluated stress distributions are used to investigate the dynamic stability characteristics of the VAT panel.

A flat VAT panel, a delaminated VAT panel with a cutout, and a curved VAT panel are tailored for enhancing the dynamic performance under periodic axial compression load. A linear fiber-angle variation with symmetric VAT layup has been considered, and the effect of fiber-angle variation on the dynamic stability behavior of the VAT composites is studied. The performance of the VAT panel is then compared with the straight-fiber laminates. In addition, the effect of various other parameters like boundary conditions, orthotropy ratio, aspect ratio, span-thickness ratio, delamination area, and radius of curvature on the dynamic stability behavior of the VAT panel is studied. Further, new evidence on the benefits of tow-steering over the straight-fiber composites in tailoring the dynamic stability and stiffness properties of the VAT panel simultaneously is reported.

Subsequently, an implicit Floquet analysis is used to determine the dynamic stability characteristics of the VAT panel. In the literature dealing with the stability of structures with time-periodic loads, Bolotin's method is widely used for determining the instability regions. However, Bolotin's approach is an approximate method, and the evaluated instability regions are accurate only up to certain limit. To avoid this, Floquet theory can be used to determine the accurate dynamic stability characteristics of the systems. In Floquet theory, a Floquet transition matrix (FTM) is computed, and the dominant eigenvalue of the FTM determine the stability of the system. However, for large degree of freedom systems like finite element models of VAT panels, calculation of FTM becomes computationally expensive. Whereas, an implicit Floquet analysis can significantly reduce the computational load. In this technique, the dominant eigenvalue of the FTM is computed without the explicit computation of the full FTM matrix. Also, unlike Bolotin's method, Floquet analysis provides information about the effective damping present at different locations in the parametric space and the nature of bifurcation through which the stability is lost.

Contents

Declaration	iii
Approval Sheet	iv
Acknowledgements	v
Abstract	vi
List of Figures	x
List of Tables	xv
Nomenclature	xvi
1 Introduction	1
1.1 Manufacturing of VAT composite panel	6
1.2 Literature review	7
1.2.1 VAT composites	7
1.2.2 Dynamic stability in composite panels	10
1.2.3 Dynamic stability in curved composite panels	16
1.3 Motivation	18
1.4 Scope of the thesis	18
1.5 Organization of the thesis	19
2 Parametric instabilities in flat VAT composite panel	23
2.1 Modeling of VAT composite panel	23
2.2 First-order shear deformation theory	24
2.2.1 Stress-strain relationship	27
2.2.2 Resultant stresses and generalized constitutive matrix	30
2.2.3 Energy expressions	31
2.2.4 Finite element analysis	33
2.3 Analysis of VAT panel	35
2.4 Results and discussion	38

2.5	Dynamic instability in VAT laminate	41
2.5.1	Case-I	41
2.5.2	Case-II	44
2.5.3	Effect of static load parameter	45
2.5.4	Effect of plate boundary conditions	45
2.5.5	Effect of orthotropy ratio	48
2.5.6	Effect of aspect ratio and span-thickness ratio	48
2.6	Summary	49
3	Parametric instabilities in delaminated VAT composite panel with a cutout	51
3.1	Modeling of VAT laminate	52
3.1.1	Finite element formulation for un-delaminated portion	53
3.1.2	Finite element formulation for delaminated portion	55
3.1.3	Continuity conditions	56
3.2	Dynamic stability analysis	58
3.3	Results and discussions	59
3.3.1	Model validation	60
3.3.2	Effect of fiber-angle variation on critical buckling load and dynamic stability in a VAT laminate with a cutout	63
3.3.3	Effect of fiber-angle variation on buckling load and dynamic stability in a delaminated VAT laminate with a cutout	68
3.4	Summary	73
4	Parametric instabilities in curved VAT composite panel	75
4.1	Modeling of VAT laminate	76
4.2	Generalized differential integral quadrature method	78
4.3	Dynamic stability in curved VAT panel	86
4.4	Results and discussion	87
4.4.1	Dynamic instability in curved VAT panel	91
4.4.2	Variation of buckling load and dynamic instability index of a curved VAT panel	92
4.5	Summary	98

5	Implicit Floquet analysis for parametric instabilities in a VAT composite panel	100
5.1	Modeling of the VAT panel	102
5.1.1	Pre-buckling analysis	104
5.1.2	Buckling analysis	106
5.1.3	Modal analysis	106
5.1.4	Boundary conditions	107
5.2	Dynamic instability using Bolotin's approach	107
5.3	Floquet theory	110
5.4	Arnoldi algorithm	111
5.4.1	Newmark integration	114
5.5	Results and discussion	115
5.5.1	Dynamic instability analysis of VAT panel	119
5.6	Summary	129
6	Conclusions	131
6.1	Remarks	133
6.2	Future work	136
	Appendices	137
A	Analytical formulation	137
A.1	Natural frequency of an orthotropic simply-supported composite laminate	137
A.2	Critical buckling load of an orthotropic simply-supported composite laminate under axial compression	138
	References	141

List of Figures

1.1	(a) Cross-sectional view of aircraft fuselage ¹ (b) Buckling of fuselage under compression load (c) Fundamental cases of compression plate buckling.	2
1.2	Composites in aerospace industry: (a) Rocket fuel-tank developed by NASA & Boeing (b) NASA's composite crew module (c) Boeing 787 Dreamliner composite fuselage.	4
1.3	Tow-placement machine producing plies with curvilinear fibre path (Courtesy of Electroimpact composite manufacturing).	4
1.4	Schematic representation of: (a) Straight-fiber composite laminate (b) Variable angle tow composite laminate.	5
1.5	Images of tow-steering and variable stiffness structures: (a) Optimized fiber-angle distribution for maximum buckling load (b) Manufacturing of an optimized variable stiffness composite plate using the continuous tow steering technique (c) A completed VAT panel [1].	5
2.1	Schematic of a VAT lamina.	24
2.2	Sign convention for the displacements and the rotations of the normal in FSDT.	25
2.3	Displacements and rotations in a plate with bending and in-plane effects: (a) Plane xz (b) Plane yz	26
2.4	Schematic representation of a VAT laminate: (a) Cross-sectional view and definition of the layers in a VAT laminate (b) VAT composite layup and axes representation.	28
2.5	VAT composite laminate subjected to uniform in-plane periodic compression load.	36
2.6	Schematic of the VAT laminate.	38
2.7	Variation of normalized frequency ($\tilde{\omega}$) with static buckling load parameter (α_0) for a simply-supported VAT laminate $[0 \pm \langle 0 30 \rangle]_{3s}$	40

2.8	First and second instability regions of a symmetric simply-supported cross-ply laminate $[0/90/90/0]$	40
2.9	Types of in-plane boundary conditions: (a) Case-I: Transverse edges are free (b) Case-II: Transverse edges are fixed.	41
2.10	Principal DIRs of a simply-supported VAT laminate $[90 \pm \langle 0 T_1 \rangle]_{3s}$ for different fiber-angles (T_1) for Case-I boundary condition under periodic axial compression.	42
2.11	Variation of normalized dynamic instability index (D_{II}) of a simply-supported VAT laminate $[90 \pm \langle T_0 T_1 \rangle]_{3s}$ for different fiber-angles T_0 and T_1 for Case-I boundary condition.	44
2.12	Variation of normalized dynamic instability index (D_{II}) of a simply supported square VAT laminate $[0 \pm \langle T_0 T_1 \rangle]_{3s}$ for different values of T_0 and T_1 for Case-II boundary condition.	45
2.13	Effect of static load parameter (α_0) on the principle DIR of the VAT laminate, $[90 \pm \langle 0 75 \rangle]_{3s}$ for different values of α_0 : (a) Normalized frequency ($\tilde{\Omega}$) versus normalized buckling load (K_{cr}) (b) Dynamic instability index (D_{II}) versus static load parameter (α_0).	46
2.14	Effect of plate boundary conditions on the principle DIR for the VAT laminate $[90 \pm \langle 0 75 \rangle]_{3s}$ subjected to periodic axial compression.	47
2.15	Variation of D_{II} of a VAT laminate $[90 \pm \langle T_0 T_1 \rangle]_{3s}$ for different values of T_0 and T_1 subjected to periodic axial compression: (a) CSCS boundary condition (b) CCCC boundary condition.	47
2.16	Effect of orthotropy on the principle DIR of a VAT laminate $[90 \pm \langle 0 75 \rangle]_{3s}$ for different values of (E_{11}/E_{22}): (a) Normalized frequency ($\tilde{\Omega}$) versus Normalized buckling load (K_{cr}) (b) Dynamic instability index (D_{II}) versus orthotropy ratio (E_{11}/E_{22}).	48
2.17	Effect of aspect ratio on the DIR of a VAT laminate $[90 \pm \langle 0 75 \rangle]_{3s}$ for different values of a/b ratio.	49
2.18	Effect of span-thickness ratio on the DIR of a VAT laminate $[90 \pm \langle 0 75 \rangle]_{3s}$ for different values of a/h ratio.	50
3.1	Schematic of a delaminated VAT laminate with a circular cutout.	52
3.2	Schematic of the laminate with delaminated and un-delaminated portions.	52
3.3	Elements at connecting boundary.	57

3.4	Variation of normalized critical buckling load (K_{cr}) with respect to NDA value of a VAT composite laminate $[0 \pm \langle 0 30 \rangle]_{4s}$ with an embedded delamination obtained for two different delamination positions (NDP = 0.5 and 0.25).	63
3.5	Variation of normalized fundamental frequency ($\tilde{\omega}$) with respect to the static in-plane compression load (K_{cr}) of the VAT laminate $[0 \pm \langle 0 30 \rangle]_{4s}$ with an embedded delamination obtained for different values of NDA (0.0, 0.25, 0.49 and 0.64).	64
3.6	Principle DIRs of a VAT laminate $[0 \pm \langle 0 30 \rangle]_{4s}$ with an embedded delamination shown in the plane of normalized frequency versus normalized critical load for different NDA values (0.0, 0.25, 0.49, 0.81).	64
3.7	Schematic diagram of a VAT laminate with a circular cutout.	65
3.8	Variation of normalized critical buckling load (K_{cr}) with respect to normalized pre-buckling stiffness (E_{vat}) of a VAT laminate $[90 \pm \langle T_0 T_1 \rangle]_{4s}$ with a circular cutout (NDH=0.2) for different fiber-angles (T_0 and T_1).	66
3.9	Principle DIRs of a VAT laminate $[90 \pm \langle 0 T_1 \rangle]_{4s}$ with a circular cutout (NDH=0.2) for different fiber-angles (T_1).	67
3.10	Variation of normalized D_{II} with respect to normalized pre-buckling stiffness (E_{vat}) of a VAT laminate $[90 \pm \langle T_0 T_1 \rangle]_{4s}$ with circular cutout (NDH=0.2) for different fiber-angles (T_0 and T_1).	68
3.11	Schematic diagram of a VAT laminate with a delamination around a circular cutout.	69
3.12	Variation of normalized critical buckling load (K_{cr}) with respect to the normalized pre-buckling stiffness (E_{vat}) of a VAT laminate $[90 \pm \langle T_0 T_1 \rangle]_{4s}$ with a circular cutout (NDH=0.2), for different fiber-angles (T_0 and T_1) and different NDA values (0.16, 0.25, 0.36 and 0.49).	70
3.13	Principle DIRs of a VAT laminate $[90 \pm \langle T_0 T_1 \rangle]_{4s}$ with a circular cutout (NDH=0.2) for different fiber-angles (T_1) and different NDA values (0.16, 0.25, 0.36 and 0.49).	71
3.14	Principle DIRs of a VAT laminate $[90 \pm \langle 0 80 \rangle]_{4s}$ for different conditions.	72
3.15	Variation of normalized D_{II} with respect to normalized pre-buckling stiffness (E_{vat}) of a VAT laminate $[90 \pm \langle T_0 T_1 \rangle]_{4s}$ with a circular cutout (NDH=0.2) for different fiber-angles (T_0 and T_1) and different NDA values (0.16, 0.25, 0.36 and 0.49).	72
4.1	Schematic representation of a curved panel with VAT laminate.	76

4.2	A one-dimensional grid of a function $f(x)$ with the grid-point numbering system.	79
4.3	A two-dimensional Chebyshev grid plotted on the surface of a curved panel with the grid-point numbering system.	80
4.4	Schematic representation of in-plane boundary conditions for pre-buckling analysis of a curved panel with VAT laminate.	84
4.5	Representation of boundaries of a curved panel with VAT laminate.	85
4.6	Numerical convergence study of normalized fundamental frequency ($\tilde{\omega}$) computed using GDIQM and FEM (ABAQUS) for the curved VAT panel with $b/R = 0.2$	88
4.7	Variation of buckling load of a curved VAT panel $[0 \pm \langle 0 T_1 \rangle]_{2s}$ with respect to fiber-angle T_1	90
4.8	Variation of normalized fundamental natural frequency ($\tilde{\omega}$) with respect to static in-plane load parameter (α_0) for a curved VAT panel $[90 \pm \langle 0 30 \rangle]_{2s}$	91
4.9	Principle DIRs of a curved VAT panel $[90 \pm \langle 0 T_1 \rangle]_{2s}$ for different fiber orientations (T_1).	92
4.10	Principle DIRs of a curved VAT panel $[90 \pm \langle 0 45 \rangle]_{2s}$ for different b/R ratios.	93
4.11	Variation of normalized critical buckling load (K_{cr}) and D_{II} for the SSSS curved VAT panel $[90 \pm \langle T_0 T_1 \rangle]_{2s}$ with $b/R = 0.2$ for different fiber orientations, T_0 and T_1	94
4.12	Variation of normalized critical buckling load and D_{II} for the SCSC curved VAT panel $[90 \pm \langle T_0 T_1 \rangle]_{2s}$ with $b/R = 0.2$ for different fiber orientations, T_0 and T_1	95
4.13	Variation of normalized critical buckling load and D_{II} for the CCCC curved VAT panel $[90 \pm \langle T_0 T_1 \rangle]_{2s}$ with $b/R = 0.2$ for different fiber orientations, T_0 and T_1	96
4.14	Principle DIRs of a curved VAT panel $[90 \pm \langle 0 30 \rangle]_{2s}$ with $b/R = 0.2$ for different boundary conditions (SSSS, SCSC and CCCC).	96
4.15	Variation of K_{cr} and D_{II} for a SSSS VAT panel $[90 \pm \langle 0 T_1 \rangle]_{2s}$ with respect to T_1 different values of b/R ratios.	97
4.16	Variation of K_{cr} of a curved VAT panel $[90 \pm \langle 0 T_1 \rangle]_{2s}$ with respect to T_1 for different values of a/b ratios.	98
4.17	Variation of Principle DIRs and D_{II} of a curved VAT panel $[90 \pm \langle 0 T_1 \rangle]_{2s}$ with respect to T_1 for different values of a/b ratios.	99

5.1	Schematic representation of a VAT lamina.	103
5.2	Principle DIRs in the VAT panel ($[0 \pm \langle 0 T_1 \rangle]_{4s}$) obtained using GDIQM and FEM.	117
5.3	First and second DIRs in a VAT panel ($[0 \pm \langle 0 45 \rangle]_{4s}$) obtained from Bolotin's approach and the implicit Floquet method for: (a) Undamped VAT panel (b) Damped VAT panel.	120
5.4	Time response at the center of an undamped VAT panel ($[0 \pm \langle 0 45 \rangle]_{4s}$) at different excitation frequencies: (a) $P_1, \tilde{\Omega} = 8$ (b) $P_2, \tilde{\Omega} = 11$ (c) $P_3, \tilde{\Omega} = 14$ (d) $P_4, \tilde{\Omega} = 18.5$ (e) $P_5, \tilde{\Omega} = 21.5$ (f) $P_6, \tilde{\Omega} = 25$ (see Fig. 5.3(a)Subfigure 5 5.3(a)subfigure.5.3.1).	122
5.5	Time response at the center of a damped VAT panel ($[0 \pm \langle 0 45 \rangle]_{4s}$) at different excitation frequencies: (a) $Q_1, \tilde{\Omega} = 10$ (b) $Q_2, \tilde{\Omega} = 11.5$ (c) $Q_3, \tilde{\Omega} = 13$ (d) $Q_4, \tilde{\Omega} = 19$ (e) $Q_5, \tilde{\Omega} = 21.5$ (f) $Q_6, \tilde{\Omega} = 24$	123
5.6	Spectral radius variation of a VAT panel $[0 \pm \langle 0 0 \rangle]_{4s}$ for the constant excitation load of $\alpha_1 = 0.75$	124
5.7	Spectral radius variation of a VAT panel $[0 \pm \langle 0 T_1 \rangle]_{4s}$ for the excitation load of $\alpha_1 K_{cr} = 0.7680$	126
5.8	Variation of spectral radius ($ \mu_{max} $) in a VAT panel $[0 \pm \langle 0 45 \rangle]_{4s}$ for different values of damping coefficient (β) at the excitation load of $\alpha_1 K_{cr} = 0.7680$	126
5.9	Variation of the dominant eigenvalue of the FTM for an undamped VAT panel $[0 \pm \langle 0 45 \rangle]_{4s}$ at: (a) First instability region and (b) Second instability region. The eigenvalues are represented by red dots and the unit circle is represented with blue.	127
5.10	Variation of the dominant eigenvalue of the FTM for a damped VAT panel $[0 \pm \langle 0 45 \rangle]_{4s}$ at: (a) First instability region and (b) Second instability region. The eigenvalues are represented by red dots and the unit circle is represented with blue.	128
5.11	Complete parametric instability analysis of VAT composite panel (a) $[0 \pm \langle 0 0 \rangle]_{4s}$ and (b) $[0 \pm \langle 0 45 \rangle]_{4s}$	129

List of Tables

1.1	Review of the literature on VAT composite panels.	11
2.1	Mesh convergence study of normalized natural frequency ($\tilde{\omega}$) and normalized critical buckling load (K_{cr}) obtained by FEM for a VAT laminate $[0 \pm \langle 0 T_1 \rangle]_{3s}$ under uniform axial compression.	39
3.1	Comparison of natural frequencies (Hz) of a cantilever beam-plate $[0/90]_{2s}$ with through-the-width delamination.	61
3.2	Comparison of normalized fundamental frequency ($\tilde{\omega}$) and normalized critical buckling load (K_{cr}) of a VAT laminate $[0 \pm \langle 0 45 \rangle]_{4s}$ with an embedded square delamination.	62
3.3	Comparison of normalized natural frequencies ($\tilde{\omega}$) and normalized critical buckling load (K_{cr}) of a VAT laminate $[0 \pm \langle 0 45 \rangle]_{4s}$ with an embedded through-the-width delamination.	62
4.1	Comparison of normalized fundamental natural frequency ($\tilde{\omega}$) of a curved VAT panel $[90 \pm \langle 0 T_1 \rangle]_{2s}$ for different b/R ratios.	89
4.2	Comparison of free vibration mode shapes of a curved VAT panel $[90 \pm \langle 0 30 \rangle]_{2s}$	89
4.3	Comparison of buckling mode shapes of a curved VAT panel $[90 \pm \langle 0 30 \rangle]_{2s}$	90
5.1	Validation of normalized the natural frequency ($\tilde{\omega}$) and critical buckling load (K_{cr}) of the VAT panel $[0 \pm \langle 0 T_1 \rangle]_{4s}$ obtained from GDIQM, FEM and ABAQUS.	116
5.2	Convergence of the dominate eigenvalue obtained from the implicit Floquet analysis for the VAT panel, $[0 \pm \langle 0 T_1 \rangle]_{4s}$	117
5.3	Time required to obtain the dominate eigenvalue from classical Floquet and implicit Floquet method using FEM and GDIQM for VAT panels $[0 \pm \langle 0 T_1 \rangle]_{4s}$ when $\alpha_1 = 0.4$ and $\tilde{\Omega} = 20.58$	118

Nomenclature

α_0	Static load parameter
α_1	Dynamic load parameter
a	Length of the panel
$\mathbf{a}_k, \mathbf{b}_k$	Coefficients in Fourier expansion
$\bar{\mathbf{A}}$	Membrane section stiffness matrix
$\bar{\mathbf{A}}'$	Membrane section stiffness matrix in delaminated portion
β	Coefficient of damping
b	Width of the panel
$\bar{\mathbf{B}}$	Membrane-bending section stiffness matrix
$\bar{\mathbf{B}}'$	Membrane-bending section stiffness matrix in delaminated portion
\mathbf{C}	Damping matrix
d	Diameter of the cutout
$\bar{\mathbf{D}}$	Bending section stiffness matrix
$\bar{\mathbf{D}}'$	Bending section stiffness matrix in delaminated portion
D_{II}	Dynamic instability index
D_{IO}	Dynamic instability opening

$\epsilon_x, \epsilon_y, \gamma_{xy}$	In-plane strains
$E_{11}, E_{22}, \nu_{13}, \nu_{21}, G_{13}, G_{23}$	Material properties
E_{iso}	Equivalent stiffness of quasi-isotropic laminate
E_{vat}	Equivalent stiffness of VAT laminate
F	Force vector
γ_{xz}, γ_{yz}	Transverse shear strains
H	Upper Hessenberg matrix
h	Thickness of the panel
h'	Thickness of the delaminated portion
$\mathbf{K}_m^e, \mathbf{K}_b^e, \mathbf{K}_s^e, \mathbf{K}_{mb}^e$	Element membrane, bending, transverse shear, and membrane-bending coupling stiffness matrices
\mathbf{K}_G^e	Element geometric stiffness matrix
\mathbf{K}^e	Element stiffness matrix
K	Global stiffness matrix
\mathbf{K}_G	Global geometric stiffness matrix
K_{cr}	Normalized critical buckling load
$\mathbf{K}'_m, \mathbf{K}'_b, \mathbf{K}'_s, \mathbf{K}'_{mb}$	Element membrane, bending, transverse and membrane-bending coupling stiffness matrices in delaminated panel
\mathbf{K}'^e	Element stiffness matrix in delaminated portion
\mathbf{K}'_G	Element geometric stiffness matrix in delaminated portion
$\bar{\mathbf{K}}'^e$	Transformed element stiffness matrix in delaminated portion
$\bar{\mathbf{K}}'_G$	Transformed element geometric stiffness matrix in delaminated portion

λ	Buckling eigenvalue
μ	Floquet multipliers
\mathbf{M}	Global mass matrix
\mathbf{M}^e	Element mass matrix
$\bar{\mathbf{M}}'^e$	Transformed element mass matrix in delaminated portion
M_x, M_y, M_{xy}	Resultant moments
n_l	Total number of layers in the panel
n_x, n_y	GDIQM grid
N_x, N_y, N_{xy}	Resultant in-plane stresses
\mathbf{N}_i	Shape functions
ω	Fundamental frequency
$\tilde{\omega}$	Normalized fundamental frequency
Ω	Excitation frequency
$\tilde{\Omega}$	Normalized excitation frequency
ϕ	Rotation of fiber path
Ψ	Fiber-angle
$\Phi_{x,y}^{1,2}$	Panel edges
Φ	Floquet transition matrix
P_{cr}	Critical buckling load
$\mathbf{Q}_1, \mathbf{Q}_2$	Reduced lamina and shear stiffness matrices
$\mathbf{Q}_p, \mathbf{Q}_s$	Constitutive matrices
ρ	Density of the panel

R	Radius of curvature of the panel
$\sigma_x, \sigma_y, \tau_{xy}$	In-plane stresses
$\bar{\mathbf{S}}$	Shear section stiffness matrix
$\bar{\mathbf{S}}'$	Shear section stiffness matrix in delaminated portion
S_x, S_y	Resultant in-plane shear stresses
τ_{xz}, τ_{yz}	Transverse shear stresses
t	Time
\tilde{t}	Normalized time
T	Time period
T_0	Fiber-angle at the center of the panel
T_1	Fiber-angle at the panel ends
T_{KE}	Kinetic energy
$\mathbf{T}_1, \mathbf{T}_2$	Transformations matrices
$\bar{\mathbf{T}}$	In-plane stress resultant matrix
$\mathbf{T}^x, \mathbf{T}^y$	First-order weighting coefficient matrices
$\mathbf{T}^{xx}, \mathbf{T}^{yy}, \mathbf{T}^{xy}$	Second-order weighting coefficient matrices
U	Strain energy
u_0, v_0	Panel mid-plane displacements
u, v, w	Panel displacements
u_{cr}	Critical displacement
$\bar{\mathbf{u}}$	Displacement variables
$\bar{\mathbf{u}}^e$	Element displacement variables

u	Displacements in x direction
u', v', w'	Panel displacements in delaminated portion of the panel
u'_0, v'_0	Panel mid-plane displacements in delaminated portion
v	Displacements in y direction
w	Mode shapes
w_0, θ_x, θ_y	Mid-plane kinematic variables for bending
$w'_0, \theta'_x, \theta'_y$	Mid-plane kinematic variables for bending in the delaminated portion of the panel
w	Displacements in z direction
x_i, y_i	Grid coordinates
$[\phi_{\pm} \langle T_0 T_1 \rangle]_s$	Representation of VAT laminate configuration

Chapter 1

Introduction

The aviation industry is one of the fastest-growing industries on the planet due to the increased demand for air travel and freight transport. Recent developments in the aviation sector have led to the availability of low-cost airlines to meet the increasing demand in the number of air travellers. According to International Air Transport Association (IATA), a total of 4.3 billion people flew in 2018, compared to 2.208 billion travellers in 2008, which shows an increase of 51.3 percent over the last ten years. With the increase in the air passengers, it is forecasted that the air traffic will double in the next 15 – 20 years. Also, because of the increase in air traffic, the emission of greenhouse gases from the aircraft has escalated environmental concerns. The International Civil Aviation Organization (ICAO) reports that the greenhouse emissions from aviation have increased by 87% between 1990 and 2018 and constitutes around 1 – 2% of global emissions per year. Moreover, the aircraft pollution has risen by about two-thirds since 2005 and will increase seven-fold by 2050 if left unchecked according to the Montreal-based ICAO. These forecasts are of concern to climate scientists and activists who claim increasing concentrations of greenhouse gases leads to the rising temperatures, extreme weather conditions and higher death tolls from natural disasters caused at least in part by human activities.

In order to control the pollution due to aviation, the European Union Emission Trading System (EU ETS) has started working on the “cap and trade” principles since 2012, by setting a cap on the emission of greenhouse gases. They proposed to limit the emission from all sectors covered by EU ETS at 2020 to be 20% lower than in 2005, and lower than 43% by 2030. Therefore to meet the proposed requirements, the ICAO has put emphasis on improving the performance of the aircraft with minimal emissions and maximum efficiency. As a result, current research programs aim at reducing the emission by designing fuel-efficient engines, reducing structural

weight and aerodynamic modifications. Upon conducting extensive research, aviation engineers proposed that reducing the mass of an aircraft is an effective way to proceed as it allows smaller size engines with reduced fuel consumption and minimal emissions. For example, a 20% weight saving in the modern Boeing 787 aircraft resulted in the reduction of fuel consumption by around 10% – 12%. In addition to the reduction of carbon footprint, flight performance improvements such as better acceleration, higher thrust, and higher payload can also be achieved by lightweight design. Therefore, the current aircraft industry is under enormous pressure to design lightweight and cost-effective structures. As a result, to achieve lighter structures, aircraft designers use thin-walled structures, which increases the susceptibility to buckle and collapse subsequently (see Fig. 1.1). Also, in aircraft structures, the primary load-carrying parts such as fuselage and wings are often subjected to dynamic loads in-addition to static loads during the different flight conditions. Since stability is the most important factor in the aerospace structural design, all the possible loading conditions on different parts of the structure have to be considered in order to create a safer design. Therefore, to design lightweight structures without compromising

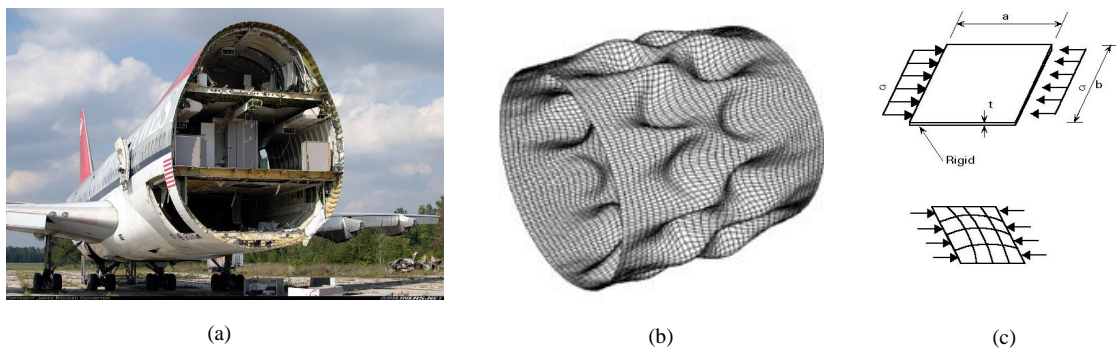


Figure 1.1: (a) Cross-sectional view of aircraft fuselage ²(b) Buckling of fuselage under compression load (c) Fundamental cases of compression plate buckling.

the structural performance, the aerospace designers started to use fiber-reinforced polymer (FRP) composites in the design of aerospace structures. The FRP composite materials have several advantages over the metallic structures in terms of weight reduction and improved structural performance. FRP structures exhibit high specific stiffness/strength, better damping properties, corrosion resistance, and improved fatigue properties. Moreover, the FRP composites have an added advantage of struc-

²Sectional view of Boeing 747-151 - Northwest Airlines. Image downloaded from: <https://www.airliners.net/photo/Northwest-Airlines/Boeing-747-151/1281454>

tural tailorability for a particular application. Unlike isotropic designs, in composites, designers have the benefit of tailoring the stiffness and strength. In the context of stability, the composite laminate can be tailored in terms of bending stiffness (by changing the fiber orientation and keeping the thickness constant) to maximize the static and dynamic properties, simultaneously.

The usage of composite materials in the design of commercial aircraft structures has increased considerably in the past few decades. Besides military aircraft like the B-2 bomber and Nighthawk F117-A fighters, the uptake of composites in the design of new generation commercial aircraft like Boeing 787 Dreamliner, Airbus A350/380, and McDonnell Douglas MD-91X has increased enormously, where the structures are composed of almost 55% composite materials by weight. Consequently, the recent aircraft is 70% more fuel-efficient than they were 40 years ago. Carbon monoxide emissions have been considerably reduced by 50%, while unburned hydrocarbon and smoke have been cut by 90%. Typical applications of the composite materials are in the aircraft structural parts like the fuselage, wing-covers, tail-planes, wing-spar, and winglets. Even in astronautics, the uptake of the composite materials in the design has begun at an earlier stage. Until recent times, the usage of composite-materials in satellites and spacecraft was restricted to the payload. However, nowadays, with an increase in the requirements for space travel in both the scale and complexity, the role of composites in astronautics extends into a wide variety of applications. Space research centers like NASA, SpaceX, ISRO, and other space agencies have incorporated composite materials in launch vehicles and orbiter applications. Rocket fuel tank (NASA & Boeing)³, Rocket inter-stages (SpaceX, 2015a), crew-capsules (NASA, 2010)⁴, and fuselage in aircraft (Boeing 787)⁵ are to name a few (see Fig. 1.2). According to NASA's technology road map - 2015, this trend in the rise of composites is predicted to carry on in the future.

As the use of composite materials in aerospace and various other industries increased, developments in the automated composite manufacturing have followed. Traditional fiber-reinforced composite laminates have plies with constant fiber-angle ori-

³18-foot-diameter (5.5-meter) Rocket fuel tank being manufactured at the Boeing Developmental Center in Tukwila, Washington. Image downloaded from: <https://www.nasa.gov/centers/marshall/news/news/releases/2014/14-043.html>

⁴Composite Crew Module at Alliant Techsystems (ATK), where it was fabricated, prior to shipping to NASA Langley Research Center. Image downloaded from: <https://www.nasa.gov/topics/moonmars/features/ccm.html>

⁵A Boeing 787 Dreamliner fuselage is being manufactured at a factory in Japan. Toray carbon fibers composites are being used in the manufacturing process which makes aircraft lighter. Image downloaded from: <https://asia.nikkei.com/Business/Companies/Carbon-fiber-costs-flatten-Toray-s-quarterly-profit>

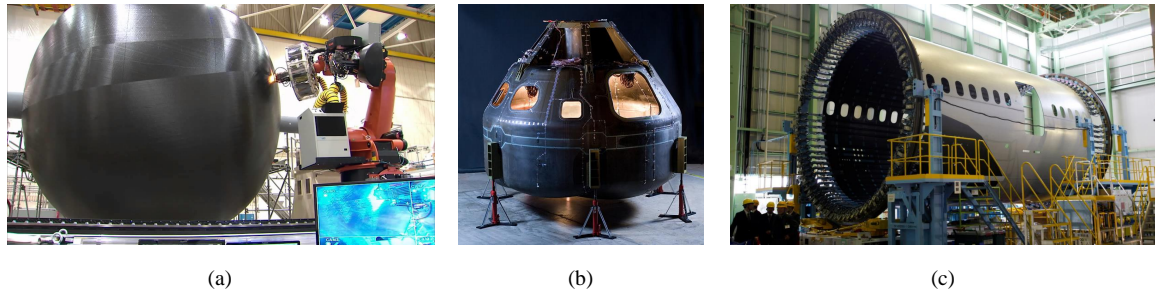


Figure 1.2: Composites in aerospace industry: (a) Rocket fuel-tank developed by NASA & Boeing (b) NASA’s composite crew module (c) Boeing 787 Dreamliner composite fuselage.



Figure 1.3: Tow-placement machine producing plies with curvilinear fibre path (Courtesy of Electroimpact composite manufacturing).

entations, and stiffness is tailored by changing the fiber-angle in the thickness direction of the laminate. Thus, the stiffness of the straight-fiber composite is constant across the plane of the laminate and limits the tailorability options for fully exploiting the anisotropic property of the composite structure. The concept of fiber-steering allows the fiber-angle to vary in the plane of laminae and allows full usage of the 3D design space of composite structures.

Modern automated composite manufacturing methods allow fabricating more complex composite structures with minimal process-induced defects and material wastage. The development of these automated tow-placement machines enables to fabricate the composite laminate with curvilinear-fiber across the plane of the lamina (see Fig. 1.3⁶). The composite laminates with curvilinear fibers are usually referred to as

⁶Picture of the automated tow-placement (ATP) machine by Electro-impact composite manufacturing laboratory. Image downloaded from: <https://www.hasmak-t.com/urunler/havacilik-ve-savunma/automated-composite-systems/electroimpact>

variable angle tow (VAT) laminate. The process of placing the fibers in the plane of the lamina to improve the structural performance is termed as elastic tailoring of composite structures. By steering the fibers along curvilinear paths, it is possible to create a laminate with continuously varying stiffness properties (see Fig. 1.4). VAT technology allows the full exploitation of the design space available to the engineer compared to traditional straight-fiber laminate. A brief review on the manufacturing techniques for VAT composite panels has been discussed in the following section.

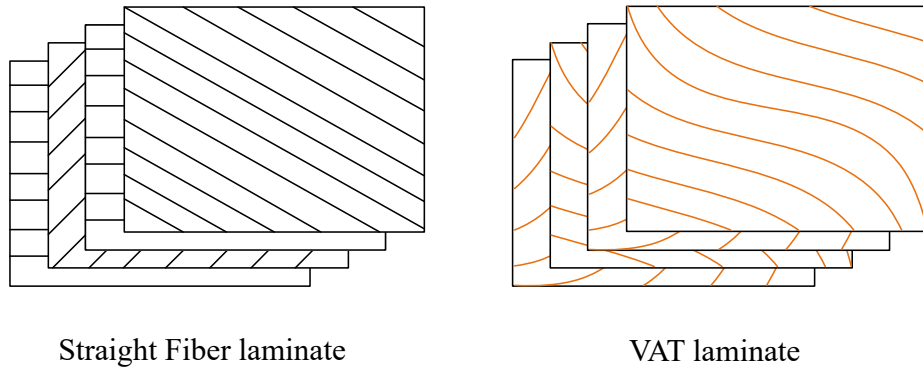


Figure 1.4: Schematic representation of: (a) Straight-fiber composite laminate (b) Variable angle tow composite laminate.

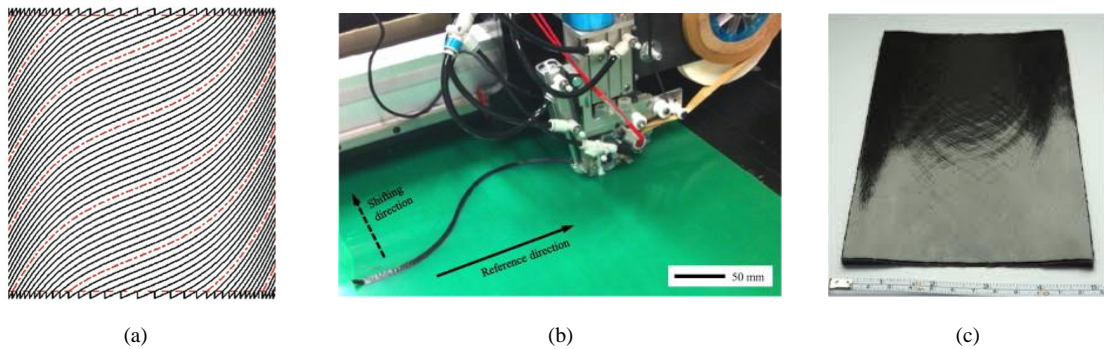


Figure 1.5: Images of tow-steering and variable stiffness structures: (a) Optimized fiber-angle distribution for maximum buckling load (b) Manufacturing of an optimized variable stiffness composite plate using the continuous tow steering technique (c) A completed VAT panel [1].

1.1 Manufacturing of VAT composite panel

Advances in manufacturing techniques such as the automated tow placement/fiber placement (AFP) allows the fabrication of the laminate by varying the fiber orientation within the lamina. This capability is not present in either filament-winding or tape-layup machines. The modern tow placement machines are equipped with the computer controlled robotic arm and fibre placement head. This enables to place the fibers on complex surfaces with precise control on the fiber orientation combined with the cut/restart capabilities [2–5]. The possibility of 3D tailoring of the fiber orientation offers the designer an enlarged design space, with respect to the traditional straight-fibre reinforced composites. This offers new feasibility for weight reduction and better performance, which is particularly important in the aviation and wind energy sector [6].

Apart from the benefits of AFP machines in continuous steering of fiber in curvilinear paths and to control the tow-placement individually; it also induces some defects [7, 8]. The fiber-steering sets constraint on the radius of the path that can be laid down without significant defects, such as local fibre buckling and ply wrinkling. When the steering radius become too small, the inner radius of the tow is smaller than the outer radius, resulting in compressive and tensile forces, respectively [9, 10]. Consequently, the tow wrinkle on the inside and results in reduction of load carrying capability. Furthermore, the resulting structure would have poor surface finish. Gaps and overlaps also appears if the course is not laid parallel to an adjacent one. In complex geometries and especially when fibre steering is introduced, these defects might be important.

However, in recent times the new developments and modifications to the AFP technology aims at improving the manufacturing of laminates with curvilinear fibres in terms of less manufacturing constraints and defects. As a means to reduce the defects induced by AFP, a new way to place curvilinear fibres designated as “Continuous Tow Shearing (CTS)” has recently been developed at Bristol University [11]. The CTS technique uses shear deformation characteristics of the dry tows instead of bending deformation in the tow placement. This technique reduces the local fibre buckling and wrinkling and avoiding gaps and overlaps [10, 11]. Tests indicate that CTS can decrease process-induced defects such as fibre wrinkling, resin rich areas and fibre discontinuity.

Another type of advanced fibre placement is tailored fibre placement (TFP), an automated textile process for the production of reinforced structures [12–14]. This

process apparently allows manufacturing of composite parts with fibre layouts of arbitrary direction using embroidery technology; the desired fibre orientations can be transferred into fibre preforms. Furthermore, a brief review on the manufacturing of variable stiffness composite laminates has been discussed in [15].

The tow-steering technology enlarges the design space available to FRP composites and offers new possibilities for light-weight design and better structural performance when compared to straight-fiber composites. Researchers have grasped the VAT technology as an opportunity of taking composite tailorability in all the possible directions. In the past decade, researchers have applied the VAT technology to improve the performance of the composite structures in terms of their static strength, buckling, post-buckling behavior (see Fig. 1.5), dynamic and vibration response, etc., which is discussed in detail in the following literature review section.

1.2 Literature review

Over the past century, researchers have carried out extensive research on designing and optimizing the composite structures for better performance under different loading conditions. A brief review of the past research that was carried out on the VAT composite panels is discussed in this section. The research that was performed on the static and dynamic characteristics of different straight-fiber composite panels and shells is also presented.

1.2.1 VAT composites

In the past few decades, research into VAT composites has produced a wealth of information. Among all the researchers, Hyer and Lee [16] were among the first to investigate the influence of curvilinear-fiber on the stress concentration factor around a cutout of the composite plate. They demonstrated the reduction in stress concentration factor by aligning the fibers along with the principal directions of the stress field. Subsequently, they worked on designing a VAT plate to maximize the buckling load [16]. They determined the optimal fiber orientation angles in different regions of the laminate using a combination of the finite element method (FEM), sensitivity analysis, and optimization techniques. Leissa and Martin [17] performed vibration and buckling analysis of composite plates with varying fiber volume fraction using the Ritz method. They observed that upon using varying fiber volume fraction distribution, there was 38% increase in the buckling load and 21% increase in the fundamental

frequency. However, the investigation was limited to a single layer composite with parallel fibers.

To simplify the modeling of VAT laminates, Gurdal and Olmedo [18] introduced a linear fiber-angle variation along the length of the composite panel, which can be mathematically described by three independent angles ($\phi\langle T_0|T_1\rangle$). The linear fiber-angle variation distribution has been adopted in the analysis, design, and manufacture of tow-steered composite structures [3, 4, 19, 20]. Later, Gurdal et al. [21] studied the buckling of VAT panels by varying the fiber orientations perpendicular to the loading direction. The buckling coefficient of VAT plates was then computed using the Rayleigh-Ritz method. In their studies, they demonstrated the load re-distribution phenomenon is responsible for the improvement of buckling performance in VAT composites. Alhajahmad et al. [22] studied the nonlinear pressure pillow problem of fuselage skin panels. From their studies, they concluded that VAT panels withstand more load when compared to straight-fiber composite panels. Weaver et al. [23] designed and manufactured variable stiffness composite panels using an embroidery based process. Their finite element simulations of VAT panels showed a similar buckling performance when compared to quasi-isotropic laminates, but exhibited superior post-buckling behavior.

Later, Raju et al. [24, 25] analyzed the buckling and post-buckling behavior of VAT panels using differential quadrature method (DQM). They obtained accurate solutions using DQM with fewer grid points compared to FEM. Apart from FEM and DQM, numerous semi-analytical approaches like Rayleigh-Ritz, Galerkin, and perturbation methods were also used to solve the buckling and post-buckling problem of composite panels [26, 27]. Coburn et al. [28] developed a semi-analytical method for the buckling analysis of blade stiffened VAT panel to explore their full potential. They also presented the benefits of variable stiffness sandwich panels for enhanced buckling performance using a Ritz approach based on first-order shear deformation theory (FSDT) [29]. Chen et al. [30] investigated the effect of delamination on the buckling behavior of VAT composite panels under compression loading. They studied the influence of delamination size, position, and varying fiber orientation on buckling response of VAT panels. White et al. [31] investigated the buckling and post-buckling behavior of the variable-stiffness cylindrical shells under axial compression using linear and nonlinear finite element methods. Their analyses provide significant insight into the mechanisms underpinning collapse behavior of the variable fiber-angle cylindrical shells. Nian et al. [32] studied the buckling behavior of a variable stiffness composite cylindrical shell using finite element analysis and demonstrated the im-

provement in buckling performance using variable fiber-angle concept. Further, Labans and Bisagni [33] performed an experimental investigation on the vibration and buckling behavior of a cylinder shell with a conventional layup and a variable-stiffness cylinder. They also developed a simplified numerical model for the variable-stiffness cylinder in their study. From the comparison of the experimental and numerical results, they showed that a simple approximation model is capable of predicting the accurate buckling load and mode shapes of the variable fiber-angle cylindrical shells.

In addition to static analysis, Honda and Narita [34], Akhavan and Ribeiro [35], and Hachemi et al. [36] studied the free vibration response of VAT composite panels. They studied the effect of fiber-angle variation on the natural frequency and mode shapes of vibration in VAT panels. From their studies, it was observed that in VAT panels, there is a significant change in mode shapes of vibration along with an increase or decrease in the natural frequencies. Houmat [37] and few other researchers [38–41] studied the non-linear vibration behavior in VAT composite laminates. Their studies reveal that for linear and nonlinear vibrations, the variation of fiber-angle within the lamina allows one to obtain different dynamic behavior with the same material and geometric properties. They also showed that certain configurations of VAT panels behave in a more rigid fashion than the conventional straight-fiber composites. Recently, Viglietti et al. [42] studied the free vibration analysis of VAT composite wing structures using Carrera unified formulation. Results from their work confirm that an appropriate tow layup can be used to improve the performance of wing structures.

Several optimization studies were also performed on VAT composites to maximize structural performance. Nagendra et al. [2] used non-uniform rational B-splines for defining fiber variations in the plane of the plate and performed FE analysis to optimize the fiber design based on buckling load and natural frequency. Setoodeh et al. [43] optimized the VAT panel for maximizing the buckling load using a reciprocal approximation technique. They employed a conforming bi-linear FEM for buckling analysis of VAT panels. Ijsselmuiden et al. [44] performed optimization studies on maximizing buckling load using lamination parameters. Their optimization results demonstrated improvement in excess of 100% in buckling loads of VAT panels compared to optimum straight-fiber laminates with the same number of piles. Wu et al. [45] used Rayleigh–Ritz approach combined with genetic algorithm for maximizing the critical buckling load of the VAT laminate with the nonlinear fiber-angle variation.

Further, most of the works on VAT concepts have shown the ability of tow steered

composite panels to exhibit better structural performance. As a result, the effort to improve aircraft performance using the tow-steered composite structures has been increased significantly. Stodieck et al. [46] studied the behavior of a full-size aero-elastically tailored wing using a three-dimensional finite element model. They performed analysis on both the straight-fiber and tow-steered composite laminate configurations. Their investigations have shown that the optimized tow-steered laminate configuration achieved larger mass reduction than the optimized straight-fiber laminate configurations. Stanford et al. [47] solved a series of optimization problems to minimize the structural mass under coupled stress, buckling, and flutter constraints on a high aspect-ratio wing-box. They have studied the effect of tow-steered composite laminate skins and curvilinear stiffeners on the performance of wing-box. From their results, they observed that both methods lead to a feasible mass reductions over their non-curvilinear structural counterparts. They also observed some degree of performance degradation when curvilinear stiffeners and curvilinear fiber towpaths were used simultaneously. Most recently, Barr and Jaworski [48] explored the concept of aero-elastic tailoring to maximize the power generation from an NREL 5-MW wind turbine blade rotating in a uniform flow. They observed that with the use of tow-steered composite fibers in the wind turbine blades, their potential in power extraction has improved while avoiding stall at higher wind speeds. Their numerical results showed that there is an increase in the turbine power extraction by up to 14% when the blade is optimized near the cut-in wind speed, and by 7% when optimized at the rated wind speed. This aero-elastic tailoring technology can also be optimized and utilize in other structural applications involving significant fluid-structure coupling effects such as helicopter blades and aircraft wings with large spans. The discussed literature review on VAT composite panels is also been given concisely in Table. 1.1.

1.2.2 Dynamic stability in composite panels

In addition to the buckling and post-buckling analysis, dynamic stability analysis is equally important while designing a structure. Aircraft structural parts like fuselage and wings are often subjected to dynamic loads in addition to static loads. These structural parts, when subjected to periodic in-plane compression loads, transverse vibrations are induced. These vibrations sometimes may not threaten the structure or its normal operation, but they can bring about failure if they continue to act. Also, for certain combinations of the excitation frequency and the load, the induced trans-

Table 1.1: Review of the literature on VAT composite panels.

Author	Work
Hyer and Lee, [16]	Demonstrated the reduction in stress concentration factor by aligning the fibers along the principal directions of the stress field in a composite plate with a cutout. They designed a VAT plate to maximize the buckling load.
Gurdal et al. [18]	Performed Buckling analysis of VAT panels by varying the fiber orientations perpendicular to the loading direction. In their studies, they demonstrated the load re-distribution phenomenon is responsible for the improvement of buckling performance in VAT composites.
Alhajahmad et al. [22]	Studied the nonlinear pressure pillowing problem of fuselage skin panels. From the studies, they concluded that VAT panel withstand more load when compared to straight-fiber composite panel.
Kim et al. [11]	Designed and manufactured VAT composite panels using an embroidery based process. Their FE simulations of VAT panel showed a similar buckling performance when compared to quasi-isotropic laminates, but exhibited superior post-buckling behavior.
Chen et al. [30]	Investigated the effect of delamination on the buckling behavior of delaminated VAT composite panels under compression load. This study shows that the residual buckling resistance of delaminated composite plates can be significantly improved through using the VAT design concept compared to straight-fiber composites.
Nian et al. [32]	Studied the buckling behavior of a VAT composite cylindrical shell using FE analysis and demonstrated the improvement in buckling performance using variable fiber-angle concept.
Honda and Narita [34], Akhavan and Ribeiro [35], Hachemi et al. [36]	Studied the effect of fiber-angle variation on the natural frequency and mode shapes of vibration in VAT panels. It was observed in VAT panels, there is significant change in the mode shapes of vibration along with an increase or decrease in the natural frequencies with the fiber-angle variation.

Houmat [37]	Studied the non-linear vibration behavior in VAT composite laminates. Their studies reveal that for linear and nonlinear vibrations, the variation of fiber-angle within the lamina allows one to obtain different dynamic behavior with the same material and geometric properties. They also showed that certain configurations of VAT panels behave in a more rigid fashion than the conventional straight-fiber composites.
Viglietti et al. [42]	Investigated the free vibration analysis of VAT composite wing structures and confirm that an appropriate tow layup can be used to improve the performance of wing structures.
Ijsselmuiden et al. [44]	Performed optimization studies on maximizing buckling load using lamination parameters. Their optimization results demonstrated improvement in excess of 100% in buckling loads of VAT panels compared to optimum straight-fiber laminates with the same number of piles.
Stodieck et al. [46]	Studied the behavior of a full-size aero-elastically tailored wing using a three-dimensional FE model. They performed analysis on both the straight-fiber and tow-steered composite laminate configurations. Their investigations have shown that the optimized tow-steered laminate configuration achieved larger mass reduction than the optimized straight-fiber laminate configurations.
Stanford et al. [47]	Solved a series of optimization problems to minimize the structural mass under coupled stress, buckling, and utter constraints on a high aspect-ratio wing-box. They have studied the effect of tow-steered composite laminate skins and curvilinear stiffeners on the performance of wing-box. From their results, they observed that both methods lead to a feasible mass reductions over their non-curvilinear structural counterparts.

verse vibrations grow unboundedly in amplitude, which ultimately results in causing structural damage. This phenomenon is known as parametric resonance (parametric/dynamic instability). The parametric resonance is a dangerous phenomenon, and can lead to unpredictable failures. Moreover, unlike principal resonance, which happens only at certain frequencies, parametric resonance occurs over a range of excitation frequencies below the critical buckling load of the structure. This means that the parametric resonance may occur at a load level much less than the static buckling load. Therefore, a structural component that is designed to withstand the static buckling load may easily fail when subjected to an in-plane periodic load at a certain range of excitation frequencies. Also, the range of excitation frequencies at which resonance occurs varies with the amplitude of the excitation load. The region of excitation frequencies and amplitude of the load at which resonance occurs is usually known as dynamic instability region and the boundary separating a stable region from an unstable region is known as stability boundary. Several means of mitigating parametric instability, such as structural damping and vibration isolation may be ineffective. Therefore, understanding the parametric instability characteristics of a structure is of great practical importance from the theoretical and design perspective.

A considerable amount of research has been carried out on the dynamic instability analysis of composite laminated plates in the past few decades. In 1965, Bolotin introduced an approach to determine the dynamic instability regions in a system and carried out a comprehensive study on the instability behavior of various elastic systems [49]. After that, many researchers have used Bolotin's approach to investigate the dynamic instability of different structures subjected to various loading conditions [50–53]. Followed by Birman [54], who studied the dynamic stability of an unsymmetrical cross-ply simply-supported rectangular laminate under a harmonically varying bi-axial compression load and evaluated the principal dynamic instability regions analytically. Srinivasan and Chellapandi [55] investigated the dynamic stability of thin laminated plates under harmonically varying uniaxial stress by using the semi-analytical finite strip method (FSM). They analyzed symmetric, anti-symmetric, and asymmetric configurations and concluded that, symmetric laminate is most stable when compared to the asymmetric configuration.

All the previous studies [50–55] were carried out using classical laminated plate theory (CLPT) to model the composite panels. However, while studying composite laminate, transverse shear effects are significant, and the use of first-order shear deformation plate theory (FSDT) provides better results when compared to CLPT. Bert and Birman [56] used FSDT in the analysis of dynamic instability of angle-ply

laminates in which both the rotary inertia and through-thickness shear effect were included. The principal instability regions were determined for the laminates, and the effect of aspect-ratio, thickness-to-length ratio, number of layers, and magnitudes of the shear correction factors were studied. Later, Chen and Yang [57] studied the dynamic instability of anti-symmetric angle-ply composite laminates subjected to a combination of the periodic in-plane and bending stresses using the Galerkin FEM. They did not consider damping in their analysis and studied the effects of various parameters and boundary conditions on the dynamic instability region (DIR). Moorthy et al. [58], carried out a similar investigation using the FEM based on the FSDT. In their study, both symmetric cross-ply laminate and anti-symmetric angle-ply laminate were considered with damping. They used Hill's method of infinite determinants and an analytical method to determine the instability regions of the laminate. The effects of damping, thickness-to-length ratio, anisotropy, boundary conditions, number of layers, and lamination angles on DIR was investigated.

Numerical methods such as the method of multiples scales and Lyapunov direct methods have also been employed for the dynamic stability analysis of composite laminates [59–62]. Chattopadhyay and Radu [63], Wang and Dawe [64] have also used FSDT in the dynamic instability analysis composite laminates. Extensive results were presented on the effects of different parameters like thickness-to-length ratio, anisotropy, boundary conditions, the number of layers, and lamination angles on dynamic stability of the composite laminates. Sahu and Datta [65] used FEM to study instability behavior of isotropic, quasi-isotropic, cross-ply and anti-symmetric angle-ply plates subjected to uniform and non-uniform periodic in-plane edge loading. Wang and Dawe [64] investigated the dynamic instability of composite laminated plate and prismatic plate structures using B-spline Finite strip method (FSM). This approach uses multi-level substructuring techniques, which greatly enhances the efficiency of the solution and enables the analysis of complicated plate structures.

Structural discontinuities like cutouts are inevitable in aerospace, civil, mechanical, and marine structures due to functional requirements. Nemeth [66] studied the buckling behavior of rectangular symmetrical angle-ply laminates with a circular cutout under displacement and stress boundary conditions. They showed that the geometry, loading, boundary conditions, and the cutout size play a significant role in the buckling behavior of the composite panel. Srivatsa and Murti [67] presented a parametric study of the compression buckling behavior of stress loaded composite panel with and without a cutout using FEM. A strong dependence of the buckling loads on fiber-angle was reported in their studies. Followed by, Lee and Lim [68] ap-

plied the point matching technique and Rayleigh method to study the free vibrations of isotropic and orthotropic square plates with cutouts subjected to in-plane forces by dividing the plate into sub-domains. Later, Prabhakara and Datta [69] studied the parametric instabilities of plates with centrally located cutouts subjected to in-plane periodic edge loading. They used FEM to model the problem and studied the effect of the static load factor, size, and shape of a cutout on the parametric behavior of the plate.

Many works have been reported on the dynamic instability of composite plates with damage to understand its effect on structural performance. Composite materials are prone to delaminations during service loading conditions and also improper manufacturing procedures. These delaminations may have a significant effect on the mechanical behavior of the composite laminates. There has been a significant amount of research reported on the dynamic response of composite laminated beam-plates or plates with delamination. Radu and Chattopadhyay [70] and Mohanty et al. [71] used the finite element method to investigate the dynamic instability of composite laminates with delamination under uniform periodic loading. They studied the effect of thickness, delamination size, and location on the natural frequency, critical buckling load, and the instability regions of the composite panels. They also studied the influence of the ply orientation on the instability region. They showed that the natural frequencies and the critical buckling load of the panel decrease with increase in delamination length, due to the reduction in stiffness caused by delamination. Yang and Fu [72] combined Rayleigh-Ritz method with CLPT to carry out the dynamic instability analysis of composite laminated cylindrical shells with delamination. The effects of the amplitude of external excitation, the delamination size, delamination location, and the material properties on the natural frequency and the principal dynamic instability region of the delaminated cylindrical shells were studied. Noh and Lee [73] investigated the dynamic instability of delaminated composite skew plates under various periodic in-plane loading using higher-order shear deformation theory (HSDT). The instability behavior of laminated skew plates with various delamination sizes was investigated to study the interactions between the skew angle and other parameters like the delamination size and the fiber-angle configuration.

Although most of the research has been carried out on composite panels with cutouts and with delamination, there are very few studies on the dynamic behavior of composite plates with delamination around a cutout. Ju et al. [74] have presented a FEM framework in conjunction with the Mindlin plate theory to analyze free vibration of a square and circular composite plates with delamination around the

centrally located internal square and circular cutouts. They discussed the effects of the cutouts and the delaminations around the cutouts on the natural frequencies and mode shapes. They showed that the delaminations might have a significant effect on natural frequencies, even though the mode shapes of the plates were not significantly affected by the delaminations. Kumar and Shrivastava [75] studied the dynamic response of square composite laminates with a centrally located rectangular cutout with and without delamination. They investigated the effect of material orthotropy, boundary conditions, and side-to-thickness ratio on the free vibration response. In addition, they also studied the effect of delamination size and its location around the cutout on the natural frequency of a square laminate with a cutout and delamination. A comparison was also made between results obtained from FSDT and HSDT.

1.2.3 Dynamic stability in curved composite panels

All the above works discussed in Sec. 1.2.2 were on the flat panels, whereas, in modern aerospace, civil, mechanical and naval engineering structures, curved panels are extensively used for load-bearing applications. Curved panels exhibit greater structural efficiency because of their ability to sustain high compression loads. The improvement in their buckling performance is mainly attributed to the curvature of the panel, which governs the membrane-bending coupling deformation kinematics.

An extensive bibliography of earlier works on dynamic stability on composite panels with curvature is given in the review papers [76–79]. Most of the researchers have studied the dynamic stability of closed cylindrical shells with simply-supported boundary conditions, using the analytical approach [80–82]. However, the study of the dynamic behavior of curved composite panels is sparsely treated in the literature. Ganapathi et al. [83] studied the effect of curvature and aspect-ratio on dynamic instability of a uniformly loaded thick composite cylindrical panels using the finite element method. They demonstrated the effectiveness of a nine-node shear flexible shell element in computing the dynamic instability region of a curved composite panel. They also studied the effect of various parameters like ply-angle, a number of layers, thickness- and radius-to-side ratio on the dynamic stability of curved composite panels. Sahu and Datta [84] used finite element analysis to investigate the dynamic stability of single and doubly curved composite panels, including spherical, elliptic, and hyperbolic paraboloids. Love’s and Donnell’s theories were used to study the effect of shallowness ratio, boundary conditions, and static load factor along with the other parameters on the principal instability regions of curved panels. The dynamic

stability of thin composite cylindrical shells under combined static and periodic axial force was investigated by Ng et al. [85] and Lam and Ng [86] using Love's theory of thin shells. They studied the effect of length-to-radius and thickness-to-radius ratios of the cylinder on the instability regions. They also examined the effects of the centrifugal and Coriolis forces on the instability regions of the cylindrical shells.

Further, Ganapathi et al. [87] studied the parametric instabilities in laminated composite conical shells using finite element method and brought out the influence of cone angle, cone orthotropicity, ply-angle and elastic-edge restraints on dynamic stability through their investigations. Sahu and Datta [88] investigated the parametric instability behavior of curved shells with cutouts subjected to in-plane static and periodic compression edge load using finite element analysis. The effects of static and dynamic load parameters, panel geometry, boundary conditions, and the cutout parameters on the dynamic instability regions of curved panels with cutouts were studied in detail. Yang et al. [72] used Rayleigh–Ritz method to investigate the dynamic stability behavior of cylindrical composite shells with delaminations. Numerical results were presented on the effect of delamination size and location on the natural frequency and the principal dynamic instability region of the delaminated cylindrical shells. Park and Lee [89] studied the dynamic stability analysis of delaminated spherical shell structures subjected to in-plane pulsating forces based on the higher-order shell theory of Sanders. They studied the effect of the interactions between the radius-length ratio and other parameters like delamination size, the layup, and location of delamination on the stability of spherical shells. Patel et al. [90] performed finite element analysis on the dynamic instability of stiffened shell panels with cutout subjected to uniform in-plane harmonic edge loading. In their work, they presented the influence of shell geometry, the radius of curvature, cutout size, and stiffening scheme on the dynamic instability behavior of stiffened shell panels. The free vibration and static stability (buckling) results were also presented in their work. Next, Panda and Ramachandra [91] investigated the dynamic instability of shear deformable cross-ply laminated and composite cylindrical panels subjected to periodic non-uniform in-plane loads. Ganapathi et al. [92] used finite element analysis to study the nonlinear instability behavior of the composite panels when subjected to periodic inplane axial load. Their analysis shows various characteristic features of the dynamic stability such as the existence of beats, their dependency on the excitation frequency, and the typical characteristics of vibrations in different regions of the stability charts. The influence of plyangle and layup of the laminate on dynamic stability behavior of the composite laminates were also presented. More recently,

Kumar and Patel [93] experimentally investigated the nonlinear dynamic response of elliptical cylindrical shell under transverse harmonic excitation. The participation of different modes, external and internal resonance and the presence of harmonics were reported.

1.3 Motivation

From the review of literature, it is evident that most of the research work reported on VAT composite panels is on static and modal analysis. Researchers have showed that steering of fiber-path in the plane of the laminate redistributes the applied load from the critical regions towards the supported edges. This load redistribution phenomenon improves the buckling and post-buckling performance of the VAT composite panels. Investigations have also been carried out on the stiffened and cylindrical VAT panels and superior structural performance of the VAT panels over straight-fiber laminates has been demonstrated. Also, researches have showed that by varying the fiber-angle within the lamina, linear and nonlinear vibration behavior of the VAT panel can be modified with the same material and geometric properties. In the case of dynamic stability analysis, all the studies have been reported on straight-fiber composite structures. It has been shown in the literature that by changing the fiber direction and the layup sequence the dynamic stability characteristics of a composite laminate can be modified significantly.

Although, significant amount of research has been carried out on straight-fiber and VAT composite panels, the parametric instability behavior of VAT composite panels has not been studied in the literature. This leaves the entire branch of parametric instabilities in VAT composites entirely unexplored. In order to use the VAT composite panels in the design of a aircraft structures, understanding the complete dynamic stability characteristics of VAT composite panels is utmost important. Therefore, the present study is mainly aimed at the proper understanding of dynamic stability behavior of VAT composite panels. The effect of fiber-angle variation on the parametric instabilities of VAT composite panels has been studied and reported in this thesis.

1.4 Scope of the thesis

The primary objective of the thesis is to investigate the effect of fiber-angle variation on the dynamic instability behavior of VAT composite panel under in-plane periodic compression load. On elastic tailoring of the dynamic behavior of VAT panels, this

thesis is confined to flat panels, flat panels with delamination and cutouts, and curved panels. These structural elements are used extensively in the design of aerospace structures, and from a mechanical point of view, they represent the spectrum of dynamic behavior. To limit the effects of cross-kinematic coupling, the VAT laminates are limited to symmetric and balanced stacking sequences.

Based on the review of literature, the different problems identified for the present investigation are presented as follows:

- Parametric instabilities in flat VAT composite panel under periodic in-plane compression load.
- Parametric instabilities in flat delaminated VAT composite panel with a cutout.
- Parametric instability in curved VAT composite panel.
- Implicit Floquet analysis for the study of parametric instability behavior of VAT composite panel.

Due to the practical importance and uniqueness in the above fields, the influence of various parameters such as aspect-ratio, static and dynamic load factors, fiber-angle variation, boundary conditions on the parametric resonance characteristics of VAT panels is investigated.

In this work, a uniaxial compression loading along with a simply-supported plate boundary conditions are chosen for the analyses. Although simplistic loading and boundary conditions are chosen for the investigation purpose, the proposed methodology can be easily extended to a wide variety of constraint conditions subjected to various loading situations. The scope of this thesis is also confined to the linear fiber-angle variation, and no manufacturing constraints are applied to the parametric studies.

1.5 Organization of the thesis

The thesis is divided into two sections. The first is devoted to the investigation of the effect of tow-steering on dynamic stability behavior of VAT composite laminates. In VAT panels, as a result of the fiber-angle variation, the stiffness properties of the laminate changes, and thus effects the static and dynamic properties of the structure. Tailoring, therefore, is targeted at controlling the extent of the stress redistribution from the critical regions to the supported edges and maximizing the buckling and

stability properties subjected to different boundary conditions. In the second section, an implicit Floquet analysis has been used to determine the dynamic stability characteristics of the VAT panel. Since the implementation of classical Floquet theory to study the dynamic stability behavior of large systems is computationally expensive, an implicit Floquet analysis has been adopted through which the computational cost reduces in a significant amount. Also, upon using the implicit Floquet theory, the approximations that are incorporated in the traditional Bolotin's approach are eliminated, and accurate DIRs can be determined. A brief overview of the contents of the thesis is given in the following sub-sections.

Chapter 2: Parametric instabilities in flat VAT composite panel

From the literature review, it is evident that a large amount of work has been conducted on the parametric instability of straight-fiber composites. It is also clear that the work that has been carried out on VAT panels is restricted to static and vibration behavior, but, the parametric behavior of VAT panels is remained unexplored.

In this chapter, the parametric stability behavior of VAT composite panels is presented. First, the modeling of VAT composite panels using first-order shear deformation theory along with finite element formulation, is discussed. Then the effect of fiber-angle variation on the instability behavior of VAT composite panels subjected to in-plane periodic compression is studied. Unlike straight-fiber composites, the pre-buckling problem of the VAT laminate has to be solved initially to obtain the plate in-plane stress distribution due to the applied uniform compression along the edges. Subsequently, the evaluated stress distributions are used in the equations governing the dynamic instability of VAT panels. The dynamic instability regions of VAT panels are then determined using Bolotin's first-order approximation. The dynamic instability results of VAT panels are evaluated for linear fiber-angle distribution, and their performance is then compared with the straight-fiber laminate. Effect of the fiber-angle configuration, load parameters, boundary conditions, orthotropy ratio, and aspect-ratio on the dynamic instability regions of VAT laminate are investigated in detail.

Chapter 3: Parametric instabilities in delaminated VAT composite panel with cutout

In this chapter, parametric instability in a VAT composite panel with a circular cutout and square delamination around the cutout is presented. The influence of cutout and

delamination on buckling load, natural frequency, and dynamic instability behavior of VAT panels are studied. A parametric study is subsequently carried out to analyze the effect of linearly varying fiber-angle on the dynamic instability regions of VAT laminate. Finally, the benefits of applying VAT technology to improve the dynamic stability performance of VAT composite laminate with cutout and delamination are reported.

Chapter 4: Parametric instabilities in curved VAT composite panel

In the preceding chapters, the parametric behavior of flat VAT panels using the finite element method is investigated. In this chapter, the dynamic instability behavior of a curved VAT composite panel subjected to periodic axial compression load is investigated. The governing energy functional of a curved symmetric VAT panel under external loading is derived using Donnell's shallow shell theory. Later, the discretized equations of motion are derived using the Rayleigh–Ritz method combined with the generalized differential integral quadrature method (GDIQM). The dynamic instability region of a curved VAT panel subjected to periodic axial compression load is determined using Bolotin's first-order approximation. Then, the dynamic instability performance is evaluated for a curved VAT panel with linear fiber-angle distribution and compared with straight-fiber laminates. The influence of fiber-angle variation, the radius-of-curvature, aspect-ratio, and plate boundary conditions on the dynamic instability of the VAT panel is presented.

Chapter 5: Implicit Floquet analysis for parametric instabilities in VAT composite panel

In Bolotin's approach to determining the DIRs of the composite panels, the periodic solutions of the governing equations on the stability boundary are approximated using Fourier series. Since the Fourier expansion contains infinite terms and it is difficult to deal with infinite series, usually in Bolotin's approach the series is truncated to a finite number of terms to solve the problem. Because of the truncation in the series, the stability boundaries obtained using Bolotin's approach is accurate only up to a certain limit, beyond which the boundary diverges from the actual solution.

To avoid this problem, Floquet theory is employed to determine the instability regions in VAT composite panels. As the direct application of Floquet theory to a large degree of freedom system is computationally expensive, an implicit Floquet analysis is implemented to reduce the computational cost. The methodology to use the implicit

Floquet analysis to determine the DIRs of VAT composite panel is discussed.

Chapter 6: Conclusions and Future work

In this chapter, a summary of the important observations presented in the proceeding chapters is given. In particular, the effect of fiber-angle variation on the parametric behavior of various VAT composite panels subjected to in-plane periodic compression load is reported. A number of potential avenues for future work are described based on the observations from the thesis.

Chapter 2

Parametric instabilities in flat VAT composite panel

In this chapter, the theory for modeling the VAT composite laminate along with the finite element formulation is explained. The procedure for static, buckling, modal, and parametric instability analysis of the laminate is also discussed. Bolotin's approach used to evaluate the dynamic stability regions of VAT laminate is presented. A symmetric VAT laminate subjected to in-plane periodic compression load is considered for the parametric studies. The effect of various parameters like tow-steering, boundary conditions, aspect ratio on the dynamic stability behavior of the VAT laminate is investigated, and their performance is compared with straight-fiber and quasi-isotropic composite laminates.

2.1 Modeling of VAT composite panel

In VAT laminate, the fiber orientation continuously changes as a function of the $x - y$ lamina coordinates. The fiber-angle distribution of a VAT lamina is usually represented using polynomials, splines, and NURBS. In this work, Lagrange polynomials are used to describe the linear fiber-angle variation [18] in one direction of the laminate and can be expressed as follows:

$$\psi(x) = \phi + \frac{2(T_1 - T_0)}{a}|x| + T_0. \quad (2.1)$$

Here, T_0 is the fiber-angle at the center of the panel ($x = 0$), T_1 is the fiber-angle at the panel ends ($x = \pm a/2$), and ϕ is the angle of rotation of the fiber path (see Fig. 2.1).

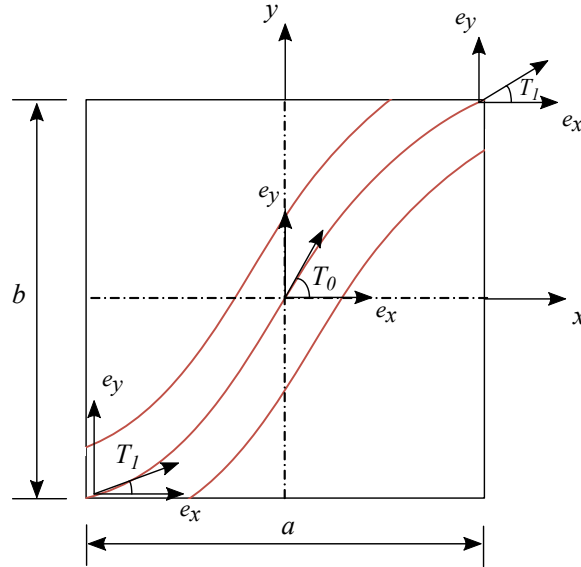


Figure 2.1: Schematic of a VAT lamina.

2.2 First-order shear deformation theory

To model the VAT composite panel, Reissner–Mindlin plate theory [94] (or commonly referred to first-order shear deformation theory (FSDT)) has been used. FSDT considers the effect of transverse shear deformations, which is significant in composite laminates with $E_{11}/G_{13} > 20$. In FSDT, it is assumed that the normal to the plate need not remain orthogonal to the mid-plane after deformation, thus allowing for the transverse deformation effects. Therefore, FSDT is adequate for studying thick plates and composite laminates for which shear deformation effects are important. The assumptions considered in FSDT are as follows:

- A straight line normal to the undeformed mid-plane remains straight even after the deformation.
- The normal stress σ_z is negligible (plane stress assumption).
- The points along a normal to the mid-plane have same vertical displacement (i.e., the thickness does not change during deformation).
- A straight line normal to the undeformed mid-plane remains straight but not necessarily orthogonal to the middle plane after deformation (see Fig. 2.2)

The sign convention for the displacements and rotations of the normal considered in this work are shown in Fig. 2.2.

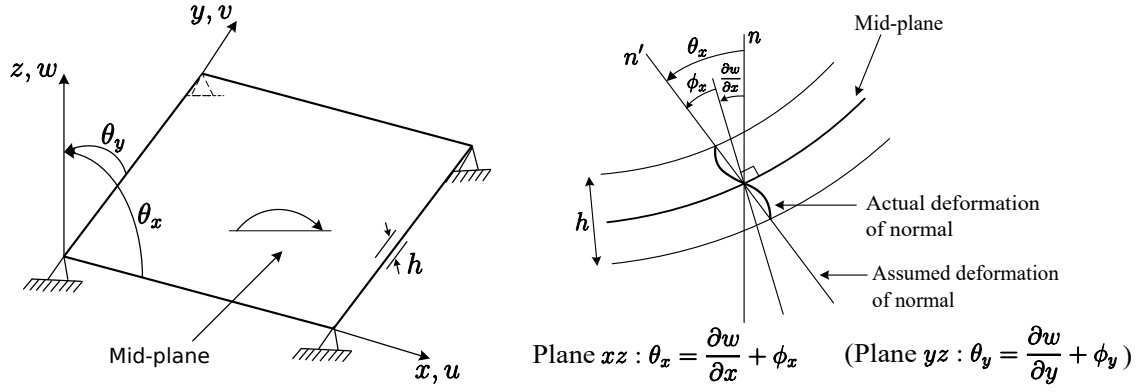


Figure 2.2: Sign convention for the displacements and the rotations of the normal in FSDT.

A composite laminate with its mid-plane represented by (x, y) coordinates and thickness along z -axis is assumed. The displacements and rotations of the plate with bending and in-plane effects are shown in Fig. 2.3. According to FSDT, the 3D displacement field in the laminate is expressed in terms of mid-plane kinematic variables w , θ_x and θ_y as follows (see Fig. 2.3):

$$\begin{aligned}
 u(x, y, z) &= u_0(x, y) - z\theta_x(x, y), \\
 v(x, y, z) &= v_0(x, y) - z\theta_y(x, y), \quad \text{and} \\
 w(x, y, z) &= w_0(x, y).
 \end{aligned} \tag{2.2}$$

Here, $(.)_0$ denoted the displacements of the laminate's mid-plane. θ_x and θ_y are the angles defining the rotation of the normal vector associated with the laminate cross-section. The rotation of the normal in each of the vertical planes xz and yz are obtained as the sum of the slope of laminate mid-plane, and an additional rotation ϕ_x or ϕ_y resulting from the lack of orthogonality of the normal with the mid-plane after deformation (see Fig. 2.3). The rotations θ_x and θ_y in addition to the out-of-plane displacement w are treated as independent variables.

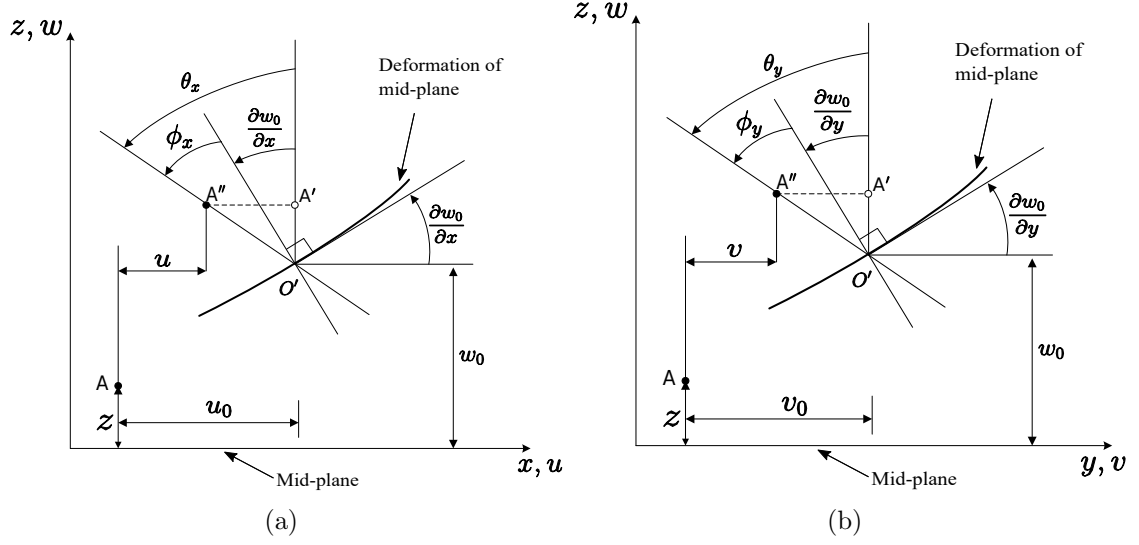


Figure 2.3: Displacements and rotations in a plate with bending and in-plane effects: (a) Plane xz (b) Plane yz .

From the displacement fields obtained in Eq. (2.2), the strain-displacement relationship for the laminate can be expressed as:

$$\boldsymbol{\epsilon} = \begin{Bmatrix} \boldsymbol{\epsilon}_p \\ \dots \\ \boldsymbol{\epsilon}_s \end{Bmatrix} = \begin{Bmatrix} \epsilon_x \\ \epsilon_y \\ \gamma_{xy} \\ \dots \\ \gamma_{xz} \\ \gamma_{yz} \end{Bmatrix} = \begin{Bmatrix} \frac{\partial u}{\partial x} \\ \frac{\partial v}{\partial y} \\ \frac{\partial u}{\partial y} + \frac{\partial v}{\partial x} \\ \dots \\ \frac{\partial u}{\partial z} + \frac{\partial w}{\partial x} \\ \frac{\partial v}{\partial z} + \frac{\partial w}{\partial y} \end{Bmatrix} = \begin{Bmatrix} \boldsymbol{\epsilon}_m \\ \mathbf{0} \end{Bmatrix} + \begin{Bmatrix} -z\boldsymbol{\epsilon}_b \\ \boldsymbol{\epsilon}_s \end{Bmatrix} = \mathbf{S}\hat{\boldsymbol{\epsilon}}, \quad (2.3)$$

where, $\hat{\boldsymbol{\epsilon}} = [\boldsymbol{\epsilon}_m \ \boldsymbol{\epsilon}_b \ \boldsymbol{\epsilon}_s]^T$. Here $\boldsymbol{\epsilon}_m$, $\boldsymbol{\epsilon}_b$, and $\boldsymbol{\epsilon}_s$ are the generalized strain vectors due to membrane, bending and transverse shear deformations, respectively and are defined

as follows:

$$\begin{aligned}
\boldsymbol{\epsilon}_m &= \left[\frac{\partial u_0}{\partial x}, \frac{\partial v_0}{\partial y}, \frac{\partial u_0}{\partial y} + \frac{\partial v_0}{\partial x} \right]^T, \\
\boldsymbol{\epsilon}_b &= \left[\frac{\partial \theta_x}{\partial x}, \frac{\partial \theta_y}{\partial y}, \left(\frac{\partial \theta_x}{\partial y} + \frac{\partial \theta_y}{\partial x} \right) \right]^T, \text{ and} \\
\boldsymbol{\epsilon}_s &= \left[\frac{\partial w_0}{\partial x} - \theta_x, \frac{\partial w_0}{\partial y} - \theta_y \right]^T,
\end{aligned} \tag{2.4}$$

with

$$\mathbf{S} = \begin{bmatrix} \mathbf{I}_3 & -z\mathbf{I}_3 & \mathbf{0} \\ \mathbf{0} & \mathbf{0} & \mathbf{I}_2 \end{bmatrix}. \tag{2.5}$$

Here, \mathbf{I}_n is the $n \times n$ unit matrix. The vectors $\boldsymbol{\epsilon}_p$ and $\boldsymbol{\epsilon}_s$ contains the in-plane strains and the transverse shear strains at a point in the laminate, respectively. The transformation of the generalized strains $\hat{\boldsymbol{\epsilon}}$ to the actual strains $\boldsymbol{\epsilon}$ at a point is performed through the matrix \mathbf{S} .

2.2.1 Stress-strain relationship

Schematic of a composite VAT laminate with n_l laminae is shown in Fig. 2.4. The x , y , z in Fig. 2.4 represents the global axes, and 1, 2, and z represent the orthotropy axes of the fiber at any given location in the lamina. The 1-axis defines the longitudinal fiber direction which is embedded in a polymer matrix. $\psi_k(x, y)$ represents the fiber-angle orientation with respect to global x -axis at the location (x, y) for the k^{th} layer. In the formulation of the stress-strain relationship for the VAT laminate, the following assumptions are considered:

- Each layer, k is defined by the planes $z = z_k$ and $z = z_{k+1}$ with $z_k \leq z \leq z_{k+1}$.
- The orthotropy directions 1 and 2 can vary for each lamina and also within the lamina, which is represented by the fiber-angle $\psi_k(x, y)$ with respect to global x -axis.
- Each layer satisfies the plane stress assumption ($\sigma_z = 0$).
- The displacement field is continuous between the layers and satisfies Eq. (2.2).

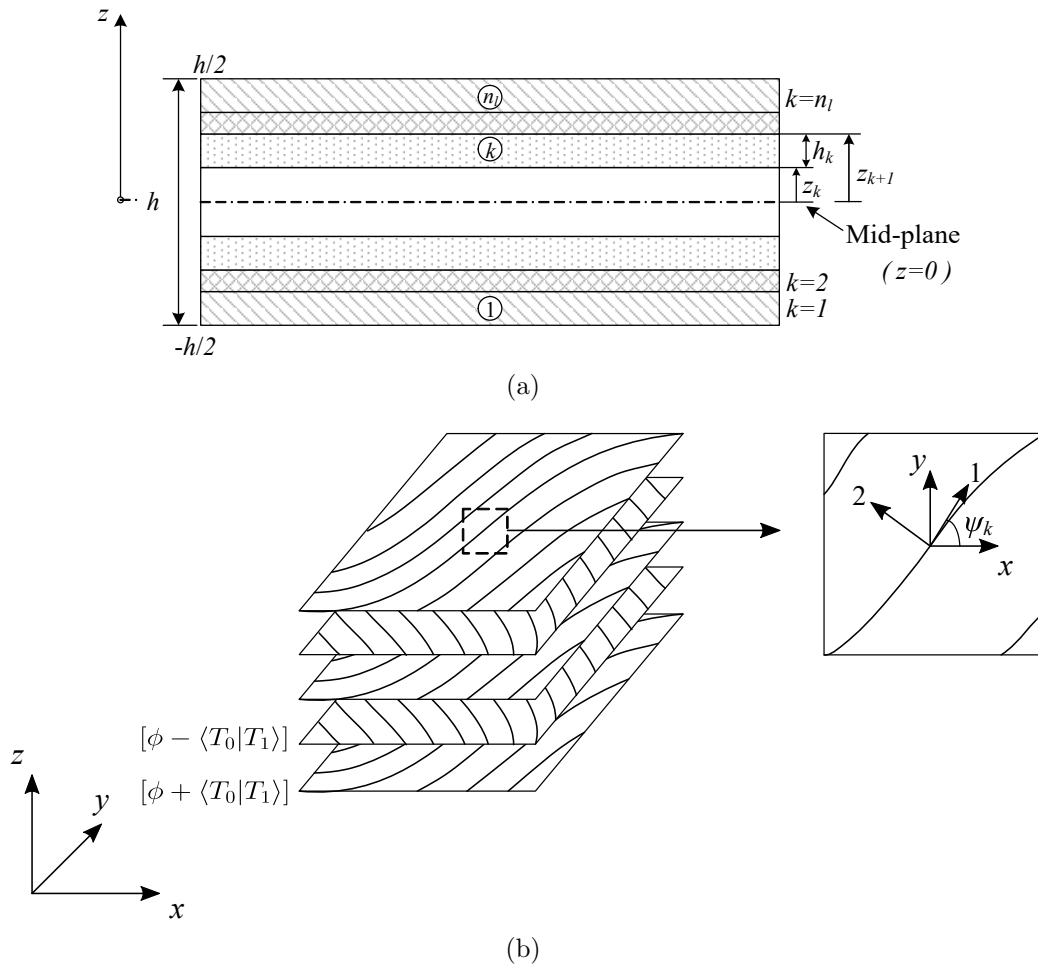


Figure 2.4: Schematic representation of a VAT laminate: (a) Cross-sectional view and definition of the layers in a VAT laminate (b) VAT composite layup and axes representation.

From the above assumptions, the stress-strain relationship of a VAT lamina in its orthogonal axes $(1, 2, z)$ can be written as [95]:

$$\bar{\boldsymbol{\sigma}} = \begin{Bmatrix} \boldsymbol{\sigma}_1 \\ \dots \\ \boldsymbol{\sigma}_2 \end{Bmatrix} = \begin{Bmatrix} \sigma_1 \\ \sigma_2 \\ \tau_{12} \\ \dots \\ \tau_{1z} \\ \tau_{2z} \end{Bmatrix} = \begin{bmatrix} \mathbf{Q}_1(x, y) & \mathbf{0} \\ \mathbf{0} & \mathbf{Q}_2(x, y) \end{bmatrix} \begin{Bmatrix} \boldsymbol{\epsilon}_1 \\ \dots \\ \boldsymbol{\epsilon}_2 \end{Bmatrix} = \bar{\mathbf{Q}}(x, y) \bar{\boldsymbol{\epsilon}}. \quad (2.6)$$

Here, $\boldsymbol{\sigma}_1 = [\sigma_1, \sigma_2, \tau_{12}]^T$ is the vector of in-plane stresses and $\boldsymbol{\sigma}_2 = [\tau_{1z}, \tau_{2z}]^T$ contains the transverse shear stresses in orthogonal axis. The matrices \mathbf{Q}_1 and \mathbf{Q}_2 are the reduced lamina stiffness matrix and reduced transverse shear lamina stiffness matrix, respectively. These matrices are dependent on the five independent material properties (E_{11} , E_{22} , ν_{12} , G_{1z} , and G_{2z}) and are given as:

$$\mathbf{Q}_1 = \begin{bmatrix} \frac{E_{11}}{1-\nu_{12}\nu_{21}} & \frac{E_{22}\nu_{12}}{1-\nu_{12}\nu_{21}} & 0 \\ \frac{E_{22}\nu_{12}}{1-\nu_{12}\nu_{21}} & \frac{E_{22}}{1-\nu_{12}\nu_{21}} & 0 \\ 0 & 0 & G_{12} \end{bmatrix}, \quad \mathbf{Q}_2 = \begin{bmatrix} G_{1z} & 0 \\ 0 & G_{2z} \end{bmatrix}, \quad (2.7)$$

The matrices \mathbf{Q}_1 and \mathbf{Q}_2 are in local orthogonal axes $(1, 2, z)$ and can be transformed into global axes (x, y, z) using the following transformation:

$$\mathbf{Q}_p(x, y) = \mathbf{T}_1^T(x, y) \mathbf{Q}_1 \mathbf{T}_1(x, y), \quad \mathbf{Q}_s(x, y) = \mathbf{T}_2^T(x, y) \mathbf{Q}_2 \mathbf{T}_2(x, y), \quad (2.8)$$

Here, $\mathbf{Q}_p(x, y)$ and $\mathbf{Q}_s(x, y)$ are the transformed reduced lamina stiffness and transverse shear stiffness matrices, respectively. $\mathbf{T}_1(x, y)$ and $\mathbf{T}_2(x, y)$ are the transformation matrices, and are given as:

$$\begin{aligned}
\mathbf{T}_1(x, y) &= \begin{bmatrix} \cos^2 \psi(x, y) & \sin^2 \psi(x, y) & \sin 2\psi(x, y) \\ \sin^2 \psi(x, y) & \cos^2 \psi(x, y) & -\sin 2\psi(x, y) \\ -\frac{1}{2} \sin 2\psi(x, y) & \frac{1}{2} \sin 2\psi(x, y) & \cos 2\psi(x, y) \end{bmatrix}, \text{ and} \\
\mathbf{T}_2(x, y) &= \begin{bmatrix} \cos \psi(x, y) & \sin \psi(x, y) \\ -\sin \psi(x, y) & \cos \psi(x, y) \end{bmatrix}.
\end{aligned} \tag{2.9}$$

From Eqs. (2.6) and (2.8), the stress-strain relationship for the lamina in its global axes (x, y, z) is written as follows:

$$\boldsymbol{\sigma} = \begin{Bmatrix} \boldsymbol{\sigma}_p \\ \dots \\ \boldsymbol{\sigma}_s \end{Bmatrix} = \begin{Bmatrix} \sigma_x \\ \sigma_y \\ \tau_{xy} \\ \dots \\ \tau_{xz} \\ \tau_{yz} \end{Bmatrix} = \begin{bmatrix} \mathbf{Q}_p(x, y) & \mathbf{0} \\ \mathbf{0} & \mathbf{Q}_s(x, y) \end{bmatrix} \begin{Bmatrix} \boldsymbol{\epsilon}_p \\ \dots \\ \boldsymbol{\epsilon}_s \end{Bmatrix} = \mathbf{Q}(x, y)\boldsymbol{\epsilon}. \tag{2.10}$$

2.2.2 Resultant stresses and generalized constitutive matrix

From the obtained in-plane and transverse shear stresses in the lamina (Eq. (2.10)), the resultant stress and moments of the laminate are obtained from the following relations:

$$\begin{aligned}
\bar{\mathbf{N}} &= \begin{Bmatrix} N_x \\ N_y \\ N_{xy} \end{Bmatrix} = \int_{-h/2}^{h/2} \boldsymbol{\sigma}_p dz, & \bar{\mathbf{M}} &= \begin{Bmatrix} M_x \\ M_y \\ M_{xy} \end{Bmatrix} = - \int_{-h/2}^{h/2} z \boldsymbol{\sigma}_p dz, \\
\bar{\mathbf{V}} &= \begin{Bmatrix} S_x \\ S_y \end{Bmatrix} = \int_{-h/2}^{h/2} \boldsymbol{\sigma}_s dz.
\end{aligned} \tag{2.11}$$

Here, the matrices $\bar{\mathbf{N}}$, $\bar{\mathbf{M}}$ and $\bar{\mathbf{V}}$ are the membrane, bending and transverse shear stress resultants, respectively. From the above stress resultants, the generalized constitutive relationship for the VAT laminate is given as:

$$\begin{Bmatrix} \bar{\mathbf{N}} \\ \bar{\mathbf{M}} \\ \bar{\mathbf{V}} \end{Bmatrix} = \begin{bmatrix} \bar{\mathbf{A}}(x, y) & \bar{\mathbf{B}}(x, y) & \mathbf{0} \\ \bar{\mathbf{B}}^T(x, y) & \bar{\mathbf{D}}(x, y) & \mathbf{0} \\ \mathbf{0} & \mathbf{0} & \bar{\mathbf{S}}(x, y) \end{bmatrix} \begin{Bmatrix} \boldsymbol{\epsilon}_m \\ \boldsymbol{\epsilon}_b \\ \boldsymbol{\epsilon}_s \end{Bmatrix}. \quad (2.12)$$

Here, $\bar{\mathbf{A}}$, $\bar{\mathbf{B}}$, $\bar{\mathbf{D}}$ and $\bar{\mathbf{S}}$ are the membrane stiffness matrix, coupling stiffness matrix, bending stiffness matrix, and shear stiffness matrix, respectively and are defined as follows:

$$\bar{\mathbf{A}}(x, y) = \int_{-h/2}^{h/2} \mathbf{Q}_p(x, y) dz = \sum_{k=1}^{n_l} h_k \mathbf{Q}_{pk}(x, y), \quad (2.13)$$

$$\bar{\mathbf{B}}(x, y) = - \int_{-h/2}^{h/2} z \mathbf{Q}_p(x, y) dz = \sum_{k=1}^{n_l} h_k \bar{z}_k \mathbf{Q}_{pk}(x, y), \quad (2.14)$$

$$\bar{\mathbf{D}}(x, y) = - \int_{-h/2}^{h/2} z^2 \mathbf{Q}_p(x, y) dz = \sum_{k=1}^{n_l} \frac{1}{3} (z_{k+1}^3 - z_k^3) \mathbf{Q}_{pk}(x, y), \quad (2.15)$$

$$\bar{\mathbf{S}}(x, y) = \int_{-h/2}^{h/2} \mathbf{Q}_s(x, y) \mathbf{R} dz = \sum_{k=1}^{n_l} h_k \mathbf{Q}_{sk}(x, y) \mathbf{R}. \quad (2.16)$$

where, $h_k = z_{k+1} - z_k$, $\bar{z}_k = \frac{1}{2}(z_{k+1} + z_k)$, $\mathbf{Q}_{pk}(x, y)$ and $\mathbf{Q}_{sk}(x, y)$ are the reduced lamina stiffness and reduced transverse shear stiffness matrices for the k_{th} layer, respectively.

2.2.3 Energy expressions

The equations of motion for the VAT composite panel subjected to in-plane periodic compression load using Hamilton's principle can be obtained as follows:

$$\delta \int (T_{KE} - U) dt = 0, \quad (2.17)$$

where, T_{KE} and U are the kinetic energy and total strain energy of the VAT panel, respectively. From Eq. (2.3) and Eq. (2.12), the strain energy stored in the VAT laminate subjected to uniform axial compression (\bar{u}_0) along the edges (neglecting

higher-order terms) is written as:

$$U = \frac{1}{2} \int_A [\boldsymbol{\epsilon}_m^T \bar{\mathbf{A}} \boldsymbol{\epsilon}_m + \boldsymbol{\epsilon}_b^T \bar{\mathbf{D}} \boldsymbol{\epsilon}_b + \boldsymbol{\epsilon}_m^T \bar{\mathbf{B}} \boldsymbol{\epsilon}_b + \boldsymbol{\epsilon}_b^T \bar{\mathbf{B}} \boldsymbol{\epsilon}_m + \boldsymbol{\epsilon}_s^T \bar{\mathbf{S}} \boldsymbol{\epsilon}_s] d\mathcal{A} + \frac{1}{2} \int_A [\boldsymbol{\epsilon}_L^T \mathbf{T} \boldsymbol{\epsilon}_L] d\mathcal{A}. \quad (2.18)$$

In Eq. (2.18), \mathbf{T} and $\boldsymbol{\epsilon}_L$ are defined as:

$$\mathbf{T} = \begin{bmatrix} \bar{\mathbf{T}} & \mathbf{0} & \mathbf{0} \\ \mathbf{0} & \bar{\mathbf{T}} & \mathbf{0} \\ \mathbf{0} & \mathbf{0} & \bar{\mathbf{T}} \end{bmatrix}, \quad \text{and} \quad \boldsymbol{\epsilon}_L = \left[\frac{\partial w}{\partial x}, \frac{\partial w}{\partial y}, \frac{\partial \theta_x}{\partial x}, \frac{\partial \theta_x}{\partial y}, \frac{\partial \theta_y}{\partial x}, \frac{\partial \theta_y}{\partial y} \right]^T. \quad (2.19)$$

Here, $\bar{\mathbf{T}}$ is the in-plane stress resultant matrix obtained when the uniform axial compression (\bar{u}_0) is applied along the edges:

$$\bar{\mathbf{T}} = \begin{bmatrix} \bar{N}_x & \bar{N}_{xy} \\ \bar{N}_{xy} & \bar{N}_y \end{bmatrix}. \quad (2.20)$$

The displacement derivatives in the integrals of Eq. (2.18) are of the first-order and therefore a C^0 continuous finite element can be used for all the displacement and rotation variables in the finite element analysis.

The kinetic energy for the plate element with a mass density (ρ) can be written as:

$$T_{KE} = \frac{1}{2} \int_A \rho \left[h(\dot{u}^2 + \dot{v}^2 + \dot{w}^2) + \frac{h^3}{12} \dot{\theta}_x^2 + \frac{h^3}{12} \dot{\theta}_y^2 \right] d\mathcal{A}. \quad (2.21)$$

Here, h is the thickness of the laminate. From Eqs. (2.17), (2.18) and (2.21) the governing equations of motion of a VAT panel subjected to periodic in-plane compression load are written as:

$$\mathbf{M}\ddot{\mathbf{u}} + \mathbf{K}\dot{\mathbf{u}} - (\alpha_0 P_{cr} + \alpha_1 P_{cr} \cos(\Omega t)) \mathbf{K}_G \mathbf{u} = 0, \quad (2.22)$$

where, \mathbf{M} , \mathbf{K} , and \mathbf{K}_G are the global mass matrix, stiffness matrix, and geometric stiffness matrix, respectively. α_0 and α_1 are the static and dynamic load parameters, while P_{cr} is the critical buckling load of the VAT panel and Ω is the frequency of excitation. In the following section, the application of finite element method for obtaining the explicit expressions for \mathbf{M} , \mathbf{K} , and \mathbf{K}_G is discussed.

2.2.4 Finite element analysis

To perform finite element analysis, the VAT laminate is discretized using a four-noded isoparametric quadrilateral Reissner–Mindlin plate elements. Inside each element, the displacements and rotations are interpolated as follows:

$$\bar{\mathbf{u}}^e = \sum_{i=1}^4 \mathbf{N}_i \bar{\mathbf{u}}_i^e, \quad (2.23)$$

where \mathbf{N}_i and $\bar{\mathbf{u}}_i^e$ are given by:

$$\mathbf{N}_i = N_i \mathbf{I} \quad \text{and} \quad \bar{\mathbf{u}}_i^e = \begin{bmatrix} u_{0i}, & v_{0i}, & w_{0i}, & \theta_{xi}, & \theta_{yi} \end{bmatrix}^T. \quad (2.24)$$

For the plate element, we use a C^0 continuous isoparametric shape function given by N_i for the node i and are given as follows:

$$\begin{aligned} N_1 &= \frac{(1-\xi)(1-\eta)}{4}; & N_2 &= \frac{(1+\xi)(1-\eta)}{4}, \\ N_3 &= \frac{(1+\xi)(1+\eta)}{4}; & N_4 &= \frac{(1-\xi)(1+\eta)}{4}, \end{aligned} \quad (2.25)$$

where ξ and η are the natural coordinates of the element. On substituting Eq. (2.23) into Eq. (2.4), we get:

$$\boldsymbol{\epsilon}_m^e = \sum_{i=1}^4 \mathbf{B}_{mi} \bar{\mathbf{u}}_i^e, \quad \boldsymbol{\epsilon}_b^e = \sum_{i=1}^4 \mathbf{B}_{bi} \bar{\mathbf{u}}_i^e, \quad \text{and} \quad \boldsymbol{\epsilon}_s^e = \sum_{i=1}^4 \mathbf{B}_{si} \bar{\mathbf{u}}_i^e, \quad (2.26)$$

where,

$$\begin{aligned} \mathbf{B}_{mi} &= \begin{bmatrix} \frac{\partial N_i}{\partial x} & 0 & 0 & 0 & 0 \\ 0 & \frac{\partial N_i}{\partial y} & 0 & 0 & 0 \\ \frac{\partial N_i}{\partial y} & \frac{\partial N_i}{\partial x} & 0 & 0 & 0 \end{bmatrix}, & \mathbf{B}_{bi} &= \begin{bmatrix} 0 & 0 & 0 & -\frac{\partial N_i}{\partial x} & 0 \\ 0 & 0 & 0 & 0 & -\frac{\partial N_i}{\partial y} \\ 0 & 0 & 0 & -\frac{\partial N_i}{\partial y} & -\frac{\partial N_i}{\partial x} \end{bmatrix}, \quad \text{and} \\ \mathbf{B}_{si} &= \begin{bmatrix} 0 & 0 & \frac{\partial N_i}{\partial x} & N_i & 0 \\ 0 & 0 & \frac{\partial N_i}{\partial y} & 0 & N_i \end{bmatrix}. \end{aligned} \quad (2.27)$$

The elemental stiffness matrix due to the first-term in strain energy expression (Eq. (2.18)) can be written as follows:

$$\mathbf{K}^e = \mathbf{K}_m^e + \mathbf{K}_b^e + \mathbf{K}_s^e + \mathbf{K}_{mb}^e. \quad (2.28)$$

The matrix \mathbf{K}^e contains stiffness contributions from membrane (\mathbf{K}_m^e), bending (\mathbf{K}_b^e), transverse shear (\mathbf{K}_s^e) and due to coupling between bending and membrane behavior \mathbf{K}_{mb}^e . These matrices are defined as follows:

$$\mathbf{K}_m^e = \int_{\mathcal{A}} \mathbf{B}_m^T \bar{\mathbf{A}} \mathbf{B}_m d\mathcal{A}, \quad (2.29)$$

$$\mathbf{K}_b^e = \int_{\mathcal{A}} \mathbf{B}_b^T \bar{\mathbf{D}} \mathbf{B}_b d\mathcal{A}, \quad (2.30)$$

$$\mathbf{K}_s^e = \int_{\mathcal{A}} \mathbf{B}_s^T \bar{\mathbf{S}} \mathbf{B}_s d\mathcal{A}, \quad (2.31)$$

$$\mathbf{K}_{mb}^e = \int_{\mathcal{A}} \mathbf{B}_m^T \bar{\mathbf{B}} \mathbf{B}_b d\mathcal{A} + \int_{\mathcal{A}} \mathbf{B}_b^T \bar{\mathbf{B}} \mathbf{B}_m d\mathcal{A}. \quad (2.32)$$

In the above equations $\mathbf{B}_k = [\mathbf{B}_{k1}, \mathbf{B}_{k2}, \mathbf{B}_{k3}, \mathbf{B}_{k4}]$, $k = \{m, b, s\}$. Gauss-quadrature is used to numerically calculate the area integrals in the above equations. The geometric-stiffness matrix (\mathbf{K}_G), due to the second term in strain energy expression (Eq. (2.18)) can be written as follows:

$$\mathbf{K}_G^e = \mathbf{K}_{Gb}^e + \mathbf{K}_{Gs}^e. \quad (2.33)$$

Here, \mathbf{K}_{Gb}^e is the contribution from bending behavior and \mathbf{K}_{Gs}^e is the contribution from transverse shear effects. These matrices are defined as follows:

$$\mathbf{K}_{Gb}^e = \int_{\mathcal{A}} \mathbf{G}_b^T \mathbf{T} \mathbf{G}_b d\mathcal{A}, \quad (2.34)$$

$$\mathbf{K}_{Gs}^e = \frac{h^3}{12} \int_{\mathcal{A}} \mathbf{G}_{s1}^T \mathbf{T} \mathbf{G}_{s1} d\mathcal{A} + \frac{h^3}{12} \int_{\mathcal{A}} \mathbf{G}_{s2}^T \mathbf{T} \mathbf{G}_{s2} d\mathcal{A}. \quad (2.35)$$

The matrices \mathbf{G}_b , \mathbf{G}_{s1} , and \mathbf{G}_{s2} are given by:

$$\mathbf{G}_b = \begin{bmatrix} \frac{\partial N_i}{\partial x} & 0 & 0 \\ \frac{\partial N_i}{\partial y} & 0 & 0 \end{bmatrix}, \quad \mathbf{G}_{s1} = \begin{bmatrix} 0 & \frac{\partial N_i}{\partial x} & 0 \\ 0 & \frac{\partial N_i}{\partial y} & 0 \end{bmatrix}, \quad \text{and} \quad \mathbf{G}_{s2} = \begin{bmatrix} 0 & 0 & \frac{\partial N_i}{\partial x} \\ 0 & 0 & \frac{\partial N_i}{\partial y} \end{bmatrix}. \quad (2.36)$$

Similarly, from Eq. (2.21), the consistent elemental mass matrix can be obtained as follows:

$$\mathbf{M}^e = \int_{\mathcal{A}} \rho \mathbf{N}_i^T \mathbf{\Lambda} \mathbf{N}_i d\mathcal{A}. \quad (2.37)$$

Here, $\mathbf{\Lambda} = \text{Diag}[h, h, h, h^3/12, h^3/12]$. From the obtained elemental matrices \mathbf{K}^e , \mathbf{K}_G^e , and \mathbf{M}^e , global stiffness (\mathbf{K}), global geometric-stiffness (\mathbf{K}_G), and global mass matrices (\mathbf{M}) can be assembled, respectively, which will be used in the analysis of VAT composite panels.

2.3 Analysis of VAT panel

In VAT panels, since the fiber-angle varies with respect to the position in the plane of the lamina, the stiffness properties of the laminate are function of $x - y$ coordinates. Therefore, pre-buckling analysis has to be carried out to determine the non-uniform in-plane stress resultants.

Static analysis

The pre-buckling analysis of the VAT laminate when subjected to uniform axial compression (\bar{u}_0) along the edges is carried out by using the following expression:

$$\mathbf{K}\bar{\mathbf{u}} = \mathbf{F}, \quad (2.38)$$

here, $\bar{\mathbf{u}}$ is the vector of unknown displacement variables, and \mathbf{F} is the equivalent compression force vector that will result due to the uniform compression of \bar{u}_0 at the edge. From the obtained displacement vector, $\bar{\mathbf{u}}$ the in-plane strains and the resultant stresses can be determined using Eq. (2.26) and Eq. (2.12), respectively. Then the obtained stress resultants ($\bar{\mathbf{N}}$), are used to determine the geometric-stiffness matrix (\mathbf{K}_G) using Eq. (2.33), which will be used in the buckling analysis.

Buckling analysis

The critical buckling load of the VAT laminate subjected to an uniform axial compression load is determined from the following eigen buckling equation:

$$\mathbf{K}\bar{\mathbf{u}} = \lambda \mathbf{K}_G \bar{\mathbf{u}}, \quad (2.39)$$

here, λ is the eigenvalue for the problem. The critical buckling load of the VAT laminate can be obtained as $P_{cr} = \lambda \int_{-b/2}^{b/2} \bar{N}_x(a/2, y) dy$, where a and b are length and width of the laminate, respectively.

Modal analysis

The modal analysis of the VAT panel can be determined from the following eigenvalue problem:

$$\mathbf{K}\mathbf{w} = -\omega^2\mathbf{M}\mathbf{w}, \quad (2.40)$$

here, ω is the fundamental frequencies and \mathbf{w} corresponds to the mode-shapes.

Dynamic stability

The equations of motion for the VAT panel subjected to periodic axial compression load, $P(t) = \alpha_0 P_{cr} + \alpha_1 P_{cr} \cos(\Omega t)$ can be written as follows:

$$\mathbf{M}\ddot{\mathbf{u}} + \mathbf{K}\mathbf{u} - (\alpha_0 P_{cr} + \alpha_1 P_{cr} \cos(\Omega t)) \mathbf{K}_G \mathbf{u} = 0, \quad (2.41)$$

here, Ω is the frequency of the periodic load and \mathbf{M} is the global mass matrix of the VAT laminate. The parameters α_0 and α_1 are static and dynamic load parameters, respectively. It should be noted that the applied load $P(t) = \alpha_0 P_{cr} + \alpha_1 P_{cr} \cos(\Omega t)$ results in uniform compression of $u(t) = \alpha_0 u_{cr} + \alpha_1 u_{cr} \cos(\Omega t)$ at the loading edges (see Fig. 2.5), here, u_{cr} is the critical displacement at which the laminate buckles.

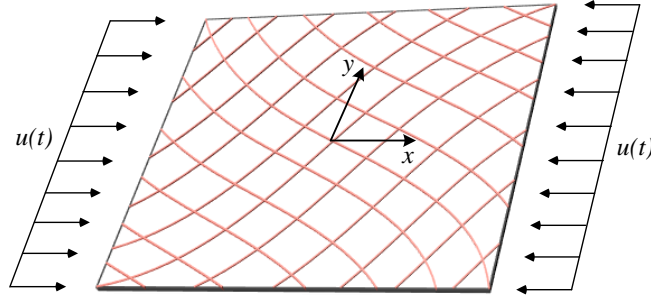


Figure 2.5: VAT composite laminate subjected to uniform in-plane periodic compression load.

Equation (2.41) represents a system of linear ordinary differential equations with time-periodic coefficients. For certain combinations of parameters α_0 , α_1 and Ω , the response of the laminate can become unbounded due to parametrically excited

resonance and is referred to as dynamic instability. The regions in the parametric space, where this dynamic instability occurs are known as dynamic instability regions (DIRs). We resort to Bolotin's approach [49] to determine the stability of boundaries of Eq. (2.41). According to Bolotin's approximation, the solutions on the stability boundary (Eq. (2.41)) are time-periodic with period $T_1 = 2\pi/\Omega$ or $T_2 = 4\pi/\Omega$. Therefore, the solution of Eq. (2.41) is expanded as follows:

$$\bar{\mathbf{u}} = \frac{1}{2}\mathbf{b}_0 + \sum_{k=2,4,6}^{\infty} (\mathbf{a}_k \sin(k\Omega t/2) + \mathbf{b}_k \cos(k\Omega t/2)), \quad (2.42)$$

$$\bar{\mathbf{u}} = \sum_{k=1,3,5}^{\infty} (\mathbf{a}_k \sin(k\Omega t/2) + \mathbf{b}_k \cos(k\Omega t/2)). \quad (2.43)$$

The coefficients \mathbf{a}_k , \mathbf{b}_k are yet to be determined and are infinite in numbers. As it is difficult to deal with infinite coefficients, a first-order approximation is often used in the literature [58, 61, 63–65] and is sufficient to accurately predict the stability boundary for a small range of α_1 . In the first-order Bolotin's approximation, only the first-three terms are considered in Eq. (2.42) and the first-two terms are considered in Eq. (2.43), therefore we get:

$$\bar{\mathbf{u}} = \frac{1}{2}\mathbf{b}_0 + \mathbf{a}_2 \sin(\Omega t) + \mathbf{b}_2 \cos(\Omega t), \quad (2.44)$$

$$\bar{\mathbf{u}} = \mathbf{a}_1 \sin(\Omega t/2) + \mathbf{b}_1 \cos(\Omega t/2). \quad (2.45)$$

We now substitute, Eq. (2.44) and Eq. (2.45) into Eq. (2.41) to get the residual equations. It should be noted that the coefficients of $\sin(\Omega t)$, $\cos(\Omega t)$, $\sin(\Omega t/2)$, $\cos(\Omega t/2)$, and the constant term must vanish in the residual equations. This leads to the following quadratic eigenvalue problems with the eigenvalue Ω :

$$[\mathbf{K} - (\alpha_0 + 0.5\alpha_1)P_{cr}\mathbf{K}_G]\{\mathbf{a}_1\} - 0.25\mathbf{M}\Omega^2\{\mathbf{a}_1\} = 0, \quad (2.46)$$

$$[\mathbf{K} - (\alpha_0 - 0.5\alpha_1)P_{cr}\mathbf{K}_G]\{\mathbf{b}_1\} - 0.25\mathbf{M}\Omega^2\{\mathbf{b}_1\} = 0, \quad (2.47)$$

$$[\mathbf{K} - \alpha_0 P_{cr}\mathbf{K}_G]\{\mathbf{a}_2\} - \mathbf{M}\Omega^2\{\mathbf{a}_2\} = 0, \quad (2.48)$$

$$\begin{bmatrix} \mathbf{K} - \alpha_0 P_{cr}\mathbf{K}_G & -\alpha_1 P_{cr}\mathbf{K}_G \\ -0.5\alpha_1 P_{cr}\mathbf{K}_G & \mathbf{K} - \alpha_0 P_{cr}\mathbf{K}_G \end{bmatrix} \begin{Bmatrix} \mathbf{b}_0 \\ \mathbf{b}_2 \end{Bmatrix} - \Omega^2 \begin{bmatrix} 0 & 0 \\ 0 & \mathbf{M} \end{bmatrix} \begin{Bmatrix} \mathbf{b}_0 \\ \mathbf{b}_2 \end{Bmatrix} = 0 \quad (2.49)$$

The solution of Eqs. (2.46)-(2.49) determines the first-order approximation of the first and second instability regions. Equations (2.46) and (2.47) determines the upper and lower boundaries of the first dynamic instability region (principle parametric resonance), whereas Eq. (2.48) and Eq. (2.49) determine boundaries of the second

instability region (secondary parametric resonance).

2.4 Results and discussion

A symmetric VAT laminate considered for the stability analysis is shown in Fig. 2.6. A finite element code for a four-noded Reissner-Mindlin plate was developed in MATLAB for analyzing the VAT laminate. The element stiffness matrix is constructed by considering the fiber-angle at the center of the element and assumed it to be uniform over the element. For numerical integration, 2×2 Gauss-points are used for calculating element mass matrix (\mathbf{M}^e), stiffness contribution from membrane (\mathbf{K}_m^e) and stiffness contribution from bending (\mathbf{K}_b^e). To avoid shear-locking problems in thin laminates, reduced integration with 1×1 Gauss-point is employed in calculating shear contribution in element stiffness matrix (\mathbf{K}_s^e) and the element geometric stiffness matrix (\mathbf{K}_G^e).

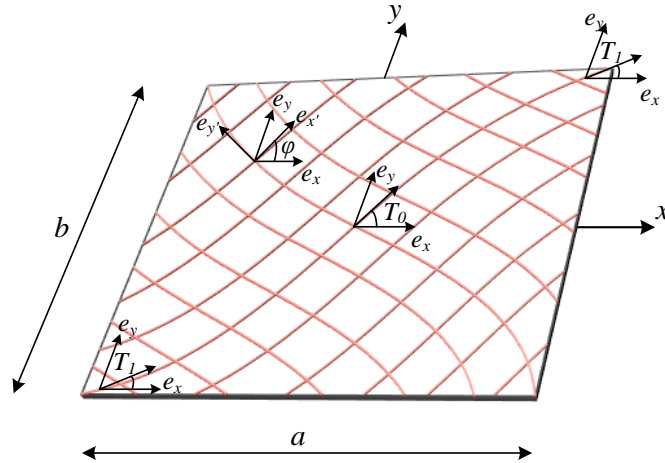


Figure 2.6: Schematic of the VAT laminate.

For the numerical study, a symmetric VAT laminate $[\phi \pm \langle T_0 | T_1 \rangle]_{3s}$ with the following material properties is considered: $E_{11} = 181$ GPa, $E_{22} = 10.27$ GPa, $\rho = 1600$ Kg/m³, $G_{12} = 7.17$ GPa, $G_{23} = 3$ GPa, $\nu_{12} = 0.28$, $G_{13} = G_{12}$, $\nu_{13} = \nu_{12}$, $a = b = 1$ m, $h = 1.5264 \times 10^{-3}$ m.

A mesh convergence study is performed first on a simply-supported square symmetrical VAT laminate $[0 \pm \langle 0 | T_1 \rangle]_{3s}$ for different fiber-angles (T_1). A convergence study is carried out by evaluating the natural frequency and critical buckling load of the laminate for different mesh densities. Normalized fundamental frequency

$\tilde{\omega} = \omega a^2 / h \sqrt{\rho / E_{22}}$ (where, ω is the first natural frequency) and critical buckling load $K_{cr} = P_{cr} a^2 / E_{11} b h^3$ are tabulated in Table 2.1 as a function of mesh density. A commercial FE software, ABAQUS is used to validate the numerical simulations from the in-house FE code. In ABAQUS, the S4 shell element with a mesh density of 50×50 is chosen for analyzing the VAT laminate, and the results are shown in Table 2.1. It is clear from the Table 2.1, that the results are converged for a mesh size of 30×30 . The $\tilde{\omega}$ and K_{cr} values for an unidirectional composite laminate ($T_1 = 0$) are also evaluated analytically and shown in Table 2.1 for verification purpose. The procedure for obtaining analytical expressions for natural frequency and critical buckling load for an orthotropic composite laminate has been discussed in Appendix. (A).

Table 2.1: Mesh convergence study of normalized natural frequency ($\tilde{\omega}$) and normalized critical buckling load (K_{cr}) obtained by FEM for a VAT laminate $[0 \pm \langle 0|T_1 \rangle]_{3s}$ under uniform axial compression.

Mesh	T_1					
	0°		30°		60°	
	$\tilde{\omega}$	K_{cr}	$\tilde{\omega}$	K_{cr}	$\tilde{\omega}$	K_{cr}
10 x 10	13.5120	1.0497	15.2612	1.3686	16.6913	1.7245
20 x 20	13.4133	1.0343	15.2719	1.3725	16.6542	1.7142
30 x 30	13.3945	1.0315	15.2675	1.3726	16.6379	1.7075
40 x 40	13.3876	1.0304	15.2625	1.3722	16.6284	1.7038
Abaqus	13.3706	1.0287	15.2606	1.3700	16.6259	1.6974
Analytical	13.3825	1.0296				

The variation of normalized fundamental frequency ($\tilde{\omega}$) with respect to the static load parameter (α_0) for a simply-supported VAT laminate $[0 \pm \langle 0|30 \rangle]_{3s}$ is shown in Fig. 2.7. The obtained results are then compared with ABAQUS and found to be in good agreement.

Subsequently, the DIRs of a simply-supported symmetrical cross-ply laminate of $[0/90/90/0]$ with the material properties: $a = 10$ in., $a/h = 25$, $\rho = 1$ lb in.⁻³, $E_{22} = 10^6$ psi, $E_{11}/E_{22} = 40$, $G_{12}/E_{22} = 0.6$, $G_{23}/E_{22} = 0.5$, $\nu_{12} = 0.25$, $G_{13} = G_{12}$, $\nu_{13} = \nu_{12}$, subjected to periodic in-plane compression is studied for validation purposes. The first and second DIRs of the laminate are plotted in Fig. 2.8 in the plane of dynamic load parameter α_1 and $\bar{\omega} = \Omega/\omega$. Here, Ω is the excitation frequency and ω

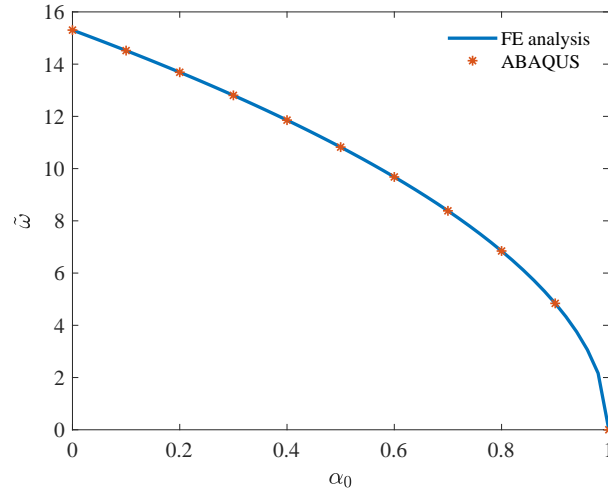


Figure 2.7: Variation of normalized frequency ($\tilde{\omega}$) with static buckling load parameter (α_0) for a simply-supported VAT laminate $[0 \pm \langle 0|30 \rangle]_{3s}$.

is the fundamental natural frequency. Figure 2.8 also includes the results of Moorthy et al. [58] and compare favorably with that of the results from the present analysis.

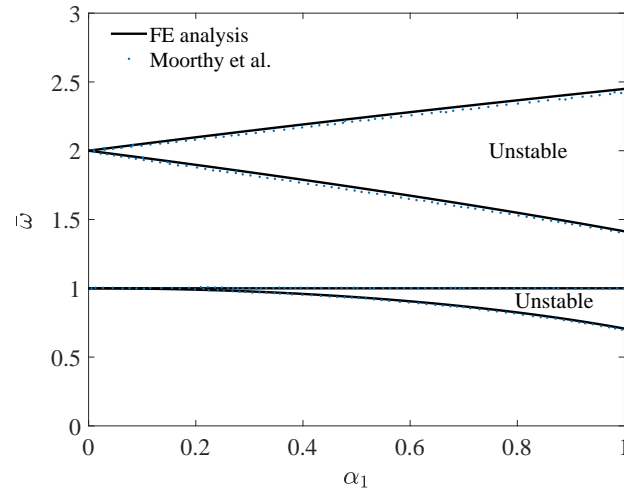


Figure 2.8: First and second instability regions of a symmetric simply-supported cross-ply laminate $[0/90/90/0]$.

2.5 Dynamic instability in VAT laminate

The effect of in-plane boundary conditions on the dynamic stability behavior of symmetric simply-supported VAT laminate is investigated. Different types of boundary conditions used in the present analysis are shown in Fig. 2.9. In all the cases the panel is subjected to a uniform periodic end-shortening, $u(t)$ at $x = \pm a/2$. However, the boundary conditions along the transverse edges are different. Two different cases have been studied in the present analysis. In the Case-I (see Fig. 2.9(a)) transverse edges of the laminate are set to be traction free and in Case-II (see Fig. 2.9(b)), transverse edges are fixed [18].

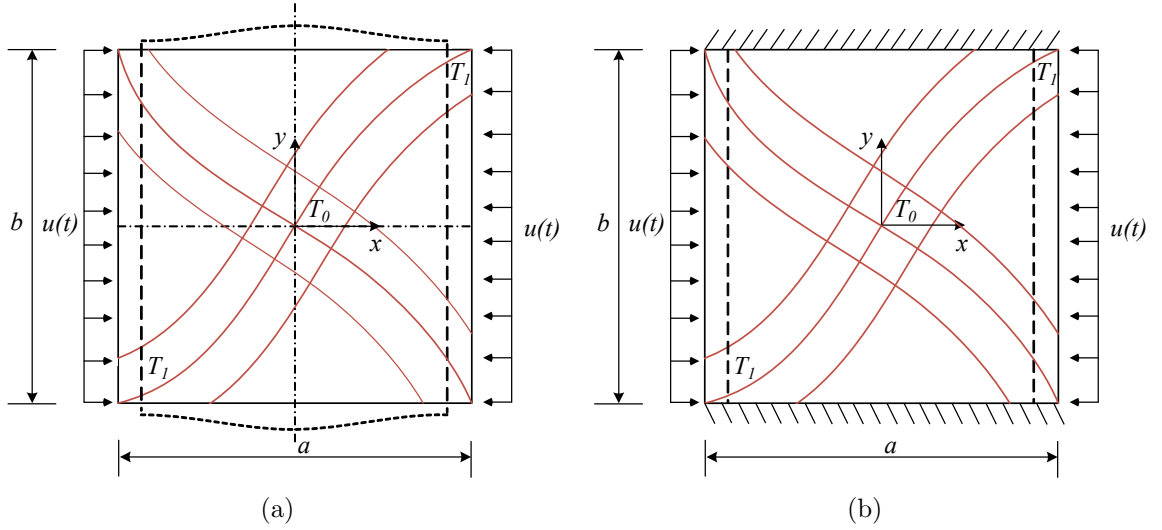


Figure 2.9: Types of in-plane boundary conditions: (a) Case-I: Transverse edges are free (b) Case-II: Transverse edges are fixed.

2.5.1 Case-I

In this case, the stability analysis is carried out on a simply-supported symmetric VAT laminate with transverse edges free to deform in the plane of the laminate. Here, the fiber-angle variation (ψ) is chosen to be a function of only y -coordinate ($\phi = 90^\circ$) under the action of a periodic uniform end shortening ($u(t)$) along the x -direction. DIR of the VAT laminate for different values of T_1 are evaluated for the fiber-angle $T_0 = 0^\circ$ and the static load parameter $\alpha_0 = 0$. The results shown in the plane of normalized critical buckling load (K_{cr}) versus normalized excitation frequency ($\tilde{\Omega} = \Omega a^2 / h \sqrt{\rho / E_{22}}$) in Fig. 2.10. It can be seen that any change in the

fiber-angle configuration influences the natural frequency, critical buckling load, and DIR for the VAT laminate.

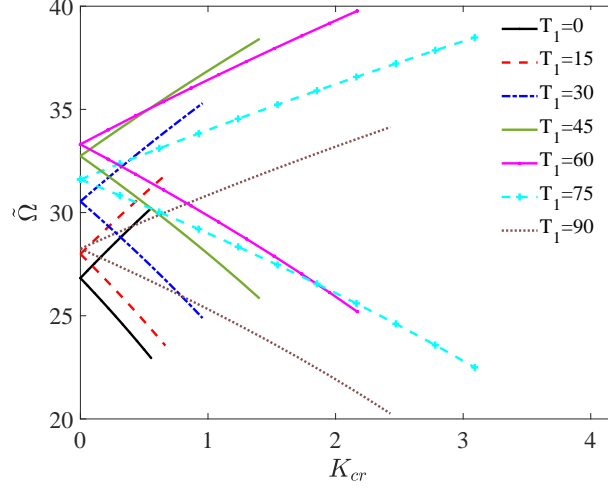


Figure 2.10: Principal DIRs of a simply-supported VAT laminate $[90 \pm \langle 0|T_1 \rangle]_{3s}$ for different fiber-angles (T_1) for Case-I boundary condition under periodic axial compression.

For example, in Fig. 2.10, for the VAT laminate with fiber-angle $T_1 = 0^\circ$, the two curves bounding the DIR extends to a small range of K_{cr} . It should be noted that the value of K_{cr} at which the stability boundary terminates corresponds to $\alpha_1 = 1$, and beyond which static instability occurs. Whereas, in the case of a VAT laminate with fiber-angle $T_1 = 60^\circ$, the natural frequency is very high. So, the onset of the DIR starts at a high resonance frequency, and this increases the range of frequency of the periodic load for which the VAT laminate is stable. But, in the case of VAT laminate with fiber-angle $T_1 = 75^\circ$, critical buckling load is very high, and hence the compression load-carrying capacity of the VAT laminate increases. This extends the boundary of the DIR to a larger K_{cr} value increasing the dynamically stable region. Both the VAT laminates with fiber-angles $T_1 = 65^\circ$ and $T_1 = 75^\circ$ have a larger dynamically stable region than that of the laminate with $T_1 = 0^\circ$ because of their higher natural frequency and critical buckling load. Therefore, for a VAT laminate to attain maximum dynamic stability, optimal fiber-angle has to be selected such that both natural frequency and critical buckling load are high.

In VAT laminate, when dynamic load parameter α_1 is very small, the parametric resonance frequency approaches 2ω and with an increase in α_1 the dynamic instability opening (D_{IO}) increases. The distance between the two instability boundaries

is termed as D_{IO} and represents the range of parametric resonance frequency at a particular load level. Since the dynamic instability of a laminate is closely related to its fundamental natural frequency and critical buckling load, a dynamic instability index (D_{II}) is used to characterize the dynamic stability of the VAT laminate [64] and is given as:

$$D_{II} = \frac{D_{IO}}{\omega K_{cr}}, \quad (2.50)$$

where, D_{IO} is evaluated at a specific value of α_1 . A higher value of D_{II} indicates that the VAT laminate is more dynamically unstable. Figure 2.11 shows a plot between $D_{II}^{vat}/D_{II}^{iso}$ and E_{vat}/E_{iso} . Here, D_{II}^{vat} and D_{II}^{iso} are evaluated for $\alpha_0 = 0$ and $\alpha_1 = 0.4$. The terms E_{vat} and E_{iso} represent the stiffness for the VAT laminate and homogeneous quasi-isotropic laminate and can be obtained as follows:

$$E_{vat} = \frac{a}{bh_{u_0}} \int_{-b/2}^{b/2} \bar{N}_x(a/2, y) dy, \quad (2.51)$$

$$E_{iso} = U_1 \left(1 - \left(\frac{U_4}{U_1} \right)^2 \right). \quad (2.52)$$

Here, the parameters U_1 and U_4 are material invariants (see Ref: [96]).

Figure 2.11 shows the family of curves corresponding to various values of T_0 (see Fig. 2.9). Each curve is generated by varying T_1 (see Fig. 2.9) from 0° (the left endpoint of the curve) to 90° (the right endpoint of the curve) with the increment of 10° for a given value of T_0 . In Fig. 2.11, the curve representing the straight-fiber laminate ($[\theta]_{3s}$) shows the variation of normalized D_{II} and stiffness with a change in fiber-angle from 0° (the right endpoint of the curve) to 90° (the left endpoint of the curve). The minimum value of normalized D_{II} for the straight-fiber laminate is found to be 0.8164 for the layup $[\pm 45]_{3s}$.

The minimum value of the normalized D_{II} for the VAT laminate is found to be 0.4398 and is obtained for a fiber orientation of $T_0 = 0^\circ$ and $T_1 = 75^\circ$. This value is 46.1% lower than the minimum value obtained by straight-fiber laminate configuration. Moreover, the VAT laminate with configuration $[90 \pm \langle 0|75 \rangle]_{3s}$ shows 56% decrease in D_{II} when compared to a quasi-isotropic laminate. The substantial decrease in the D_{II} value of the VAT laminate is due to its high critical buckling load. In VAT laminate, the applied dynamic compression load gets distributed away from the center of the panel to edges and therefore has higher buckling load $K_{cr} = 3.09$.

VAT laminate with most of the fiber-angle configurations have less D_{II} value than the optimal straight-fiber laminate configuration $[\pm 45]_{3s}$. Unlike conventional com-

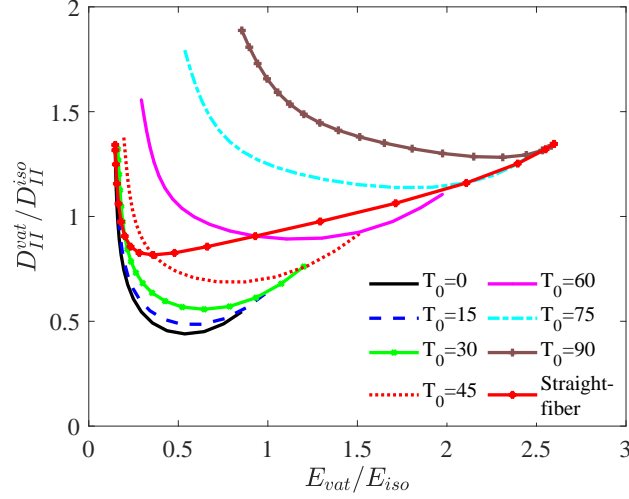


Figure 2.11: Variation of normalized dynamic instability index (D_{II}) of a simply-supported VAT laminate $[90 \pm \langle T_0 | T_1 \rangle]_{3s}$ for different fiber-angles T_0 and T_1 for Case-I boundary condition.

posites, for a given value of stiffness E_{vat}/E_{iso} , one can design VAT laminates with different D_{II} values and vice-versa. This provides an added advantage to the designer by allowing more room for tailoring the D_{II} and stiffness of the VAT laminate, simultaneously.

2.5.2 Case-II

Dynamic stability of the VAT laminate for Case-II type boundary condition where the transverse edges are fixed has been analyzed. In this case, a fiber-angle variation of the VAT laminate was chosen to be a function of x -coordinate, $\psi = \psi(x)$ (i.e., in the loading direction). Variation of D_{II} with the various VAT fiber-angles is shown in Fig. 2.12. The D_{II} values in Fig. 2.12 are evaluated when $\alpha_0 = 0$ and $\alpha_1 = 0.4$.

From the Fig. 2.12, it is seen that minimum value of normalized D_{II} is 0.9061 and is achieved for the straight-fiber layup $[\pm 35]_{3s}$. For VAT laminate, the minimum value of D_{II} is 0.7605 for the fiber orientation $T_0 = 0^\circ$ and $T_1 = 50^\circ$ which is 16.07% less when compared to the straight-fiber laminate $[\pm 35]_{3s}$ and 23.95% less when compared to quasi-isotropic laminate. In this case, the decrease in D_{II} is not high as the Case-I as there is less load redistribution towards the supported edges of the laminate. However, the improvement in the dynamically stable behavior of the VAT laminate is due to the tensile nature of the transverse stress resultant induced at the center

of the panel which has to be overcome by the applied compression load. Thus, the in-plane boundary conditions have a considerable influence on the dynamic stability behavior of the VAT laminate.

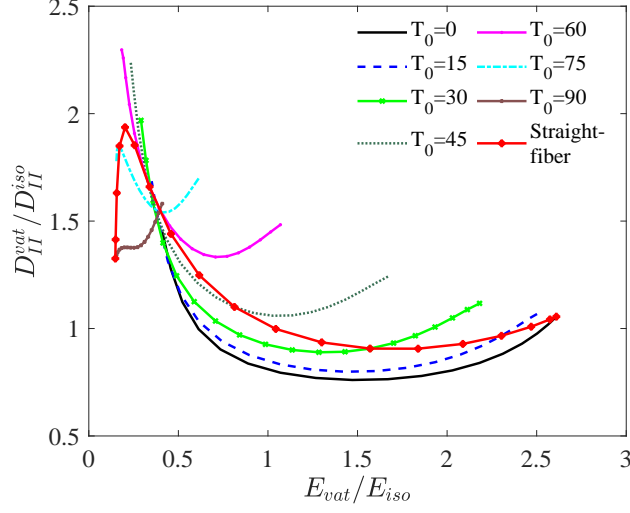


Figure 2.12: Variation of normalized dynamic instability index (D_{II}) of a simply supported square VAT laminate $[0 \pm \langle T_0 | T_1 \rangle]_{3s}$ for different values of T_0 and T_1 for Case-II boundary condition.

2.5.3 Effect of static load parameter

Next, the effect of static load parameter, α_0 on dynamic stability behavior of VAT laminate is studied. The analysis is carried on a VAT laminate, $[90 \pm \langle 0 | 75 \rangle]_{3s}$ by varying α_0 from 0 to 0.8 in steps of 0.2 and the results are shown in Fig. 2.13(a). It is observed from Fig. 2.13(a) that an increase in static load leads to an early onset and a wider DIR. This implies that the presence of the static compression load reduces the stiffness of the laminate, and thus shifts the resonance frequencies or the DIR towards the lower frequency. The variation of D_{II} with static load parameter is shown in Fig. 2.13(b). The value of α_1 in calculating D_{II} is chosen to be 0.4. Figure 2.13(b) shows that with the increase in α_0 the value of D_{II} increases, indicating the decrease in the stability of the laminate with a higher static load.

2.5.4 Effect of plate boundary conditions

The effect of plate boundary conditions on the dynamic stability of the VAT laminate is studied in this section. The analysis is carried out on a VAT laminate $[90 \pm \langle 0 | 75 \rangle]_{3s}$

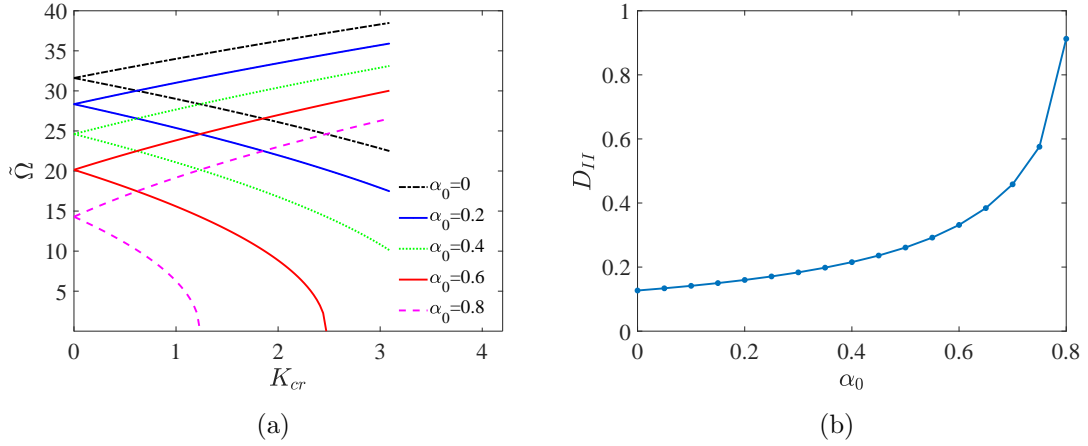


Figure 2.13: Effect of static load parameter (α_0) on the principle DIR of the VAT laminate, $[90 \pm \langle 0|75 \rangle]_{3s}$ for different values of α_0 : (a) Normalized frequency ($\tilde{\Omega}$) versus normalized buckling load (K_{cr}) (b) Dynamic instability index (D_{II}) versus static load parameter (α_0).

with the Case-I boundary conditions. DIRs for the VAT laminate with different plate boundary conditions (SSSS, CSCS, and CCCC) are evaluated and shown in Fig. 2.14. The static load parameter (α_0) is chosen to be zero for the analysis. Figure 2.14 clearly illustrates that from SSSS to CCCC, the onset of DIR shifts toward the higher frequency along with the increase in buckling load. Moreover, the region of instability becomes narrower from SSSS to CCCC plate boundary conditions, increasing the dynamic stability of the laminate because of the restraining of the edges. The variation of D_{II} with the fiber orientation of the VAT laminate $[90 \pm \langle T_0|T_1 \rangle]_{3s}$ was evaluated for CSCS and CCCC plate boundary conditions and results are shown in Fig. 2.14 and Fig. 2.15. The value of D_{II} was evaluated for $\alpha_0 = 0$ and $\alpha_1 = 0.4$. Variation of D_{II} for SSSS boundary condition was already shown in Fig. 2.11. In the case of CSCS plate boundary condition, the minimum value of normalized D_{II} for the straight-fiber laminate is 0.6744 and is obtained for a fiber-angle of 90° . For VAT laminate the minimum value of D_{II} is 0.5877 for the fiber-angle $T_0 = 0^\circ$ and $T_1 = 80^\circ$, which is 12.86% less when compared to straight-fiber laminate and 41.23% less when compared to quasi-isotropic laminate. Moreover, in the CCCC plate boundary condition, the straight-fiber laminate shows the minimum value of normalized D_{II} 0.9527 for the layup $[\pm 15]_{3s}$. For VAT laminate the minimum value of D_{II} is 0.5488 for the fiber-angles $T_0 = 0^\circ$ and $T_1 = 85^\circ$, which is 42.4% less when compared to straight-fiber laminate and 45.12% less when compared to quasi-isotropic laminate.

In both the cases (CSCS, CCCC), many VAT configurations are possible for a lower D_{II} value when compared to the laminate with straight-fiber configuration.

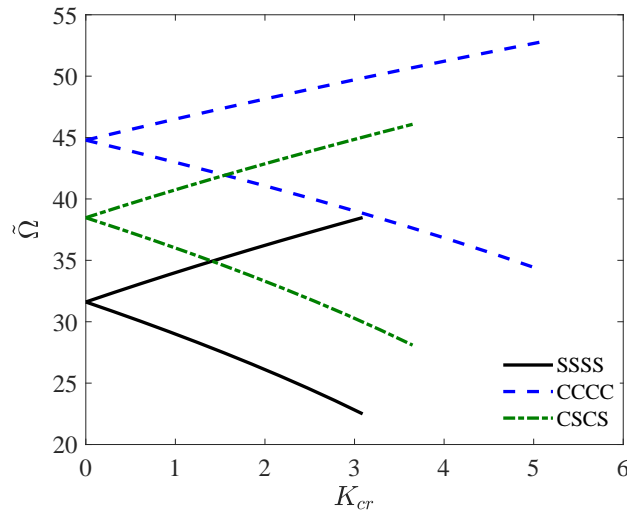


Figure 2.14: Effect of plate boundary conditions on the principle DIR for the VAT laminate $[90 \pm \langle 0|75 \rangle]_{3s}$ subjected to periodic axial compression.

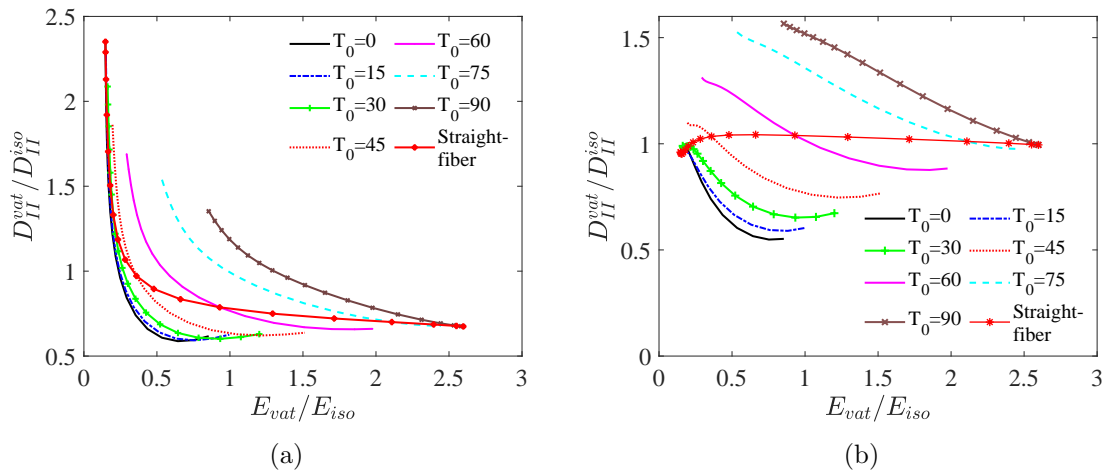


Figure 2.15: Variation of D_{II} of a VAT laminate $[90 \pm \langle T_0|T_1 \rangle]_{3s}$ for different values of T_0 and T_1 subjected to periodic axial compression: (a) CSCS boundary condition (b) CCCC boundary condition.

2.5.5 Effect of orthotropy ratio

The effect of orthotropy ratio (E_1/E_2) on dynamic stability of the VAT laminate is analyzed. The analysis is carried out for the VAT laminate configuration $[90 \pm \langle 0|75 \rangle]_{3s}$ with material properties, $E_{11}/E_{22} = 40$, $G_{12}/E_{22} = 0.6$, $G_{23}/E_{22} = 0.5$, $\nu_{12} = 0.25$, $G_{13} = G_{12}$, $\nu_{13} = \nu_{12}$, $\rho = 1$, $a = b = 1$, $a/h = 100$. The E_{11}/E_{22} ratios considered for the analysis are 10, 20, 30 and 40. DIRs are evaluated for the laminate for different E_{11}/E_{22} ratios and results are shown in Fig. 2.16 for $\alpha_0 = 0$. Results clearly show that with an increase in E_{11}/E_{22} ratio, the onset of DIR shifts towards the higher frequency with wider instability region along with an increase in buckling load. D_{II} is also calculated for different values E_{11}/E_{22} ratio when $\alpha_1 = 0.4$ and the variation of D_{II} with respect to orthotropy ratio is shown in Fig. 2.16(b). Figures 2.16(a) and 2.16(b) clearly shows that the dynamic stability of the laminate increases with increase in E_{11}/E_{22} ratio.

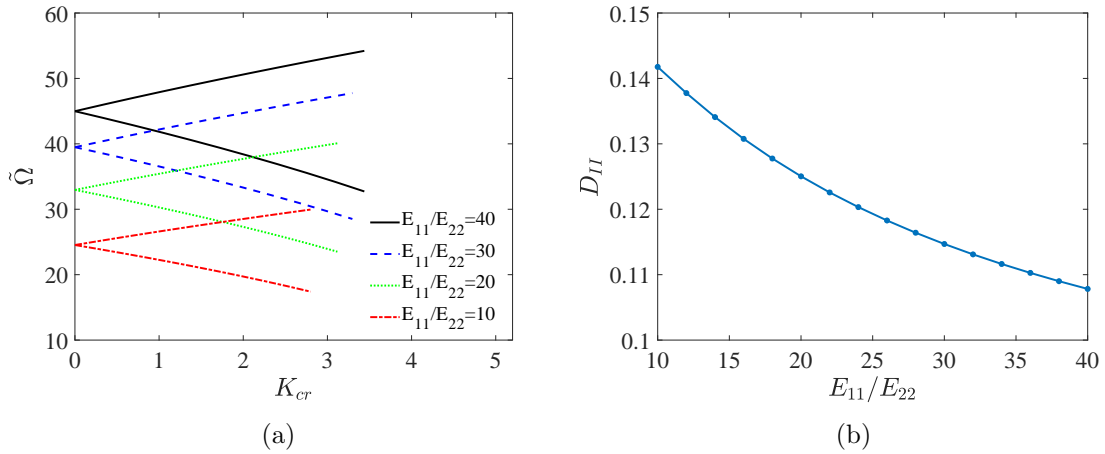


Figure 2.16: Effect of orthotropy on the principle DIR of a VAT laminate $[90 \pm \langle 0|75 \rangle]_{3s}$ for different values of (E_{11}/E_{22}): (a) Normalized frequency ($\tilde{\Omega}$) versus Normalized buckling load (K_{cr}) (b) Dynamic instability index (D_{II}) versus orthotropy ratio (E_{11}/E_{22}).

2.5.6 Effect of aspect ratio and span-thickness ratio

Effect of aspect ratio (a/b) on the dynamic stability behavior of the VAT laminate is studied. DIR for aspect ratios 0.5, 1, 2 and 3 are evaluated for the VAT laminate configuration $[90 \pm \langle 0|75 \rangle]_{3s}$. It is noted from the Fig. 2.17 that with an increase in the aspect ratio, the onset of DIR shifts towards the higher frequencies along with

an increase in the K_{cr} . Moreover, it is observed that the instability region becomes narrow, with an increase in the aspect ratio.

Finally, the effect of span-thickness ratio (a/h) on the DIR of the VAT laminate is studied. DIR for span-thickness ratios of 100, 50, 30 and 20 are evaluated for the VAT laminate configuration $[90 \pm \langle 0|75 \rangle]_{3s}$ and are shown in Fig. 2.18. It is noted that with an increase in the span-thickness ratio, the onset of DIR shifts towards the higher resonance frequencies along with an increase in the K_{cr} value. Also, the instability region becomes wider with the increase in span-thickness ratio.

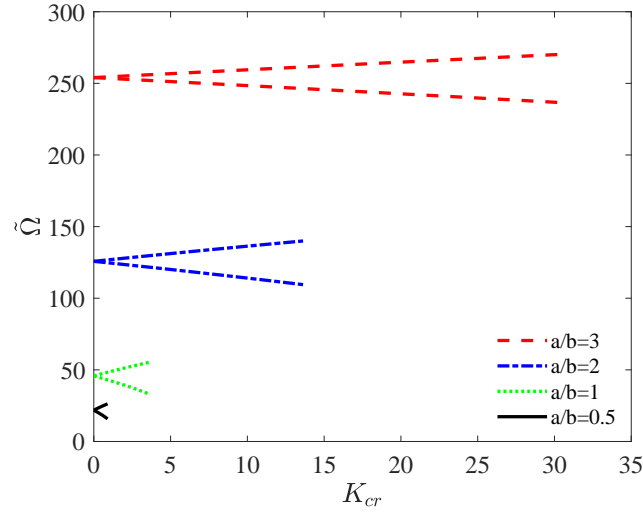


Figure 2.17: Effect of aspect ratio on the DIR of a VAT laminate $[90 \pm \langle 0|75 \rangle]_{3s}$ for different values of a/b ratio.

2.6 Summary

In this chapter, the dynamic stability behavior of VAT laminate under periodic axial compression is studied. The first-order shear deformation plate element has been used to study the effect of fiber-angle variation on stability behavior of the VAT laminate.

Initially, the effect of tow-steering on the stability of the VAT laminate for two different types of in-plane boundary conditions has been studied. It is observed that the fiber-angle variation has a significant effect on the stability behavior of the VAT laminate. For some fiber-angle configurations, VAT laminate show much higher dynamic stability than straight-fiber laminate. The improvement in the dynamic stability is attributed to the increase in the natural frequency and buckling load of

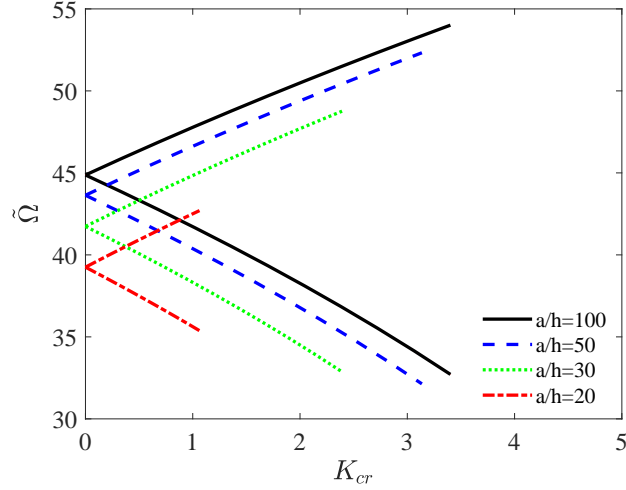


Figure 2.18: Effect of span-thickness ratio on the DIR of a VAT laminate $[90\pm(0|75)]_{3s}$ for different values of a/h ratio.

the VAT laminate. Also, VAT laminate has the added advantage over straight-fiber laminate in tailoring the dynamic instability index (D_{II}) and stiffness properties of the laminate simultaneously.

The static load parameter also influences the instability region of the laminate. With the increase in static load parameter, the onset of DIR shifts towards lower frequencies with wider instability region. Also, the out-of-plane boundary conditions on the edges of the laminate also have an influence on the dynamic stability of VAT laminate. It is observed that with an increase in the number of out-of-plane constraints, DIR shifts towards higher frequencies with narrow instability regions, and thus increasing the stability region. Increase in orthotropy ratio also improves the dynamic stability of the VAT laminate as a result of improved stiffness properties.

Moreover, with the increase in the aspect ratio and span-thickness ratio, DIR of the VAT laminate shifts toward higher frequencies and buckling load. From this study, the benefits of fiber-steering in improving the dynamic stability behavior of VAT laminate is demonstrated.

Chapter 3

Parametric instabilities in delaminated VAT composite panel with a cutout

Structural discontinuities like cutouts are inevitable in aerospace, civil, mechanical, and marine structures because of the functional requirements. Cutouts in wing spars and cover panels of commercial transport and military fighter aircraft are needed to provide access to hydraulic lines and damage inspection. They are also made to provide ventilation and for modifying the resonant frequencies of the structures. Also, the designers often need to incorporate cutouts or openings in a structure to serve as doors and windows. Moreover, composite structures are often prone to delamination (separation of adjoining plies), which leads to the failure of the structure initiated by buckling under compression load. Delaminations can be caused because of the various service loading conditions or improper manufacturing procedures. These delaminations may have a significant effect on the mechanical behavior of the structure. Thus, understanding the dynamic stability behavior of composite laminate with cutout and delamination are critical for the design.

In this chapter, the dynamic stability behavior of a VAT laminate with a circular cutout and delamination around the cutout are investigated. First-order shear deformation theory is used to model the VAT laminate, and a finite element analysis has been used to perform the analysis. The dynamic instability regions are then obtained using Bolotin's first-order approximation. The effect of tow-steering, cutout, and delamination on the stability behavior of VAT laminate are investigated, and their parametric resonance behavior is then compared with straight-fiber and quasi-isotropic composites.

3.1 Modeling of VAT laminate

A delaminated VAT composite laminate with a cutout shown in Fig. 3.1 is considered for the analysis. The delamination is located at the center of the laminate, and the distance to the top and bottom surfaces are h_1 and h_2 , respectively (see Fig. 3.2).

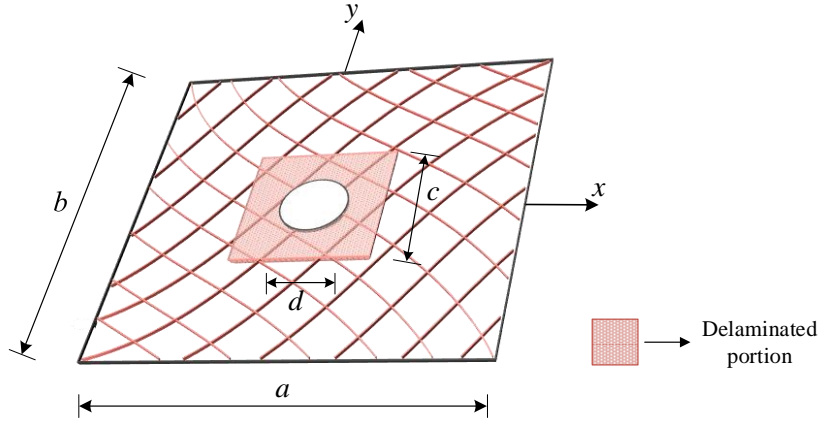


Figure 3.1: Schematic of a delaminated VAT laminate with a circular cutout.

For the analysis, laminate is divided into three portions: un-delaminated (represented by 0), upper, and lower delaminated portions (represented by 1 and 2, respectively). Each of the portions are meshed individually, and the displacement continuity conditions are introduced at the nodes connecting boundaries of un-delaminated and delaminated portions. For the analysis, the delamination is chosen close to the mid-surface of the laminate. Hence the only free model is considered for the analysis, and both the opening and contact problems of the sub-laminates in the delaminated region are not taken into account [97,98].

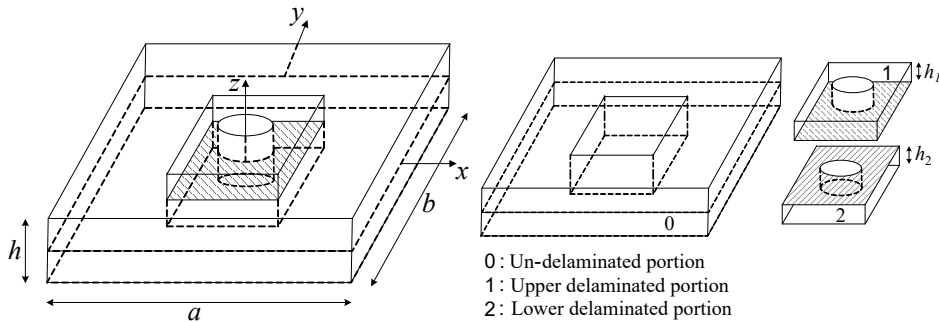


Figure 3.2: Schematic of the laminate with delaminated and un-delaminated portions.

Reissner-Mindlin plate theory [94] is used to model the VAT laminate. Based on

the theory, displacement fields (u, v, w) are expressed as:

$$\begin{aligned} u(x, y, z) &= u_0(x, y) - z\theta_x(x, y), \\ v(x, y, z) &= v_0(x, y) - z\theta_y(x, y), \quad \text{and} \\ w(x, y, z) &= w_0(x, y). \end{aligned} \quad (3.1)$$

Here, w_0 , θ_x and θ_y are the mid-plane kinematic variables for bending and u_0 , v_0 are the in-plane displacements for membrane behavior.

The constitutive relationships for the VAT laminate can be written as follows:

$$\begin{Bmatrix} \bar{\mathbf{N}} \\ \bar{\mathbf{M}} \\ \bar{\mathbf{V}} \end{Bmatrix} = \begin{bmatrix} \bar{\mathbf{A}}(x, y) & \bar{\mathbf{B}}(x, y) & \mathbf{0} \\ \bar{\mathbf{B}}^T(x, y) & \bar{\mathbf{D}}(x, y) & \mathbf{0} \\ \mathbf{0} & \mathbf{0} & \bar{\mathbf{S}}(x, y) \end{bmatrix} \begin{Bmatrix} \boldsymbol{\epsilon}_m \\ \boldsymbol{\epsilon}_b \\ \boldsymbol{\epsilon}_s \end{Bmatrix}. \quad (3.2)$$

In Eq. (3.2), $\bar{\mathbf{N}} = [\bar{N}_x, \bar{N}_y, \bar{N}_{xy}]^T$ is the membrane stress resultant, $\bar{\mathbf{M}} = [\bar{M}_x, \bar{M}_y, \bar{M}_{xy}]^T$ is the bending moment resultant and $\bar{\mathbf{V}} = [\bar{V}_{xz}, \bar{V}_{yz}]^T$ is the transverse shear stress resultant. $\boldsymbol{\epsilon}_m$, $\boldsymbol{\epsilon}_b$ and $\boldsymbol{\epsilon}_s$ are the generalized strain vectors due to membrane, bending and transverse shear deformations, respectively. It should be noted that for a VAT laminate, the in-plane stiffness matrix ($\bar{\mathbf{A}}$), coupling stiffness matrix ($\bar{\mathbf{B}}$), bending stiffness matrix ($\bar{\mathbf{D}}$) and shear stiffness matrix ($\bar{\mathbf{S}}$) are all functions of the panel spatial coordinates (x, y) and are defined as:

$$\begin{aligned} [\bar{\mathbf{A}}(x, y), \bar{\mathbf{B}}(x, y), \bar{\mathbf{D}}(x, y)] &= \sum_{k=1}^n \int_{z_{k-1}}^{z_k} [\mathbf{Q}_p(x, y)]_k \{1, z, z^2\} dz, \quad \text{and} \\ \bar{\mathbf{S}} &= \sum_{k=1}^n \int_{z_{k-1}}^{z_k} [\mathbf{Q}_s(x, y)]_k \mathbf{R} dz. \end{aligned} \quad (3.3)$$

Here, $z_k - z_{k-1}$ is the thickness of the k^{th} layer of the lamina. The matrices $\mathbf{Q}_{pk}(x, y)$ and $\mathbf{Q}_{sk}(x, y)$ are the transformed bending and shear stiffness matrix for k^{th} layer at (x, y) location.

3.1.1 Finite element formulation for un-delaminated portion

The VAT laminate is discretized using a four-noded iso-parametric quadrilateral Reissner-Mindlin plate element (Refer Chapter 2 for the detailed finite element for-

mulation of the VAT laminate). The strain energy of a VAT laminate subjected to uniaxial compression can be written as:

$$U = \frac{1}{2} \int_A [\boldsymbol{\epsilon}_m^T \bar{\mathbf{A}} \boldsymbol{\epsilon}_m + \boldsymbol{\epsilon}_b^T \bar{\mathbf{D}} \boldsymbol{\epsilon}_b + \boldsymbol{\epsilon}_m^T \bar{\mathbf{B}} \boldsymbol{\epsilon}_b + \boldsymbol{\epsilon}_b^T \bar{\mathbf{B}} \boldsymbol{\epsilon}_m + \boldsymbol{\epsilon}_s^T \bar{\mathbf{S}} \boldsymbol{\epsilon}_s] d\mathcal{A} + \frac{1}{2} \int_A [\boldsymbol{\epsilon}_L^T \mathbf{T} \boldsymbol{\epsilon}_L] d\mathcal{A}. \quad (3.4)$$

Here, \mathbf{T} is the in-plane stress resultant matrix due to the applied uniform axial compression (u_0) along the edges. The elemental stiffness matrix due to the first term in strain energy expression (Eq. (3.4)) can be written as follows:

$$\mathbf{K}^e = \mathbf{K}_m^e + \mathbf{K}_b^e + \mathbf{K}_s^e + \mathbf{K}_{mb}^e. \quad (3.5)$$

The matrix \mathbf{K}^e contains stiffness contributions from membrane (\mathbf{K}_m^e), bending (\mathbf{K}_b^e), transverse shear (\mathbf{K}_s^e) and due to coupling between bending and membrane behavior (\mathbf{K}_{mb}^e). These matrices are defined as follows:

$$\mathbf{K}_m^e = \int_A \mathbf{B}_m^T \bar{\mathbf{A}} \mathbf{B}_m d\mathcal{A}, \quad (3.6)$$

$$\mathbf{K}_b^e = \int_A \mathbf{B}_b^T \bar{\mathbf{D}} \mathbf{B}_b d\mathcal{A}, \quad (3.7)$$

$$\mathbf{K}_s^e = \int_A \mathbf{B}_s^T \bar{\mathbf{S}} \mathbf{B}_s d\mathcal{A}, \quad (3.8)$$

$$\mathbf{K}_{mb}^e = \int_A \mathbf{B}_m^T \bar{\mathbf{B}} \mathbf{B}_b d\mathcal{A} + \int_A \mathbf{B}_b^T \bar{\mathbf{B}} \mathbf{B}_m d\mathcal{A}. \quad (3.9)$$

The geometric stiffness matrix (\mathbf{K}_G) due to the second term in strain energy expression (Eq. (3.4)) can be written as follows:

$$\mathbf{K}_G^e = \mathbf{K}_{Gb}^e + \mathbf{K}_{Gs}^e. \quad (3.10)$$

Here, \mathbf{K}_{Gb}^e is the contribution from bending behavior and \mathbf{K}_{Gs}^e is the contribution from transverse shear effects and the matrices are defined as follows:

$$\mathbf{K}_{Gb}^e = \int_A \mathbf{G}_b^T \mathbf{T} \mathbf{G}_b d\mathcal{A}, \quad \text{and} \quad (3.11)$$

$$\mathbf{K}_{Gs}^e = \frac{h^3}{12} \int_A \mathbf{G}_{s1}^T \mathbf{T} \mathbf{G}_{s1} d\mathcal{A} + \frac{h^3}{12} \int_A \mathbf{G}_{s2}^T \mathbf{T} \mathbf{G}_{s2} d\mathcal{A}, \quad (3.12)$$

where, matrices \mathbf{G}_b , \mathbf{G}_{s1} and \mathbf{G}_{s2} are given by:

$$\mathbf{G}_b = \begin{bmatrix} \frac{\partial N_i}{\partial x} & 0 & 0 \\ \frac{\partial N_i}{\partial y} & 0 & 0 \end{bmatrix}, \quad \mathbf{G}_{s1} = \begin{bmatrix} 0 & \frac{\partial N_i}{\partial x} & 0 \\ 0 & \frac{\partial N_i}{\partial y} & 0 \end{bmatrix}, \quad \text{and} \quad \mathbf{G}_{s2} = \begin{bmatrix} 0 & 0 & \frac{\partial N_i}{\partial x} \\ 0 & 0 & \frac{\partial N_i}{\partial y} \end{bmatrix}. \quad (3.13)$$

The kinetic energy for the plate element with a mass density (ρ) can be written as:

$$T_{KE} = \frac{1}{2} \int_{\mathcal{A}} \rho \left[h(\dot{u}^2 + \dot{v}^2 + \dot{w}^2) + \frac{h^3}{12} \dot{\theta}_x^2 + \frac{h^3}{12} \dot{\theta}_y^2 \right] d\mathcal{A}. \quad (3.14)$$

From Eq. (3.14), consistent elemental mass matrix can be written as:

$$\mathbf{M}^e = \int_{\mathcal{A}} \rho \mathbf{N}_i^T \mathbf{\Lambda} \mathbf{N}_i d\mathcal{A}, \quad (3.15)$$

where, $\mathbf{\Lambda} = \text{Diag}[h, h, h, h^3/12, h^3/12]$.

3.1.2 Finite element formulation for delaminated portion

Now, the earlier FEM model for the un-delaminated portion is extended further to delaminated portions. The upper and lower portions of the delaminated VAT laminate are meshed separately. The local coordinate system for the element in the delaminated portion is x', y' and z' , which is similar to the one used in un-delaminated portion. The displacement field of the element is assumed to be of the following form relative to its own local coordinate system as given below:

$$\begin{aligned} u'(x', y', z') &= u'_0(x', y') - z' \theta'_x(x', y'), \\ v'(x', y', z') &= v'_0(x', y') - z' \theta'_y(x', y'), \quad \text{and} \\ w'(x', y', z') &= w'_0(x', y'). \end{aligned} \quad (3.16)$$

Here, u'_0 , v'_0 and w'_0 are the translations of the mid-plane of the delaminated segment in the local coordinate system, and θ'_x , θ'_y are the rotations of the normal to the mid-plane in the $x' - z'$ and $y' - z'$ planes, respectively. The corresponding element

stiffness and mass matrices can be obtained as:

$$\mathbf{K}'_m = \int_{\mathcal{A}} \mathbf{B}_m^T \bar{\mathbf{A}}' \mathbf{B}_m d\mathcal{A}, \quad (3.17)$$

$$\mathbf{K}'_b = \int_{\mathcal{A}} \mathbf{B}_b^T \bar{\mathbf{D}}' \mathbf{B}_b d\mathcal{A}, \quad (3.18)$$

$$\mathbf{K}'_s = \int_{\mathcal{A}} \mathbf{B}_s^T \bar{\mathbf{S}}' \mathbf{B}_s d\mathcal{A}, \quad (3.19)$$

$$\mathbf{K}'_{mb} = \int_{\mathcal{A}} \mathbf{B}_m^T \bar{\mathbf{B}}' \mathbf{B}_b d\mathcal{A} + \int_{\mathcal{A}} \mathbf{B}_b^T \bar{\mathbf{B}}' \mathbf{B}_m d\mathcal{A}, \quad (3.20)$$

where,

$$[\bar{\mathbf{A}}'(x, y), \bar{\mathbf{B}}'(x, y), \bar{\mathbf{D}}'(x, y)] = \sum_{k=k_1}^{k_2} \int_{z'_{k-1}}^{z'_k} [\mathbf{Q}(x, y)]_k \{1, z', z'^2\} dz', \quad (3.21)$$

$$\bar{\mathbf{S}}'(x, y) = \sum_{k=k_1}^{k_2} \int_{z'_{k-1}}^{z'_k} [\mathbf{Q}_s(x, y)]_k \mathbf{R} dz', \quad (3.22)$$

$$\mathbf{M}'^e = \int_{\mathcal{A}} \rho \mathbf{N}_i^T \mathbf{\Lambda}' \mathbf{N}_i d\mathcal{A}. \quad (3.23)$$

Here, for top delaminated portion $k_1 = 1, k_2 = r$ and for bottom delaminated portion $k_1 = r + 1, k_2 = n_l$, where the delamination occurs between r and $r + 1$ layers. $\mathbf{\Lambda}' = \text{Diag}[h', h', h', h'^3/12, h'^3/12]$ and h' is the thickness of the delaminated portion and n_l is the total number of layers in the laminate.

3.1.3 Continuity conditions

In the previous Sections (3.1.1 and 3.1.2), the displacement field variables of the elements in un-delaminated and delaminated portions are derived separately, and all the variables are independent. However, at the boundary connecting these two portions (un-delaminated and delaminated), the continuity conditions for the displacement field must be satisfied. Figure 3.3 shows the elements connecting at the boundary (delaminated section on the right and un-delaminated section on the left). Consider one element each in un-delaminated and delaminated portions, i, j , respectively. The nodes 2 and 3 are the common nodes connecting the un-delaminated and delaminated section. Let the element stiffness, mass, geometric stiffness matrices and element nodal displacement vectors be denoted by $\mathbf{K}^e, \mathbf{M}^e, \mathbf{K}_G^e$ and \mathbf{u} for element i , and $\mathbf{K}'^e, \mathbf{M}'^e, \mathbf{K}'_G^e$ and $\bar{\mathbf{u}}'$ for element j .

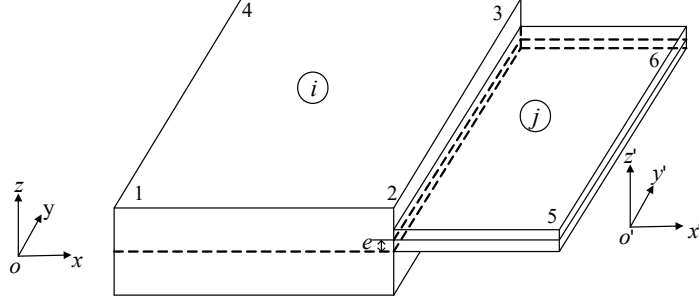


Figure 3.3: Elements at connecting boundary.

For common nodes 2 and 3, the displacements are shown below:

$$\begin{aligned}\bar{\mathbf{u}}_k^e &= [u_{0k}, v_{0k}, w_{0k}, \theta_{xk}, \theta_{yk}]^T, \quad k = 2, 3 \text{ (for element } i) \\ \bar{\mathbf{u}}_k^e &= [u'_{0k}, v'_{0k}, w'_{0k}, \theta'_{xk}, \theta'_{yk}]^T, \quad k = 2, 3 \text{ (for element } j).\end{aligned}\quad (3.24)$$

To satisfy the continuity conditions for the connecting nodes at the boundary, the following relations must hold:

$$\begin{aligned}u'_{0k} &= u_{0k} + e\theta_{xk}, \quad v'_{0k} = v_{0k} + e\theta_{yk}, \quad w'_{0k} = w_{0k}, \\ \theta'_{xk} &= \theta_{xk}, \quad \theta'_{yk} = \theta_{yk}. \quad \text{for } k = 2, 3.\end{aligned}\quad (3.25)$$

Here, e is the distance between the mid-plane of element i and the mid-plane of element j (see Fig. 3.3), and is taken positive in $+z$ direction. Therefore,

$$\bar{\mathbf{u}}_k^e = \boldsymbol{\lambda} \bar{\mathbf{u}}_k^e, \quad k = 2, 3 \quad (3.26)$$

where,

$$\boldsymbol{\lambda} = \begin{bmatrix} 1 & 0 & 0 & e & 0 \\ 0 & 1 & 0 & 0 & e \\ 0 & 0 & 1 & 0 & 0 \\ 0 & 0 & 0 & 1 & 0 \\ 0 & 0 & 0 & 0 & 1 \end{bmatrix}. \quad (3.27)$$

Using Eq. (3.26), transformation of displacements for element j at the nodes connecting boundary between un-delaminated and delaminated portions can be written

as

$$\bar{\mathbf{u}}'^e = \underline{\mathbf{T}}\tilde{\mathbf{u}}'^e, \quad (3.28)$$

where,

$$\begin{aligned} \tilde{\mathbf{u}}'^e &= \left[\bar{\mathbf{u}}_1'^{eT}, \bar{\mathbf{u}}_2^{eT}, \bar{\mathbf{u}}_3^{eT}, \bar{\mathbf{u}}_4'^{eT} \right]^T, \quad \text{and} \\ \underline{\mathbf{T}} &= \text{Diag}[\boldsymbol{\lambda}, \mathbf{I}, \mathbf{I}, \boldsymbol{\lambda}]. \end{aligned} \quad (3.29)$$

Here, \mathbf{I} is identity matrix of size 5×5 . The transformations for the stiffness, geometric stiffness and mass matrices of element j can be expressed as,

$$\bar{\mathbf{K}}'^e = \underline{\mathbf{T}}^T \mathbf{K}'^e \underline{\mathbf{T}}, \quad (3.30)$$

$$\bar{\mathbf{K}}_G'^e = \underline{\mathbf{T}}^T \mathbf{K}_G'^e \underline{\mathbf{T}}, \quad (3.31)$$

$$\bar{\mathbf{M}}'^e = \underline{\mathbf{T}}^T \mathbf{M}'^e \underline{\mathbf{T}}. \quad (3.32)$$

The displacement continuity conditions have been incorporated into $\bar{\mathbf{K}}'^e$, $\bar{\mathbf{K}}_G'^e$ and $\bar{\mathbf{M}}'^e$ and the nodal displacement $\tilde{\mathbf{u}}'^e$ is replaced by $\bar{\mathbf{u}}^e$ for $j = 2$ and 3 . The matrices $\bar{\mathbf{K}}'^e$, $\bar{\mathbf{K}}_G'^e$ and $\bar{\mathbf{M}}'^e$ are subsequently used to assemble the global stiffness, geometric stiffness and mass matrices. A similar treatment can be carried out for the connecting nodes at boundaries of the two segments at other edges.

3.2 Dynamic stability analysis

In this section, the governing equations for the dynamic stability of VAT laminate subjected to periodic uniaxial compression using FEM is presented. The equations of motion of a VAT laminate under periodic uniaxial compression load $P(t) = \alpha_0 P_{cr} + \alpha_1 P_{cr} \cos(\Omega t)$ can be written as follows:

$$\mathbf{M}\ddot{\mathbf{u}} + \mathbf{K}\bar{\mathbf{u}} - (\alpha_0 P_{cr} + \alpha_1 P_{cr} \cos(\Omega t)) \mathbf{K}_G \bar{\mathbf{u}} = 0. \quad (3.33)$$

Here, Ω is the frequency of the periodic load and \mathbf{M} is the global mass matrix of the VAT laminate. $P_{cr} = \lambda \int_{-b/2}^{+b/2} \bar{N}_x(a/2, y) dy$ is the critical buckling load of the VAT laminate obtained by applying uniform compression of u_0 at the edges, a and b are the length and width of the laminate respectively, and λ is the eigenvalue obtained by solving the buckling eigenvalue problem $\mathbf{K}\bar{\mathbf{u}} = \lambda \mathbf{K}_G \bar{\mathbf{u}}$. The parameters α_0 and α_1 are static and dynamic load parameters, respectively. It should be noted that

the applied load $P(t) = \alpha_0 P_{cr} + \alpha_1 P_{cr} \cos(\Omega t)$ will cause a uniform compression of $u(t) = \alpha_0 u_{cr} + \alpha_1 u_{cr} \cos(\Omega t)$ at the loading edges.

Bolotin's approach [49] has been used to determine the stability boundaries of Eq. (3.33). According to Bolotin's approach the solution of Eq. (3.33) on the stability boundary are periodic with period $T_1 = 4\pi/\Omega$ or $T_2 = 2\pi/\Omega$. Therefore, the solution of Eq. (3.33) is expanded as follows:

$$\bar{\mathbf{u}} = \sum_{k=1,3,5}^{\infty} (\mathbf{a}_k \sin(k\Omega t/2) + \mathbf{b}_k \cos(k\Omega t/2)), \quad (3.34)$$

$$\bar{\mathbf{u}} = \frac{1}{2}\mathbf{b}_0 + \sum_{k=2,4,6}^{\infty} (\mathbf{a}_k \sin(k\Omega t/2) + \mathbf{b}_k \cos(k\Omega t/2)). \quad (3.35)$$

The coefficients $\mathbf{a}_k, \mathbf{b}_k$ are yet to be determined and are infinite in numbers. As it is difficult to deal with infinite coefficients, a first-order approximation (where only first two terms are considered) is often used in the literature [58, 63–65] and is sufficient to predict the stability boundary accurately. In the first order Bolotin's approximation, only the first two terms are considered in Eq. (3.34) and the first three terms are considered in Eq. (3.35), therefore we get:

$$\bar{\mathbf{u}} = \mathbf{a}_1 \sin(\Omega t/2) + \mathbf{b}_1 \cos(\Omega t/2), \quad (3.36)$$

$$\bar{\mathbf{u}} = \frac{1}{2}\mathbf{b}_0 + \mathbf{a}_2 \sin(\Omega t) + \mathbf{b}_2 \cos(\Omega t). \quad (3.37)$$

These expressions (Eq. (3.36) and Eq. (3.37)) are substituted in Eq. (3.33) and the coefficients of each sine, cosine and constant terms are set equal to zero. For nontrivial solutions, the determinants of the coefficients of these group of linear homogeneous equations are equal to zero. Solving the set of equations for a given value of α_0 , the variation of Ω with respect to α_1 can be obtained. Such a plot shows the dynamic instability regions (DIR) associated with the laminate subjected to periodic in-plane load.

3.3 Results and discussions

Results from the dynamic stability analysis of delaminated VAT composite laminate with a cutout is presented in this section. A finite element code for a quadrilateral Reissner-Mindlin plate element (see Sec. 3.1) is developed in MATLAB for analyzing VAT laminate. The element stiffness matrix is constructed by considering the fiber-angle at the center of the element and assumed it to be uniform over the element. For numerical integration, 2×2 Gauss points are used for calculating element mass matrix

(\mathbf{M}^e), stiffness contribution from membrane (\mathbf{K}_m^e) and stiffness contribution from bending (\mathbf{K}_b^e). To avoid shear-locking problems in thin laminate, reduced integration with 1×1 Gauss point is employed in calculating shear contribution in element stiffness matrix (\mathbf{K}_s^e) and the element geometric stiffness matrix (\mathbf{K}_G^e).

To facilitate the comparison of the numerical results, a few normalized parameters are defined: normalized diameter of cutout ($\text{NDH}=d/a$); normalized delamination position ($\text{NDP}=h_1/h$); normalized delamination length ($\text{NDL}=c/a$) and normalized delamination area ($\text{NDA}=c^2/ab$) (see Fig. (3.7 and 3.11)).

For the numerical study, a symmetric simply-supported VAT laminate having the following material properties are considered: $E_{11} = 181$ GPa, $E_{22} = 10.3$ GPa, $\rho = 1540$ Kg/m³, $G_{12} = 7.17$ GPa, $G_{23} = 7.17$ GPa, $\nu_{12} = 0.28$, $G_{13} = G_{12}$, $\nu_{13} = \nu_{12}$, $a = b = 1$ m, $h = 2.032 \times 10^{-3}$ m. To check the accuracy of present numerical results, a VAT composite laminate with single delamination is modeled using commercial FEM software (ABAQUS). A subroutine is developed to generate shell elements (SC8R) with each having independent fiber orientations. A mesh ($50 \times 50 \times 16$) is used to obtain converged results. In delamination modeling, two sets of collocated shells, each of which represents an intact sub-laminate, are incorporated into the FE model. The nodal degree of freedom for two adjacent surfaces of two sub-laminates over the un-delaminated regions are tied using the multi-point constraints (MPCs).

3.3.1 Model validation

To validate the efficacy of the developed MATLAB code, fundamental frequencies of a straight-fiber composite laminate with an embedded through-the-width delamination is studied and validated with the results published in literature [99]. The analysis is carried out on a T300/934 graphite/epoxy cantilever beam-plate with a $[0/90]_{2s}$ stacking sequence. The lamina properties chosen for the analysis are $E_{11} = 134.5$ GPa, $E_{22} = 10.3$ GPa, $G_{12} = 5.0$ GPa, $\nu_{12} = 0.33$, $\rho = 1480$ Kg/m³, ply thickness of 0.127 mm with dimensions of the cantilever beam-plate are chosen as $a = 127$ mm and $b = 12.7$ mm, respectively.

Different delamination positions ($\text{NDP}=0.5, 0.375$ and 0.25) for five different delamination sizes ($\text{NDL}= 0.0$ (intact), $0.2, 0.4, 0.6$ and 0.8) are chosen for the study [99]. Table 3.1 list the fundamental frequencies (ω) of cantilever beam-plate with delamination for different NDP/NDL combinations. The results obtained using present method are compared with those given by Shen and Grady [99], Luo and Hanagud [100], Shu and Della [101], and ABAQUS simulations. From the Table 3.1, it is clear that the

fundamental frequencies predicted by the present model are in good agreement with the experimental [99], analytical [100, 101] and ABAQUS results.

Table 3.1: Comparison of natural frequencies (Hz) of a cantilever beam-plate $[0/90]_{2s}$ with through-the-width delamination.

		ω				
NDP	NDL	Present	Shen [99]	Luo [100]	Shu [101]	Abaqus
0.5000	0.0	82.14	79.83	81.86	81.88	82.10
	0.2	80.89	78.17	81.45	80.47	81.11
	0.4	76.25	75.38	76.81	75.36	76.36
	0.6	67.56	66.96	67.64	66.14	67.00
	0.8	57.37	57.54	56.95	55.67	56.10
0.3750	0.0	82.14	79.83	81.86	81.88	82.10
	0.2	81.43	77.79	80.86	80.58	81.27
	0.4	77.14	75.13	76.62	75.81	76.67
	0.6	68.46	67.96	68.80	67.05	67.92
	0.8	58.07	48.33	59.34	56.86	57.15
0.2500	0.0	82.14	79.83	81.86	81.88	82.10
	0.2	81.52	80.13	82.01	81.53	81.87
	0.4	79.95	79.75	80.74	80.09	80.45
	0.6	76.66	76.96	77.52	76.75	77.01
	0.8	71.57	72.46	71.73	70.92	71.00

The buckling and vibration response of VAT laminate of configuration $[0\pm\langle 0|45\rangle]_{4s}$ with an embedded square and through-the-width delamination are also studied. In buckling analysis, delaminated VAT laminate is loaded by a uniform displacement compression with transverse edges free to deform and simply-supported on all the edges. The analysis is carried out for two delaminated positions (NDP= 0.5 and 0.25) for both square and through-the-width delaminations for different NDA and NDL, respectively. Fundamental natural frequencies and buckling loads are normalized: $\tilde{\omega} = \frac{\omega a^2}{h} \sqrt{\rho/E_{22}}$ and $K_{cr} = \frac{P_{cr} a^2}{E_{11} b h^3}$ and is shown in Table 3.2 and Table 3.3 for a VAT laminate with embedded square and through-the-width delaminations, respectively. The results are then compared with ABAQUS simulations, and it seems to be in good

agreement with each other.

Table 3.2: Comparison of normalized fundamental frequency ($\tilde{\omega}$) and normalized critical buckling load (K_{cr}) of a VAT laminate $[0 \pm \langle 0|45 \rangle]_{4s}$ with an embedded square delamination.

NDA	NDP=0.5				NDP=0.2500			
	$\tilde{\omega}$		K_{cr}		$\tilde{\omega}$		K_{cr}	
	Present	Abaqus	Present	Abaqus	Present	Abaqus	Present	Abaqus
0.00	16.3947	16.3840	1.6485	1.6462	16.3947	16.3840	1.6485	1.6462
0.01	16.3947	16.3356	1.6485	1.6603	16.3947	16.3501	1.6485	1.6680
0.04	16.3941	16.3312	1.6485	1.6598	16.3941	16.3444	1.6485	1.6664
0.09	16.3828	16.2985	1.6468	1.6543	16.3796	16.3036	1.6451	1.6341
0.16	16.3275	16.1779	1.6372	1.6286	16.2961	16.1207	1.5500	1.5432
0.25	16.1245	16.0824	1.5951	1.6099	15.9392	15.9065	0.9951	0.9871
0.36	15.6590	15.6174	1.4819	1.4959	14.7272	14.6869	0.6576	0.6541
0.49	14.6964	14.7315	1.2671	1.2899	12.1228	12.0725	0.4608	0.4593

Table 3.3: Comparison of normalized natural frequencies ($\tilde{\omega}$) and normalized critical buckling load (K_{cr}) of a VAT laminate $[0 \pm \langle 0|45 \rangle]_{4s}$ with an embedded through-the-width delamination.

NDL	NDP=0.5				NDP=0.2500			
	$\tilde{\omega}$		K_{cr}		$\tilde{\omega}$		K_{cr}	
	Present	Abaqus	Present	Abaqus	Present	Abaqus	Present	Abaqus
0.00	16.3947	16.3840	1.6485	1.6462	16.3947	16.3840	1.6485	1.6462
0.20	16.3708	16.2608	1.6442	1.6462	16.3764	16.2929	1.6451	1.6549
0.40	16.0642	15.7450	1.5844	1.5061	16.0422	15.7035	1.2807	1.2792
0.60	14.7811	14.7013	1.2350	1.2376	13.7425	13.6445	0.5179	0.5121

Further, the normalized buckling loads of a VAT laminate $[0 \pm \langle 0|30 \rangle]_{4s}$ with embedded square delamination for different NDA value are plotted for two different delamination positions, NDP=0.25 and NDP=0.5 in Fig. 3.4. The results are then compared with those published in [102]. Figure 3.4 shows an excellent agreement of the present FEM model with analytical results.

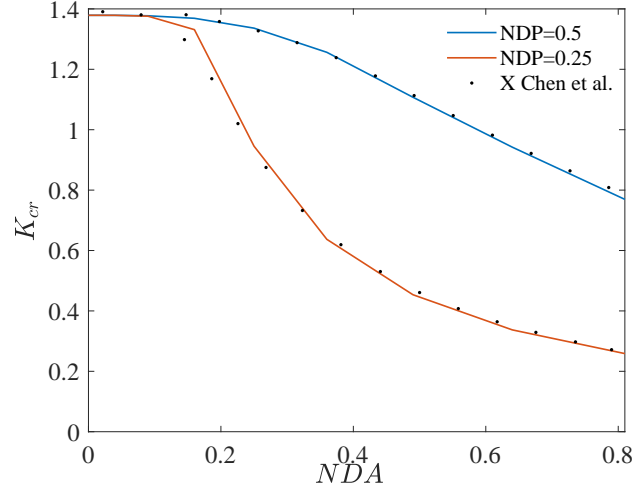


Figure 3.4: Variation of normalized critical buckling load (K_{cr}) with respect to NDA value of a VAT composite laminate $[0 \pm \langle 0|30 \rangle]_{4s}$ with an embedded delamination obtained for two different delamination positions (NDP = 0.5 and 0.25).

Subsequently, the influence of static in-plane compression load on the natural frequencies of delaminated VAT composite laminate is studied. The delamination position chosen for the analysis is NDP=0.5. The delaminated VAT composite laminate is loaded by uniform axial compression with static load parameter (α_0) ranging from 0.0 to 1.0, and the corresponding natural frequencies are plotted in Fig. 3.5. Here, $\alpha_0 = 0$ denotes the state of free vibration of delaminated VAT composites, and $\alpha_0 = 1$ indicates the buckling of delaminated VAT composite. The analysis is carried out for four different delamination sizes (NDA = 0.0, 0.25, 0.49, and 0.64), and validated with the results published in [102].

Finally, the dynamic stability of the delaminated VAT laminated subjected to periodic in-plane compression is studied. The principal DIR of the VAT laminate with different delamination sizes (NDA=0.0, 0.25, 0.49 and 0.81) is shown in Fig. 3.6. The analysis is carried out using $\alpha_0 = 0$. Fig. 3.6 also includes the results in Chen et al. [102] and our results match favorably with the published results.

3.3.2 Effect of fiber-angle variation on critical buckling load and dynamic stability in a VAT laminate with a cutout

Buckling and dynamic stability analysis of VAT composite laminate with a circular cutout is studied in this section. The schematic diagram of the VAT laminate with

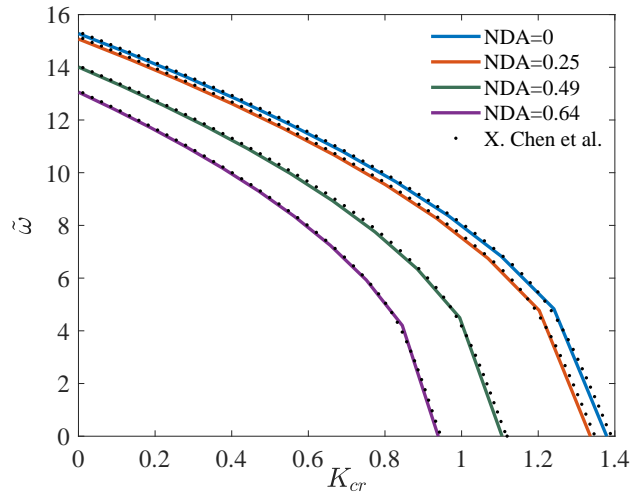


Figure 3.5: Variation of normalized fundamental frequency ($\tilde{\omega}$) with respect to the static in-plane compression load (K_{cr}) of the VAT laminate $[0 \pm \langle 0|30 \rangle]_{4s}$ with an embedded delamination obtained for different values of NDA (0.0, 0.25, 0.49 and 0.64).

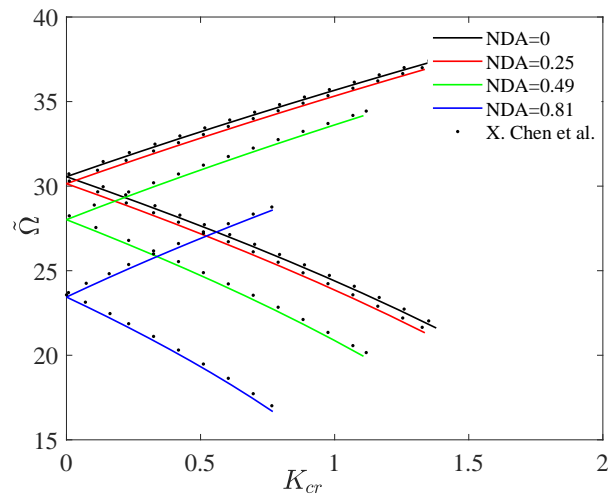


Figure 3.6: Principle DIRs of a VAT laminate $[0 \pm \langle 0|30 \rangle]_{4s}$ with an embedded delamination shown in the plane of normalized frequency versus normalized critical load for different NDA values (0.0, 0.25, 0.49, 0.81).

a cutout is shown in Fig. 3.7. From here on, all the analysis are performed on a VAT laminate with fiber-angle configuration $[90 \pm \langle T_0|T_1 \rangle]_{4s}$. The value of NDH is chosen to be 0.2. Simply-supported boundary conditions are chosen while keeping the transverse edges free to deform in in-plane directions for all analyses.

Buckling analysis

The influence of fiber-angle variation on the buckling load of VAT laminate with a circular cutout is studied. Critical buckling loads of a VAT laminate for different values of T_0 and T_1 varied between 0° and 90° in intervals of 10° are shown with respect to pre-buckling stiffness of laminate in Fig. 3.8. Results are shown in Fig. 3.8 are normalized with respect to an intact quasi-isotropic laminate. The equivalent stiffness for quasi-isotropic laminate (E_{iso}) and VAT laminate (E_{vat}) are calculated as:

$$E_{vat} = \frac{a}{bh u_0} \int_{-b/2}^{b/2} \bar{N}_x(a/2, y) dy, \quad (3.38)$$

$$E_{iso} = U_1 \left(1 - \left(\frac{U_4}{U_1} \right)^2 \right). \quad (3.39)$$

Here the parameters U_1 and U_4 are material invariants (see Ref: [103]).

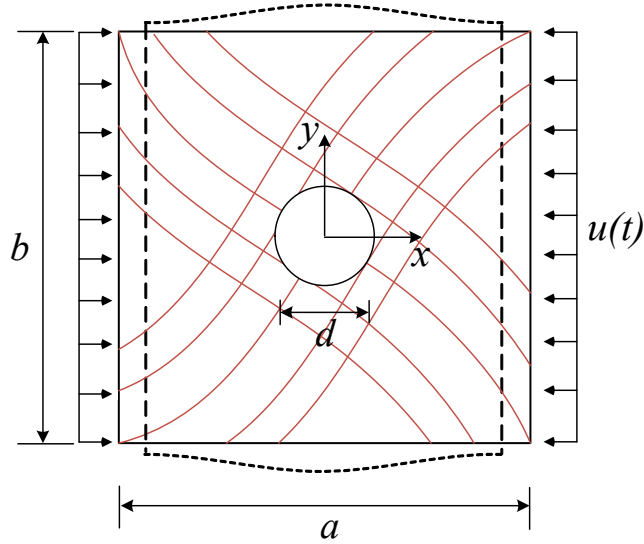


Figure 3.7: Schematic diagram of a VAT laminate with a circular cutout.

Each curve in Fig. 3.8 is generated by varying T_1 from 0° (left endpoint of the curve) to 90° (right endpoint of the curve) with an increment of 10° for a given value

of T_0 . Variation of critical buckling load with respect to stiffness of a straight-fiber laminate ($[\pm\theta]_{4s}$) is also shown in plot (see Fig. 3.8) with the change in fiber-angle θ from 0° (right endpoint of the curve) to 90° (left endpoint of the curve). The critical buckling load values of the VAT laminate for fiber-angle $T_0 = 60^\circ$ from ABAQUS is also shown in Fig. 3.8 for validation purposes. From the results, it is clear that with any change in the fiber-angle configuration, buckling load of the laminate changes significantly. The highest value for K_{cr} achieved for a VAT laminate is 2.106 for fiber-angles $T_0 = 0^\circ$ and $T_1 = 80^\circ$. The maximum value of normalized K_{cr} for a straight-fiber laminate is 1.127 for the fiber-angle $\pm[45]_{4s}$ and is 47.15% lower than the optimal VAT laminate configuration. The significant increase in the critical buckling load in the case of VAT laminate is because of the redistribution of the stress by the curvilinear fiber from the center of the laminate towards the supported edges. From the results, it is observed that VAT laminate with a circular cutout exhibit higher buckling load value than a healthy quasi-isotropic laminate.

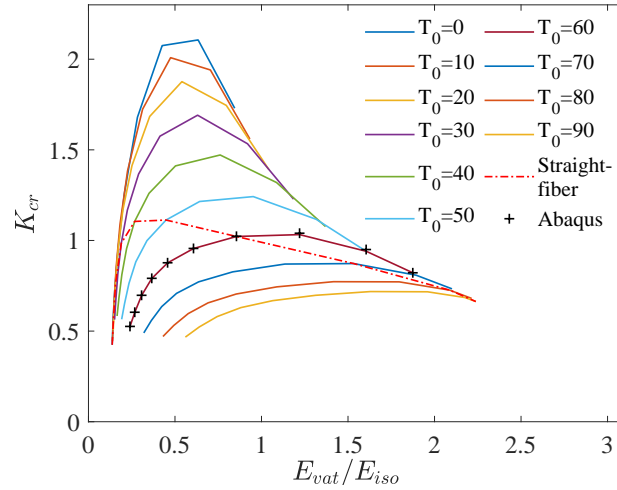


Figure 3.8: Variation of normalized critical buckling load (K_{cr}) with respect to normalized pre-buckling stiffness (E_{vat}) of a VAT laminate $[90 \pm \langle T_0 | T_1 \rangle]_{4s}$ with a circular cutout (NDH=0.2) for different fiber-angles (T_0 and T_1).

Dynamic stability

Next, the dynamic stability behavior of a VAT laminate with a circular cutout for different fiber-angle configurations is studied. First, the principle DIRs of a VAT laminate for the fiber-angles $T_0 = 0$ and T_1 varying from 0° to 90° in increments of 15° are shown in Fig. 3.9. The static load parameter chosen for the analysis is

$\alpha_0 = 0$, and the dynamic load parameter (α_1) varies from 0 to 1. The DIRs are shown in the plane of normalized fundamental frequency ($\tilde{\Omega} = \Omega a^2 / h \sqrt{\rho / E_{22}}$) versus buckling load (K_{cr}) (see Fig. 3.9). From the results, it is clear that with any change in the fiber-angle influences the natural frequency and buckling load, which in-turn influences the DIRs of the VAT laminate. It should be noted that the K_{cr} value at which the stability boundary terminates corresponding to $\alpha_1 = 1$, beyond which static instability occurs.

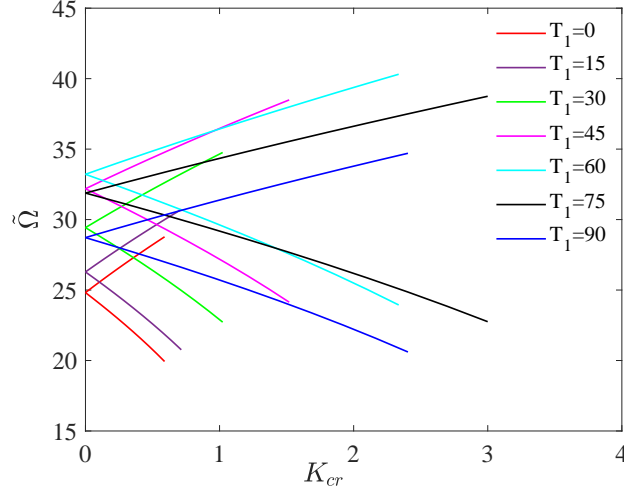


Figure 3.9: Principle DIRs of a VAT laminate $[90 \pm \langle 0|T_1 \rangle]_{4s}$ with a circular cutout (NDH=0.2) for different fiber-angles (T_1).

The variation of D_{II} with respect to the fiber-angle of a VAT laminate with a cutout is shown in Fig. 3.10. The analysis is carried out on a VAT laminate for different values of T_0 and T_1 . The D_{II} values are evaluated at $\alpha_0 = 0$ and $\alpha_1 = 0.3$. The D_{II} and stiffness (E_{vat}) values of VAT laminate are normalized with respect to a healthy quasi-isotropic laminate and shown in the plane of normalized D_{II} versus normalized stiffness (see Fig. 3.10). From the results, it is observed that the fiber-angle configuration influences the D_{II} value of the laminate significantly. The minimum value of normalized D_{II} obtained for the VAT laminate with a circular cutout is 0.4555 for the fiber-angles $T_0 = 0$ and $T_1 = 80$. In the case of straight-fiber composites, the minimum D_{II} value obtained is 0.8794 for the fiber-angle $\theta = 45^\circ$. Thus an optimal VAT laminate configuration shows almost 48.7% higher dynamic stability when compared to optimal straight-fiber laminate. This substantial increase in D_{II} for the VAT laminate is due to the higher buckling and higher fundamental natural frequency. Moreover, a VAT laminate with a circular cutout shows 54.4% lower

normalized D_{II} value when compared to a healthy quasi-isotropic laminate.

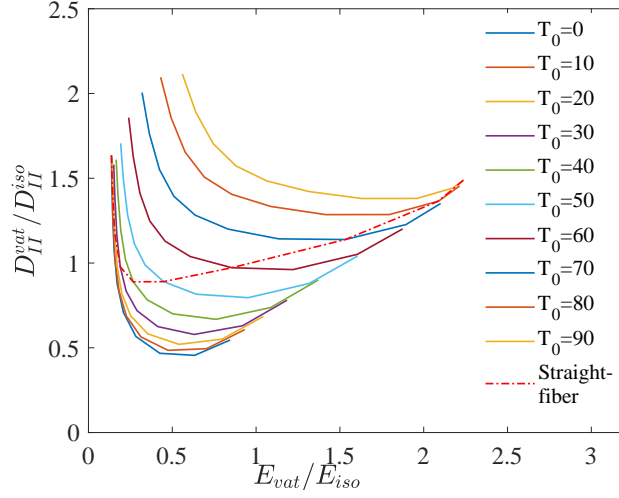


Figure 3.10: Variation of normalized D_{II} with respect to normalized pre-buckling stiffness (E_{vat}) of a VAT laminate $[90 \pm \langle T_0 | T_1 \rangle]_{4s}$ with circular cutout (NDH=0.2) for different fiber-angles (T_0 and T_1).

3.3.3 Effect of fiber-angle variation on buckling load and dynamic stability in a delaminated VAT laminate with a cutout

In this section, a square delamination is introduced around the circular cutout for a VAT laminate (see Fig. 3.11) and the influence of NDA and fiber-angle variation on the buckling load, DIR and D_{II} are studied in detail.

Buckling

In Fig. 3.12 the variation of buckling load with respect to the fiber-angle configuration of a delaminated VAT laminate with a circular cutout for different values of NDA (0.16, 0.25, 0.36 and 0.49) are shown. As shown in Fig. 3.12, with the increase in delamination area, the buckling load of the laminate reduces. The inclusion of delamination around the cutout is the reason for the reduction of the critical buckling load of the laminate. However, VAT laminate shows higher critical buckling load when compared with straight-fiber laminate for all NDA values. For each NDA value of 0.16, 0.25, 0.36 and 0.49, optimal fiber-angle configuration of $T_0 = 0$ and $T_1 = 80$ shows an improvement of 46.8%, 47.7% , 47.9% and 50.9% in critical buckling load

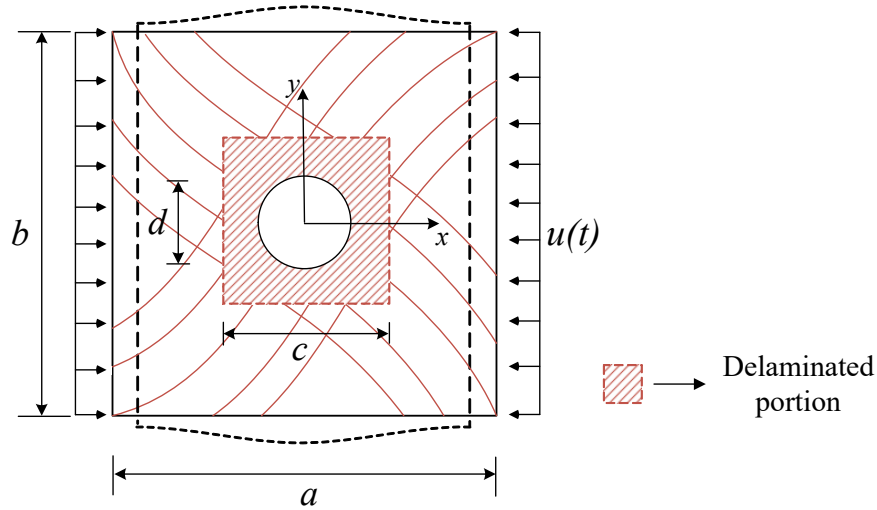


Figure 3.11: Schematic diagram of a VAT laminate with a delamination around a circular cutout.

when compared to optimal straight-fiber laminate configuration, respectively. In addition, the decrease in critical buckling load of a straight-fiber laminate $[\pm 45]_{4s}$ with the increase of NDA from 0.16 to 0.49 is 33.9%, whereas for an optimal VAT laminate configuration $T_0 = 0$ and $T_1 = 80$ the decrease in critical buckling load is only 28.4%. As explained previously, redistribution of the load from the center of the laminate towards the edges by the fiber is the reason for the increase in critical buckling load of the VAT laminate.

Dynamic stability

Further, principal DIR for the delaminated VAT laminate with a circular cutout for different values of NDA (0.16, 0.25, 0.36 and 0.49) are studied. The static load parameter is chosen to be $\alpha_0 = 0$, and dynamic load parameter α_1 is varied from 0 to 1. It is seen from the Fig. 3.13 that, increase in the delamination area around the cutout leads to early onset of dynamic instability regions. This is due to the reduction of fundamental parametric resonance frequency with the occurrence of delamination. The buckling load (K_{cr}) of the laminate also decreases with an increase in delamination area and results in shrinkage of DIR. However, in VAT laminate for all the NDA values, the onset of instability region starts at higher frequencies and extends towards larger K_{cr} values when compared to the straight-fiber laminate because of the higher frequencies and buckling load values. Also, DIRs for a VAT laminate with optimal fiber-angle configuration $[90 \pm \langle 0|80 \rangle]_{4s}$ of different types (healthy laminate,

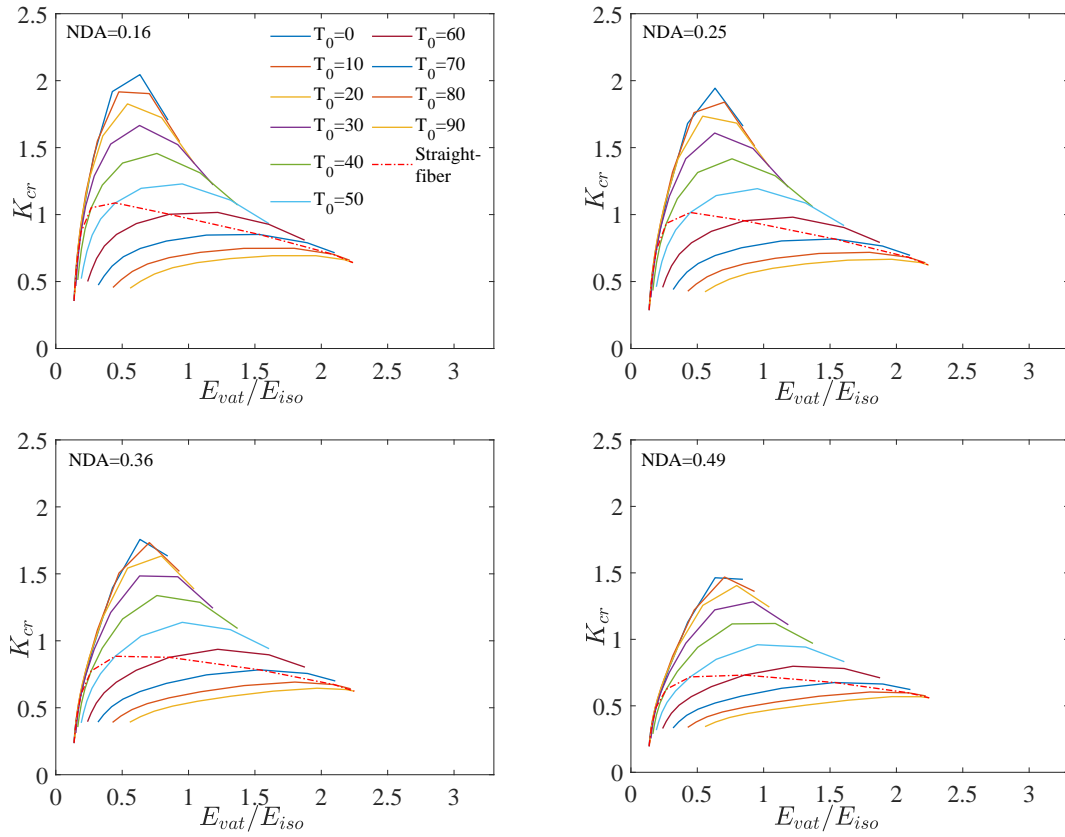


Figure 3.12: Variation of normalized critical buckling load (K_{cr}) with respect to the normalized pre-buckling stiffness (E_{vat}) of a VAT laminate $[90 \pm \langle T_0|T_1 \rangle]_{4s}$ with a circular cutout (NDH=0.2), for different fiber-angles (T_0 and T_1) and different NDA values (0.16, 0.25, 0.36 and 0.49).

laminate with a cutout (NDH=0.2) and with delamination around cutout (NDL=0.25 and 0.49)) is shown in Fig. 3.14. It is clearly seen that a laminate with no defects shows high dynamic stability when compared to all other laminates (laminate with a cutout and delaminations). However, the introduction of cutout into the laminate decreases the critical buckling load, which in turn reduces the dynamic stability of the laminate. In addition, laminate with square delamination around the cutout further decreases the natural frequency and critical buckling load and thus the dynamic stability of the laminate decreases significantly, and this is because of the reduction in stiffness of the laminate with the introduction of delamination.

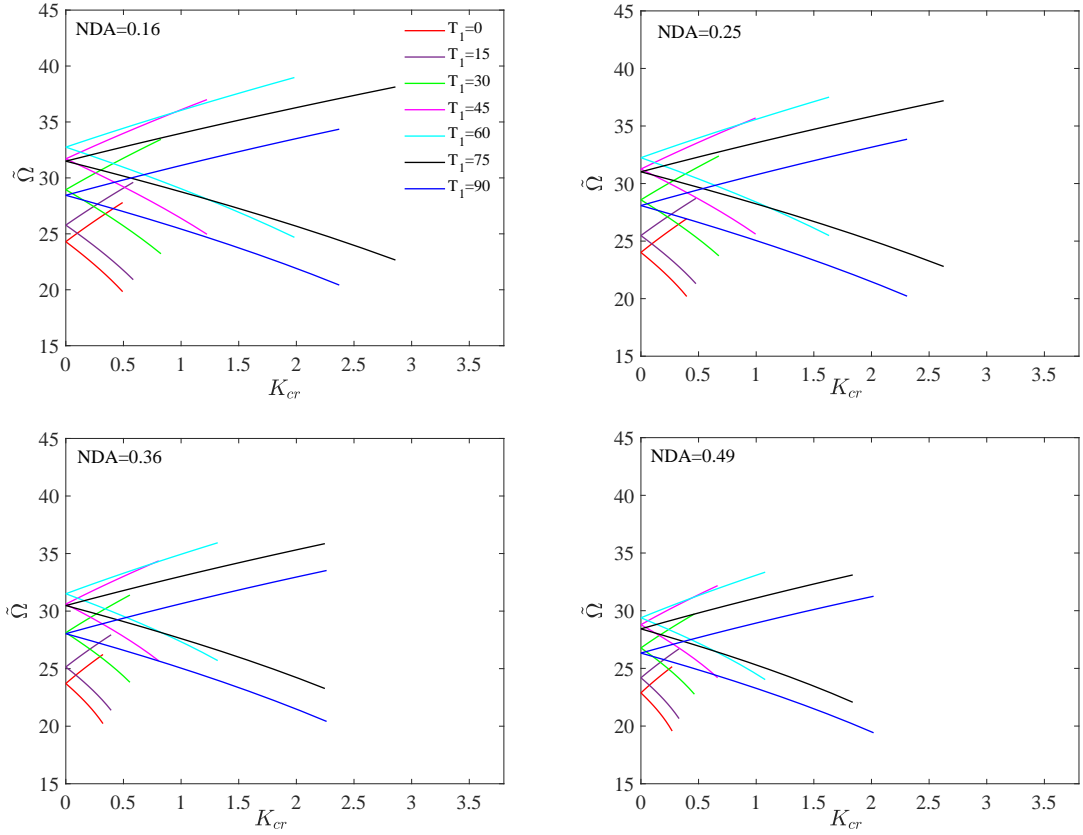


Figure 3.13: Principle DIRs of a VAT laminate $[90 \pm \langle T_0 | T_1 \rangle]_{4s}$ with a circular cutout (NDH=0.2) for different fiber-angles (T_1) and different NDA values (0.16, 0.25, 0.36 and 0.49).

Finally, the variation of D_{II} for the delaminated VAT laminate with a cutout, for different fiber-angles and NDA values (0.16, 0.25, 0.36 and 0.49) are shown in Fig. 3.15. The static and dynamic load parameters are chosen as $\alpha_0 = 0$ and $\alpha_1 = 0.3$, respectively. As shown in Fig. 3.15 for all the VAT fiber-angle configurations, the normalized

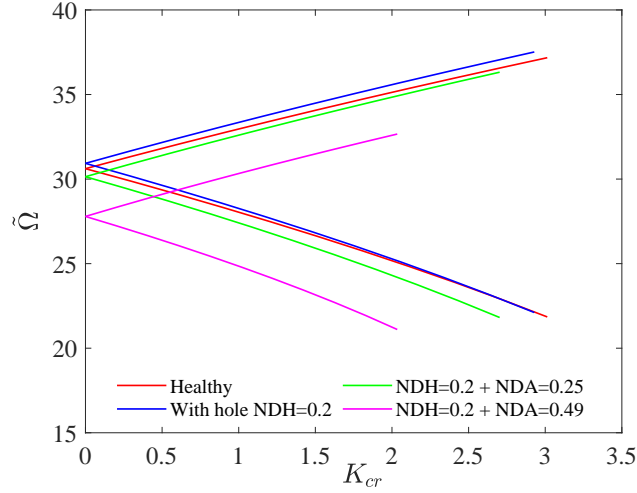


Figure 3.14: Principle DIRs of a VAT laminate $[90 \pm \langle 0|80 \rangle]_{4s}$ for different conditions.

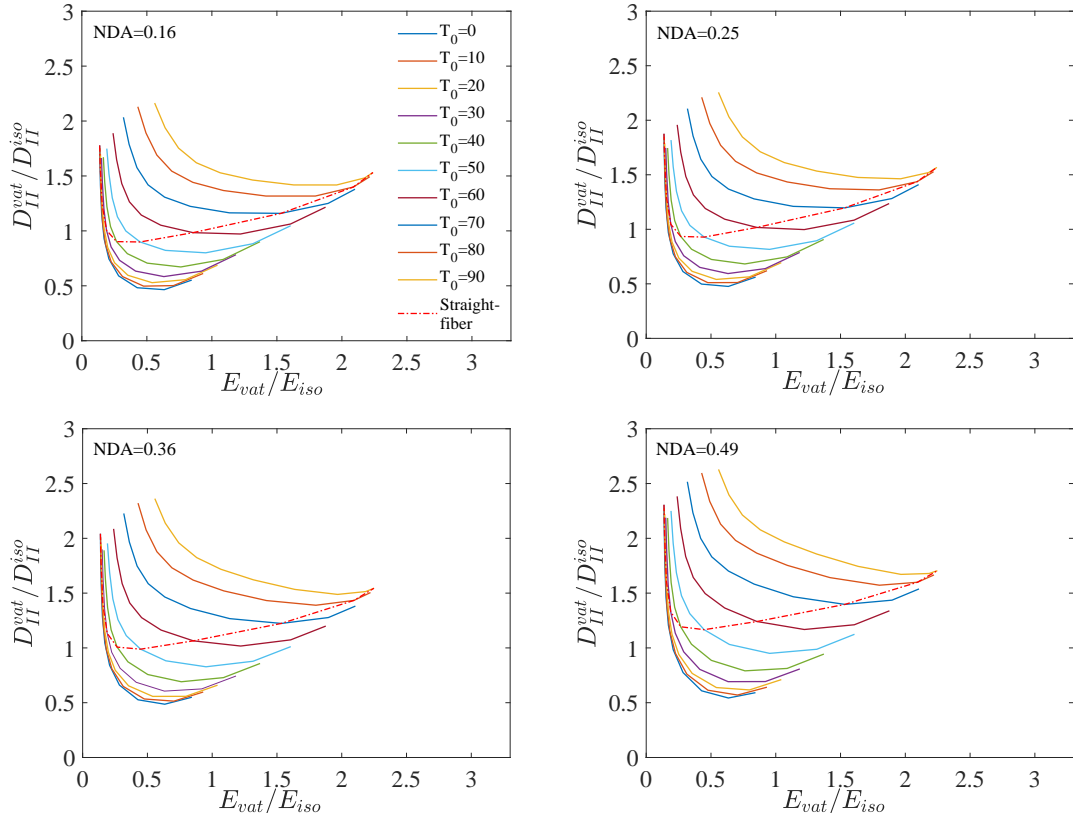


Figure 3.15: Variation of normalized D_{II} with respect to normalized pre-buckling stiffness (E_{vat}) of a VAT laminate $[90 \pm \langle T_0|T_1 \rangle]_{4s}$ with a circular cutout (NDH=0.2) for different fiber-angles (T_0 and T_1) and different NDA values (0.16, 0.25, 0.36 and 0.49).

D_{II} value increases with increase in the delamination area. It thus indicates that the laminates with delamination around the cutout become more dynamically unstable with an increase in the delamination area. This increase in D_{II} is because of the reduction in natural frequency and critical buckling load with the increase in the delamination area. However, it was observed that the VAT laminate with fiber-angles $T_0 = 0$ and $T_1 = 80$ shows a minimum D_{II} values for all the NDA values. Corresponding to each NDA value of 0.16, 0.25, 0.36 and 0.49, the D_{II} value for the VAT laminate shows an improvement of 48.4%, 49.0%, 51.7% and 54.4% over the straight-fiber laminate with optimal configuration $[\pm 45]_{4s}$. Also, increase in D_{II} value for the straight-fiber laminate with an increase in NDA value from 0.16 to 0.49 is 32.2%, whereas in the case of VAT laminate the increase is only 16.8% and shows that the VAT laminates are more stable when compared to straight-fiber laminates. Also, the decrease in stability with the increase in the delamination around the cutout in VAT laminate is much less compared to straight-fiber laminate. These results clearly demonstrate the distinct superiority of applying tow steering concepts to enhance the dynamic stability response of composite laminates with delamination and a cutout.

3.4 Summary

In this chapter, the dynamic stability behavior of the delaminated VAT laminate with a cutout under periodic axial in-plane compression is studied. The first-order shear deformation theory has been used to model the VAT laminate. Dynamic instability regions of the VAT laminate are then determined using a first-order approximation of Bolotin's method. Initially, the effect of tow-steering on critical buckling load and dynamic stability of VAT laminate with a centrally placed circular cutout has been studied. It was observed that the fiber-angle variation has a significant effect on critical buckling load and dynamic stability of the VAT laminate. For some fiber-angle configurations, VAT laminate with a circular cutout show much higher critical buckling load and dynamic stability than a healthy straight-fiber laminate. The significant increase in the dynamic stability of VAT laminate with a circular cutout is because of redistribution of stress from the center of the laminate towards fixed edges, which inturn increases the critical buckling load.

Next, square delamination is introduced around the circular cutout, and the influence of delamination on critical buckling load and dynamic stability is studied. It is observed that with the increase in delamination area around the cutout critical buckling load and natural frequency of the laminate decreases. The onset of dy-

dynamic instability regions started at lower frequencies and shrunk to a smaller range of critical buckling loads with an increase in the delamination area. This leads to the decrease in dynamic stability of the VAT laminate with the increase in delamination area. However, VAT laminate for some fiber-angle configuration shows much higher critical buckling load and dynamic stability even in the case of delamination and the cutout when compared to a healthy straight-fiber laminate. This study demonstrates the superiority of fiber-steering in improving the critical buckling load and dynamic stability of VAT laminate with delamination and cutout.

Chapter 4

Parametric instabilities in curved VAT composite panel

In the preceding chapters, the dynamic instability analysis is performed on the flat VAT composite panels, and the effect of fiber-angle variation on the dynamic behavior of the VAT panel is presented. However, in modern aerospace, civil, mechanical and naval engineering structures, curved panels are extensively used for load-bearing applications. Curved panels can exhibit greater structural efficiency because of their ability to sustain high compression loads. The improvement in their buckling performance is mainly attributed to the curvature of the panel and to their ability to develop membrane loads. In order to use the VAT concepts in the design of aircraft structures with curvature, a complete understanding of their dynamic behavior under different loading conditions is absolutely necessary.

In this chapter, the dynamic stability behavior of a curved VAT panel subjected to the periodic in-plane axial compression is investigated. For the analysis, a symmetric curved VAT panel with linear fiber-angle variation is considered. The generalized differential integral quadrature method (GDIQM) is used to solve the integral energy expressions, and Bolotin's first-order approximation is used to determine the dynamic instability boundary of a curved VAT panel. The effect of tow-steering, the radius of curvature, aspect ratio and plate boundary conditions on buckling and dynamic stability behavior of curved VAT panel under periodic axial compression load is investigated, and compared with straight-fiber composite panels.

4.1 Modeling of VAT laminate

A curved panel with VAT laminate considered for the analysis is shown in Fig. 4.1. In this work, the thickness of the laminate is assumed to be small. In thin laminates,

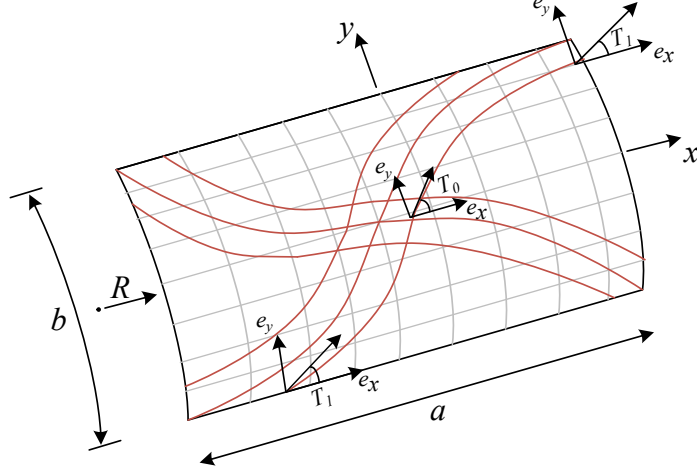


Figure 4.1: Schematic representation of a curved panel with VAT laminate.

the shear deformation of the shell section has less influence on the global behavior of VAT panels like natural frequency and critical buckling load [104, 105]. Therefore, the shear deformation of the shell's section in $x - z$ and $y - z$ planes are neglected. Using Donnell's shallow shell kinematic equations [104] and neglecting higher-order strain terms, the mid-plane strains (ϵ) and curvatures (κ) of the laminate are written as:

$$\epsilon = \left[\frac{\partial u}{\partial x}, \left(\frac{\partial v}{\partial y} + \frac{w}{R} \right), \left(\frac{\partial u}{\partial y} + \frac{\partial v}{\partial x} \right) \right]^T, \quad (4.1)$$

$$\kappa = - \left[\frac{\partial^2 w}{\partial x^2}, \frac{\partial^2 w}{\partial y^2}, 2 \frac{\partial^2 w}{\partial x \partial y} \right]^T, \quad (4.2)$$

where, u , v , and w are the mid-plane displacement fields corresponding to x , y and z directions, respectively. The variation of the fiber-angle over the laminate results in the following constitutive relationship:

$$\begin{Bmatrix} \bar{\mathbf{N}} \\ \bar{\mathbf{M}} \end{Bmatrix} = \begin{bmatrix} \bar{\mathbf{A}}(x, y) & \bar{\mathbf{B}}(x, y) \\ \bar{\mathbf{B}}^T(x, y) & \bar{\mathbf{D}}(x, y) \end{bmatrix} \begin{Bmatrix} \epsilon \\ \kappa \end{Bmatrix}. \quad (4.3)$$

Here, $\bar{\mathbf{N}} = [\bar{N}_x, \bar{N}_y, \bar{N}_{xy}]^T$ is the membrane stress resultant vector and $\bar{\mathbf{M}} = [\bar{M}_x, \bar{M}_y, \bar{M}_{xy}]^T$ is the bending moment resultant vector. Since the fiber-angle varies with respect to position over the lamina, the in-plane stiffness matrix ($\bar{\mathbf{A}}$), coupling stiffness matrix ($\bar{\mathbf{B}}$) and the bending stiffness matrix ($\bar{\mathbf{D}}$) are all functions of spatial coordinates (x, y) .

The equations of motion for the VAT composite panel subjected to in-plane periodic compression load can be obtained using Hamilton's principle as follows:

$$\delta \int (T_{KE} - U) dt = 0, \quad (4.4)$$

where, T_{KE} and U are the kinetic energy and strain energy, respectively. From Eq. (4.1) and Eq. (4.3), the strain energy stored in the VAT laminate subjected to uniform axial compression (\bar{u}_0) along the edges (neglecting higher-order terms) is written as [106]:

$$U = \frac{1}{2} \int_{\mathcal{A}} [\boldsymbol{\epsilon}^T \bar{\mathbf{A}} \boldsymbol{\epsilon} + \boldsymbol{\kappa}^T \bar{\mathbf{D}} \boldsymbol{\kappa}] d\mathcal{A} + \int_{\mathcal{A}} [\boldsymbol{\epsilon}_L^T \bar{\mathbf{T}} \boldsymbol{\epsilon}_L] d\mathcal{A}, \quad (4.5)$$

where, $\bar{\mathbf{T}}$ and $\boldsymbol{\epsilon}_L$ are defined as follows:

$$\bar{\mathbf{T}} = \begin{bmatrix} \bar{N}_x & \bar{N}_{xy} \\ \bar{N}_{xy} & \bar{N}_y \end{bmatrix}; \quad \boldsymbol{\epsilon}_L = \left[\frac{\partial w}{\partial x}, \frac{\partial w}{\partial y} \right]^T. \quad (4.6)$$

The kinetic energy for the plate element with a mass density (ρ) is given as:

$$T_{KE} = \frac{1}{2} \int_{\mathcal{A}} \rho [h(\dot{u}^2 + \dot{v}^2 + \dot{w}^2)] d\mathcal{A}, \quad (4.7)$$

where, h is the thickness of the panel. We combined the Rayleigh–Ritz method with GDIQM and applied them to the strain energy functional of the VAT panel (Eq. (4.5)) and solve for the dynamic instability. Unlike straight-fiber composites, the varying stiffness properties of the VAT panel induces non-uniform stress resultant distribution across the plane of the panel under pure compression. Therefore, the pre-buckling analysis of a curved VAT panel is carried out initially by applying uniform compression load to obtain the resultant stress distribution. Next, the obtained stress resultant distribution is used to calculate the geometric stiffness matrix (\mathbf{K}_G). From the obtained \mathbf{K}_G matrix, the dynamic stability behavior of a VAT panel is determined

from the following equations of motion:

$$\mathbf{M}\ddot{\mathbf{u}} + \mathbf{K}\mathbf{u} - (\alpha_0 P_{cr} + \alpha_1 P_{cr} \cos(\Omega t)) \mathbf{K}_G \mathbf{u} = 0. \quad (4.8)$$

Here, \mathbf{K} represents the structural stiffness matrix, \mathbf{M} is the mass matrix, \mathbf{u} is the vector of unknown variables, P_{cr} is the critical buckling load of the VAT panel, α_0 and α_1 are static and dynamic load parameters, respectively and Ω is the excitation frequency. In the following section, the application of GDIQM and the Rayleigh–Ritz method for obtaining the explicit expressions for \mathbf{M} , \mathbf{K} , and \mathbf{K}_G in the equations of motion (Eq. (4.8)) is discussed.

4.2 Generalized differential integral quadrature method

In the literature, buckling and post-buckling problems of the VAT panels have been successfully solved with the differential quadrature method (DQM) [24,25]. The DQM approach is based on the approximation of a derivative using a weighted linear sum of the function values at the discretized grid points in the domain. It should be noted that on the application of DQM discretization, the partial differential equation (PDE) governing the plate behavior is converted into a system of algebraic equations. The numerical incorporation of the strong form of plate boundary conditions along the boundary grid points in DQM is nontrivial and challenging. To overcome this difficulty, the problem is expressed in weak form using the strain energy functional, and then the Rayleigh–Ritz method combined with GDIQM is used to get the equilibrium equations. However, one of the major limitations of GDIQM is that it cannot be applied to the structures with geometric discontinuities. White et al. [107] introduced the GDIQM approach to solve the integro-differential post-buckling equations of a VAT laminate. Raju et al. [108] applied a perturbation based asymptotic numerical method coupled with GDIQM to perform the post-buckling of VAT laminates. In this work, GDIQM is used to solve the problems of pre-buckling, buckling, and dynamic stability of a curved VAT panel subjected to a periodic axial compression load.

As an example to demonstrate the application of DQM [109] to the derivative of a function, a one-dimensional function $f(x)$ is considered. It is assumed that $f(x)$ is sufficiently smooth over the whole domain. In DQM, the derivative of the function $f(x)$ with respect to x at a grid point x_i , is approximated by a linear sum of all the

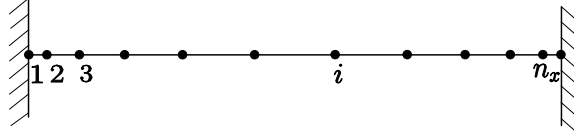


Figure 4.2: A one-dimensional grid of a function $f(x)$ with the grid-point numbering system.

functional values in the whole domain as follow:

$$\left. \frac{df}{dx} \right|_{x_i} = \sum_{j=1}^{n_x} \tilde{T}_{ij}^x \cdot f(x_j), \quad i = 1, 2, \dots, n_x \quad (4.9)$$

where, \tilde{T}_{ij}^x represents the weighting coefficients, and n_x is the number of grid points in the domain. In DQ approach, the weighting coefficients \tilde{T}_{ij}^x are different for different locations of x_i . Similar to the one-dimensional problem, the partial derivatives of a two-dimensional function $f(x, y)$ can be written in DQM form as:

$$\frac{\partial}{\partial x} f(x_i, y_j) = \sum_{k=1}^{n_x} \tilde{T}_{ik}^x f(x_k, y_j), \quad i = 1, \dots, n_x \quad (4.10)$$

$$\frac{\partial}{\partial y} f(x_i, y_j) = \sum_{k=1}^{n_y} \tilde{T}_{jk}^y f(x_i, y_k), \quad j = 1, \dots, n_y. \quad (4.11)$$

Here, $f(x_i, y_j)$ is the function value at the grid point (x_i, y_j) and n_x, n_y represents the number of grid points along x and y directions, respectively (see Fig. 4.3). \tilde{T}_{ik}^x and \tilde{T}_{jk}^y are the corresponding weighting coefficients. Lagrange interpolation polynomial and Fourier series expansions are usually used as test functions in the DQM. However, for plate bending and buckling problems, the DQM solutions converged quickly when Lagrange polynomials were used as basis functions along with Chebyshev grid spacing [24, 110, 111], and therefore, the same is used in the present analysis. The Lagrange interpolation polynomial used as the test functions for the computation of weighting coefficients (T_{ik}^x) and are given as:

$$r_k(x) = \frac{M(x)}{(x - x_k)M^x(x_k)}, \quad j = 1, 2, \dots, n_x \quad (4.12)$$

where,

$$M(x) = \prod_{k=1}^{n_x} (x - x_k), \quad M^x(x_i) = \frac{\partial M(x)}{\partial x} \Big|_{x=x_i} = \prod_{k=1, k \neq i}^{n_x} (x_i - x_k). \quad (4.13)$$

Here, $M^x = \frac{\partial M}{\partial x}$. Further, the elements of the first-order weighting coefficient matrix can be written as follows:

$$\tilde{T}_{ik}^x = \frac{M^x(x_i)}{(x_i - x_k)M^x(x_k)}, \quad i \neq k, \quad i, k = 1, 2, \dots, n_x \quad (4.14)$$

$$\tilde{T}_{ii}^x = - \sum_{k=1, i \neq k}^{n_x} T_{ik}^x. \quad (4.15)$$

The coordinates of the Chebyshev grid (x_i, y_j) used in the Lagrange polynomials are given as:

$$x_i = \frac{a \left(1 - \cos \left(\frac{\pi(i-1)}{(n_x-1)} \right) \right)}{2}; \quad y_j = \frac{b \left(1 - \cos \left(\frac{\pi(j-1)}{(n_y-1)} \right) \right)}{2}. \quad (4.16)$$

The schematic representation of a discretized Chebyshev grid of a curved panel along with the GDIQM numbering system is shown in Fig. 4.3.

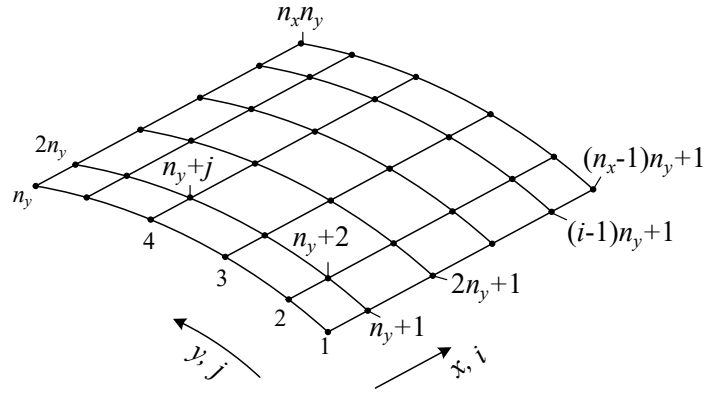


Figure 4.3: A two-dimensional Chebyshev grid plotted on the surface of a curved panel with the grid-point numbering system.

The matrices $\tilde{\mathbf{T}}^x$ and $\tilde{\mathbf{T}}^y$ are the first-order derivative weighting coefficient matrices having the dimensions $n_x \times n_x$ and $n_y \times n_y$, respectively. The grid point variables $(f(x_i, y_j))$ can be written in a vector form as \mathbf{f} and the first-order partial derivatives can be written as:

$$\frac{\partial}{\partial x} \mathbf{f} = \mathbf{T}^x \mathbf{f}, \quad \frac{\partial}{\partial y} \mathbf{f} = \mathbf{T}^y \mathbf{f}. \quad (4.17)$$

Here, \mathbf{T}^x and \mathbf{T}^y are the weighting coefficient matrices for the derivative of the grid point variables \mathbf{f} . They can be obtained by arranging the matrices $\tilde{\mathbf{T}}^x$ and $\tilde{\mathbf{T}}^y$ according to the grid point numbering scheme. In the same way, higher-order derivative weighting coefficient matrices can be derived on the basis of Eq. (4.11) (i.e., by ma-

trix multiplication) or by recursive formulas [112]. For example, second-order partial derivatives can be written as:

$$\frac{\partial^2}{\partial x^2} \mathbf{f} = \frac{\partial}{\partial x} \left(\frac{\partial}{\partial x} \mathbf{f} \right) = \frac{\partial}{\partial x} (\mathbf{T}^x \mathbf{f}) = \mathbf{T}^x (\mathbf{T}^x \mathbf{f}) = \mathbf{T}^{xx} \mathbf{f}, \quad (4.18)$$

$$\frac{\partial^2}{\partial y^2} \mathbf{f} = \frac{\partial}{\partial y} \left(\frac{\partial}{\partial y} \mathbf{f} \right) = \frac{\partial}{\partial y} (\mathbf{T}^y \mathbf{f}) = \mathbf{T}^y (\mathbf{T}^y \mathbf{f}) = \mathbf{T}^{yy} \mathbf{f}, \quad (4.19)$$

$$\frac{\partial^2}{\partial x \partial y} \mathbf{f} = \frac{\partial}{\partial x} \left(\frac{\partial}{\partial y} \mathbf{f} \right) = \frac{\partial}{\partial x} (\mathbf{T}^y \mathbf{f}) = \mathbf{T}^x (\mathbf{T}^y \mathbf{f}) = \mathbf{T}^{xy} \mathbf{f}. \quad (4.20)$$

Here, \mathbf{T}^{xx} , \mathbf{T}^{yy} and \mathbf{T}^{xy} are the second-order derivative weighting coefficient matrices. In GDIQM, the integral operations in the strain energy functional Eq. (4.5) are replaced by an integral-quadrature matrix operator [112]. The pseudo-inverse operator can be used [113] to compute the integral weighting coefficient matrices. For a one-dimensional function $g(x)$, the weighting coefficient matrix for an arbitrary grid spacing can be written as:

$$\int g(x) dx \approx \mathbf{P}^x \mathbf{g} + \mathbf{c} \quad \text{with} \quad \mathbf{P}^x = (\mathbf{T}^x)^+, \quad (4.21)$$

where, $()^+$ is the Moore-Penrose pseudo-inverse operator, the vector \mathbf{g} contains the value of the function at grid points and \mathbf{c} is the vector of integration constants. Here, \mathbf{P}^x has the same dimension as \mathbf{T}^x . In order to approximate one-dimensional definite integrals, we define the following vectors \mathbf{j}^x and \mathbf{j}^y as:

$$\mathbf{j}^x = P_{(n_x, i)}^x - P_{(1, i)}^x, \quad i = 1, \dots, n_x \quad \text{and} \quad \mathbf{j}^y = P_{(n_y, k)}^y - P_{(1, k)}^y, \quad k = 1, \dots, n_y, \quad (4.22)$$

where, the vectors \mathbf{j}^x and \mathbf{j}^y have dimensions $1 \times n_x$ and $1 \times n_y$, respectively. Using the vectors \mathbf{j}^x and \mathbf{j}^y the definite integrals of a function $g(x, y)$ along the lines of constant y or x can be constructed as:

$$\int_0^a [g(x, y_1), g(x, y_2), \dots, g(x, y_{n_y})]^T dx \approx \mathbf{J}^x \mathbf{g}, \quad (4.23)$$

$$\int_0^a [g(x_1, y), g(x_2, y), \dots, g(x_{n_x}, y)]^T dy \approx \mathbf{J}^y \mathbf{g}. \quad (4.24)$$

Here, the matrices \mathbf{J}^x and \mathbf{J}^y contains the elements of vectors \mathbf{j}^x and \mathbf{j}^y arranged according to the grid-point numbering scheme. When the system defined in Fig. 4.3 is used, then the matrices can be computed by the matrix Kronecker product [114],

denoted by \otimes . Therefore,

$$\mathbf{J}^x = \mathbf{j}^x \otimes \mathbf{I}^y \quad \text{and} \quad \mathbf{J}^y = \mathbf{I}^x \otimes \mathbf{j}^y, \quad (4.25)$$

where, $\mathbf{I}^x \in \mathbb{R}^{n_x}$ and $\mathbf{I}^y \in \mathbb{R}^{n_y}$ are identity matrices and $\mathbf{J}^x \in \mathbb{R}^{n_y \times n_x n_y}$, $\mathbf{J}^y \in \mathbb{R}^{n_x \times n_x n_y}$ are two dimensional integral weighting matrices. For evaluating, two-dimensional integrals, Eq. (4.24) is written as:

$$\int_0^a \int_0^b g(x, y) dx dy \approx (\mathbf{j}^y \mathbf{J}^x) \mathbf{g} = \mathbf{s}^{xy} \mathbf{g}. \quad (4.26)$$

The integral of a product of two functions $f(x, y)$ and $g(x, y)$ can be calculated approximately by constructing a matrix $\mathbf{S} = \text{diag}(\mathbf{s}^{xy})$:

$$\int_0^a \int_0^b f(x, y)g(x, y) dx dy \approx \mathbf{f}^T \mathbf{S} \mathbf{g}. \quad (4.27)$$

In the next section, the GDIQM approach is applied to Eq. (4.5) using the weighting coefficient matrices \mathbf{T}^x , \mathbf{T}^y , \mathbf{T}^{xx} , \mathbf{T}^{yy} , \mathbf{T}^{xy} and \mathbf{S} .

Pre-buckling analysis

On applying Rayleigh–Ritz to the first term in the strain energy functional (Eq. (4.5)), the system of equations that governs the pre-buckling behavior of a VAT panel can be written as:

$$\begin{bmatrix} \mathbf{K}_{uu} & \mathbf{K}_{uv} & \mathbf{K}_{uw} \\ \mathbf{K}_{vu} & \mathbf{K}_{vv} & \mathbf{K}_{vw} \\ \mathbf{K}_{wu} & \mathbf{K}_{wv} & \mathbf{K}_{ww} \end{bmatrix} \begin{Bmatrix} \mathbf{u} \\ \mathbf{v} \\ \mathbf{w} \end{Bmatrix} = \begin{Bmatrix} \mathbf{F}_u \\ \mathbf{F}_v \\ \mathbf{F}_w \end{Bmatrix} \quad (4.28)$$

and can be written in compact form as:

$$\mathbf{K}_s \bar{\mathbf{u}} = \mathbf{F}, \quad (4.29)$$

where, $\bar{\mathbf{u}}$ represents the pre-buckling solution and \mathbf{F} represents the forces applied along the x , y and z directions, respectively.

The terms of \mathbf{K}_s matrix in Eq. (4.28) are expressed as follows:

$$\begin{aligned}
\mathbf{K}_{uu} &= \int_{\mathcal{A}} \left[\frac{\partial'}{\partial x} A_{11} \frac{\partial}{\partial x} + \frac{\partial'}{\partial y} A_{16} \frac{\partial}{\partial x} + \frac{\partial'}{\partial x} A_{16} \frac{\partial}{\partial y} + \frac{\partial'}{\partial y} A_{66} \frac{\partial}{\partial y} \right] d\mathcal{A} \\
&= A_{11} \mathbf{T}^{x'} \mathbf{S} \mathbf{T}^{xx} + A_{16} \mathbf{T}^{y'} \mathbf{S} \mathbf{T}^{xx} + A_{16} \mathbf{T}^{x'} \mathbf{S} \mathbf{T}^{yy} + A_{66} \mathbf{T}^{y'} \mathbf{S} \mathbf{T}^{yy} \\
\mathbf{K}_{uv} &= \int_{\mathcal{A}} \left[\frac{\partial'}{\partial x} A_{12} \frac{\partial}{\partial y} + \frac{\partial'}{\partial y} A_{26} \frac{\partial}{\partial y} + \frac{\partial'}{\partial x} A_{16} \frac{\partial}{\partial x} + \frac{\partial'}{\partial y} A_{66} \frac{\partial}{\partial x} \right] d\mathcal{A} \\
&= A_{12} \mathbf{T}^{x'} \mathbf{S} \mathbf{T}^{yy} + A_{26} \mathbf{T}^{y'} \mathbf{S} \mathbf{T}^{yy} + A_{16} \mathbf{T}^{x'} \mathbf{S} \mathbf{T}^{xx} + A_{66} \mathbf{T}^{y'} \mathbf{S} \mathbf{T}^{xx} \\
\mathbf{K}_{vu} &= \mathbf{K}_{uv} \\
\mathbf{K}_{vv} &= \int_{\mathcal{A}} \left[\frac{\partial'}{\partial y} A_{22} \frac{\partial}{\partial y} + \frac{\partial'}{\partial x} A_{26} \frac{\partial}{\partial y} + \frac{\partial'}{\partial y} A_{26} \frac{\partial}{\partial x} + \frac{\partial'}{\partial x} A_{66} \frac{\partial}{\partial x} \right] d\mathcal{A} \\
&= A_{22} \mathbf{T}^{y'} \mathbf{S} \mathbf{T}^{yy} + A_{26} \mathbf{T}^{x'} \mathbf{S} \mathbf{T}^{yy} + A_{26} \mathbf{T}^{y'} \mathbf{S} \mathbf{T}^{xx} + A_{66} \mathbf{T}^{x'} \mathbf{S} \mathbf{T}^{xx} \\
\mathbf{K}_{uw} &= \int_{\mathcal{A}} \left[\frac{1}{R} \left(\frac{\partial'}{\partial x} A_{12} + \frac{\partial'}{\partial y} A_{26} \right) \right] d\mathcal{A} \\
&= (A_{12} \mathbf{T}^{x'} \mathbf{S} + A_{26} \mathbf{T}^{y'} \mathbf{S}) \frac{1}{R} \\
\mathbf{K}_{wu} &= \mathbf{K}_{uw} \\
\mathbf{K}_{vw} &= \int_{\mathcal{A}} \left[\frac{1}{R} \left(\frac{\partial'}{\partial y} A_{22} + \frac{\partial'}{\partial x} A_{26} \right) \right] d\mathcal{A} \\
&= (A_{22} \mathbf{T}^{y'} \mathbf{S} + A_{26} \mathbf{T}^{x'} \mathbf{S}) \frac{1}{R} \\
\mathbf{K}_{wv} &= \mathbf{K}_{vw} \\
\mathbf{K}_{ww} &= \int_{\mathcal{A}} A_{22}/R^2 d\mathcal{A} \\
&+ \int_{\mathcal{A}} \left[\frac{\partial'^2}{\partial x^2} D_{11} \frac{\partial^2}{\partial x^2} + \frac{\partial'^2}{\partial y^2} D_{12} \frac{\partial^2}{\partial x^2} + 2 \frac{\partial'^2}{\partial x \partial y} D_{16} \frac{\partial^2}{\partial x^2} \right. \\
&+ \frac{\partial'^2}{\partial x^2} D_{12} \frac{\partial^2}{\partial y^2} + \frac{\partial'^2}{\partial y^2} D_{22} \frac{\partial^2}{\partial y^2} + 2 \frac{\partial'^2}{\partial x \partial y} D_{26} \frac{\partial^2}{\partial y^2} \\
&+ \left. 2 \frac{\partial'^2}{\partial x^2} D_{16} \frac{\partial^2}{\partial x \partial y} + 2 \frac{\partial'^2}{\partial y^2} D_{26} \frac{\partial^2}{\partial x \partial y} + 4 \frac{\partial'^2}{\partial x \partial y} D_{66} \frac{\partial^2}{\partial x \partial y} \right] d\mathcal{A} \\
&= A_{22}/R^2 + D_{11} \mathbf{T}^{xx'} \mathbf{S} \mathbf{T}^{xx} + D_{12} \mathbf{T}^{yy'} \mathbf{S} \mathbf{T}^{xx} + 2D_{16} \mathbf{T}^{xy'} \mathbf{S} \mathbf{T}^{xx} \\
&+ D_{12} \mathbf{T}^{xx'} \mathbf{S} \mathbf{T}^{yy} + D_{22} \mathbf{T}^{yy'} \mathbf{S} \mathbf{T}^{yy} + 2D_{26} \mathbf{T}^{xy'} \mathbf{S} \mathbf{T}^{yy} \\
&+ 2D_{16} \mathbf{T}^{xx'} \mathbf{S} \mathbf{T}^{xy} + 2D_{26} \mathbf{T}^{yy'} \mathbf{S} \mathbf{T}^{xy} + 4D_{66} \mathbf{T}^{xy'} \mathbf{S} \mathbf{T}^{xy}.
\end{aligned} \tag{4.30}$$

Here, $()'$ represents the transpose of a given matrix.

The pre-buckling analysis of a curved VAT panel is carried out by applying the in-plane boundary conditions: $u_x = v_x = 0$ at $x = -a/2$, $v_x = 0$ at $x = a/2$ and a uniform compression is applied along the edge $x = a/2$ as shown in Fig. 4.4. The uniform compression is applied by connecting all nodes on the edge to a control node and an equivalent compression force (f_c) is applied on the control node point (see Fig. 4.4). The uniform displacement constraint is implemented in GDIQM by using the equations $u_{slave} - u_{control} = 0$, which is similar to a multi-point constraint (MPC) approach used in the commercial finite element analysis. These constraint equations can be written in matrix form as $\mathbf{K}_c \bar{\mathbf{u}} = 0$. The constraint matrix, \mathbf{K}_c is added to the structural stiffness matrix \mathbf{K}_s to obtain the final stiffness matrix \mathbf{K} .

$$\mathbf{K} = \begin{bmatrix} \mathbf{K}_s & \mathbf{K}'_c \\ \mathbf{K}_c & \mathbf{0} \end{bmatrix}. \quad (4.31)$$

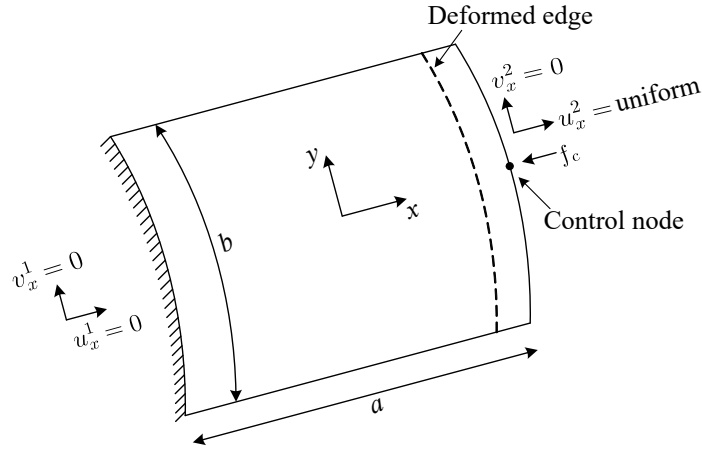


Figure 4.4: Schematic representation of in-plane boundary conditions for pre-buckling analysis of a curved panel with VAT laminate.

The pre-buckling problem of VAT panels is solved by using the equation $\mathbf{K}\bar{\mathbf{u}} = \mathbf{F}$ for the displacement vector, $\bar{\mathbf{u}}$. From the obtained displacements, the resultant stress distributions of the VAT panel can be calculated from Eqs. (4.1) and (4.3), which are used in buckling analysis of the VAT panel.

Buckling analysis

By applying the Rayleigh–Ritz method to Eq. (4.5), that governs the buckling behavior of the VAT panel, the system of equilibrium equations can be written as an eigenvalue problem:

$$[\mathbf{K} - P_{cr}\mathbf{K}_G] \bar{\mathbf{u}} = 0, \quad (4.32)$$

where,

$$\begin{aligned} \mathbf{K}_G &= \int_{\mathcal{A}} \left[\frac{\partial'}{\partial x} \bar{N}_x \frac{\partial}{\partial x} + \frac{\partial'}{\partial y} \bar{N}_y \frac{\partial}{\partial y} + 2 \frac{\partial'}{\partial x} \bar{N}_{xy} \frac{\partial}{\partial y} \right] d\mathcal{A} \\ &= \bar{N}_x \mathbf{T}^{x'} \mathbf{S} \mathbf{T}^x + \bar{N}_y \mathbf{T}^{y'} \mathbf{S} \mathbf{T}^y + 2 \bar{N}_{xy} \mathbf{T}^{x'} \mathbf{S} \mathbf{T}^y. \end{aligned} \quad (4.33)$$

Here, \mathbf{K} , \mathbf{K}_G represents the structural and geometric stiffness matrices, respectively and \bar{N}_x , \bar{N}_y and \bar{N}_{xy} represents the pre-buckling stress resultants obtained when a uniform compression load is applied along the edge of the panel.

Boundary conditions

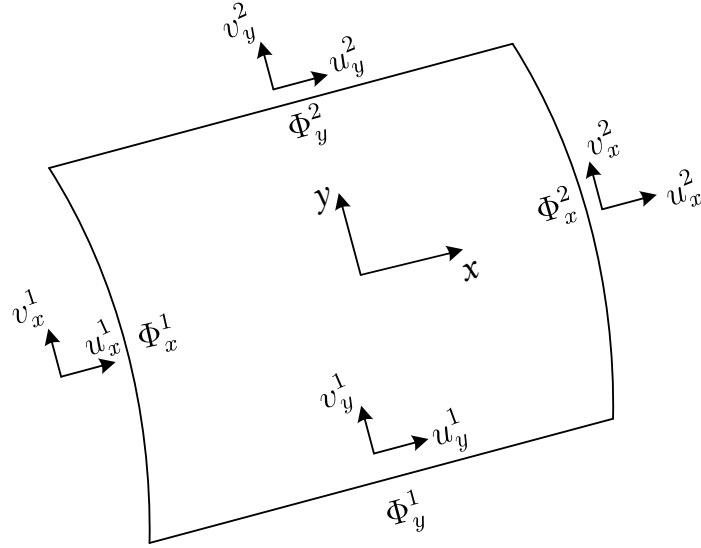


Figure 4.5: Representation of boundaries of a curved panel with VAT laminate.

In order to solve the equilibrium equations, corresponding plate boundary conditions have to be specified along the edges. The designation of boundary regions are shown in Fig. 4.5. The shell ends (i.e., at $x \in \{-\frac{a}{2}, \frac{a}{2}\}$) are designated as Φ_x^1 and Φ_x^2 , and its sides (i.e., at $y \in \{-\frac{b}{2}, \frac{b}{2}\}$) are designated as Φ_y^1 and Φ_y^2 . Three different types

of plate boundary conditions considered in this work, they are: (i) all edges simply-supported (SSSS): $w(\Phi_x^i) = w(\Phi_y^i) = 0$, (ii) simply-supported sides (Φ_y^1 and Φ_y^2) and clamped ends (Φ_x^1 and Φ_x^2) (SCSC): $\frac{dw}{dx}(\Phi_x^i) = 0$, $w(\Phi_x^i) = w(\Phi_y^i) = 0$ (iii) clamped on all the edges (CCCC): $\frac{dw}{dx}(\Phi_x^i) = 0$, $\frac{dw}{dy}(\Phi_y^i) = 0$, $w(\Phi_x^i) = w(\Phi_y^i) = 0$, $i = 1, 2$. The above boundary conditions are implemented by writing them in the GDIQM form. Equation (4.32) is solved along with the plate boundary conditions to obtain the critical buckling load, P_{cr} and their corresponding mode shapes.

4.3 Dynamic stability in curved VAT panel

Dynamic stability analysis is performed on a curved VAT panel subjected to a periodic axial compression load of form $P(t) = \alpha_0 P_{cr} + \alpha_1 P_{cr} \cos(\Omega t)$. Here, P_{cr} is the critical buckling load of the panel, α_0 and α_1 are the static and dynamic load parameters, respectively and Ω is the forcing frequency. The equations of motion of a symmetric curved VAT panel under periodic axial compression load are expressed as:

$$\mathbf{M}\ddot{\mathbf{u}} + \mathbf{K}\bar{\mathbf{u}} - (\alpha_0 P_{cr} + \alpha_1 P_{cr} \cos(\Omega t)) \mathbf{K}_G \bar{\mathbf{u}} = 0, \quad (4.34)$$

where, \mathbf{M} represents the mass matrix of the VAT panel and is obtained from the kinetic energy expression of the panel shown in Eq. (4.7). On applying GDIQM to Eq. (4.7), the mass matrix for the panel can be written as:

$$\mathbf{M} = \rho \begin{bmatrix} h\mathbf{S} & 0 & 0 \\ 0 & h\mathbf{S} & 0 \\ 0 & 0 & h\mathbf{S} \end{bmatrix}. \quad (4.35)$$

In Eq. (4.34), for certain combinations of α_0 , α_1 and Ω , the response of the panel can become unbounded due to parametric resonance and is referred to as dynamic instability. The region in the parametric space, where the dynamic instability occurs is known as the dynamic instability region (DIR). In this work, Bolotin's approach [49] has been used to determine the stability boundary of Eq. (4.34). According to Bolotin's theory, the solutions of Eq. (4.34) are periodic with period $T_1 = 4\pi/\Omega$ or $T_2 = 2\pi/\Omega$ on the stability boundary. Since, the principle dynamic instability region is the most dominant among all other instability regions and has the boundary with the solutions

of period $4\pi/\Omega$, the solution of Eq. (4.34) can be expanded as:

$$\bar{\mathbf{u}} = \sum_{k=1,3,5}^{\infty} (\mathbf{a}_k \sin(k\Omega t/2) + \mathbf{b}_k \cos(k\Omega t/2)), \quad (4.36)$$

where, the coefficients $\mathbf{a}_k, \mathbf{b}_k$ are unknowns and infinite in number. Therefore, a first-order approximation is often used in the literature [58, 64, 70] to predict the stability boundary. In the first-order Bolotin's approximation, only the first two terms in Eq. (4.36) are considered, and therefore we get:

$$\bar{\mathbf{u}} = \mathbf{a}_1 \sin(\Omega t/2) + \mathbf{b}_1 \cos(\Omega t/2). \quad (4.37)$$

Upon substituting Eq. (4.37) into Eq. (4.34) we obtain the residual equations. It should be noted that the coefficients of $\sin(\Omega t/2)$ and $\cos(\Omega t/2)$ must vanish in the residual equations. This leads to the following quadratic eigenvalue problems:

$$[\mathbf{K} - (\alpha_0 + 0.5\alpha_1)P_{cr}\mathbf{K}_G]\{\mathbf{a}_1\} - 0.25\mathbf{M}\Omega^2\{\mathbf{a}_1\} = 0, \quad (4.38)$$

$$[\mathbf{K} - (\alpha_0 - 0.5\alpha_1)P_{cr}\mathbf{K}_G]\{\mathbf{b}_1\} - 0.25\mathbf{M}\Omega^2\{\mathbf{b}_1\} = 0. \quad (4.39)$$

The solution of Eqs. (4.38)-(4.39) determines two boundaries of the first dynamic instability region (principle parametric resonance).

4.4 Results and discussion

In this section, the dynamic stability analysis of a symmetric curved VAT panel subjected to a periodic in-plane compression load is presented. An in-house MATLAB program is developed to analyze the curved VAT panel using GDIQM. For numerical study, a symmetric curved VAT panel $[\phi \pm \langle T_0|T_1 \rangle]_{2s}$ of dimensions, $a = b = 0.3$ m and thickness, $h = 1.048 \times 10^{-3}$ m is considered. The material properties of the lamina are given as: $E_{11} = 163$ GPa, $E_{22} = 10$ GPa, $G_{12} = 5$ GPa, $\nu_{12} = 0.3$, $\rho = 1480$ kg/m³. Simply-supported boundary conditions have been used for all analyses unless otherwise specified. Firstly, the accuracy of the GDIQM is verified by comparing with the results published in literature and with ABAQUS simulations. For ABAQUS, a subroutine is developed to generate four-noded shell elements (S4R) of curved VAT panel, each having independent fiber orientations.

To study the convergence of GDIQM, the normalized fundamental frequency ($\tilde{\omega} = \frac{\omega a^2}{h} \sqrt{\rho/E_{22}}$) of the curved VAT panels ($[90 \pm \langle 0|0 \rangle]_{2s}$ and $[90 \pm \langle 0|30 \rangle]_{2s}$) with $b/R = 0.2$

for different number of grid points ($n_x \times n_y$) is shown in Fig. 4.6. FEM results were computed using ABAQUS for different mesh sizes (see Fig. 4.6) to obtain convergence. From Fig. 4.6 it is observed that a grid size of $n_x = n_y = 21$ is sufficient to obtain accurate results and therefore, the same grid size has been used for all analyses in this work. Also, it is observed that GDIQM requires fewer grid points when compared to FEM (ABAQUS) to obtain converged results. This study shows the fast convergence and less computational effort required by GDIQM than FEM.

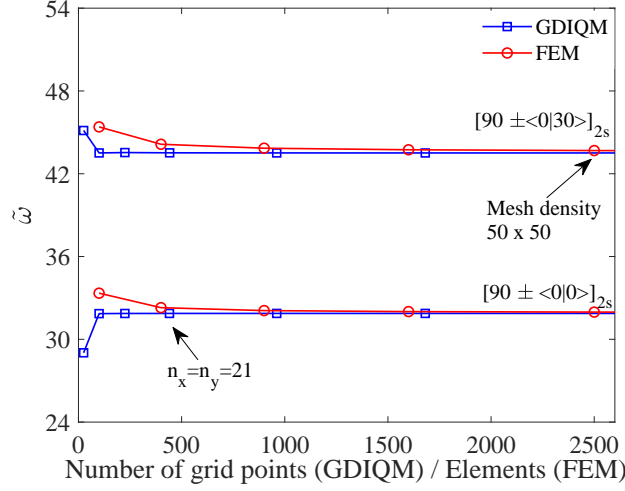


Figure 4.6: Numerical convergence study of normalized fundamental frequency ($\tilde{\omega}$) computed using GDIQM and FEM (ABAQUS) for the curved VAT panel with $b/R = 0.2$.

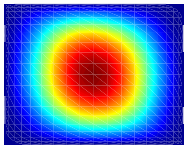
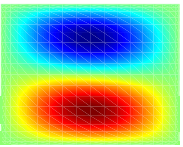
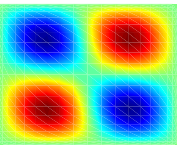
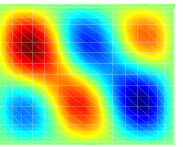
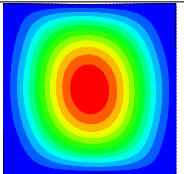
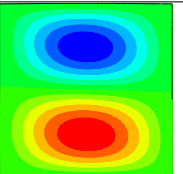
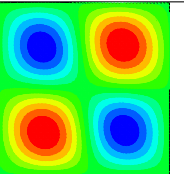
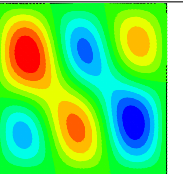
Modal analysis of a curved VAT panel was undertaken using GDIQM, and the results are now compared with ABAQUS simulations. The analysis is performed on a curved VAT panel $[90 \pm \langle 0|T_1 \rangle]_{2s}$ for the different radius of curvature and the corresponding normalized fundamental natural frequencies along with the ABAQUS simulation results are presented in Table 4.1. The first four vibration mode shapes of a curved VAT panel $[90 \pm \langle 0|30 \rangle]_{2s}$ with $b/R = 0.2$ obtained from the present analysis are compared with the ABAQUS results in Table 4.2. As shown in Table 4.1 and Table 4.2, normalized natural frequencies and mode shapes obtained using the GDIQM match closely with the ABAQUS results.

Next, the buckling load of a VAT panel for different curvatures ($b/R = 0.0, 0.1, 0.2$) and fiber-angles are determined using GDIQM and is presented in Fig. 4.7 along with the results published in the literature [115] and ABAQUS simulation results. Fig. 4.7 clearly illustrates good agreement between the present model and the results published

Table 4.1: Comparison of normalized fundamental natural frequency ($\tilde{\omega}$) of a curved VAT panel $[90 \pm \langle 0|T_1 \rangle]_{2s}$ for different b/R ratios.

b/R	T_1					
	0°		30°		60°	
	Present	Abaqus	Present	Abaqus	Present	Abaqus
0	12.7417	12.7611	14.5619	14.5431	15.8927	15.8518
0.05	14.9408	14.9552	18.3324	18.3368	22.3216	22.3216
0.075	17.2744	17.3014	22.0270	22.0621	28.3152	28.3560
0.1	20.0754	20.1144	26.2844	26.3441	34.9854	35.0545
0.2	33.3794	33.4812	45.5694	45.7410	45.9540	46.0105

Table 4.2: Comparison of free vibration mode shapes of a curved VAT panel $[90 \pm \langle 0|30 \rangle]_{2s}$.

	Mode 1	Mode 2	Mode 3	Mode 4
GDIQM				
$\tilde{\omega}$	7.2526	7.8205	10.7711	14.8973
FEM				
$\tilde{\omega}$	7.2799	7.8346	10.7892	14.9334

in the literature and ABAQUS results. The comparison of first four buckling mode shapes along with the normalized critical buckling load values ($K_{cr} = P_{cr}a^2/(E_{11}bh^3)$) of the curved VAT panel $[90 \pm \langle 0|30 \rangle]_{2s}$ with $b/R = 0.2$ from the present model with ABAQUS is shown in Table 4.3.

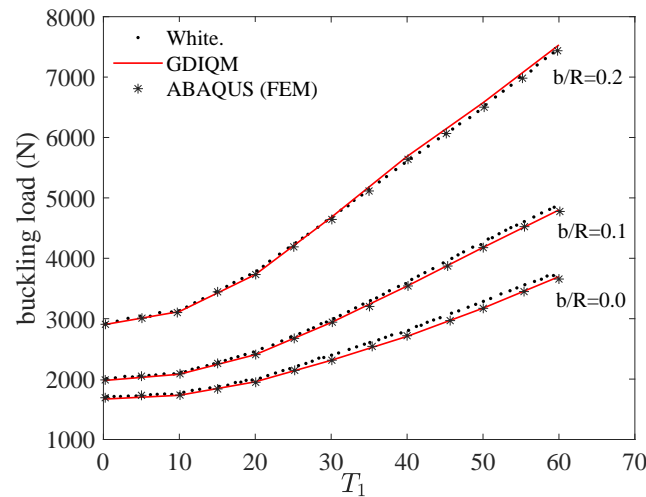
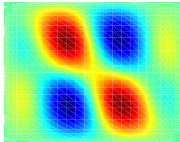
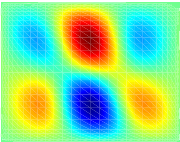
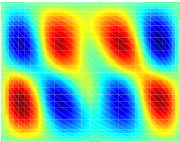
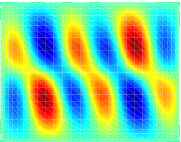
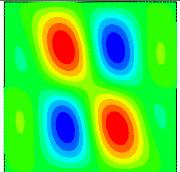
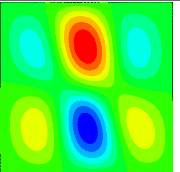
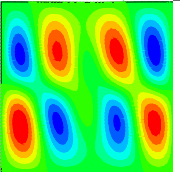
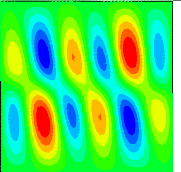


Figure 4.7: Variation of buckling load of a curved VAT panel $[0 \pm \langle 0|T_1 \rangle]_{2s}$ with respect to fiber-angle T_1 .

Table 4.3: Comparison of buckling mode shapes of a curved VAT panel $[90 \pm \langle 0|30 \rangle]_{2s}$.

	Mode 1	Mode 2	Mode 3	Mode 4
GDIQM				
K_{cr}	5.9480	5.9613	6.3820	6.4853
FEM				
K_{cr}	5.9497	5.9641	6.3901	6.4939

We also study, the variation of normalized natural frequency with respect to the static in-plane load parameter (α_0) for a curved VAT panel $[90 \pm \langle 0|30 \rangle]_{2s}$ with $b/R =$

0.1. Here, the VAT panel is subjected to a uniform axial compression load with the static load parameter, α_0 varying from 0.0 to 1.0 and the corresponding normalized natural frequencies are plotted in Fig. 4.8. The results are then compared with ABAQUS and found to be in good agreement with each other.

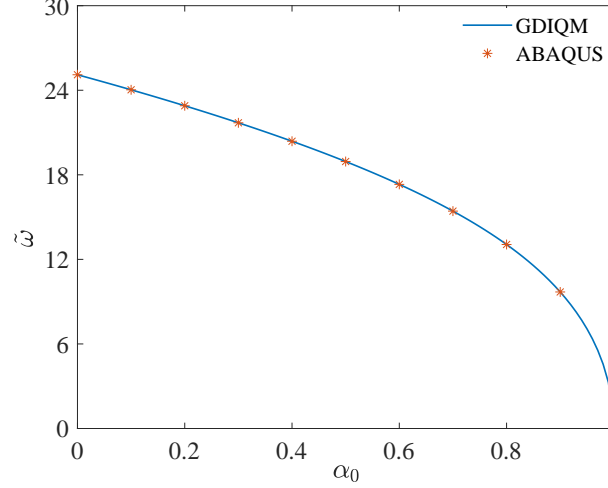


Figure 4.8: Variation of normalized fundamental natural frequency ($\tilde{\omega}$) with respect to static in-plane load parameter (α_0) for a curved VAT panel $[90 \pm \langle 0|30 \rangle]_{2s}$.

4.4.1 Dynamic instability in curved VAT panel

In this section, the effect of fiber-angle variation on DIR of a curved VAT panel is studied. The analysis is performed on a VAT panel $[90 \pm \langle 0|T_1 \rangle]_{2s}$ for different values of T_1 ranging from 0° to 90° in increments of 15° . The radius of curvature of the panel is taken as $b/R = 0.2$, and the static load parameter is chosen as $\alpha_0 = 0.0$ for the analysis. The results are shown in Fig. 4.9 in the plane of normalized frequency ($\tilde{\Omega} = \Omega a^2 / h \sqrt{\rho / E_{22}}$) versus normalized buckling load ($K_{cr} = P_{cr} a^2 / (E_{11} b h^3)$). From Fig. 4.9 it is clearly seen that a change in the fiber-angle configuration influences the DIR of a VAT panel. The onset of DIR shifts towards higher frequency when T_1 increases, reaches a maximum when $T_1 = 45^\circ$ and then decreases. Likewise, the extension of DIR towards the K_{cr} value increases with T_1 , reaches a maximum when $T_1 = 60^\circ$ and then decreases, as shown in Fig. 4.9. This change in the parametric frequency and critical buckling load occurs as a consequence of the change in the membrane and bending stiffness of the VAT panel due to the variation in fiber-angle.

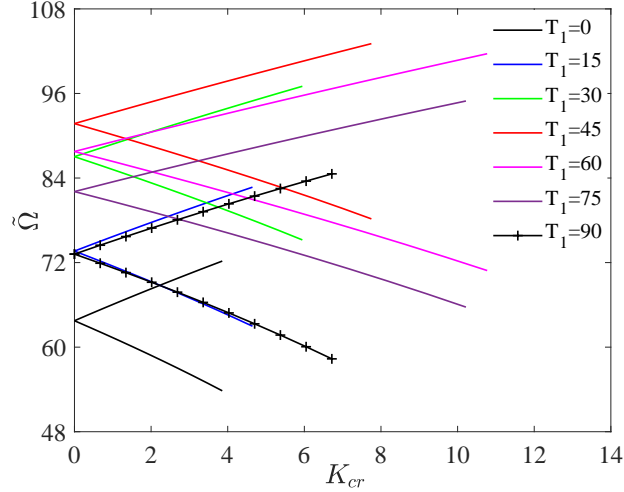


Figure 4.9: Principle DIRs of a curved VAT panel $[90 \pm \langle 0|T_1 \rangle]_{2s}$ for different fiber orientations (T_1).

Now, the influence of radius of curvature (b/R) on DIR of a curved VAT panel is studied. The analysis is carried out on a VAT panel $[90 \pm \langle 0|30 \rangle]_{2s}$ for four different b/R ratios (0.0, 0.05, 0.075, 0.1, 0.2) and the results are presented in Fig. 4.10. The ratio $b/R = 0$ in Fig. 4.10 corresponds to a flat laminate. In Fig. 4.10, for the VAT panel when $b/R = 0$, the onset of DIR starts at $\tilde{\Omega} = 4.97$ and extends up to $K_{cr} = 3.92$. In the case of $b/R = 0.2$, the onset of DIR shifts to $\tilde{\Omega} = 15.29$ and extends up to $K_{cr} = 13.03$, thus increasing the dynamic stability region of the VAT panel. Also, the width of the DIR shrinks with an increase in the b/R ratio of the panel. This study clearly illustrates the increase in dynamic stability of the curved VAT panel with an increase in the b/R ratio.

4.4.2 Variation of buckling load and dynamic instability index of a curved VAT panel

In this section, the variation of critical buckling load and dynamic instability index of a curved VAT panel with respect to fiber-angle variation is studied. The analysis is carried out on a VAT panel $[90 \pm \langle T_0|T_1 \rangle]_{2s}$ with radius of curvature $b/R = 0.2$. The variation of K_{cr} with respect to the fiber-angle T_1 for different values of T_0 is shown in Fig. 4.11(a). Each curve is generated by varying T_1 from 0° to 90° with an increment of 5° by considering T_0 as a constant value. Variation of K_{cr} for a straight-fiber laminate ($[\pm\theta]_{2s}$) is also shown in Fig. 4.11(a). From the results, it is clearly

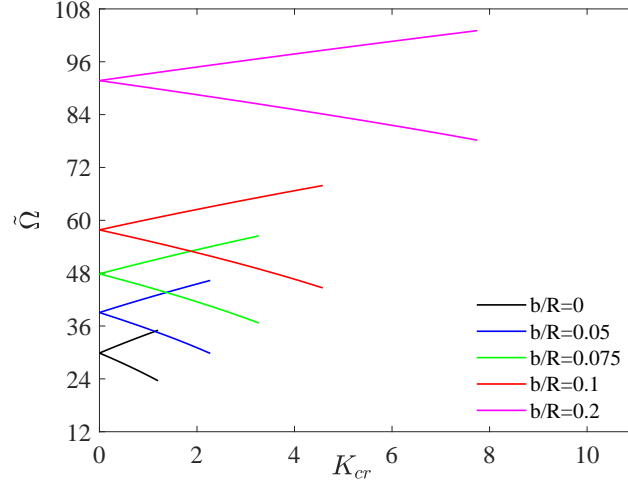


Figure 4.10: Principle DIRs of a curved VAT panel $[90 \pm \langle 0|45 \rangle]_{2s}$ for different b/R ratios.

observed that the K_{cr} value of a VAT panel changes significantly with the fiber-angles (T_0 and T_1). This phenomenon arises due to the variation in the membrane ($\bar{\mathbf{A}}$) and bending ($\bar{\mathbf{D}}$) stiffness of the VAT panel with the linearly varying fiber paths. As shown in previous works [21, 24], on flat VAT laminate, the majority of the applied compression load is redistributed from the center towards the supported edges by the fiber orientation paths. Likewise, in the case of curved VAT panels, the benign load redistribution enables VAT layups to attain high buckling resistance. The load redistribution in curved VAT panels is governed by the fiber-angle variation and the radius of curvature. From Fig. 4.11(a) it is observed that the redistribution of applied compression load from the buckling regions to the supported edges is attained maximum for the fiber-angle $T_0 = 15^\circ$ and then decreases with increase in T_0 from 15° to 90° . Moreover, for a constant T_0 , the normalized critical buckling load first increases with increase in the fiber-angle T_1 and then decreases. In Fig. 4.11(a), among all the straight-fiber laminate configurations, $[\pm 60]_{2s}$ shows maximum normalized critical buckling load value of 7.6. In the case of VAT panels, the highest normalized K_{cr} value is 11.48 for the fiber-angles $T_0 = 15^\circ$ and $T_1 = 60^\circ$. Thus, the VAT panel ($[90 \pm \langle 15|60 \rangle]_{2s}$) exhibits 51% improvement in buckling performance when compared to the optimal straight-fiber laminate ($[\pm 60]_{2s}$). Also, VAT panels with the fiber-angles between $T_0 = 0^\circ$ to 45° shows higher critical buckling load values for a range of $T_1 = 45^\circ$ to 90° , when compared to straight-fiber laminates.

The variation of D_{II} with respect to fiber-angle, T_1 is shown in Fig. 4.11(b). The

results are generated by varying T_1 from 0° to 90° with an increment of 5° for a given value of T_0 . The static and dynamic load parameters are chosen as $\alpha_0 = 0$ and $\alpha_1 = 0.3$ for the analysis. The results clearly show that the variation in the fiber-angle configuration of the VAT panel affects the D_{II} value considerably. From Fig. 4.11(b) it is observed that many of the VAT panel configurations from $T_1 = 40^\circ$ to $T_1 = 90^\circ$ show lower D_{II} values when compared to straight-fiber laminate. The minimum value of D_{II} observed for a straight-fiber laminate is 0.02155 for the layup $[\pm 30]_{2s}$. However, in the case of a VAT panel, the minimum value of D_{II} is found to be 0.0188 for the fiber-angle orientations $T_0 = 0$ and $T_1 = 65^\circ$, and this value is 14% less than the minimum value obtained for optimal straight-fiber laminate configuration. This substantial decrease in D_{II} value occurs because of the increase in critical buckling load and the natural frequency by the linearly varying fiber orientation paths of the VAT panel. This increase in critical buckling and natural frequency reduces the D_{II} value, and this makes the VAT panel dynamically more stable.

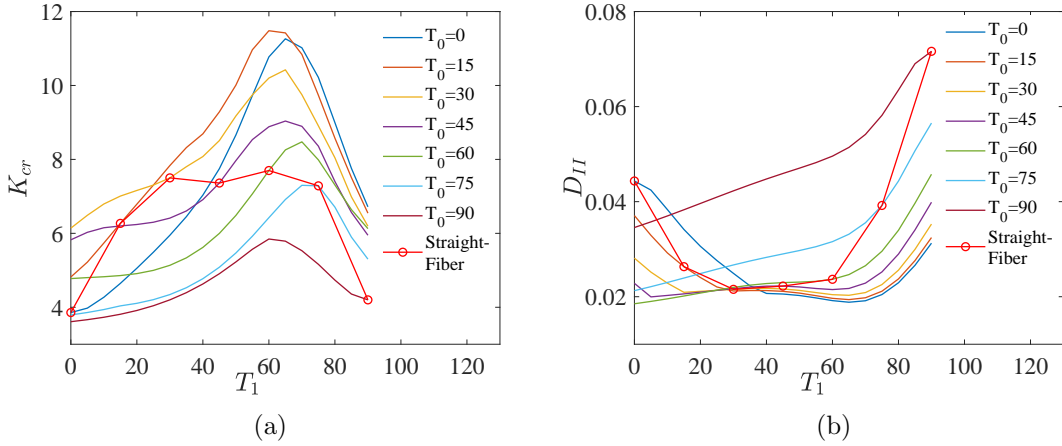


Figure 4.11: Variation of normalized critical buckling load (K_{cr}) and D_{II} for the SSSS curved VAT panel $[90 \pm \langle T_0|T_1 \rangle]_{2s}$ with $b/R = 0.2$ for different fiber orientations, T_0 and T_1 .

A similar analysis is carried out on a curved VAT panel $[90 \pm \langle T_0|T_1 \rangle]_{2s}$ with SCSC (clamped sides and simply-supported ends), CCCC (clamped on all the edges) boundary conditions and the results are shown in Fig. 4.12 and Fig. 4.13, respectively. In the SCSC case, the optimal VAT panel with fiber-angles $T_0 = 15^\circ$ and $T_1 = 65^\circ$ shows 44% higher normalized critical buckling load than the optimal straight-fiber laminate with layup $[\pm 60]_{2s}$. Also, the minimum value of D_{II} observed in the case of a VAT panel is 0.01835 for the fiber-angles $T_0 = 0^\circ$ and $T_1 = 70^\circ$, which is 20% less than

the optimal straight-fiber laminate $[\pm 30]_{2s}$. Whereas, in the case of CCCC boundary condition, a curved VAT panel with configuration $[90 \pm \langle 15|60 \rangle]_{2s}$ shows 43.79% higher normalized critical buckling load value and a VAT panel of $[90 \pm \langle 0|65 \rangle]_{2s}$ shows 9.22% decrease in D_{II} value when compared to the optimal straight-fiber laminate $[\pm 45]_{2s}$. Furthermore, Fig. 4.11, Fig. 4.12 and Fig. 4.13 collectively show that many VAT panel configurations with different fiber-angles exhibit higher buckling resistance and dynamic stability than straight-fiber laminates, thus providing additional freedom in tailoring the stiffness of the laminate. The results clearly demonstrate the advantages and the potential of applying variable angle tow fiber paths to improve the buckling and dynamic performance of a curved VAT panel. As an additional consideration, DIR of a VAT panel with fiber-angle configuration $[90 \pm \langle 0|30 \rangle]_{2s}$ and $b/R = 0.2$ for different boundary conditions (SSSS, SCSC and CCCC) is shown in Fig. 4.14. The static load parameter α_0 is chosen to be zero for the analysis. From Fig. 4.14 it is observed that from SSSS to CCCC the onset of DIR shifts towards higher $\tilde{\Omega}$ and extends towards larger K_{cr} values. This behavior occurs because of the increase in both natural frequency and critical buckling load of the VAT panel under clamped boundary conditions.

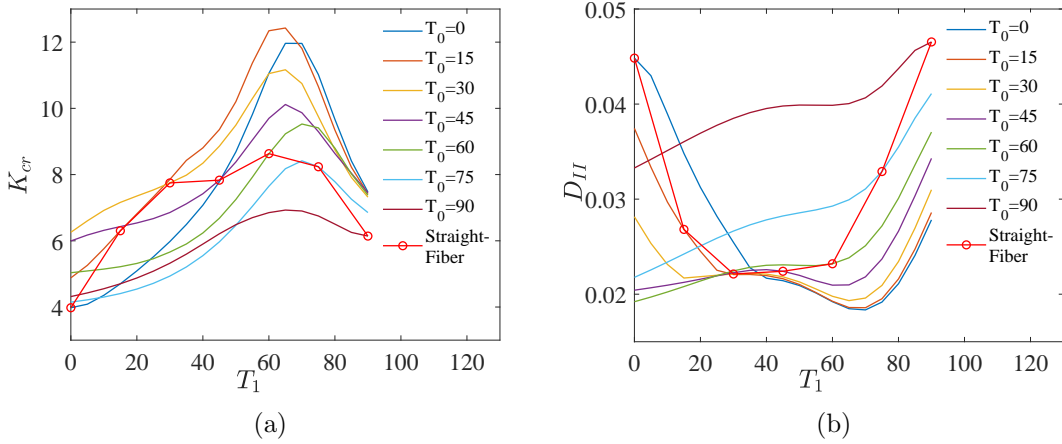


Figure 4.12: Variation of normalized critical buckling load and D_{II} for the SCSC curved VAT panel $[90 \pm \langle T_0|T_1 \rangle]_{2s}$ with $b/R = 0.2$ for different fiber orientations, T_0 and T_1 .

The variation of K_{cr} and D_{II} of a curved VAT panel with respect to the radius of curvature is shown in Fig. 4.15(a). The analysis is carried out on a VAT panel $[90 \pm \langle 0|T_1 \rangle]_{2s}$ for different values of T_1 . In Fig. 4.15(a) each curve is generated by varying the fiber-angle T_1 from 0° to 90° for a particular b/R ratio. From the

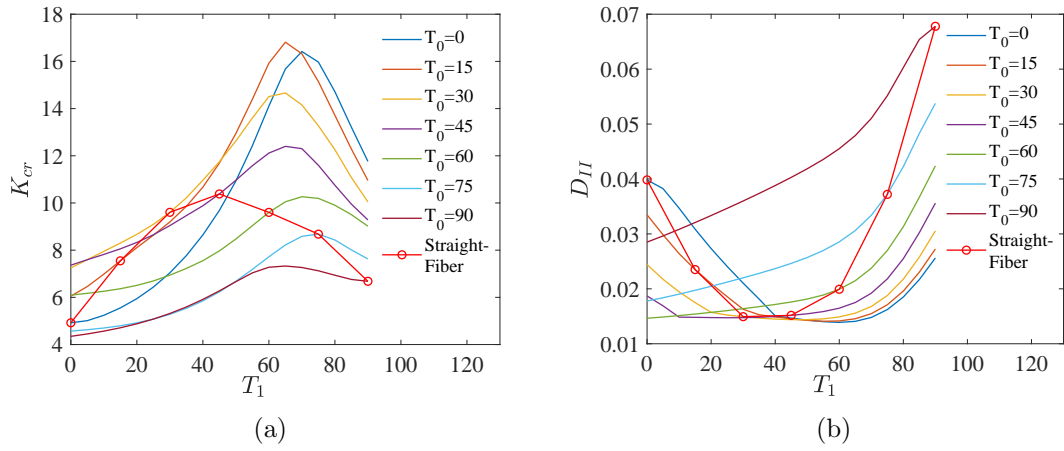


Figure 4.13: Variation of normalized critical buckling load and D_{II} for the CCCC curved VAT panel $[90 \pm \langle T_0|T_1 \rangle]_{2s}$ with $b/R = 0.2$ for different fiber orientations, T_0 and T_1 .

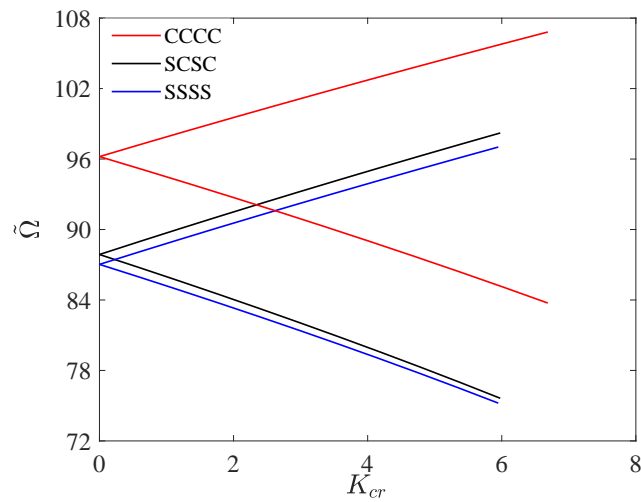


Figure 4.14: Principle DIRs of a curved VAT panel $[90 \pm \langle 0|30 \rangle]_{2s}$ with $b/R = 0.2$ for different boundary conditions (SSSS, SCSC and CCCC).

results, it can be deduced that with an increase in b/R ratio (i.e., decrease in radius of curvature), the critical buckling load increases for all fiber-angle orientations of a VAT panel. For a particular b/R ratio, K_{cr} value increases when the fiber-angle T_1 increases from 0° to 70° and then decreases. This behavior happens because of the redistribution of the in-plane stresses by the fiber paths. This redistribution of stresses from the center of the panel towards the supported edges increases until the fiber-angle T_1 reaches 70° and then decreases. The variation of D_{II} with respect to fiber-angle T_1 is also shown in Fig. 4.15(b). In this case, the value of D_{II} decreases with an increase in b/R ratio (decrease in radius of curvature) of the panel and clearly indicates that the buckling phenomenon governs the dynamic stability of a VAT panel.

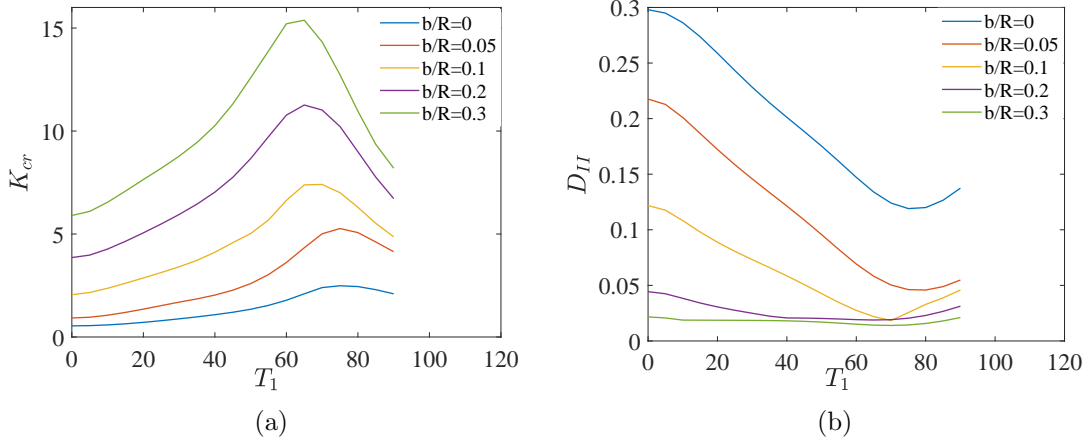


Figure 4.15: Variation of K_{cr} and D_{II} for a SSSS VAT panel $[90 \pm \langle 0|T_1 \rangle]_{2s}$ with respect to T_1 for different values of b/R ratios.

Finally, the variation of K_{cr} with respect to the fiber-angle T_1 , for different aspect ratios (a/b) is studied. The analysis is done on a VAT panel $[90 \pm \langle 0|T_1 \rangle]_{2s}$ for different values of a/b ratio (0.5, 1.0, 2.0, 3.0) by varying fiber-angle T_1 from 0° to 90° . The analysis is carried out by fixing the width ($b = 100 \times 10^{-3}$ m) and varying the length of the panel. The radius of curvature of the panel is taken as ($b/R = 0.2$), and the results are shown in Fig. 4.16. From the results, it is observed that with the increase in a/b ratio, normalized critical buckling load of the VAT panel increases significantly for all fiber-angle configurations. For a particular value of a/b ratio the value of K_{cr} increases when the fiber-angle T_1 increases from 0° to 70° and then decreases. DIRs of a VAT panel $[90 \pm \langle 0|45 \rangle]_{2s}$ for different values of a/b ratio is shown in Fig. 4.17(a). It can be seen from the figure that with an increase in a/b ratio DIR shifts to the

higher parametric frequency and extends to larger K_{cr} value, indicating an increase in critical buckling load and natural frequency of the VAT panel. Also, the width of DIR shrinks with the increase in a/b ratio, illustrating the increase in dynamic stability of the panel. The variation of D_{II} with respect to the fiber-angle T_1 for different a/b ratios is shown in Fig. 4.17(b). As expected, the D_{II} value of a VAT panel decreases with an increase in a/b ratio, because of the increase in critical buckling load and natural frequency of the panel.

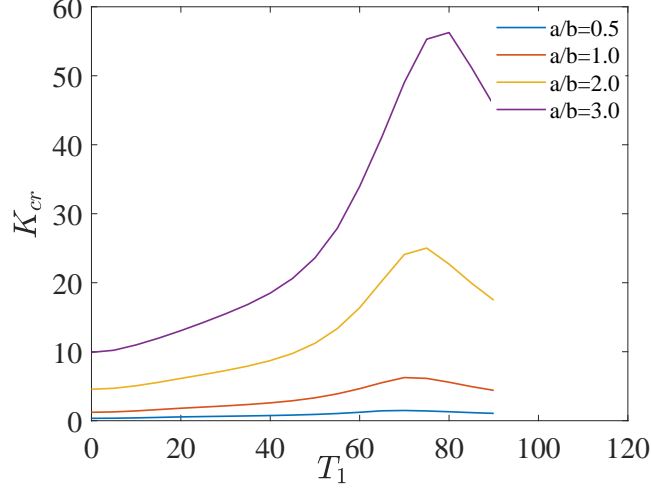


Figure 4.16: Variation of K_{cr} of a curved VAT panel $[90 \pm \langle 0|T_1 \rangle]_{2s}$ with respect to T_1 for different values of a/b ratios.

From all results presented, it is clearly observed that the curved panel with VAT laminate for some fiber-angle configurations shows better buckling and dynamic performance when compared to conventional optimal straight-fiber laminate. Moreover, the steering of fiber orientation over the curved lamina provides an added advantage to the designer by allowing more scope for tailoring K_{cr} , D_{II} and stiffness of the VAT laminate simultaneously.

4.5 Summary

In this work, the dynamic stability behavior of a curved panel with VAT laminate subjected to periodic axial compression load has been studied. Donnell's shallow shell theory was used to model the curved VAT panel and solved using the generalized differential integral quadrature method. Bolotin's first-order approximation was used to determine the dynamic instability region of a curved VAT panel. Initially, the

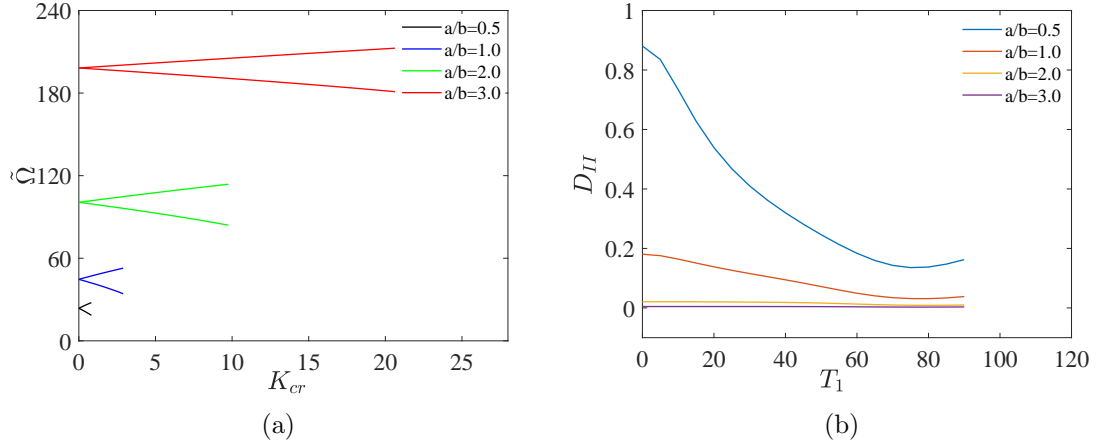


Figure 4.17: Variation of Principle DIRs and D_{II} of a curved VAT panel $[90 \pm (0|T_1)]_{2s}$ with respect to T_1 for different values of a/b ratios.

effect of tow steering on buckling and dynamic stability behavior of a curved VAT panel for three different types of boundary conditions is studied. It is observed that the fiber-angle variation has a significant effect on critical buckling load as well as the dynamic stability of the curved VAT panel. For some fiber-angle configurations, curved VAT panel shows much higher critical buckling load and dynamic stability than straight-fiber laminates. This improvement in the performance of a curved VAT panel is because of the redistribution of the applied load from the center of the panel towards the supported edges by the curvilinear fiber paths.

In addition, the influence of the radius of curvature on the behavior of a curved VAT panel has been presented. It is observed that the critical buckling load and dynamic stability increases with the decrease in the radius of curvature of a curved VAT panel irrespective of the fiber-angle configurations. Also, with the increase in the aspect ratio, buckling, and dynamic performance of a curved VAT panel improves. From this study, the benefits of fiber steering in improving the buckling and dynamic behavior of a curved VAT panel has been demonstrated.

Chapter 5

Implicit Floquet analysis for parametric instabilities in a VAT composite panel

In the previous chapters, Bolotin's approach has been used to determine the dynamic instability regions in a VAT panel. Bolotin's approach [49] was introduced in 1965 by V. V. Bolotin and been extensively used in the literature to determine the instability regions in a structure under in-plane periodic loads. An extensive bibliography of earlier works on dynamic instability is given in some review papers. [78, 79]. In Bolotin's theory, it was shown that the solutions of governing equations on the stability boundary are time-periodic. Therefore, a Fourier series is employed to approximate the solutions, and the instability boundary is obtained using an eigenvalue approach. Since the Fourier expansion has infinite terms and it is difficult to deal with an infinite series, the series is truncated to the finite number of terms. In the literature, a first-order approximation (considers only one term in the series) has often been used to determine the dynamic instability boundaries of structures. A number of researchers [56, 57, 64, 83, 106, 116–118] have investigated the dynamic stability characteristics of various composite structures using Bolotin's first-order approximation. However, Moorthy et al. [58], Srinivasan and Chellapandi [55], Chattopadhyay and Radu [63], and Partha and Singha [119] have studied the effect of both first and second-order approximations, on the dynamic instability boundaries of rectangular composite plates. Significant deviations in the stability charts were observed between first and second-order Bolotin's approximations. Moreover, because of the truncation of the Fourier series expansion to a finite number of terms, the solution boundary obtained from Bolotin's approach is erroneous. To overcome this problem,

Floquet theory can be used to determine the stability boundary of a system instead of Bolotin's approach.

In the Floquet theory, the stability of a first-order time-periodic system is determined by constructing a Floquet transition matrix (FTM). This matrix relates all the states of a system at a given instant to the same states after one time-period. The eigenvalues of the FTM (which are known as Floquet multipliers) can be used to determine the stability of the system. To obtain the FTM, the equations for the time-periodic system has to be integrated over the time period for a set of linearly independent initial conditions. This approach has been widely used for the assessment of the stability of the systems with periodic coefficients [120]. However, the application of Floquet theory is limited to systems with fewer degrees of freedom. To construct the FTM for a periodic system of size N , the system has to be integrated N times with independent initial conditions. Therefore, to determine the stability of systems with large degrees of freedom, the application of Floquet theory becomes computationally overwhelming. In the analysis of plate, shell or any continuous structures where finite element method (FEM), Rayleigh–Ritz or differential quadrature method (DQM) are used, results in a system with a very large number of degrees of freedom. Therefore, obtaining a dynamic stability boundary using Floquet theory for such systems is computationally prohibitive. However, with emerging massive parallel computer architectures, the transition matrix can be computed by distributing the linearly independent integration operations among the independent processors. This process reduces the computational time, but cannot reduce the computational cost that would be required to calculate the FTM. Bauchau and Nikishkov [121] used implicit Floquet analysis for the first time to determine the stability of a rotor-craft without explicit computation of the FTM, which reduces the computational cost and time, simultaneously. In their work, they used the Arnoldi algorithm to determine the eigenvalues of the FTM. However, it appears that no work has been reported to determine the dynamic stability characteristics of the composite panels using implicit Floquet analysis.

In this chapter, dynamic instability regions in a variable angle tow (VAT) composite panel subjected to in-plane compression load is determined using Floquet theory combined with the Arnoldi algorithm. The generalized differential integral quadrature method (GDIQM) combined with the Rayleigh–Ritz procedure is used for the analysis of the VAT panel. The dynamic instability boundaries for the VAT panels are then determined using implicit Floquet method and Bolotin's approach. The variation in instability boundaries obtained from the Bolotin's approach and Floquet

theory has been investigated. The exactness of the obtained stability boundaries are then verified with the time response of the VAT panel, which is obtained using numerical integration. Structural damping has been included in the present model, and we studied the effect of damping on the dynamic behavior of the VAT panel. Further, the spectral radius variation in the parameter space, bifurcation analysis, and stability charts for both undamped and damped VAT panels are reported.

5.1 Modeling of the VAT panel

In this work, a VAT panel shown in Fig. 5.1 is considered for the analysis. The thickness of the panel is assumed to be small for the present analyses, and therefore the shear deformation of the panel's section in $x - z$ and $y - z$ planes are neglected. Using classical laminate plate theory (CLPT) [122], the mid-plane strains ($\boldsymbol{\epsilon}$) and curvatures ($\boldsymbol{\kappa}$) of the panel can be written as:

$$\begin{aligned}\boldsymbol{\epsilon} &= \left[\frac{\partial u}{\partial x}, \frac{\partial v}{\partial y}, \left(\frac{\partial u}{\partial y} + \frac{\partial v}{\partial x} \right) \right]^T, \\ \boldsymbol{\kappa} &= - \left[\frac{\partial^2 w}{\partial x^2}, \frac{\partial^2 w}{\partial y^2}, 2 \frac{\partial^2 w}{\partial x \partial y} \right]^T.\end{aligned}\tag{5.1}$$

Here, u , v , and w are the mid-plane displacement fields which correspond to x , y , and z directions, respectively. In VAT panels, the constitutive relationship is written as:

$$\begin{Bmatrix} \bar{\mathbf{N}} \\ \bar{\mathbf{M}} \end{Bmatrix} = \begin{bmatrix} \bar{\mathbf{A}}(x, y) & \bar{\mathbf{B}}(x, y) \\ \bar{\mathbf{B}}^T(x, y) & \bar{\mathbf{D}}(x, y) \end{bmatrix} \begin{Bmatrix} \boldsymbol{\epsilon} \\ \boldsymbol{\kappa} \end{Bmatrix}.\tag{5.2}$$

Here, $\bar{\mathbf{N}} = [\bar{N}_x, \bar{N}_y, \bar{N}_{xy}]^T$, $\bar{\mathbf{M}} = [\bar{M}_x, \bar{M}_y, \bar{M}_{xy}]^T$ are the membrane stress resultant and the bending moment resultant vectors, respectively. In VAT panels, as a result of the varying fiber-angle, the matrices $\bar{\mathbf{A}}$ (in-plane stiffness matrix), $\bar{\mathbf{B}}$ (coupling stiffness matrix), and $\bar{\mathbf{D}}$ (bending stiffness matrix) are not constant as in the case of straight-fiber laminate, but are functions of spatial coordinates x and y .

The strain energy stored in the VAT laminate subjected to uniform axial compression (\bar{u}_0) along the edges (neglecting higher-order terms) is written as [106]:

$$U = \frac{1}{2} \int_{\mathcal{A}} [\boldsymbol{\epsilon}^T \bar{\mathbf{A}} \boldsymbol{\epsilon} + \boldsymbol{\kappa}^T \bar{\mathbf{D}} \boldsymbol{\kappa}] d\mathcal{A} + \int_{\mathcal{A}} [\boldsymbol{\epsilon}_L^T \bar{\mathbf{T}} \boldsymbol{\epsilon}_L] d\mathcal{A}.\tag{5.3}$$

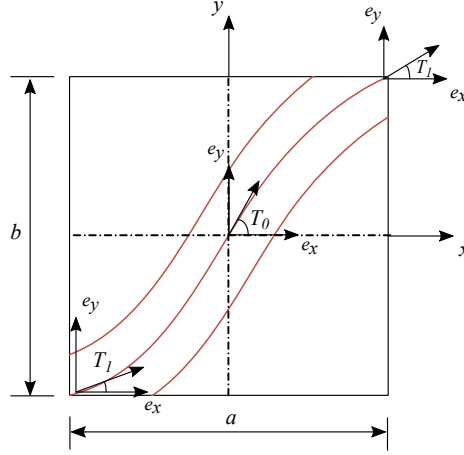


Figure 5.1: Schematic representation of a VAT lamina.

Here, $\bar{\mathbf{T}}$ and ϵ_L are defined as follows:

$$\bar{\mathbf{T}} = \begin{bmatrix} \bar{N}_x & \bar{N}_{xy} \\ \bar{N}_{xy} & \bar{N}_y \end{bmatrix}; \quad \epsilon_L = \left[\frac{\partial w}{\partial x}, \frac{\partial w}{\partial y} \right]^T. \quad (5.4)$$

The kinetic energy for the plate element can be written as:

$$T_{KE} = \frac{1}{2} \int_{\mathcal{A}} \rho [h(\dot{u}^2 + \dot{v}^2 + \dot{w}^2)] d\mathcal{A}, \quad (5.5)$$

where, ρ is the density, and h is the thickness of the panel. In this work, the strain energy functional of a VAT panel (Eq. (5.3)) is solved using the Rayleigh–Ritz method combined with GDIQM. The governing equations of motions for the VAT panel with damping subjected to in-plane periodic compression load is written as follows:

$$\mathbf{M}\ddot{\mathbf{u}} + \mathbf{C}\dot{\mathbf{u}} + \mathbf{K}\mathbf{u} - (\alpha_0 P_{cr} + \alpha_1 P_{cr} \cos(\Omega t)) \mathbf{K}_G \mathbf{u} = 0. \quad (5.6)$$

Here, \mathbf{M} is the mass matrix, \mathbf{K} represents the structural stiffness matrix, P_{cr} is the critical buckling load of the VAT panel, Ω is the excitation frequency and α_0 , α_1 are the static and dynamic load parameters, respectively. The damping matrix \mathbf{C} is added to the system to include the energy dissipation and is assumed to be a mass proportional damping which is given by [58]:

$$\mathbf{C} = \beta \mathbf{M}. \quad (5.7)$$

Here, β is the damping coefficient. In the following subsections, the application of the GDIQM approach to the governing equation (Eq. (5.3)) for the pre-buckling, buckling, and modal analyses are discussed.

5.1.1 Pre-buckling analysis

In the pre-buckling analysis of a VAT panel subjected to uniform axial compression load, GDIQM is applied to the first term of the strain-energy functional (Eq. (5.3)), and we obtained the following governing equations:

$$\begin{bmatrix} \mathbf{K}_{uu} & \mathbf{K}_{uv} & \mathbf{0} \\ \mathbf{K}_{uv} & \mathbf{K}_{vv} & \mathbf{0} \\ \mathbf{0} & \mathbf{0} & \mathbf{K}_{ww} \end{bmatrix} \begin{Bmatrix} \mathbf{u} \\ \mathbf{v} \\ \mathbf{w} \end{Bmatrix} = \begin{Bmatrix} \mathbf{F}_u \\ \mathbf{F}_v \\ \mathbf{F}_w \end{Bmatrix}. \quad (5.8)$$

Equation (5.8) can be written in compact form as:

$$\mathbf{K}_s \bar{\mathbf{u}} = \mathbf{F}. \quad (5.9)$$

Here, the vector $\bar{\mathbf{u}}$ represents the panel mid-plane displacement variables, and \mathbf{F} vector represents the forces applied along x , y , and z directions, respectively. The expansion of the terms in matrix \mathbf{K}_s in Eq. (5.8) are expressed in GDIQM form as

follows:

$$\begin{aligned}
\mathbf{K}_{uu} &= \int_{\mathcal{A}} \left[\frac{\partial'}{\partial x} A_{11} \frac{\partial}{\partial x} + \frac{\partial'}{\partial y} A_{16} \frac{\partial}{\partial x} + \frac{\partial'}{\partial x} A_{16} \frac{\partial}{\partial y} + \frac{\partial'}{\partial y} A_{66} \frac{\partial}{\partial y} \right] d\mathcal{A} \\
&= A_{11} \mathbf{T}^{x'} \mathbf{S} \mathbf{T}^x + A_{16} \mathbf{T}^{y'} \mathbf{S} \mathbf{T}^x + A_{16} \mathbf{T}^{x'} \mathbf{S} \mathbf{T}^y + A_{66} \mathbf{T}^{y'} \mathbf{S} \mathbf{T}^y \\
\mathbf{K}_{uv} &= \int_{\mathcal{A}} \left[\frac{\partial'}{\partial x} A_{12} \frac{\partial}{\partial y} + \frac{\partial'}{\partial y} A_{26} \frac{\partial}{\partial y} + \frac{\partial'}{\partial x} A_{16} \frac{\partial}{\partial x} + \frac{\partial'}{\partial y} A_{66} \frac{\partial}{\partial x} \right] d\mathcal{A} \\
&= A_{12} \mathbf{T}^{x'} \mathbf{S} \mathbf{T}^y + A_{26} \mathbf{T}^{y'} \mathbf{S} \mathbf{T}^y + A_{16} \mathbf{T}^{x'} \mathbf{S} \mathbf{T}^x + A_{66} \mathbf{T}^{y'} \mathbf{S} \mathbf{T}^x \\
\mathbf{K}_{vv} &= \int_{\mathcal{A}} \left[\frac{\partial'}{\partial y} A_{22} \frac{\partial}{\partial y} + \frac{\partial'}{\partial x} A_{26} \frac{\partial}{\partial y} + \frac{\partial'}{\partial y} A_{26} \frac{\partial}{\partial x} + \frac{\partial'}{\partial x} A_{66} \frac{\partial}{\partial x} \right] d\mathcal{A} \\
&= A_{22} \mathbf{T}^{y'} \mathbf{S} \mathbf{T}^y + A_{26} \mathbf{T}^{x'} \mathbf{S} \mathbf{T}^y + A_{26} \mathbf{T}^{y'} \mathbf{S} \mathbf{T}^x + A_{66} \mathbf{T}^{x'} \mathbf{S} \mathbf{T}^x \\
\mathbf{K}_{ww} &= \int_{\mathcal{A}} \left[\frac{\partial'^2}{\partial x^2} D_{11} \frac{\partial^2}{\partial x^2} + \frac{\partial'^2}{\partial y^2} D_{12} \frac{\partial^2}{\partial x^2} + 2 \frac{\partial'^2}{\partial x \partial y} D_{16} \frac{\partial^2}{\partial x^2} \right. \\
&\quad + \frac{\partial'^2}{\partial x^2} D_{12} \frac{\partial^2}{\partial y^2} + \frac{\partial'^2}{\partial y^2} D_{22} \frac{\partial^2}{\partial y^2} + 2 \frac{\partial'^2}{\partial x \partial y} D_{26} \frac{\partial^2}{\partial y^2} \\
&\quad \left. + 2 \frac{\partial'^2}{\partial x^2} D_{16} \frac{\partial^2}{\partial x \partial y} + 2 \frac{\partial'^2}{\partial y^2} D_{26} \frac{\partial^2}{\partial x \partial y} + 4 \frac{\partial'^2}{\partial x \partial y} D_{66} \frac{\partial^2}{\partial x \partial y} \right] d\mathcal{A} \\
&= D_{11} \mathbf{T}^{xx'} \mathbf{S} \mathbf{T}^{xx} + D_{12} \mathbf{T}^{yy'} \mathbf{S} \mathbf{T}^{xx} + 2D_{16} \mathbf{T}^{xy'} \mathbf{S} \mathbf{T}^{xx} \\
&\quad + D_{12} \mathbf{T}^{xx'} \mathbf{S} \mathbf{T}^{yy} + D_{22} \mathbf{T}^{yy'} \mathbf{S} \mathbf{T}^{yy} + 2D_{26} \mathbf{T}^{xy'} \mathbf{S} \mathbf{T}^{yy} \\
&\quad + 2D_{16} \mathbf{T}^{xx'} \mathbf{S} \mathbf{T}^{xy} + 2D_{26} \mathbf{T}^{yy'} \mathbf{S} \mathbf{T}^{xy} + 4D_{66} \mathbf{T}^{xy'} \mathbf{S} \mathbf{T}^{xy}
\end{aligned} \tag{5.10}$$

Here, $(\)'$ represents the transpose of a given matrix. \mathbf{T}^{xx} , \mathbf{T}^{yy} , and \mathbf{T}^{xy} represents the second-order derivative weighting coefficient matrices (see Chapter 4 for reference).

The pre-buckling analysis on a VAT panel is carried out by applying a uniform compression load along one edge of the panel ($x = a/2$) and by considering the in-plane boundary conditions as: $u = v = 0$ at $x = -a/2$ and $v = 0$ at $x = a/2$, while leaving the transverse edges free to deform. To apply the uniform displacement constraint, we followed a multi-point constraint approach, where, all the nodes on the loading edge are first connected, and an equivalent compression force (f_c) is applied on the control node point. These uniform displacement conditions can be written as an additional constraint equations as: $u_{slave} - u_{control} = 0$. By writing the constraint equations in the matrix form as $\mathbf{K}_c \bar{\mathbf{u}} = 0$, and adding them to Eq. (5.9), the final

stiffness matrix will be obtained as:

$$\mathbf{K} = \begin{bmatrix} \mathbf{K}_s & \mathbf{K}'_c \\ \mathbf{K}_c & \mathbf{0} \end{bmatrix}. \quad (5.11)$$

Upon solving the $\mathbf{K}\bar{\mathbf{u}} = \mathbf{F}$ for the displacement vector ($\bar{\mathbf{u}}$), the in-plane stress resultants can be evaluated from the Eqs. (5.1) and (5.2).

5.1.2 Buckling analysis

On applying GDIQM to the strain energy equation (Eq. (5.3)) of a VAT panel subjected to uniform compression load, the following eigenvalue problem will be obtained:

$$[\mathbf{K} - P_{cr}\mathbf{K}_G] \bar{\mathbf{u}} = 0, \quad (5.12)$$

where,

$$\begin{aligned} \mathbf{K}_G &= \int_{\mathcal{A}} \left[\frac{\partial'}{\partial x} \bar{N}_x \frac{\partial}{\partial x} + \frac{\partial'}{\partial y} \bar{N}_y \frac{\partial}{\partial y} + 2 \frac{\partial'}{\partial x} \bar{N}_{xy} \frac{\partial}{\partial y} \right] d\mathcal{A} \\ &= \bar{N}_x \mathbf{T}^{x'} \mathbf{S} \mathbf{T}^x + \bar{N}_y \mathbf{T}^{y'} \mathbf{S} \mathbf{T}^y + 2 \bar{N}_{xy} \mathbf{T}^{x'} \mathbf{S} \mathbf{T}^y. \end{aligned} \quad (5.13)$$

Here, \mathbf{K}_G represents the geometric stiffness matrix. \bar{N}_x , \bar{N}_y and \bar{N}_{xy} represents in-plane stress resultants obtained from the pre-buckling analysis of the VAT panel.

5.1.3 Modal analysis

The modal analysis of a VAT panel can be carried out using the following generalized eigenvalue equation:

$$[\omega^2 \mathbf{M} + \mathbf{K}] \mathbf{w} = 0. \quad (5.14)$$

Here, ω is the natural frequency and \mathbf{w} represents the mode shape of the VAT panel. \mathbf{M} is the mass matrix and can be obtained from the kinetic energy expression of a VAT panel obtained in Eq. (5.5) On applying GDIQM to Eq. (5.5), the mass matrix

for the panel can be written as:

$$\mathbf{M} = \rho \begin{bmatrix} h\mathbf{S} & 0 & 0 \\ 0 & h\mathbf{S} & 0 \\ 0 & 0 & h\mathbf{S} \end{bmatrix}. \quad (5.15)$$

5.1.4 Boundary conditions

In order to carry out the analysis, the corresponding plate boundary conditions have to be specified along the edges. In this work, simply-supported boundary conditions have been used for all the analysis i.e., $w = 0$, at all the edges corresponding to the locations $x = \{-a/2, a/2\}$ and $y = \{-b/2, b/2\}$. Equations (5.12) and (5.14) are solved along with the plate boundary conditions to obtain the critical buckling load (P_{cr}) and natural frequencies (ω) of the VAT panel, respectively.

The obtained \mathbf{M} , \mathbf{K} , \mathbf{K}_G and P_{cr} from the pre-buckling, buckling and kinetic energy expressions, will be used to determine the dynamic instability regions (DIRs) in a VAT panel from the equations of motion given by Eq. (5.6). The detailed procedure for determining the DIRs in VAT panels using Bolotin's approach and Floquet theory is explained in the following sections.

5.2 Dynamic instability using Bolotin's approach

When a VAT composite panel is subjected to in-plane periodic compression load of the form $P(t) = \alpha_0 P_{cr} + \alpha_1 P_{cr} \cos(\Omega t)$, (governed by Eq. (5.6)) for certain combinations of α_0 , α_1 and Ω , the response of the panel becomes unbounded due to parametric resonance. The region in the parametric space, where the dynamic instability occurs is known as the DIR. According to Bolotin's theory, the solutions of Eq. (5.6) on the stability boundary (boundary separating stable and unstable regions) are periodic with period $T_1 = 2\pi/\Omega$ or $T_2 = 4\pi/\Omega$. Therefore, the solutions of the Eq. (5.6) can be expanded as:

$$\bar{\mathbf{u}} = \sum_{k=1,3,5}^{\infty} (\mathbf{a}_k \sin(k\Omega t/2) + \mathbf{b}_k \cos(k\Omega t/2)), \quad (5.16)$$

$$\bar{\mathbf{u}} = \frac{1}{2} \mathbf{b}_0 + \sum_{k=2,4,6}^{\infty} (\mathbf{a}_k \sin(k\Omega t/2) + \mathbf{b}_k \cos(k\Omega t/2)). \quad (5.17)$$

The coefficients \mathbf{a}_k , \mathbf{b}_k in Eq. (5.16) and Eq. (5.17) are unknowns and are infinite in number. As it is difficult to deal with an infinite number of coefficients, only a

few terms are considered in the approximate solution. In the literature, a first-order approximation was often used to determine the approximate stability boundaries of the system [58, 64, 70]. In a first-order Bolotin's approximation, only the first term is considered in Eq. (5.16) and Eq. (5.17), therefore we get:

$$\bar{\mathbf{u}} = \mathbf{a}_1 \sin(\Omega t/2) + \mathbf{b}_1 \cos(\Omega t/2), \quad (5.18)$$

$$\bar{\mathbf{u}} = \frac{1}{2}\mathbf{b}_0 + \mathbf{a}_2 \sin(\Omega t) + \mathbf{b}_2 \cos(\Omega t). \quad (5.19)$$

On substituting, Eq. (5.18) and Eq. (5.19) in Eq. (5.6), residual equations will be obtained. In the residual equations, coefficients of $\sin(\Omega t)$, $\cos(\Omega t)$, $\sin(\Omega t/2)$, $\cos(\Omega t/2)$, and the constant term must vanish. This results in the following homogeneous linear algebraic equations:

$$\begin{bmatrix} \mathbf{K} - (\alpha_0 - \frac{1}{2}\alpha_1) P_{cr}\mathbf{K}_G - \frac{\Omega^2}{4}\mathbf{M} & -\frac{1}{2}\Omega\mathbf{C} \\ \frac{1}{2}\Omega\mathbf{C} & \mathbf{K} - (\alpha_0 + \frac{1}{2}\alpha_1) P_{cr}\mathbf{K}_G - \frac{\Omega^2}{4}\mathbf{M} \end{bmatrix} \begin{Bmatrix} \mathbf{a}_1 \\ \mathbf{b}_1 \end{Bmatrix} = 0, \quad (5.20)$$

$$\begin{bmatrix} \frac{1}{2}\mathbf{K} - \frac{1}{2}\alpha_0 P_{cr}\mathbf{K}_G & \mathbf{0} & -\frac{1}{2}\alpha_1 P_{cr}\mathbf{K}_G \\ \mathbf{0} & \mathbf{K} - \alpha_0 P_{cr}\mathbf{K}_G - \Omega^2\mathbf{M} & -\Omega\mathbf{C} \\ -\frac{1}{2}\alpha_1 P_{cr}\mathbf{K}_G & \Omega\mathbf{C} & \mathbf{K} - \alpha_0 P_{cr}\mathbf{K}_G - \Omega^2\mathbf{M} \end{bmatrix} \begin{Bmatrix} b_0 \\ a_2 \\ b_2 \end{Bmatrix} = 0. \quad (5.21)$$

Equations (5.20) and (5.21) can be written in the form of a quadratic eigenvalue problem as follows:

$$(\Omega^2\mathbf{M}_E^i + \Omega\mathbf{C}_E^i + \mathbf{K}_E^i)\mathbf{q}^i = 0, \quad i = 1, 2 \quad (5.22)$$

where,

$$\mathbf{q}^1 = [a_1, b_1]^T; \quad \mathbf{M}_E^1 = \frac{1}{4} \begin{bmatrix} \mathbf{M} & \mathbf{0} \\ \mathbf{0} & \mathbf{M} \end{bmatrix}; \quad \mathbf{C}_E^1 = \frac{1}{2} \begin{bmatrix} \mathbf{0} & \mathbf{C} \\ -\mathbf{C} & \mathbf{0} \end{bmatrix};$$

$$\mathbf{K}_E^1 = - \begin{bmatrix} \mathbf{K} - (\alpha_0 - \frac{1}{2}\alpha_1) P_{cr}\mathbf{K}_G & \mathbf{0} \\ \mathbf{0} & \mathbf{K} - (\alpha_0 + \frac{1}{2}\alpha_1) P_{cr}\mathbf{K}_G \end{bmatrix} \quad (5.23)$$

and

$$\mathbf{q}^2 = [b_0, a_2, b_2]^T; \quad \mathbf{M}_E^2 = \begin{bmatrix} \mathbf{0} & \mathbf{0} & \mathbf{0} \\ \mathbf{0} & \mathbf{M} & \mathbf{0} \\ \mathbf{0} & \mathbf{0} & \mathbf{M} \end{bmatrix}; \quad \mathbf{C}_E^2 = \begin{bmatrix} \mathbf{0} & \mathbf{0} & \mathbf{0} \\ \mathbf{0} & \mathbf{0} & \mathbf{C} \\ \mathbf{0} & -\mathbf{C} & \mathbf{0} \end{bmatrix};$$

$$\mathbf{K}_E^2 = - \begin{bmatrix} \frac{1}{2}\mathbf{K} - \frac{1}{2}\alpha_0 P_{cr} \mathbf{K}_G & \mathbf{0} & -\frac{1}{2}\alpha_1 P_{cr} \mathbf{K}_G \\ \mathbf{0} & \mathbf{K} - \alpha_0 P_{cr} \mathbf{K}_G & \mathbf{0} \\ -\frac{1}{2}\alpha_1 P_{cr} \mathbf{K}_G & \mathbf{0} & \mathbf{K} - \alpha_0 P_{cr} \mathbf{K}_G \end{bmatrix} \quad (5.24)$$

Upon using the standard linearization approach [123], Eq. (5.22) can be expressed as a generalized eigenvalue problems as follows:

$$(\mathbf{A}^i - \Omega \mathbf{B}^i) \mathbf{r} = 0, \quad i = 1, 2 \quad (5.25)$$

where,

$$\mathbf{r} = [\Omega \mathbf{q}, \mathbf{q}]^T; \quad \mathbf{A}^i = \begin{bmatrix} \mathbf{0} & -\mathbf{K}_E^i \\ \mathbf{M}_E^i & \mathbf{0} \end{bmatrix}; \quad \mathbf{B}^i = \begin{bmatrix} \mathbf{M}_E^i & \mathbf{C}_E^i \\ \mathbf{0} & \mathbf{M}_E^i \end{bmatrix} \quad (5.26)$$

The eigenvalues of Eq. (5.25) represent the excitation frequencies that define the boundary between the stable and unstable regions of the damped VAT panel. For $i = 1$ in Eq. (5.25), the obtained eigenvalues represent the boundaries of the first instability region, and for $i = 2$, the solution represents the boundaries of the second instability region. The solution boundaries obtained from Eq. (5.25) are a first-order approximation, as only one term from the infinite series (Eqs. (5.16)-(5.17)) is considered for the series solution. Higher-order approximations can be evaluated by considering more number of terms in the series solution and following the same procedure as explained to get better approximations [49, 63]. However, for a system with a large number of degrees of freedom, considering more number of terms in the solution expansion (Eqs. (5.16)-(5.17)), results in an increase in the size of the matrix and evaluation of eigenvalue become complex. Since we use only a limited number of terms in Eqs. (5.16)-(5.17), the instability boundaries obtained are inaccurate and over-predicts the instability in the system. To overcome these problems, the Floquet

theory can be used to determine the exact stability boundaries of a system. The detailed procedure for determining the dynamic instability behavior of a periodic system using Floquet theory is explained in the next section.

5.3 Floquet theory

Floquet theory is used to determine the stability of a system of differential equations with periodic coefficients. For example, consider a system of N_p differential equations with periodic coefficients as follow:

$$\dot{\mathbf{X}} = \mathbf{A}(t)\mathbf{X}, \quad (5.27)$$

Here, $\mathbf{A}(t + T) = \mathbf{A}(t)$ is a periodic matrix with time period T . Let $\Psi(t)$ be a fundamental solution matrix of Eq. (5.27), and therefore it has to obey:

$$\dot{\Psi}(t) = \mathbf{A}(t)\Psi(t). \quad (5.28)$$

Since, $\mathbf{A}(t)$ is a periodic matrix, from Eqs. (5.27) and (5.28), it is clear that:

$$\dot{\Psi}(t + T) = \mathbf{A}(t + T)\Psi(t + T) = \mathbf{A}(t)\Psi(t + T). \quad (5.29)$$

Therefore, $\Psi(t + T)$ is also a fundamental matrix solution of the system Eq. (5.27). From the property of linearity it can be shown that the two fundamental matrices, $\Psi(t + T)$ and $\Psi(t)$ are uniquely dependent. The FTM denoted as $\Phi(0, T)$ relates the states of a system at 0 and T as follows:

$$\mathbf{X}(T) = \Phi(0, T)\mathbf{X}(0). \quad (5.30)$$

From Eq. (5.28), the same relationship will also hold for the fundamental solution:

$$\Psi(T) = \Phi(0, T)\Psi(0). \quad (5.31)$$

Therefore, integrating the system $\dot{\Psi}(t) = \mathbf{A}(t)\Psi(t)$ from $t = 0$ to $t = T$ with the initial condition of $\Psi(0) = \mathbf{I}$ (identity matrix), yields the FTM $\Phi = \Psi(T)$. Then the Floquet multiplier (μ) can be obtained from eigenvalues of the FTM (Φ) and can be used to determine the stability of the system. If and only if all the Floquet multipliers (μ) of the FTM are less than 1, i.e., $|\mu| < 1$, then the system is stable. Even if one of the multipliers is greater than 1, i.e., $|\mu| > 1$, then the system becomes unstable.

Therefore, Floquet theory can be used to determine the stability of the system with periodic coefficients. However, upon using Floquet theory, evaluation of the FTM requires one integration of the system of equations over the entire time period for each state of the system. With the increase in the number of degrees of freedom of the system, the computational effort needed in calculating the Floquet multipliers becomes prohibitive. Therefore, using Floquet theory to predict the stability of large systems is computationally demanding. To overcome the issue, the Arnoldi algorithm is combined with the Floquet theory to determine the stability of large degree of freedom systems in very few integrations $j \ll N_p$, without explicit computation of the FTM.

5.4 Arnoldi algorithm

In this section, the Arnoldi algorithm, which can be used to determine the eigenvalues of the FTM (Floquet multipliers (μ)), $\Phi \in \mathbb{R}^{N_p \times N_p}$ is discussed. Following the review of [121, 124] a brief overview of the algorithm is discussed in this section. The detailed mathematical formulation of the algorithm can be found in [125]. The algorithm is based on an iterative construction of the Krylov subspace [125]:

$$\kappa_j(\Phi, \mathbf{y}) = [\mathbf{y}, \Phi \mathbf{y}, \Phi^2 \mathbf{y}, \dots, \Phi^{j-1} \mathbf{y}]. \quad (5.32)$$

Here, \mathbf{y} is an arbitrary vector, and this Krylov subspace is used to reduce Φ to an upper Hessenberg matrix (\mathbf{H}), whose eigenvalues approximate those of the original FTM (Φ). On each iteration (j) of the Arnoldi algorithm, a new vector in the Krylov subspace, $\mathbf{x}_{j+1} \in \mathbb{R}^{N_p}$, is constructed using the following recurrence relation [125]:

$$h_{j+1,j} \mathbf{x}_{j+1} = \Phi \mathbf{x}_j - \sum_{i=1}^j h_{i,j} \mathbf{x}_i = \mathbf{t}_j. \quad (5.33)$$

Here, $h_{i,j}$ is the $(i, j)^{\text{th}}$ entry of the matrix \mathbf{H} . The vector \mathbf{x}_{j+1} should be orthonormal to all \mathbf{x}_i , for $i = 1, 2, \dots, j$ to maintain stability. Therefore, we use the Gram–Schmidt process to construct the vectors $\mathbf{x}_{(\cdot)}$, such that they form an orthonormal basis for the Krylov subspace. Equation (5.33) can be rearranged and expressed in the matrix

form as:

$$\Phi \mathbf{x}_j = \mathbf{Q}_j \begin{bmatrix} h_{1,j} \\ h_{2,j} \\ \dots \\ h_{j,j} \end{bmatrix} + h_{j+1,j} \mathbf{x}_{j+1}, \quad (5.34)$$

where, $\mathbf{Q}_j = [\mathbf{x}_1, \mathbf{x}_2, \dots, \mathbf{x}_j]$. Equation (5.34) can be written in compact form for all iterations as:

$$\Phi \mathbf{Q}_j = \mathbf{Q}_j \mathbf{H}_j + h_{j+1,j} \mathbf{x}_{j+1} \mathbf{e}_j^T. \quad (5.35)$$

Here, $\mathbf{e}_j^T = [0, \dots, 0, 1] \in \mathbb{R}^j$, and the upper Hessenberg matrix (\mathbf{H}_j) is defined as:

$$\mathbf{H}_j = \begin{bmatrix} h_{1,1} & h_{1,2} & \dots & h_{1,j} \\ h_{2,1} & h_{2,2} & \dots & h_{2,j} \\ 0 & h_{3,2} & \dots & h_{3,j} \\ \vdots & \vdots & \ddots & \vdots \\ 0 & 0 & \dots & h_{j,j} \end{bmatrix}. \quad (5.36)$$

The eigenvalues of the upper Hessenberg matrix (\mathbf{H}) are the approximations of the original matrix, Φ . At each iteration (j) of the Arnoldi algorithm, a new column of the \mathbf{H} matrix is obtained, and increasingly accurate approximations of the j dominant eigenvalues (eigenvalues with the largest magnitudes) of the system can be determined.

For example, consider an eigenvalue problem of the following form:

$$\Phi v = \lambda v. \quad (5.37)$$

Here, λ denotes the exact eigenvalues of the matrix Φ . In the j^{th} iteration of the Arnoldi algorithm, the matrix \mathbf{Q}_j is used to map the vector v onto the Krylov sub-space:

$$v = \mathbf{Q}_j \mathbf{s}. \quad (5.38)$$

By substituting Eq. (5.38) into Eq. (5.37) and pre-multiplying by \mathbf{Q}_j^T :

$$\mathbf{Q}_j^T \Phi \mathbf{Q}_j \mathbf{s} = \hat{\lambda} \mathbf{Q}_j^T \mathbf{Q}_j \mathbf{s}. \quad (5.39)$$

Here, $\hat{\lambda}$ denotes the approximations of the j dominant eigenvalues of Φ . By substituting Eq. (5.35) into Eq. (5.39) and using the relation $\mathbf{Q}_j^T \mathbf{Q}_j = \mathbf{I}$, the simplified expression can be written as:

$$\mathbf{H}_j \mathbf{s} = \hat{\lambda} \mathbf{s}. \quad (5.40)$$

Thus, the eigenvalues of \mathbf{H}_j , approximate those of the original matrix Φ . The complete Arnoldi algorithm has been summarized under Algorithm 1. In N_p Arnoldi

Algorithm 1 : Arnoldi algorithm

Given: Matrix $\Phi \in \mathbb{R}^{N_p \times N_p}$, whose eigenvalues has to be determined. Starting arbitrary vector, $\mathbf{t} \in \mathbb{R}^{N_p}$. Maximum number of iterations, j_{max} .

Find: Upper Hessenberg matrix (\mathbf{H}) whose eigenvalues approximate to those of given matrix (Φ).

$h_{1,0} \leftarrow \|\mathbf{t}\|$

$\mathbf{x}_1 \leftarrow (1/h_{1,0})\mathbf{t}$

for j from 1 to j_{max} **do**

$\mathbf{z} \leftarrow \Phi \mathbf{x}_j$

for i from 1 to j **do**

$h_{i,j} \leftarrow \mathbf{x}_i^T \mathbf{z}$

$\mathbf{t} \leftarrow \mathbf{t} - h_{i,j} \mathbf{x}_i$

$h_{j+1,j} \leftarrow \|\mathbf{t}\|$

$\mathbf{x}_{j+1} \leftarrow (1/h_{j+1,j})\mathbf{t}$

Modified Gram-Schmidt orthogonalization.

for i from 1 to j **do**

$\mathbf{x}_{j+1} \leftarrow \mathbf{x}_{j+1} - (\mathbf{x}_i^T \mathbf{x}_{j+1})\mathbf{x}_i$

steps (i.e., $j = N_p$), Φ is transformed into an $N_p \times N_p$ upper Hessenberg matrix \mathbf{H}_{N_p} , whose eigenvalues are identical to those of Φ . However, the eigenvalues of \mathbf{H}_j , converge very rapidly to the dominant eigenvalues of Φ for $j \ll N_p$. Since the dominant eigenvalue itself is sufficient to determine the stability of the system, the calculation of any other eigenvalues is not required. Since the convergence starts from the dominant eigenvalue in the Arnoldi algorithm, it is perfectly suitable for the stability analysis of periodic systems. The rate of convergence of the dominant eigenvalues is determined only by the spacing between the eigenvalues (physical characteristics of the system) but not on the size of the system (number of degrees of freedom). It has to be noted that the original matrix, Φ appears only on the matrix multiplication

operation $\mathbf{z} \leftarrow \Phi \mathbf{x}_j$ while extracting its eigenvalues with the Arnoldi algorithm. This makes the Arnoldi algorithm ideally suited for determining the dominant eigenvalues of large, sparse matrices.

Using Floquet theory, the stability of systems with periodic coefficients can be predicted from the dominant eigenvalues of the FTM. In the classical Floquet analysis, the FTM of the system is first explicitly evaluated, and then its eigenvalues are computed. However, the evaluation of the FTM involves much computational effort. Therefore, implicit Floquet analysis is used in the present work to extract the dominant eigenvalues of the FTM without the explicit computation of the transition matrix. This method relies on the properties of the Arnoldi algorithm, which only requires the matrix multiplication operation $\mathbf{z} = \Phi \mathbf{x}_j$. Moreover, at each Arnoldi iteration, the operation $\mathbf{z} = \Phi \mathbf{x}_j$ corresponds to the response (\mathbf{z}) of the system after one period to the initial conditions \mathbf{x}_j . This means that the computation of the complete FTM (Φ) before extracting the dominant eigenvalues of the system is not necessary. This further means that at each iteration in the Arnoldi algorithm, the response of the system (given in Eq. (5.28)) after one time period is calculated to the initial conditions $\Psi_j(0) = \mathbf{I}_j$ (j^{th} column of \mathbf{I}) i.e., $\mathbf{z} = \Psi(T)$ subjected to the initial conditions $\Psi(0) = \mathbf{I}_j$. In order to determine all the eigenvalues of the system, N_p integrations have to be performed, in which case, the implicit Floquet analysis requires the same computational effort as that would be required for a complete Floquet analysis, and yields the same results. However, upon employing the implicit Floquet analysis, the dominant eigenvalues of the FTM (Φ) can be approximated with the desired accuracy in $j \ll N_p$ iterations and this results in a considerable reduction of computational effort.

5.4.1 Newmark integration

In order to integrate the system of differential equations to obtain the FTM, a Newmark integration scheme [126] has been used in this work, where the displacement and velocity are approximated as follows:

$$\dot{\mathbf{U}}^{t+\Delta t} = \dot{\mathbf{U}}^t + \left[(1 - \delta) \ddot{\mathbf{U}}^t + \delta \ddot{\mathbf{U}}^{t+\Delta t} \right] \Delta t, \quad (5.41)$$

$$\mathbf{U}^{t+\Delta t} = \mathbf{U}^t + \dot{\mathbf{U}}^t \Delta t + \left[\left(\frac{1}{2} - \alpha \right) \ddot{\mathbf{U}}^t + \alpha \ddot{\mathbf{U}}^{t+\Delta t} \right] \Delta t^2. \quad (5.42)$$

Here, α and δ are the parameters that can be determined to obtain integration accuracy and stability. In this work $\delta = \frac{1}{2}$ and $\alpha = \frac{1}{4}$ are considered, which cor-

responds to the constant-average-acceleration method that provides unconditionally stable solutions. The main advantage of the Newmark integration procedure is that the second-order differential equation can be directly solved without having to convert it into the first-order form. This reduces the size of the system, which in-turn decreases the computational cost involved. Also, Newmark integration is an implicit scheme and unconditionally stable even for larger time-steps. As the finite element and GDIQM analysis of VAT composite panels results in a large degree-of-freedom systems, it is computationally efficient to use Newmark integration technique for the analysis. Therefore the same has been used in the present work.

5.5 Results and discussion

In this section, the DIRs in the simply-supported VAT composite panel subjected to in-plane periodic compression load is determined using implicit Floquet method. For numerical analyses, a symmetric VAT panel $[\phi \pm \langle T_0 | T_1 \rangle]_{4s}$ having dimensions $a = b = 1$ m and thickness $h = 2.096 \times 10^{-3}$ m is considered. The material properties of the lamina are taken as: $E_{11} = 181$ GPa, $E_{22} = 10.273$ GPa, $G_{12} = 7.17$ GPa, $\nu_{12} = 0.28$, $\rho = 1580$ kg/m³. The damping coefficient, β is chosen as 15 for all the analyses in this work unless and otherwise specified.

An in-house GDIQM and FEM MATLAB programs are developed to analyze the VAT panel. An FEM code is developed for a four-noded quadrilateral Reissner–Mindlin plate element [106]. In finite element analysis, the element stiffness matrix is constructed by considering the fiber-angle at the center of the element and assuming it to be uniform over the element. For numerical computation, full integration is used for calculating the element stiffness matrix (stiffness contribution from membrane and stiffness contribution from bending) and element mass matrix. To avoid shear locking in thin panels, reduced integration has been used in calculating the shear contribution in the element stiffness matrix and the element geometric stiffness matrix.

To start with, the accuracy of the GDIQM and FEM results are verified by comparing them with ABAQUS simulations. For ABAQUS, a subroutine is developed to generate four-noded shell elements (S4R) with a mesh density of 50×50 each having independent fiber orientations. To validate the in-house MATLAB programs, the normalized natural frequency ($\tilde{\omega} = \omega a^2 / h \sqrt{\rho / E_{22}}$) and critical buckling load ($K_{cr} = P_{cr} a^2 / E_{11} b h^3$) of the VAT panel $[0 \pm \langle 0 | T_1 \rangle]_{4s}$ for different fiber-angles ($T_1 = \{0^\circ, 15^\circ, 30^\circ, 45^\circ\}$) are evaluated and compared with those from the ABAQUS simulations and the results are shown in Table 5.1. For GDIQM and FEM simu-

lations, a converged grid size of 21×21 and 30×30 are used, respectively. From Table 5.1, it is observed that the results obtained from GDIQM and FEM match accurately with ABAQUS simulations.

Table 5.1: Validation of normalized the natural frequency ($\tilde{\omega}$) and critical buckling load (K_{cr}) of the VAT panel $[0 \pm \langle 0|T_1 \rangle]_{4s}$ obtained from GDIQM, FEM and ABAQUS.

Method	T_1							
	0°		15°		30°		45°	
	$\tilde{\omega}$	K_{cr}	$\tilde{\omega}$	K_{cr}	$\tilde{\Omega}$	K_{cr}	$\tilde{\omega}$	K_{cr}
GDIQM	13.3806	1.0247	13.9918	1.1129	15.3198	1.2907	16.4412	1.3877
FEM	13.3923	1.0269	13.9935	1.1175	15.3235	1.3048	16.4459	1.3921
Abaqus	13.3845	1.0252	13.9920	1.1163	15.3175	1.2994	16.4484	1.3904

Next, by using the first-order Bolotin's approximation the DIR of a VAT panel $[0 \pm \langle 0|T_1 \rangle]_{4s}$ for three different fiber-angles ($T_1 = \{0^\circ, 30^\circ, 45^\circ\}$) are evaluated with GDIQM, FEM models and the results are shown in Fig. 5.2. The instability regions are generated by increasing the dynamic load parameter (α_1) from 0 to 1 in a step-size of 0.01 while keeping the static load parameter, $\alpha_0 = 0$. The stability boundary frequencies are normalized as $\tilde{\Omega} = \Omega a^2 / h \sqrt{\rho / E_{22}}$. From the results (Fig. 5.2) it is clear that the DIRs obtained from the GDIQM model matches very well with those from the FEM.

Further, to study the convergence of the dominant eigenvalue obtained from the implicit Floquet analysis, the dominant eigenvalue for the VAT panel ($[0 \pm \langle 0|T_1 \rangle]_{4s}$) is calculated for different fiber-angles, T_1 . The dominant eigenvalue obtained at different Arnoldi steps and their corresponding absolute error when compared to the eigenvalue obtained from the classical Floquet analysis is shown in Table 5.2. For the analysis, the static and dynamic load parameters are chosen as $\alpha_0 = 0$ and $\alpha_1 = 0.5$, respectively, while the normalized excitation frequency is chosen as $\tilde{\Omega} = 30.87$. The absolute error in the eigenvalue from the implicit Floquet analysis is the difference between the eigenvalue obtained at a particular step to the eigenvalue obtained from the classical Floquet analysis. It is observed from Table 5.2 that the dominant eigenvalue converges very rapidly using implicit Floquet approach and is determined accurately up to an order of 10^{-4} within 8 Arnoldi steps. This represents an approximately 295 times reduction in computational effort when compared to the 2360 steps that would be required for the classical Floquet method (as the size of the stiffness matrix after

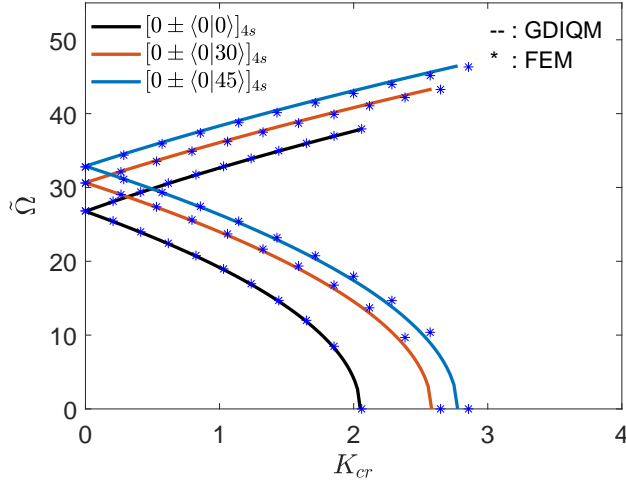


Figure 5.2: Principle DIRs in the VAT panel ($[0 \pm \langle 0|T_1 \rangle]_{4s}$) obtained using GDIQM and FEM.

applying boundary conditions for a grid size of 21×21 is 1180×1180).

Table 5.2: Convergence of the dominate eigenvalue obtained from the implicit Floquet analysis for the VAT panel, $[0 \pm \langle 0|T_1 \rangle]_{4s}$.

T_1	Dominant eigenvalue (absolute value of error)				
	1 step	2 steps	4 steps	8 steps	Classical Floquet
0°	0.9873 (0.0127)	1.0026 (0.0026)	1.0001 (1.1750×10^{-4})	1.0000 (1.7565×10^{-6})	1.000
15°	1.0360 (0.2149)	1.2024 (0.0485)	1.2502 (6.9311×10^{-4})	1.2509 (4.4253×10^{-5})	1.2509
30°	1.0891 (0.3881)	1.4721 (0.0052)	1.4758 (0.0014)	1.4773 (1.0677×10^{-5})	1.4773
45°	1.0757 (0.3460)	1.4258 (0.0041)	1.4200 (0.0017)	1.4214 (4.0611×10^{-4})	1.4218

Furthermore, the time required to obtain the dominant eigenvalue for the VAT panel $[0 \pm \langle 0|T_1 \rangle]_{4s}$ using the GDIQM and FEM methods for the classical Floquet and implicit Floquet method are studied. The parameters considered for the analysis are: $\alpha_0 = 0$, $\alpha_1 = 0.4$ and $\tilde{\Omega} = 20.58$. The analysis is carried out on a VAT panel for four different fiber-angles ($T_1 = \{0^\circ, 15^\circ, 30^\circ, 45^\circ\}$). All the simulations are performed

using MATLAB[®] R2018b on a 2.60 GHz Intel[®] Xeon[®] E5-2670 processor with an installed memory of 48GB. The time required to obtain the dominant eigenvalue using classical Floquet and implicit Floquet for the FEM and GDIQM is shown in Table 5.3. In the implicit Floquet analysis, the convergence criterion is chosen as the difference between the magnitudes of the eigenvalue at two consecutive steps is less than 10^{-3} . It is observed from Table 5.3 that the dominant eigenvalue obtained from classical Floquet method matches very well with the implicit Floquet analysis in both GDIQM and FEM. Moreover, by using implicit Floquet analysis combined with GDIQM, the dominant eigenvalue of the FTM can be obtained in just 0.13% of the time as compared to the classical Floquet analysis with GDIQM. Also, in the case of FEM and implicit Floquet analysis, the dominant eigenvalue can be obtained in 0.44% of the time that would be needed for the case of FEM with classical Floquet method. These results demonstrate that upon using the implicit Floquet analysis, the dominant eigenvalue of the system can be obtained accurately in less time and with a fewer number of steps when compared to the classical Floquet analysis.

Table 5.3: Time required to obtain the dominate eigenvalue from classical Floquet and implicit Floquet method using FEM and GDIQM for VAT panels $[0 \pm \langle 0|T_1\rangle]_{4s}$ when $\alpha_1 = 0.4$ and $\tilde{\Omega} = 20.58$.

T_1	FEM		GDIQM	
	Classical Floquet (time)	Implicit Floquet (time)(steps)	Classical Floquet (time)	Implicit Floquet (time)(steps)
0°	$-0.6403 + 0.7682i$ (59040s)	$-0.6401 + 0.7682i$ (263.51s)(3)	$-0.6355 + 0.7721i$ (10776s)	$-0.6355 + 0.7720i$ (14.20s)(3)
15°	$-0.4828 + 0.8757i$ (55971s)	$-0.4862 + 0.8758i$ (262.20s)(3)	$-0.4731 + 0.8810i$ (10727s)	$-0.4730 + 0.8812i$ (13.83s) (3)
30°	$-0.0961 + 0.9954i$ (56329s)	$-0.0979 + 0.9948i$ (263.50s)(3)	$-0.0735 + 0.9973i$ (10274s)	$-0.0736 + 0.9977i$ (13.85s) (3)
45°	$0.2466 + 0.9691i$ (56662s)	$0.2440 + 0.9698i$ (264.77s)(3)	$0.2726 + 0.9621i$ (10180s)	$0.2724 + 0.9621i$ (13.74s)(3)

5.5.1 Dynamic instability analysis of VAT panel

In this section, DIRs in a VAT panel, $[0 \pm \langle 0|45 \rangle]_{4s}$ with and without damping are determined using the implicit Floquet approach. The static load parameter for the analysis is chosen as $\alpha_0 = 0$. The instability boundaries in the VAT panel are determined by starting with initial excitation frequencies $\tilde{\Omega} = 2\tilde{\omega}$ and $\tilde{\Omega} = \tilde{\omega}$ for the first and second instability regions, respectively. Starting with the dynamic load parameter $\alpha_1 = 0.01$, the upper and lower instability boundaries are identified by using line search with an increment of $\tilde{\Omega} = 0.1$, and the frequency at which the magnitude of the dominant eigenvalue (μ_{max}) falls inside the unit circle (i.e., $\mu_{max} \leq 1$) is identified as the instability boundary. Next, α_1 is increased and using the previous boundary frequencies as the initial conditions, the instability boundaries for the current step are calculated. In evaluating the dominant eigenvalue using the Arnoldi algorithm, the convergence criterion for the dominant eigenvalue between two successive iterations has been taken as 10^{-3} . The first and second DIRs in an undamped and damped VAT panel determined using implicit Floquet analysis are shown in Fig. 5.3(a) and Fig. 5.3(b), respectively. The first two DIRs obtained from the Bolotin's method up to a third-order approximation are also shown in Fig. 5.3 for comparison. It is observed from Fig. 5.3(b), that for a damped VAT panel, the onset of instability regions begins at the same excitation frequency as in the case of an undamped VAT panel. However, because of the damping in the system, DIRs shifts towards higher load amplitudes providing more stability region. Also, it is noticed from Fig. 5.3 that Bolotin's first-order approximation (which is widely used in the literature) gives a sufficiently accurate stability boundary only up to $\alpha_1 = 0.5$ in an undamped system and up to $\alpha_1 = 1$ in a damped system, after which the boundary diverges from the actual solution and gives a completely inaccurate solution beyond $\alpha_1 = 1$. However, by using Bolotin's second-order approximation, the accuracy of the solution seems to improve slightly, whereas, from a third-order approximation and beyond, no significant improvement in the solution is observed. Therefore, the stability boundary obtained from Bolotin's approach is sufficiently accurate only up to $\alpha_1 = 0.5$ in the case of an undamped VAT panel and up to $\alpha_1 = 1$ in the case of a damped VAT panel, beyond which the stability boundary obtained from the method is completely inaccurate. This is because of the approximations and the neglected terms in the assumed Fourier solution. However, by using the implicit Floquet method, the instability boundaries of the VAT panels in both the cases (damped and undamped) can be determined accurately, even beyond $\alpha_1 = 1$.

To verify the accuracy of stability boundaries obtained from Bolotin's approach

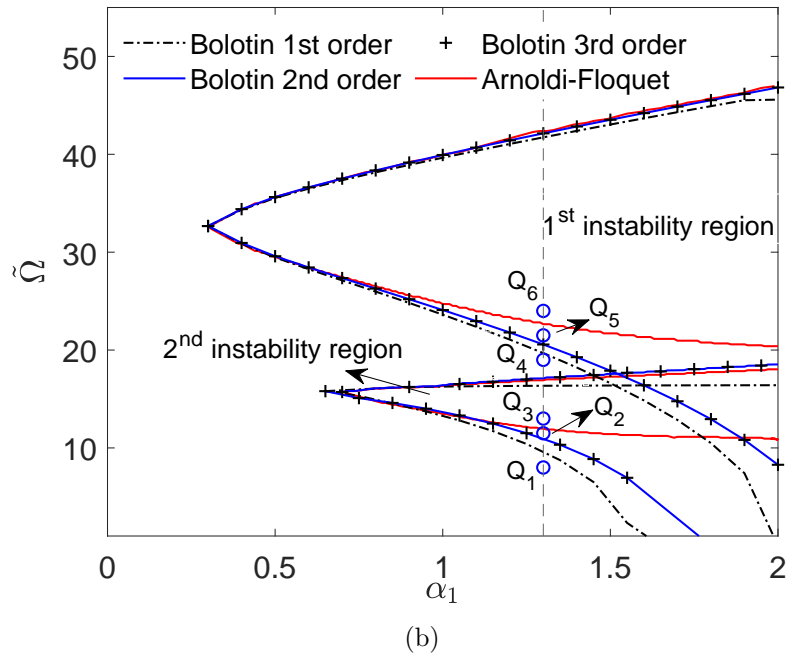
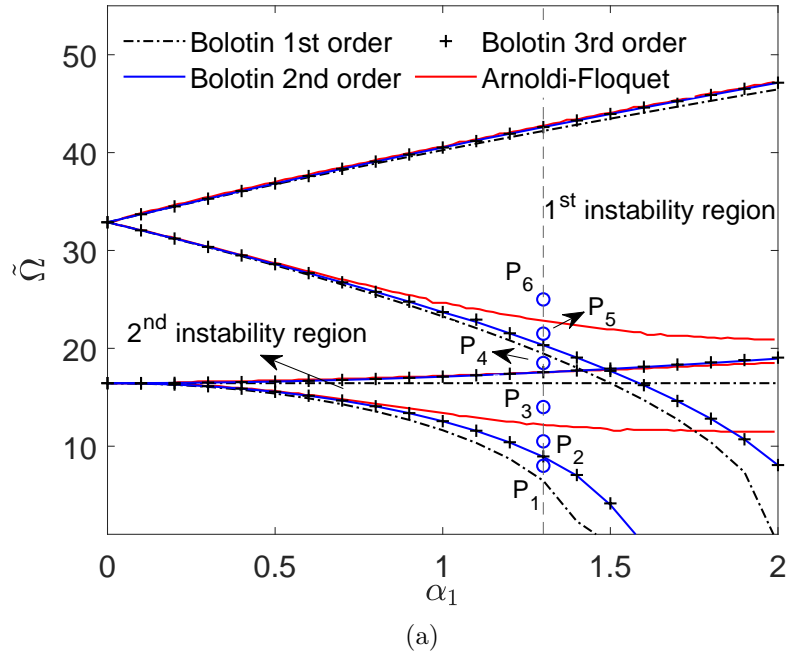


Figure 5.3: First and second DIRs in a VAT panel ($[0 \pm \langle 0|45 \rangle]_{4s}$) obtained from Bolotin's approach and the implicit Floquet method for: (a) Undamped VAT panel (b) Damped VAT panel.

and the implicit Floquet method, the time response of the VAT panel at different excitation frequencies is presented. The time response at the center of an undamped and damped VAT panel with configuration $[0 \pm \langle 0|45 \rangle]_{4s}$ at different excitation frequencies is studied. To carry out the analysis, six different excitation frequencies, P_{1-6} and Q_{1-6} near the first and second instability boundaries are chosen at $\alpha_1 = 1.3$ for each of the undamped and damped VAT panels ($[0 \pm \langle 0|45 \rangle]_{4s}$), respectively (see Fig. 5.3), and the results are shown in Fig. 5.4 and Fig. 5.5. The analysis is carried out by integrating the system (Eq. (5.6)) at the corresponding excitation frequency. The time response plots are presented by normalizing the time with respect to their corresponding time period of the panel ($\tilde{t} = \frac{t}{T}$). It is seen from Fig. 5.3(a) that both Bolotin's approach and the implicit Floquet method predicts a stable solution when the undamped VAT panel is subjected to the in-plane periodic compression load with an excitation frequency of P_1 and P_4 . The time response at the center of the VAT panel when excited with the same frequencies P_1 and P_4 (as shown in Figs. 5.4(a) and 5.4(d)) shows a stable response. Therefore, from Fig. 5.3(a), Fig. 5.4(a) and Fig. 5.4(d), it is clear that the solution predicted by both Bolotin's method and implicit Floquet approach are identical. Also, for the excitation frequencies of P_3 and P_6 , both the methods (Bolotin and implicit Floquet) predict an unstable solution. Again, this can be verified from the response plots shown in Fig. 5.4(c) and 5.4(f), which shows an unstable time response. From the results (Figs. 5.3(a), 5.4(a), 5.4(c), 5.4(d) and 5.4(f)), it is clear that the stability information obtained from both the methods is accurate and matches very well with the time response of the panel. However, at the excitation frequencies P_2 and P_5 , the implicit Floquet method predicts the solution as stable, while Bolotin's approximation shows the solution as unstable. Whereas, the time response of the panel shown in Fig. 5.4(b) and Fig. 5.4(e) shows a stable solution. Therefore, from the results shown in Fig. 5.3(a) and Fig. 5.4, it clear that even higher-order Bolotin's approximations predict an inaccurate and unreliable solution for certain excitation frequencies, whereas, the implicit Floquet method predicts an accurate solution for all the excitation frequencies at all amplitude of loads.

A similar analysis is carried out on a damped VAT composite panel with configuration $[0 \pm \langle 0|45 \rangle]_{4s}$. Six excitation frequencies (Q_{1-6}) near the first and second instability boundaries are chosen for the analysis (see Fig. 5.3(b)). The time response at the center of the damped VAT panel at the corresponding excitation frequencies is shown in Fig. 5.5. From Fig. 5.3(b) and Fig. 5.5, it is clear that both Bolotin's approach and the implicit Floquet method predict an accurate solution at frequencies

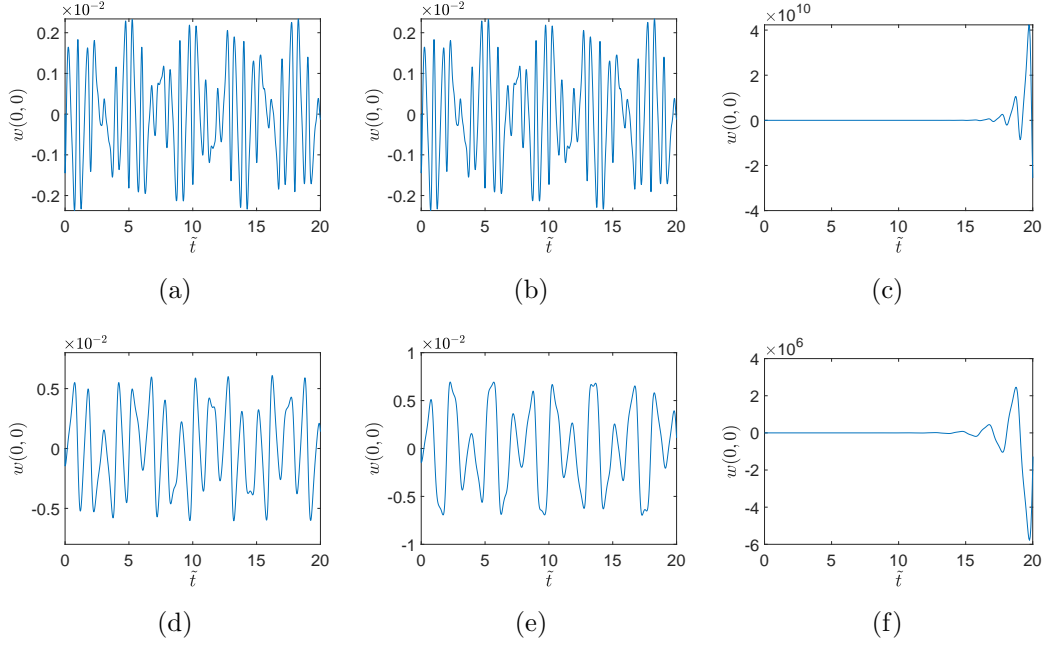


Figure 5.4: Time response at the center of an undamped VAT panel $([0 \pm \langle 0|45 \rangle]_{4s})$ at different excitation frequencies: (a) $P_1, \tilde{\Omega} = 8$ (b) $P_2, \tilde{\Omega} = 11$ (c) $P_3, \tilde{\Omega} = 14$ (d) $P_4, \tilde{\Omega} = 18.5$ (e) $P_5, \tilde{\Omega} = 21.5$ (f) $P_6, \tilde{\Omega} = 25$ (see Fig. 5.3(a)).

$Q_1, Q_3, Q_4,$ and Q_6 . On the other hand, at the excitation frequencies Q_2 and Q_5 , Bolotin's approach predicts the solution as unstable and implicit Floquet predicts the same frequencies as stable. However, the numerical time response at the frequencies Q_2 and Q_5 shows a stable response. Therefore, once again, Bolotin's method fails to predict the accurate stability information, while the implicit Floquet method provides the error-free solution. From the results shown in Fig. 5.3, 5.4 and 5.5, it is clear that the instability regions obtained from the implicit Floquet method are more precise and reliable when compared to Bolotin's approach. It should be noted that the oscillations in a stable response for an undamped system shown in Fig. 5.4 will not decay with time, but have a steady-state response. However, in the case of a damped system, the oscillations for a stable response decays with time, as shown in Fig. 5.5 because of the energy dissipation.

Further, the variation of magnitude of the dominant eigenvalue, $|\mu_{max}|$ (i.e., spectral radius) with respect to the excitation frequency of an undamped and damped composite panels $([0 \pm \langle 0|0 \rangle]_{4s})$ is presented in Fig. 5.6(a) and 5.6(b), respectively. The analysis is carried out by considering the static load parameter as $\alpha_0 = 0$ and the dynamic load parameter as $\alpha_1 = 0.75$. The value of μ_{max} is determined at the

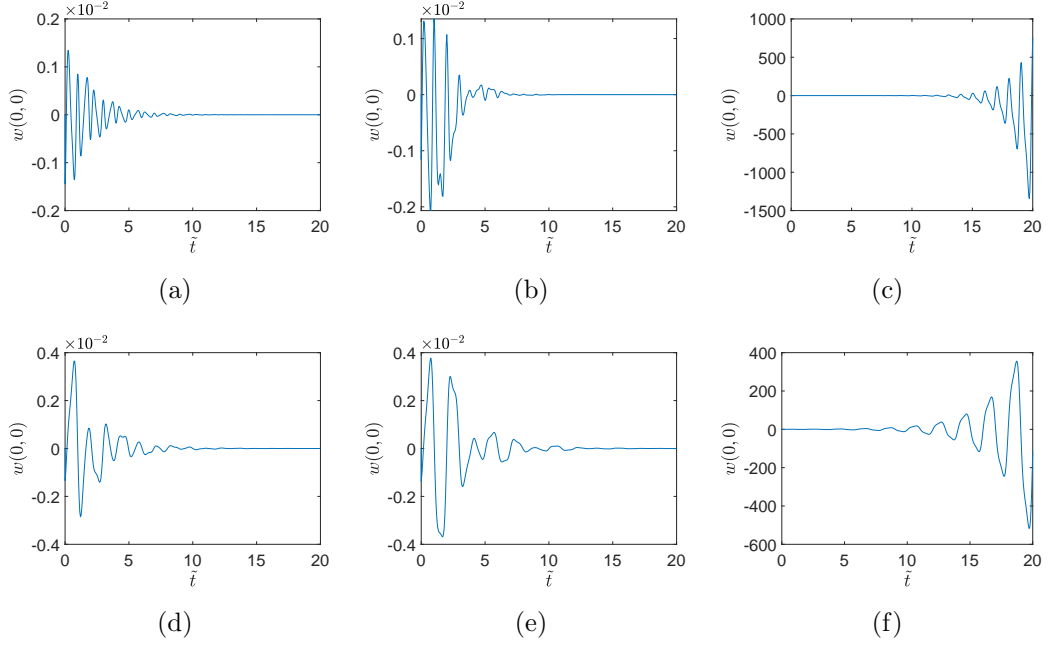


Figure 5.5: Time response at the center of a damped VAT panel ($[0 \pm \langle 0|45 \rangle]_{4s}$) at different excitation frequencies: (a) $Q_1, \tilde{\Omega} = 10$ (b) $Q_2, \tilde{\Omega} = 11.5$ (c) $Q_3, \tilde{\Omega} = 13$ (d) $Q_4, \tilde{\Omega} = 19$ (e) $Q_5, \tilde{\Omega} = 21.5$ (f) $Q_6, \tilde{\Omega} = 24$.

normalized excitation frequencies in the range of 0 to 45 with a step-size of 0.05. From Fig. 5.6, it should be noted that for an undamped system the dominant eigenvalues (μ_{max}) lies on the unit circle and represents the steady-state response of the system (see Fig. 5.6(a)). Contrarily, in the case of a damped system, μ_{max} lies inside the unit circle, which represents the decay in oscillations with time (see Fig. 5.6(b)). Also, the magnitude of μ_{max} represents the rate at which the oscillations in the system grow or decay with time. In Fig. 5.6, the range of excitation frequencies at which $|\mu_{max}| > 1$ represents an instability region. It is observed that the spectral radius variation for an undamped composite panel shown in Fig. 5.6(a), has five peaks. All of them correspond to $|\mu_{max}| > 1$, and they represent the first five instability regions of the panel, starting from the first on the extreme right to the fifth on the left. In the case of a damped composite panel, four peaks are observed among which only the first peak is unstable (instability region), since it corresponds to $|\mu_{max}| > 1$. On the other hand, the other three peaks are stable (damped instability regions) since they correspond to $|\mu_{max}| < 1$. Moreover, in the case of a damped system, $|\mu_{max}|$ is not constant as it is in the case of an undamped system but varies with respect to the excitation frequency. It is also noticed from Fig. 5.6(b) that $|\mu_{max}|$ increases with an

increase in the excitation frequency while having peaks at the presence of instability regions.

From the spectral radius variation analysis, all the unstable frequencies at a particular excitation load (α_1) can be determined. Whereas, in Bolotin's approach, all the instability regions have to be determined individually to compute the unstable frequencies at a particular excitation load. Moreover, Bolotin's approach cannot determine the number of instability regions (range of unstable frequencies) that exist at a constant excitation load, and therefore, all the instability regions have to be determined individually. More importantly, the range of unstable frequencies that are obtained using Bolotin's approach is approximate. However, a better approximation can be made using higher-order approximations, determining all the instability regions, especially from third and beyond with higher-order approximation will be cumbersome. Also, it is evident from Fig. 5.3 that even with higher-order approximation the instability regions obtained are accurate only up to a certain range of α_1 and beyond which even a higher-order approximation fails to provide a reliable solution. Also, Bolotin's method cannot provide any information on the spectral radius value, that is crucial for understanding the rate of growth or decay of oscillations in a system.

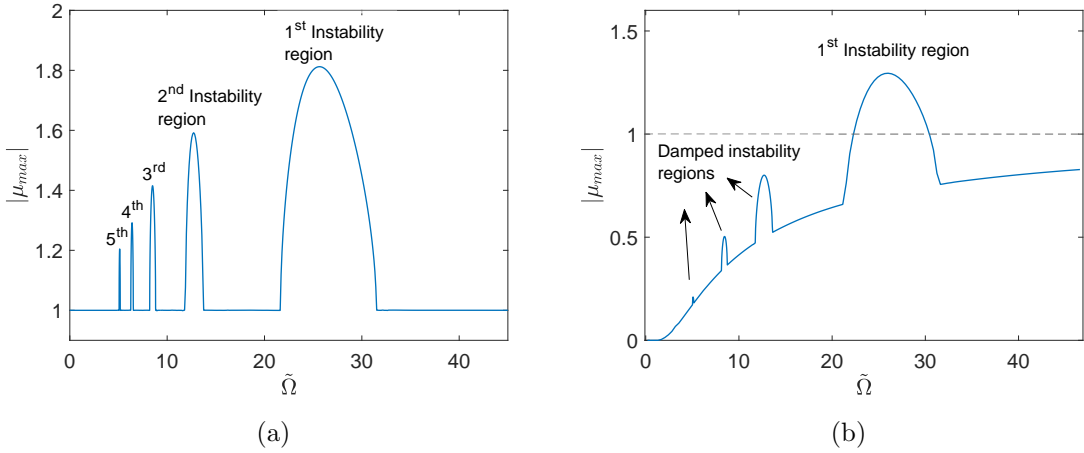


Figure 5.6: Spectral radius variation of a VAT panel $[0 \pm \langle 0|0 \rangle]_{4s}$ for the constant excitation load of $\alpha_1 = 0.75$.

Furthermore, the variation of the spectral radius with respect to the excitation frequency in a VAT panel $[0 \pm \langle 0|T_1 \rangle]_{4s}$ for three different fiber-angles ($T_1 = \{0^\circ, 30^\circ, 45^\circ\}$) is studied. The excitation load parameter for the analysis is chosen in such a way that $\alpha_1 K_{cr} = 0.7860$ while keeping the static load parameter (α_0) as zero. The results

from the analysis for both, the undamped and damped VAT panels are presented in Fig. 5.7(a) and Fig. 5.7(b), respectively. From the result shown in Fig. 5.7, it is clearly observed that with a change in the fiber-angle configuration in the VAT panel, the onset of dynamic instability regions shifts towards higher excitation frequency in both damped and undamped VAT panels. Also, the height of the unstable peaks decreases with increase in the fiber-angle from $T_0 = 0^\circ$ to $T_0 = 45^\circ$, which implies that the growth in the amplitude of oscillations in VAT panels with $T_0 = 45^\circ$ is less when compared to the panel with $T_0 = 30^\circ$ and $T_0 = 0^\circ$. Also, the width of all the instability regions (range of unstable excitation frequencies) decreases with increase in the fiber-angle T_1 from 0° to 45° . Moreover, for an undamped VAT panel with fiber-angle $T_1 = 0^\circ$ five instability regions are observed, whereas in the case of VAT panel with the fiber-angle $T_1 = 45^\circ$ only four instability regions appear, and that makes the VAT panel more stable. In the case of a damped VAT panel, the spectral radius increases with an increase in excitation frequency for all the fiber-angle configurations (see Fig. 5.7(b)). It is also noticed from the results that an increase in the spectral radius with respect to the excitation frequency for all the fiber-angles $T_0 = \{0^\circ, 30^\circ, 45^\circ\}$ follows a similar trend. This is because of the constant damping that has been used for all the analyses. Also, there exists only one instability region in all three VAT panels.

Upon using the spectral radius variation analysis, all the instability regions at a particular excitation load for different composite panels can be compared. Instead of using approximated primary instability regions (obtained from Bolotin's approach) to characterize the dynamic stability behavior of a structure, spectral-radius variation analysis provides information about all the existing instability regions and renders more insights to compare the dynamic characteristics of different structures.

Now, the variation of the spectral radius ($|\mu_{max}|$) with respect to the excitation frequency in a VAT panel ($[0 \pm \langle 0|45 \rangle]_{4s}$) for different values of damping coefficient ($\beta = \{5, 15, 25\}$) is studied. The static load parameter (α_0) is chosen to be zero, and the dynamic load parameter is chosen in such a way that $\alpha_1 K_{cr} = 0.7680$ and the results are shown in Fig. 5.8. It is observed from the results that with an increase in the damping coefficient in the VAT panel, the rate of increase in the $|\mu_{max}|$ decreases with the increase in excitation frequency. This means that the rate of decay in oscillations in the VAT panel with higher damping coefficient will be much faster. Moreover, it is also noticed from Fig. 5.8, that peaks in the spectral radius variation in the VAT panel begin and ends at the same excitation frequencies irrespective to the damping present in the system. However, the number of peaks with unstable

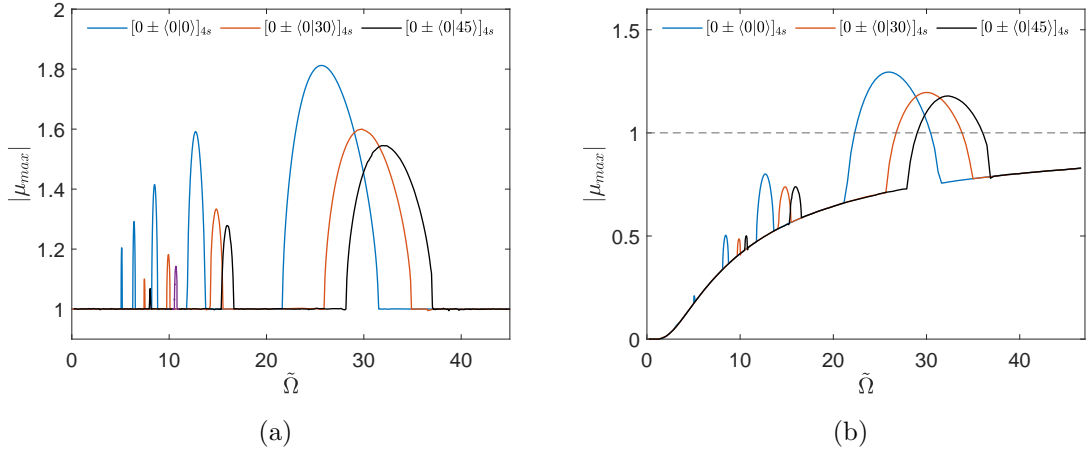


Figure 5.7: Spectral radius variation of a VAT panel $[0 \pm \langle 0|T_1 \rangle]_{4s}$ for the excitation load of $\alpha_1 K_{cr} = 0.7680$.

excitation frequencies ($|\mu_{max}| > 1$) decreases with an increase in β . That is, there exist 2 unstable peaks in the VAT panel with the damping coefficient $\beta = 5$, only 1 unstable peak for $\beta = 15$ and there exist no unstable frequencies in the case of $\beta = 25$.

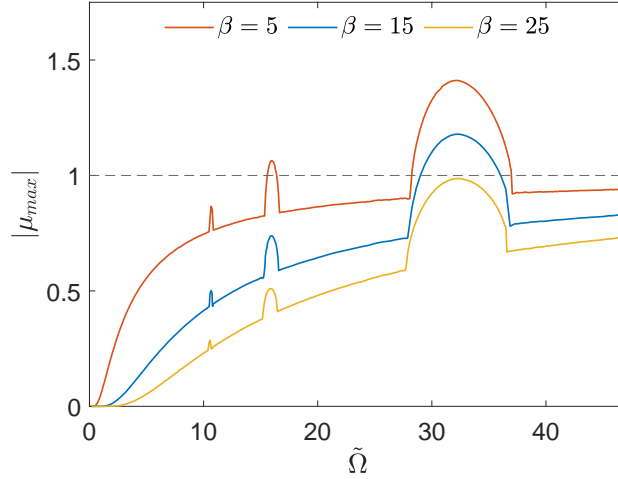


Figure 5.8: Variation of spectral radius ($|\mu_{max}|$) in a VAT panel $[0 \pm \langle 0|45 \rangle]_{4s}$ for different values of damping coefficient (β) at the excitation load of $\alpha_1 K_{cr} = 0.7680$.

Next, the bifurcation analysis is carried out on the VAT panels subjected to in-plane periodic load at the first and second instability regions. The analysis is performed by studying the variation in dominant eigenvalues of the FTM (μ_{max}) with

respect to the excitation frequencies. By varying the excitation frequency, the corresponding real and imaginary parts of the eigenvalues for undamped and damped VAT panels are plotted in Fig. 5.9 and Fig. 5.10 (represented in red dots), respectively, along with the unit circle shown in blue, for reference. It should be noted that the excitation frequencies whose corresponding eigenvalues lie inside or on the unit circle will be stable and the frequencies at which the eigenvalues lie outside the unit circle are unstable. From Fig. 5.9(a), it is noticed that with an increase in the excitation frequency from 23.6 to 24.6, μ_{max} moves on the unit circle and reaches -1 at the frequency 24.6 which is on the stability boundary. Beyond this, with an increase in the excitation frequency, μ_{max} escapes the unit circle along the negative real axis (i.e., -1) resulting in the period-doubling bifurcation or flip bifurcation. Similarly, at the second instability region with the decrease in the excitation frequency from 17.5 to 17.1, μ_{max} lies on the unit circle and reaches 1 when the frequency becomes 17.1 which is exactly on the stability boundary. With the further decrease in the frequency, μ_{max} escapes the unit circle through the positive real axis (i.e., $+1$). In this case, the VAT panel loses its stability through one of the three bifurcations: (i) symmetry-breaking (ii) cyclic-fold or (iii) transcritical bifurcation [127].

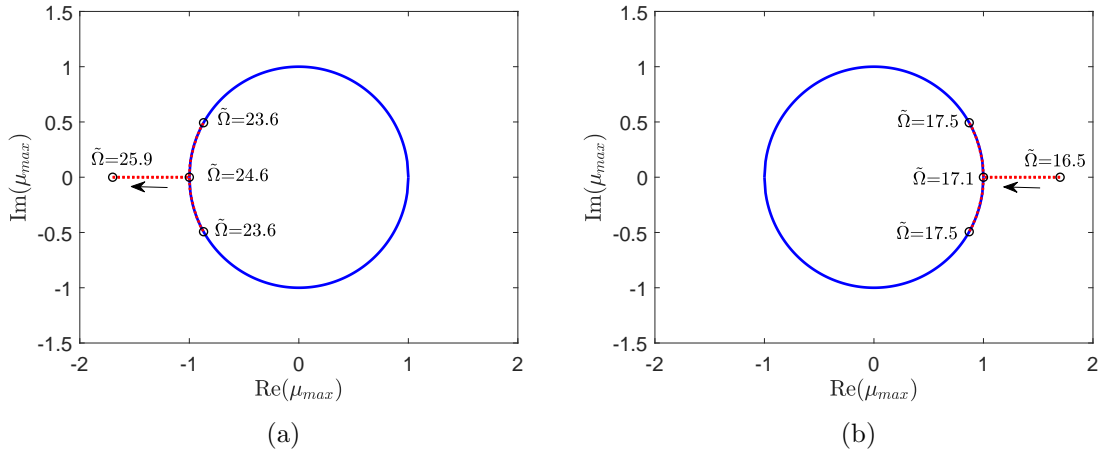


Figure 5.9: Variation of the dominant eigenvalue of the FTM for an undamped VAT panel $[0 \pm \langle 0|45 \rangle]_{4s}$ at: (a) First instability region and (b) Second instability region. The eigenvalues are represented by red dots and the unit circle is represented with blue.

Similar analysis has been carried out on a damped VAT panel, and the results are shown in Fig. 5.10. In the case of the damped VAT panels as well the dominant eigenvalues (μ_{max}) escapes the unit circle along the negative real axis at the first

instability region and along the positive real axis at the second instability region. This shows that the VAT panel undergoes a period-doubling bifurcation at the first instability region and one of the three bifurcations (symmetry-breaking, cyclic-fold or transcritical) at the second instability region. It is also noticed from the Fig. 5.10, that unlike undamped VAT panels, the dominant eigenvalues does not lie on the unit circle in the stable region, but lie inside the unit circle which indicates that the oscillations will decay with time.

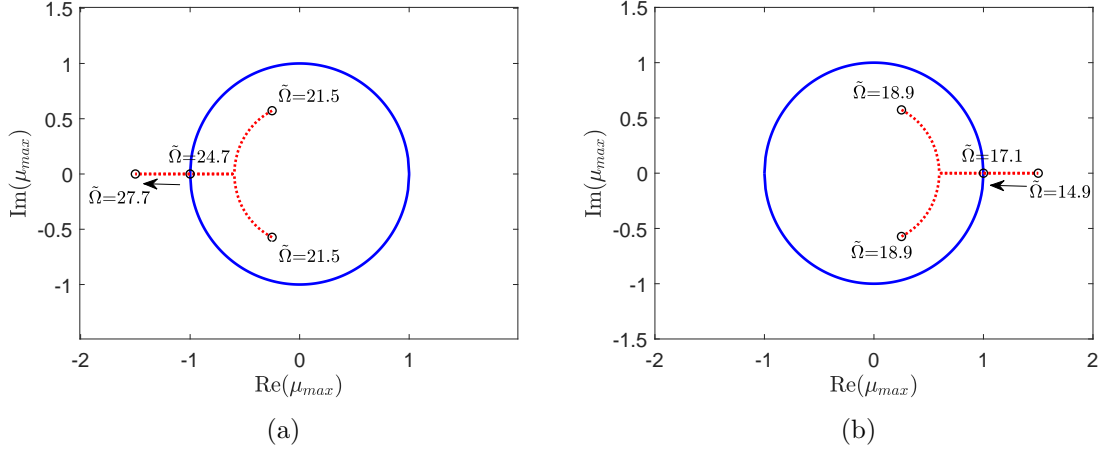


Figure 5.10: Variation of the dominant eigenvalue of the FTM for an damped VAT panel $[0 \pm \langle 0|45 \rangle]_{4s}$ at: (a) First instability region and (b) Second instability region. The eigenvalues are represented by red dots and the unit circle is represented with blue.

Finally, the complete dynamic instability analysis is carried out on an undamped and damped VAT panel with configuration $[0 \pm \langle 0|45 \rangle]_{4s}$. To carry out the analysis, the static load parameter is chosen as $\alpha_0 = 0$. The analysis is performed for the dynamic load parameter over a range of $\alpha_1 = 0$ to $\alpha_1 = 2$ in intervals of 0.01 and excitation frequencies in the range of $\tilde{\Omega} = 0$ to $\tilde{\Omega} = 45$ with a step size of 0.1. The contour plot of the spectral radius against α_1 , and $\tilde{\Omega}$ is shown in Fig. 5.11. Since the spectral radius is very large when α_1 is greater than 1 and $\tilde{\Omega}$ is very small, all values of spectral radius greater than 2 are normalized to 2 in order to generate a clear contour plot. It should be noted from Fig. 5.11(a) that in the case of an undamped VAT panel, the dominant eigenvalue (μ_{max}) lies on the unit circle. Therefore the magnitude of μ_{max} is always 1 in the stable region. Contrarily, in the case of a damped VAT panel, μ_{max} lies inside the unit circle in the stable region, and hence, the magnitude of μ_{max} varies with respect to the excitation frequency ($\tilde{\Omega}$), which can be clearly noticed from

Fig. 5.11(b). It is observed from the results that all the instability regions of the VAT panels can be obtained accurately along with the spectral radius values by using the implicit Floquet approach. Whereas, to obtain all DIRs in Bolotin's method, each instability region has to be approximated individually. Moreover, Bolotin's theory cannot provide any information on the values of the spectral radius.

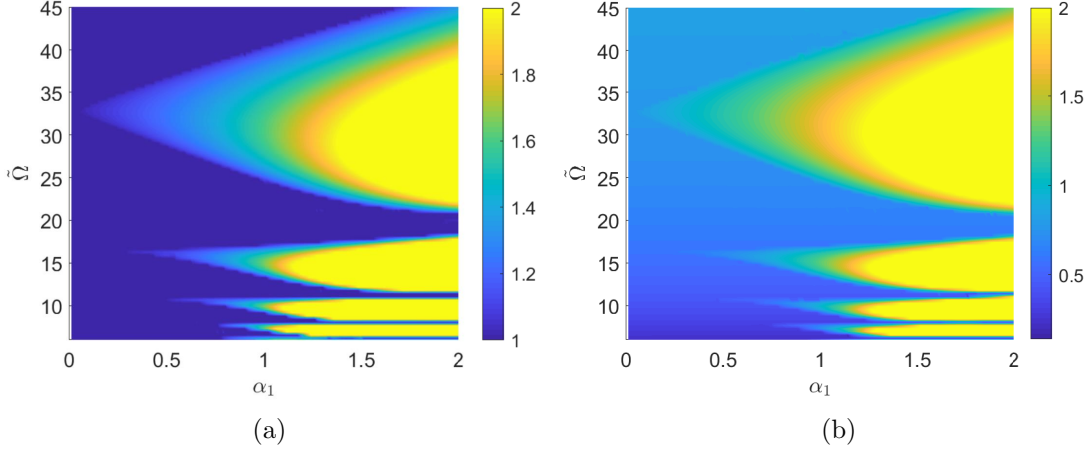


Figure 5.11: Complete parametric instability analysis of VAT composite panel (a) $[0 \pm \langle 0|0 \rangle]_{4s}$ and (b) $[0 \pm \langle 0|45 \rangle]_{4s}$.

Therefore, upon using the implicit Floquet approach to determine the DIRs in a structure subjected to periodic loads, all the instability regions can be determined accurately in a parametric space with very less time and computational effort. Moreover, this approach provides the spectral radius information that will be helpful for the designers in designing a dynamically safer structure.

5.6 Summary

In this work, the Floquet theory is used to determine the dynamic instability regions in a VAT panel. The generalized differential integral quadrature method (GDIQM) combined with the Rayleigh–Ritz procedure is used to solve the governing differential equations of the VAT panel. As the application of classical Floquet theory to a large degree of freedom system is computationally expensive, Arnoldi algorithm has been combined with the Floquet theory (implicit Floquet analysis) to evaluate the Floquet multipliers of the Floquet transition matrix (FTM). Therefore, in the implicit Floquet analysis, the stability of the system can be determined without the explicit

computation of the FTM. Also, upon using the implicit Floquet method, there will be a significant reduction in the computational cost as well as the computational time when compared to the classical Floquet analysis. The time required to determine the dominant eigenvalue of the FTM using the classical Floquet method and implicit Floquet method with FEM and GDIQM has been studied. It is observed that with the use of GDIQM and implicit Floquet analysis, the dominant eigenvalue of the FTM can be determined in 0.13% of time as compared to that of the classical Floquet method.

Dynamic instability regions in an undamped and damped VAT composite panels are determined using implicit Floquet analysis and then compared with the results from Bolotin's method. The instability regions that are obtained from the implicit Floquet analysis are also validated with the time response of the VAT panel at different excitation frequencies. Significant deviations are observed between the instability regions obtained from the implicit Floquet analysis and Bolotin's approach. Spectral radius variation (μ_{max}) in VAT panel with different fiber-angle variations for a range of excitation frequencies at a constant load has been investigated. It is observed that through the spectral radius analysis, all the unstable excitation frequency ranges at a constant load can be determined. In VAT panels, with the increase in the fiber-angle from $T_1 = 0^\circ$ to $T_1 = 45^\circ$, the height of the unstable peaks (spectral radius) decreases. Also, the width of the instability regions (range of excitation frequencies) decreases with increase in the fiber-angle (T_1), and this makes the VAT panel more stable. Further, the effect of structural damping on the variation of μ_{max} in a VAT panel is studied for different values of damping coefficients (β). It is observed that, with the increase in the damping coefficient in VAT panels, the rate of change in μ_{max} decreases. Also, the number of unstable peaks present in the VAT panel reduces with the increase in the damping coefficient.

Furthermore, variation in the eigenvalues of the system at the stability boundary is studied, through which the mode of bifurcation that the structure loses its stability can be found. It is observed from the results that, the VAT panel undergo a flip bifurcation at the first instability region, and one of the three types of bifurcations (symmetry-breaking, cyclic-fold or transcritical) at the second instability region. Finally, a complete stability analysis on both, undamped and damped VAT panels is carried out, through which all the instability regions can be determined along with the spectral radius values over a parametric space.

Chapter 6

Conclusions

The potentiality of applying tow-steering technique to improve the dynamic stability behavior of composite panels and shells have been investigated. The important observations from the present study are as follows:

- The fiber-angle variation has a significant effect on the dynamic stability behavior of the tow-steered composite panels.
- VAT panels over a range of fiber-angle configurations exhibit better dynamic stability compared to straight-fiber composite laminates. This improvement in the dynamic stability is attributed to increase in the natural frequency and critical buckling load of the VAT laminates, which is attained due to the load redistribution away from the critical regions by the curvilinear fibers.
- Flat VAT composite panel with the fiber-angle configuration of $[90 \pm \langle 0|75 \rangle]_{3s}$ have shown approximately 46% higher dynamic stability when compared to straight-fiber laminate and about 56% higher stability when compared to quasi-isotropic laminate.
- Increase in the delamination area in composite structures decreases their buckling resistance and the dynamic stability. However in VAT composites, the decrease in buckling load and dynamic stability due to the increase in delamination is much less when compared to straight-fiber composites.
- In the case of curved panels, VAT laminate with the fiber-angle configuration $[90 \pm \langle 15|65 \rangle]_{2s}$ exhibits 51% improvement in the buckling performance and 14% increase in the dynamic stability when compared to the optimal straight-fiber composite panels.

- Unlike straight-fiber composites, VAT panels have the added advantage of tailoring the dynamic instability index (D_{II}) and stiffness properties of the panel simultaneously.
- The GDIQM have been combined with implicit Floquet analysis, through which the dominant eigenvalue of the FTM can be computed in approximately 0.13% of the time as compared to that of the classical Floquet method.
- The first and second DIRs of a VAT panel are determined using implicit Floquet analysis and verified with the time response of the panel obtained through numerical integration. The DIRs thus obtained are compared with the results from Bolotin's approach and significant deviations are observed between solutions obtained from both the approaches.
- With increase in the damping coefficient (β) in the VAT panels, the rate of change in μ_{max} decreases with respect to the excitation frequency. Also, the number of unstable peaks present in the VAT panel reduces with the increase in the damping coefficient.
- The VAT panel loses its stability through a flip bifurcation at the first instability region, and one of the three types of bifurcations (symmetry-breaking, cyclic-fold or transcritical) at the second instability region.

6.1 Remarks

The dynamic stability behavior of flat VAT composite panels subjected to in-plane periodic compression load is investigated first. A first-order shear deformation theory is used to model the VAT panel, and finite element analysis has been used to perform the analyses. The effect of tow-steering on the dynamic stability behavior of the VAT panels is studied. Initially, the analysis is performed on two different types of in-plane boundary conditions. Where the transverse edges are free to deform in the plane of the laminate in one case and are constrained in the second case. From the results, it is found that the fiber-angle variation has a significant effect on the dynamic stability behavior of the VAT panels in both cases. For some fiber-angle configurations, VAT panels exhibit better dynamic stability when compared to straight-fiber and quasi-isotropic laminates. This improvement in the dynamic stability is attributed to the increase in the natural frequency and buckling load of the VAT panel, which is attained because of the stress redistribution by the curved fibers from the center of the VAT panel towards the supported edges.

Next, the effect of geometric discontinuity and material damage like, a circular cutout and delamination are introduced to the VAT panel. The analysis has been performed to study the effect of delamination and cutout along with the fiber-angle variation, on the buckling and dynamic stability behavior of the VAT panels. It is found that the VAT panels, even with a cutout, exhibit higher buckling resistance compared to a healthy straight-fiber laminate. Also, in the case of dynamic stability, VAT panels exhibit better dynamic performance than the straight-fiber and quasi-isotropic laminates. It is also found that with the increase in delamination area around the cutout, the critical buckling load and natural frequency of the laminate decreases. The onset of DIR in VAT laminates start at lower frequencies and reduces to a smaller range of critical buckling loads with an increase in the delamination area. This leads to decrease in the dynamic stability of the VAT panels. However, the decrease in the stability in VAT panels with an increase in the delamination area is much less than the case of straight-fiber laminates. Moreover, VAT laminates for some fiber-angle configurations exhibit higher buckling resistance and dynamic stability when compared to straight-fiber and quasi-isotropic laminates even in the presence of damages like delamination and cutout.

Further, the analysis has been extended to the curved panels with VAT laminate. Donnell's shallow shell theory is used to model the curved VAT panel and solved using the generalized differential integral quadrature method. The analysis is performed

for three different types of boundary conditions (SSSS, CCCC, SCSC). In all the cases, curved VAT panels exhibit better structural performance compared to straight-fiber laminates as in the case of flat VAT panels. The effect of radius of curvature and the fiber-angle variation on the structural performance of the curved panels is investigated. It is found that the critical buckling load and dynamic stability increases with the decrease in the radius of curvature of a curved VAT panel irrespective to the fiber-angle variation. Also, with an increase in the aspect ratio, buckling, and dynamic performance of a curved VAT panel improves.

From the investigations performed in this thesis, it is evident that the VAT panels over a range of fiber-angle configurations exhibit better buckling and dynamic stability characteristics than the traditional straight-fiber composite laminates. Also, VAT panels have the added advantage of tailoring the stiffness and dynamic properties of the panel simultaneously. The VAT designs show promise for lightweight structural applications, providing that the behavior is robust and that other factors (including strength and manufacturability) do not outweigh the benefits.

In the second part of the thesis, the Floquet theory has been used to determine the dynamic stability characteristics of the VAT panel. As the implementation of the Floquet theory to a large degree of freedom system is computationally expensive, an implicit Floquet analysis has been used. The Arnoldi algorithm is combined with the Floquet theory to determine the stability behavior of the periodic systems. Upon using implicit Floquet analysis, a significant reduction in computational cost, as well as computational time, is observed when compared to that of the classical Floquet analysis. The dynamic instability regions in an undamped and damped VAT composite panels are then determined using implicit Floquet method and compared with that of the solutions obtained from Bolotin's method. Further, the instability regions obtained from the implicit Floquet analysis are verified using the time response of the VAT panel from the numerical integration. It is found that significant deviations are observed between the instability regions obtained from the implicit Floquet analysis and Bolotin's approach. Upon using implicit Floquet analysis, in addition to the stability boundary, spectral radius information can also be obtained through which the rate of growth or decay of oscillations in a damped VAT panel can be found.

Additionally, the effect of structural damping on the variation of μ_{max} in a VAT panel is studied for different values of damping coefficients (β). It is observed that, with the increase in the damping coefficient in VAT panels, the rate of change in μ_{max} decreases. Also, the number of unstable peaks present in the VAT panel reduces with the increase in the damping coefficient. Furthermore, by studying the variation in the

eigenvalues of the system at the stability boundaries, it is found that the VAT panel loses its stability through a flip bifurcation (or period-doubling bifurcation) at the first instability region and at the second instability region the panel undergo one of the three types of bifurcation (i) symmetry-breaking (ii) cyclic-fold and (iii) transcritical bifurcation. These analyses clearly demonstrate the benefits of using implicit Floquet analysis over Bolotin's method to analyze the dynamic stability behavior of the VAT panels.

6.2 Future work

While an attempt has been made to thoroughly examine the dynamic stability behavior of the VAT composite panel under in-plane periodic compression load, other considerations still exist. A few of them are discussed below:

- **Optimization studies**

Based on the results obtained from this work, it is clear that VAT composite panel with certain fiber-angle configuration exhibit better buckling and dynamic properties compared to straight-fiber composite panel. However, a structural optimization framework will be needed to determine the optimal fiber-angle configuration to maximize the VAT panel performance.

- **Analysis on complicated VAT structures**

Even though the stability analysis in this work is limited to flat and curved VAT panels with simple boundary conditions, the analysis can be extended to a wide variety of complicated structures like stiffened VAT panels, cylindrical VAT structures, box-beam structures with physical boundary conditions.

- **Experimental studies on dynamics of VAT panel**

There has been an enormous work being carried out on the static and dynamic analysis of the VAT composite panels, but still there exists a lack of experimental analysis especially for dynamics of VAT panel. Therefore, experiments has to be carried out on the dynamic behavior of VAT panel to understand them completely.

- **Non-linear behavior of VAT composite panels**

For many practical and engineering applications it was recognized that linearized models which provide no more than first-order approximation are inadequate. To predict the nonlinear behavior of VAT composite panels under various loading conditions, large deformation effects have to be considered. Such that the complex nonlinear VAT response can be captured accurately.

Appendix A

Analytical formulation

A.1 Natural frequency of an orthotropic simply-supported composite laminate

Analytical expression to calculate the natural frequency of an orthotropic symmetric composite laminate is discussed in this section. In a balanced-symmetric composite laminate, neither the shear-extension nor bending-extension coupling exists. Further, the anisotropic bend-twist coupling effects of the laminate are ignored. That is, the laminate stiffness solely consists of A_{11} , A_{12} , A_{22} , A_{66} , D_{11} , D_{12} , D_{22} , and D_{66} . The partial differential equation that governs the modal behavior of an orthotropic symmetric laminate is given as:

$$D_{11} \frac{\partial^4 w}{\partial x^4} + 2(D_{12} + 2D_{66}) \frac{\partial^4 w}{\partial x^2 \partial y^2} + D_{22} \frac{\partial^4 w}{\partial y^4} + \rho \frac{\partial^2 w}{\partial t^2} = 0 \quad (\text{A.1})$$

The simply-supported boundary conditions are given as follows:

$$x = 0, a : \quad w = 0, \quad M_x = -D_{11} \frac{\partial^2 w}{\partial x^2} - D_{12} \frac{\partial^2 w}{\partial y^2} = 0 \quad (\text{A.2})$$

$$y = 0, b : \quad w = 0, \quad M_y = -D_{22} \frac{\partial^2 w}{\partial y^2} - D_{12} \frac{\partial^2 w}{\partial x^2} = 0 \quad (\text{A.3})$$

The free vibration of an elastic continuum is harmonic, and the solution can be chosen as follows:

$$w(x, y, t) = (A \cos(\omega t) + B \sin(\omega t)) w(x, y) \quad (\text{A.4})$$

The transverse displacement function that satisfies the simply-supported plate boundary conditions is chosen as:

$$w(x, y) = \sin\left(\frac{m\pi x}{a}\right) \sin\left(\frac{n\pi y}{b}\right) \quad (\text{A.5})$$

On substituting Eqs. (A.4) and (A.5) in Eq. (A.1), the expression for the natural frequency of an orthotropic laminate is obtained as follows:

$$\omega^2 = \frac{\pi^4}{\rho} \left[D_{11} \left(\frac{m}{a}\right)^4 + 2(D_{12} + 2D_{66}) \left(\frac{m}{a}\right)^2 \left(\frac{n}{b}\right)^2 + D_{22} \left(\frac{n}{b}\right)^4 \right] \quad (\text{A.6})$$

Here, ω corresponds to the natural frequencies and m, n corresponds to the different mode shapes of w . The fundamental (first) natural frequency of the laminate can be evaluated by choosing $m = n = 1$.

A.2 Critical buckling load of an orthotropic simply-supported composite laminate under axial compression

Analytical expression for the critical buckling load of an orthotropic composite laminate under uniaxial compression is discussed in this section. In the derivation, the anisotropic effects of shear-extension and bend-twist coupling effects are neglected. The governing differential equation for the buckling of an orthotropic laminate is expressed as follows:

$$D_{11} \frac{\partial^4 w}{\partial x^4} + 2(D_{12} + 2D_{66}) \frac{\partial^4 w}{\partial x^2 \partial y^2} + D_{22} \frac{\partial^4 w}{\partial y^4} + \bar{N}_x \frac{\partial^2 w}{\partial x^2} = 0, \quad (\text{A.7})$$

The simply-supported boundary conditions are given as:

$$x = 0, a : \quad w = 0, \quad M_x = -D_{11} \frac{\partial^2 w}{\partial x^2} - D_{12} \frac{\partial^2 w}{\partial y^2} = 0 \quad (\text{A.8})$$

$$y = 0, b : \quad w = 0, \quad M_y = -D_{22} \frac{\partial^2 w}{\partial y^2} - D_{12} \frac{\partial^2 w}{\partial x^2} = 0 \quad (\text{A.9})$$

The solution of the fourth-order partial differential equation and associated boundary conditions are satisfied by the following lateral displacement function:

$$w(x, y) = A_{mn} \sin\left(\frac{m\pi x}{a}\right) \sin\left(\frac{n\pi y}{b}\right) \quad (\text{A.10})$$

Here, m and n are the number of buckle half wavelengths in the x- and y- directions, respectively. After substitution and simplification, the critical buckling load of an orthotropic laminate is given as:

$$\bar{N}_x = \pi^2 \left[D_{11} \left(\frac{m}{a}\right)^2 + 2(D_{12} + 2D_{66}) \left(\frac{n}{b}\right)^2 + D_{22} \left(\frac{n}{b}\right)^2 \left(\frac{a}{m}\right)^2 \right] \quad (\text{A.11})$$

For a square laminate the smallest value of \bar{N}_x occurs when $m = n = 1$.

List of publications

- **S. Samukham**, Gangadharan R., and C. P. Vyasarayani, "*Parametric instabilities of variable angle tow composite laminate under axial compression*", Composite Structures, 166, pp. 229-238, 2017.
- **S. Samukham**, Gangadharan R., Z. Wu, and C. P. Vyasarayani, "*Dynamic instability analysis of variable angle tow composite plate with delamination around a cut-out*", Mechanics of Advanced Materials and Structures, 26(1), pp. 62-70, 2019.
- **S. Samukham**, Gangadharan R., C. P. Vyasarayani, P. Weaver, "*Dynamic instability of curved variable angle tow composite panel under axial compression*", Thin-Walled Structures, 138, pp. 302-312, 2019.
- **S. Samukham**, C. P. Vyasarayani, and Gangadharan R., "*Implicit Floquet analysis for the parametric instabilities in variable angle tow composite panels*", Composite Structures, 111637, 2019.

References

- [1] B. C. Kim, P. M. Weaver, and K. Potter. Manufacturing characteristics of the continuous tow shearing method for manufacturing of variable angle tow composites. *Composites Part A: Applied Science and Manufacturing* 61, (2014) 141–151.
- [2] S. Nagendra, S. Kodiyalam, J. Davis, and V. Parthasarathy. Optimization of tow fiber paths for composite design. In 36th Structures, Structural Dynamics and Materials Conference. 1995 1275.
- [3] C. Waldhart, Z. Gurdal, and C. Ribbens. Analysis of tow placed, parallel fiber, variable stiffness laminates. In 37th Structure, Structural Dynamics and Materials Conference. 1996 1569.
- [4] B. F. Tatting, Z. Gurdal, and D. Jegley. Design and manufacture of elastically tailored tow placed plates. *NASA Technical Reports Server* .
- [5] D. C. Jegley, B. F. Tatting, and Z. Guerdal. Automated Finite Element Analysis of Elastically-Tailored Plates. *NASA Technical Reports Server* .
- [6] H. J. L. Dirk, C. Ward, and K. D. Potter. The engineering aspects of automated prepreg layup: History, present and future. *Composites Part B: Engineering* 43, (2012) 997–1009.
- [7] Z. Gurdal, B. Tatting, and K. Wu. Tow-placement technology and fabrication issues for laminated composite structures. In 46th AIAA/ASME/ASCE/AHS/ASC Structures, Structural Dynamics and Materials Conference. 2005 2017.
- [8] C. Lopes. Damage and failure of non-conventional composite laminates .
- [9] S. T. IJsselmuiden. Optimal design of variable stiffness composite structures using lamination parameters .

- [10] B. Kim, K. Hazra, P. Weaver, and K. Potter. Limitations of fibre placement techniques for variable angle tow composites and their process-induced defects. In Proceedings of the 18th International Conference on Composite Materials (ICMM18), Jeju, Korea. 2011 21–26.
- [11] B. C. Kim, K. Potter, and P. M. Weaver. Continuous tow shearing for manufacturing variable angle tow composites. *Composites Part A: Applied Science and Manufacturing* 43, (2012) 1347–1356.
- [12] K. Gliesche, T. Hübner, and H. Orawetz. Application of the tailored fibre placement (TFP) process for a local reinforcement on an open-hole tension plate from carbon/epoxy laminates. *Composites Science and Technology* 63, (2003) 81–88.
- [13] P. Mattheij, K. Gliesche, and D. Feltin. Tailored fiber placement-mechanical properties and applications. *Journal of reinforced plastics and composites* 17, (1998) 774–786.
- [14] A. Spickenheuer, M. Schulz, K. Gliesche, and G. Heinrich. Using tailored fibre placement technology for stress adapted design of composite structures. *Plastics, Rubber and Composites* 37, (2008) 227–232.
- [15] G. G. Lozano, A. Tiwari, C. Turner, and S. Astwood. A review on design for manufacture of variable stiffness composite laminates. *Proceedings of the Institution of Mechanical Engineers, Part B: Journal of Engineering Manufacture* 230, (2016) 981–992.
- [16] M. W. Hyer and H. Lee. The use of curvilinear fiber format to improve buckling resistance of composite plates with central circular holes. *Composite Structures* 18, (1991) 239–261.
- [17] A. Leissa and A. Martin. Vibration and buckling of rectangular composite plates with variable fiber spacing. *Composite Structures* 14, (1990) 339–357.
- [18] Z. Gurdal and R. Olmedo. In-plane response of laminates with spatially varying fiber orientations-variable stiffness concept. *AIAA Journal* 31, (1993) 751–758.
- [19] R. Olmedo and Z. Gurdal. Buckling response of laminates with spatially varying fiber orientations. In 34th Structures, Structural Dynamics and Materials Conference. 1993 1567.

- [20] K. C. Wu and Z. Gurdal. Variable stiffness panel structural analyses with material nonlinearity and correlation with tests. In 47th AIAA/ASME/ASCE/AHS/ASC Structures, Structural Dynamics, and Materials Conference 14th AIAA/ASME/AHS Adaptive Structures Conference 7th. 2006 2165.
- [21] Z. Gurdal, B. F. Tatting, and C. Wu. Variable stiffness composite panels: effects of stiffness variation on the in-plane and buckling response. *Composites Part A: Applied Science and Manufacturing* 39, (2008) 911–922.
- [22] A. Alhajahmad, M. M. Abdalla, and Z. Gurdal. Design tailoring for pressure pillowling using tow-placed steered fibers. *Journal of Aircraft* 45, (2008) 630–640.
- [23] P. Weaver, K. Potter, K. Hazra, M. Saverymuthapulle, and M. Hawthorne. Buckling of variable angle tow plates: from concept to experiment. In 50th AIAA/ASME/ASCE/AHS/ASC Structures, Structural dynamics, and Materials Conference. 2009 2509.
- [24] G. Raju, Z. Wu, B. C. Kim, and P. M. Weaver. Prebuckling and buckling analysis of variable angle tow plates with general boundary conditions. *Composite Structures* 94, (2012) 2961–2970.
- [25] G. Raju, Z. Wu, and P. M. Weaver. Postbuckling analysis of variable angle tow plates using differential quadrature method. *Composite Structures* 106, (2013) 74–84.
- [26] Z. Wu, G. Raju, and P. M. Weaver. Postbuckling analysis of variable angle tow composite plates. *International Journal of Solids and Structures* 50, (2013) 1770–1780.
- [27] R. Groh, P. M. Weaver, S. White, G. Raju, and Z. Wu. A 2D equivalent single-layer formulation for the effect of transverse shear on laminated plates with curvilinear fibres. *Composite Structures* 100, (2013) 464–478.
- [28] B. H. Coburn, Z. Wu, and P. M. Weaver. Buckling analysis of stiffened variable angle tow panels. *Composite Structures* 111, (2014) 259–270.
- [29] B. H. Coburn and P. M. Weaver. Buckling analysis, design and optimisation of variable-stiffness sandwich panels. *International Journal of Solids and Structures* 96, (2016) 217–228.

- [30] X. Chen, Z. Wu, G. Nie, and P. Weaver. Buckling analysis of variable angle tow composite plates with a through-the-width or an embedded rectangular delamination. *International Journal of Solids and Structures* 138, (2018) 166–180.
- [31] S. C. White, P. M. Weaver, and K. C. Wu. Post-buckling analyses of variable-stiffness composite cylinders in axial compression. *Composite Structures* 123, (2015) 190–203.
- [32] C. B. Nian, X. P. Wang, and J. Y. Pei. Buckling Analysis of Variable Stiffness Composite Cylindrical Shells Based on Hermite Curves. In *Key Engineering Materials*, volume 805. Trans. Tech. Publ., 2019 191–197.
- [33] E. Labans and C. Bisagni. Buckling and free vibration study of variable and constant-stiffness cylindrical shells. *Composite Structures* 210, (2019) 446–457.
- [34] S. Honda and Y. Narita. Vibration design of laminated fibrous composite plates with local anisotropy induced by short fibers and curvilinear fibers. *Composite Structures* 93, (2011) 902–910.
- [35] H. Akhavan and P. Ribeiro. Natural modes of vibration of variable stiffness composite laminates with curvilinear fibers. *Composite Structures* 93, (2011) 3040–3047.
- [36] M. Hachemi, S. Hamza Cherif, and A. Houmat. Free vibration analysis of variable stiffness composite laminate plate with circular cutout. *Australian Journal of Mechanical Engineering* 50, (2017) 1–17.
- [37] A. Houmat. Nonlinear free vibration analysis of variable stiffness symmetric skew laminates. *European Journal of Mechanics-A/Solids* 50, (2015) 70–75.
- [38] P. Ribeiro and S. Stoykov. Forced periodic vibrations of cylindrical shells in laminated composites with curvilinear fibres. *Composite Structures* 131, (2015) 462–478.
- [39] H. Akhavan and P. Ribeiro. Geometrically non-linear periodic forced vibrations of imperfect laminates with curved fibres by the shooting method. *Composites Part B: Engineering* 109, (2017) 286–296.
- [40] P. Ribeiro and H. Akhavan. Non-linear vibrations of variable stiffness composite laminated plates. *Composite Structures* 94, (2012) 2424–2432.

- [41] P. Ribeiro. Non-linear modes of vibration of thin cylindrical shells in composite laminates with curvilinear fibres. *Composite Structures* 122, (2015) 184–197.
- [42] A. Viglietti, E. Zappino, and E. Carrera. Free vibration analysis of variable angle-tow composite wing structures. *Aerospace Science and Technology* .
- [43] S. Setoodeh, M. M. Abdalla, S. T. IJsselmuiden, and Z. Gurdal. Design of variable-stiffness composite panels for maximum buckling load. *Composite Structures* 87, (2009) 109–117.
- [44] S. T. IJsselmuiden, M. M. Abdalla, and Z. Gurdal. Optimization of variable-stiffness panels for maximum buckling load using lamination parameters. *AIAA Journal* 48, (2010) 134–143.
- [45] Z. Wu, P. M. Weaver, G. Raju, and B. C. Kim. Buckling analysis and optimisation of variable angle tow composite plates. *Thin-walled Structures* 60, (2012) 163–172.
- [46] O. Stodieck, J. Cooper, P. Weaver, and P. Kealy. Aeroelastic tailoring of a representative wing box using tow-steered composites. *AIAA Journal* 1425–1439.
- [47] B. K. Stanford and C. V. Jutte. Comparison of curvilinear stiffeners and tow steered composites for aeroelastic tailoring of aircraft wings. *Computers & Structures* 183, (2017) 48–60.
- [48] S. M. Barr and J. W. Jaworski. Optimization of tow-steered composite wind turbine blades for static aeroelastic performance. *Renewable Energy* 139, (2019) 859–872.
- [49] V. Bolotin. The dynamic stability of elastic systems. *American Journal of Physics* 33, (1965) 752–753.
- [50] D. Krajcinovic and G. Herrmann. Numerical solution of the dynamic stability problems. *International Journal for Numerical Methods in Engineering* 2, (1970) 551–561.
- [51] R. C. Duffield and N. Willems. Parametric resonance of stiffened rectangular plates. *Journal of Applied Mechanics* 39, (1972) 217–226.
- [52] R. G. Merritt and N. Willems. Parametric resonance of skew stiffened plates. *Journal of Applied Mechanics* 40, (1973) 439–444.

- [53] J. Tani and T. Nakamura. Dynamic stability of annular plates under periodic radial loads. *The Journal of the Acoustical Society of America* 64, (1978) 827–831.
- [54] V. Birman. Dynamic stability of unsymmetrically laminated rectangular plates. *Mechanics Research Communications* 12, (1985) 81–86.
- [55] R. Srinivasan and P. Chellapandi. Dynamic stability of rectangular laminated composite plates. *Computers & Structures* 24, (1986) 233–238.
- [56] C. W. Bert and V. Birman. Dynamic instability of shear deformable anti-symmetric angle-ply plates. *International Journal of Solids and Structures* 23, (1987) 1053–1061.
- [57] C. Lien-Wen and Y. Jenq Yiing. Dynamic stability of laminated composite plates by the finite element method. *Computers & Structures* 36, (1990) 845–851.
- [58] J. Moorthy, J. Reddy, and R. Plaut. Parametric instability of laminated composite plates with transverse shear deformation. *International Journal of Solids and Structures* 26, (1990) 801–811.
- [59] G. Cederbaum. Dynamic instability of shear-deformable laminated plates. *AIAA Journal* 29, (1991) 2000–2005.
- [60] M. Mond and G. Cederbaum. Dynamic instability of antisymmetric laminated plates. *Journal of Sound and Vibration* 154, (1992) 271–279.
- [61] R. Pavlovic. Dynamic stability of antisymmetrically laminated angle-ply rectangular plates subjected to random excitation. *Journal of Sound and Vibration* 171, (1994) 87–95.
- [62] M. Rasool and M. Singha. Stability of Variable Stiffness Composite laminates under Compressive and Shearing Follower Forces. *Composite Structures* 111003.
- [63] A. Chattopadhyay and A. G. Radu. Dynamic instability of composite laminates using a higher order theory. *Computers & Structures* 77, (2000) 453–460.
- [64] S. Wang and D. Dawe. Dynamic instability of composite laminated rectangular plates and prismatic plate structures. *Computer Methods in Applied Mechanics and Engineering* 191, (2002) 1791–1826.

- [65] S. Sahu and P. Datta. Dynamic instability of laminated composite rectangular plates subjected to non-uniform harmonic in-plane edge loading. *Proceedings of the Institution of Mechanical Engineers, Part G: Journal of Aerospace Engineering* 214, (2000) 295–312.
- [66] M. P. Nemeth. Buckling behavior of compression-loaded symmetrically laminated angle-ply plates with holes. *AIAA Journal* 26, (1988) 330–336.
- [67] K. Srivatsa and A. K. Murty. Stability of laminated composite plates with cut-outs. *Computers & Structures* 43, (1992) 273–279.
- [68] H. Lee and S. Lim. Free vibration of isotropic and orthotropic square plates with square cutouts subjected to in-plane forces. *Computers & Structures* 43, (1992) 431–437.
- [69] D. Prabhakara and P. Datta. Vibration, buckling and parametric instability behaviour of plates with centrally located cutouts subjected to in-plane edge loading (tension or compression). *Thin-Walled Structures* 27, (1997) 287–310.
- [70] A. G. Radu and A. Chattopadhyay. Dynamic stability analysis of composite plates including delaminations using a higher order theory and transformation matrix approach. *International Journal of Solids and Structures* 39, (2002) 1949–1965.
- [71] J. Mohanty, S. K. Sahu, and P. K. Parhi. Parametric instability of delaminated composite plates subjected to periodic in-plane loading. *Journal of Vibration and Control* 21, (2015) 419–434.
- [72] J. Yang and Y. Fu. Analysis of dynamic stability for composite laminated cylindrical shells with delaminations. *Composite Structures* 78, (2007) 309–315.
- [73] M. H. Noh and S. Y. Lee. Dynamic instability of delaminated composite skew plates subjected to combined static and dynamic loads based on HSDT. *Composites Part B: Engineering* 58, (2014) 113–121.
- [74] F. Ju, H. Lee, and K. Lee. Free vibration of composite plates with delaminations around cutouts. *Composite Structures* 31, (1995) 177–183.
- [75] A. Kumar and R. Shrivastava. Free vibration of square laminates with delamination around a central cutout using HSDT. *Composite Structures* 70, (2005) 317–333.

- [76] R. M. Evan-Iwanowski. On the parametric response of structures. *Applied Mechanics Review*, 18, (1965) 699–702.
- [77] R. Ibrahim. Parametric Vibration, Part-III, Current Problems 1. *Shock Vib. Dig.* 10, (1978) 41–57.
- [78] G. J. Simitzes. Instability of dynamically-loaded structures. *Applied Mechanics Reviews* 40, (1987) 1403–1408.
- [79] S. Sahu and P. Datta. Research advances in the dynamic stability behavior of plates and shells: 1987–2005 Part I: conservative systems. *Applied Mechanics Reviews* 60, (2007) 65–75.
- [80] J. C. Yao. Dynamic stability of cylindrical shells under static and periodic axial and radial loads. *AIAA Journal* 1, (1963) 1391–1396.
- [81] G. Cederbaum. Analysis of parametrically excited laminated shells. *International Journal of Mechanical Sciences* 34, (1992) 241–250.
- [82] A. Argento and R. Scott. Dynamic instability of layered anisotropic circular cylindrical shells, Part I: Theoretical development. *Journal of Sound and Vibration* 162, (1993) 311–322.
- [83] M. Ganapathi, T. Varadan, and V. Balamurugan. Dynamic instability of laminated composite curved panels using finite element method. *Computers & Structures* 53, (1994) 335–342.
- [84] S. Sahu and P. Datta. Parametric resonance characteristics of laminated composite doubly curved shells subjected to non-uniform loading. *Journal of Reinforced Plastics and Composites* 20, (2001) 1556–1576.
- [85] T. Ng, K. Lam, and J. Reddy. Parametric resonance of a rotating cylindrical shell subjected to periodic axial loads. *Journal of Sound and Vibration* 214, (1998) 513–529.
- [86] K. Lam and T. Ng. Dynamic stability of cylindrical shells subjected to conservative periodic axial loads using different shell theories. *Journal of Sound and Vibration* 207, (1997) 497–520.
- [87] M. Ganapathi, B. Patel, and C. Sambandam. Parametric dynamic instability analysis of laminated composite conical shells. *Journal of Reinforced Plastics and Composites* 18, (1999) 1336–1346.

- [88] S. Sahu and P. Datta. Dynamic stability of laminated composite curved panels with cutouts. *Journal of Engineering Mechanics* 129, (2003) 1245–1253.
- [89] T. Park and S.-Y. Lee. Parametric instability of delaminated composite spherical shells subjected to in-plane pulsating forces. *Composite Structures* 91, (2009) 196–204.
- [90] S. Patel, P. Datta, and A. Sheikh. Dynamic stability analysis of stiffened shell panels with cutouts. *Journal of Applied Mechanics* 76, (2009) 041,004.
- [91] S. K. Panda and L. Ramachandra. Parametric instability of laminated composite cylindrical panels subjected to periodic non-uniform in-plane loads. *International Journal of Applied Mechanics* 3, (2011) 845–865.
- [92] M. Ganapathi, P. Boisse, and D. Solaut. Non-linear dynamic stability analysis of composite laminates under periodic in-plane compressive loads. *International Journal for Numerical Methods in Engineering* 46, (1999) 943–956.
- [93] A. Kumar and B. Patel. Nonlinear dynamic response of elliptical cylindrical shell under Harmonic excitation. *International Journal of Non-Linear Mechanics* 98, (2018) 102–113.
- [94] J. Whitney. The effect of transverse shear deformation on the bending of laminated plates. *Journal of Composite Materials* 3, (1969) 534–547.
- [95] E. Oñate. Structural analysis with the finite element method. Linear statics: volume 2: beams, plates and shells. Springer Science & Business Media, 2013.
- [96] R. M. Jones. Mechanics of Composite Materials. CRC press, 2014.
- [97] H. Suemasu, T. Kumagai, and K. Gozu. Compressive behavior of multiply delaminated composite laminates Part I: Experiment and analytical development. *AIAA Journal* 36, (1998) 1279–1285.
- [98] D. Shu. Buckling of multiple delaminated beams. *International Journal of Solids and Structures* 35, (1998) 1451–1465.
- [99] M. H. Shen and J. Grady. Free vibrations of delaminated beams. *AIAA Journal* 30, (1992) 1361–1370.
- [100] H. Luo and S. Hanagud. Dynamics of delaminated beams. *International Journal of Solids and Structures* 37, (2000) 1501–1519.

- [101] D. Shu and C. N. Della. Vibrations of multiple delaminated beams. *Composite Structures* 64, (2004) 467–477.
- [102] X. Chen, G. Nie, and Z. Wu. Dynamic instability of variable angle tow composite plates with delamination. *Composite Structures* 187, (2018) 294–307.
- [103] R. M. Jones. Mechanics of composite materials, volume 193. Scripta Book Company, Washington, DC, 1975.
- [104] L. H. Donnell. Stability of thin-walled tubes under torsion. *No.NACA-R-479 California Inst. of Tech., Pasadena, USA.* .
- [105] K. Soldatos. A comparison of some shell theories used for the dynamic analysis of cross-ply laminated circular cylindrical panels. *Journal of Sound and Vibration* 97, (1984) 305–319.
- [106] S. Samukham, G. Raju, and C. P. Vyasarayani. Parametric instabilities of variable angle tow composite laminate under axial compression. *Composite Structures* 166, (2017) 229–238.
- [107] S. C. White, G. Raju, and P. M. Weaver. Initial post-buckling of variable-stiffness curved panels. *Journal of the Mechanics and Physics of Solids* 71, (2014) 132–155.
- [108] G. Raju, Z. Wu, S. White, and P. M. Weaver. Optimal postbuckling design of variable angle tow composite plates. *AIAA Journal* 56, (2018) 2045–2061.
- [109] R. Bellman, B. Kashef, and J. Casti. Differential quadrature: a technique for the rapid solution of nonlinear partial differential equations. *Journal of Computational Physics* 10, (1972) 40–52.
- [110] A. Sherbourne and M. Pandey. Differential quadrature method in the buckling analysis of beams and composite plates. *Computers & Structures* 40, (1991) 903–913.
- [111] X. Wang, M. Tan, and Y. Zhou. Buckling analyses of anisotropic plates and isotropic skew plates by the new version differential quadrature method. *Thin-Walled Structures* 41, (2003) 15–29.
- [112] C. Shu. Differential quadrature and its application in engineering. Springer Science & Business Media, 2012.

- [113] R. Penrose. A generalized inverse for matrices. In *Mathematical proceedings of the Cambridge philosophical society*, volume 51. Cambridge University Press, 1955 406–413.
- [114] H. Zhang and F. Ding. On the Kronecker products and their applications. *Journal of Applied Mathematics* 2013.
- [115] S. C. White. Post-buckling of variable-stiffness shell structures. *PhD Thesis, University of Bristol* .
- [116] M. Ganapathi, B. Patel, C. Sambandam, and M. Touratier. Dynamic instability analysis of circular conical shells. *Composite Structures* 46, (1999) 59–64.
- [117] J. Oh, M. Cho, and J. S. Kim. Dynamic analysis of composite plate with multiple delaminations based on higher-order zigzag theory. *International Journal of Solids and Structures* 42, (2005) 6122–6140.
- [118] A. Srivastava, P. Datta, and A. Sheikh. Dynamic instability of stiffened plates subjected to non-uniform harmonic in-plane edge loading. *Journal of Sound and Vibration* 262, (2003) 1171–1189.
- [119] P. Dey and M. Singha. Dynamic stability analysis of composite skew plates subjected to periodic in-plane load. *Thin-Walled Structures* 44, (2006) 937–942.
- [120] S. Subramanian, G. Gaonkar, J. Nagabhushanam, and R. Nakadi. Parallel computing concepts and methods for Floquet analysis of helicopter trim and stability. *Journal of the American Helicopter Society* 41, (1996) 370–382.
- [121] O. A. Bauchau and Y. G. Nikishkov. An implicit Floquet analysis for rotorcraft stability evaluation. *Journal of the American Helicopter Society* 46, (2001) 200–209.
- [122] J. N. Reddy. *Mechanics of laminated composite plates and shells: theory and analysis*. CRC press, 2004.
- [123] Z. Bai, J. Demmel, J. Dongarra, A. Ruhe, and H. Van Der Vorst. *Templates for the solution of algebraic eigenvalue problems: a practical guide*. SIAM, 2000.
- [124] W. E. Arnoldi. The principle of minimized iterations in the solution of the matrix eigenvalue problem. *Quarterly of Applied Mathematics* 9, (1951) 17–29.

- [125] Y. Saad. Krylov subspace methods for solving large unsymmetric linear systems. *Mathematics of Computation* 37, (1981) 105–126.
- [126] N. M. Newmark. A method of computation for structural dynamics. American Society of Civil Engineers, 1959 .
- [127] A. H. Nayfeh and B. Balachandran. Applied nonlinear dynamics: analytical, computational, and experimental methods. John Wiley & Sons, 2008.